Heinrich Heine
Universität
Düsseldorf

Identifying new components in plasmodesmal gating

Inaugural-Dissertation

zur Erlangung des Doktorgrades
der Mathematisch-Naturwissenschaftlichen Fakultät
der Heinrich-Heine-Universität Düsseldorf

vorgelegt von

Jona Obinna Ejike
aus Düsseldorf

Düsseldorf, Dezember 2024

aus dem Institut für Molekulare Physiologie
der Heinrich-Heine-Universität Düsseldorf

Gedruckt mit der Genehmigung der
Mathematisch-Naturwissenschaftlichen Fakultät der
Heinrich-Heine-Universität Düsseldorf

Berichterstatter:

1. Prof. Dr. Wolf B. Frommer

2. Prof. Dr. Rüdiger Simon

Tag der mündlichen Prüfung: 09.05.2025
(bitte bei der Abgabe Ihrer Dissertation noch offenlassen)

„ Ich hatte leider keine Zeit mehr ein cooles Zitat rauszusuchen :-(“

-Jona Obinna Ejike
(am Abend vor der Abgabe)

Summary
Intercellular communication is an ancient evolutionary trait and a prerequisite for multicellularity. Most multicellular species evolved intercellular connections that enable and control molecular exchange. Filamentous cyanobacteria harbor septal junctions, animals gap junctions, and fungi septal pores. The green lineage, including green algae and terrestrial plants, evolved plasmodesmata (PD). Plasma membrane (PM)-lined nanometer-sized channels that traverse the cell wall and create a cytoplasmic continuum of inter-connected cells (symplasm). PD also connect the endoplasmic reticulum (ER) of adjacent cells by a constricted ER tubule, termed the desmotubule. The PD's cytoplasmic sleeve between PM and desmotubule membrane is described as the main passageway for intercellular exchange. PD exchange small species like ions, metabolites, plant hormones and peptides, as well as macromolecules like proteins and RNAs, and hence are essential for coordinated plant growth, development, and immunity. Despite their prerequisite for plant multicellularity, the composition structure and transport mechanism of PD remain elusive.
In this thesis, I aimed to identify novel components that contribute to PD-mediated intercellular transport. Therefore, firstly, I contributed to the generation of a high-confidence PD-proteome of the basal terrestrial plant *Physcomitrium patens*. This allowed to identify evolutionary conserved PD protein families by an iterative combination of PD protein enrichment, feature scoring, and systematic-large-scale localization *in planta*. In particular, cell wall residual protein families could be robustly separated in PD- and non-PD localized phylogenetic clades. Cell wall modifications have long been described to regulate the PD aperture. Specifically, callose turnover at PD neck regions has been widely accepted as one of the regulators of the plasmodesmal transport mechanism. Where callose accumulations constrict, and callose depletion dilates the PD aperture. Notably, many transport phenomena across PD cannot be described by the size of the PD aperture alone. As PD are cytoplasmic bridges, I set out to challenge the common model and asked if there might be cytoplasmic components that control PD passage. Inspired by the nuclear pore complex (NPC), a nanometer-sized pore with similar transport properties, I hypothesized that PD might harbor a similar permeability barrier. NPCs control nucleocytoplasmic transport, forming conduits that connect transcription and translation. The permeability barrier in NPCs is a phase-separation domain formed by phenylalanine-glycine-rich nucleoporins (FG-NUP). Nucleocytoplasmic cargo transport can be facilitated by FG-interacting nuclear transport receptors (NTRs). Surprisingly, NUPs found in our *P. patens* PD proteome, localized to PD *in planta.* Further analysis of *Arabidopsis thaliana* NUPs validated the dual-localization of 7 NUPs to NPC and PD. Mutants of the plant-specific transmembrane NUP CPR5 showed callose-independent reduction of macromolecular cell-cell transport. These results indicated the functional role of NUPs in intercellular transport. To further test NUP involvement at PD, I generated an extensive list of *P. patens nup* knock-out mutants and *NUP-fluorescent protein (FP)* knock-in lines via CRISPR-Cas9 and prime editing. Finally, I provide evidence that, like in the NPC, PD passage is not only dependent on the cargo's mass and dimensions but also facilitated by NTR-like surface properties. This is demonstrated by the intercellular mobility of an engineered tetrameric NTR-like GFP, compared to a non-mobile 3xmCherry tandem of similar diameter and reduced mass. Conversely, only the movement of the tetrameric NTR-like GFP is reduced in a *fg-nup98a/b* mutant that contain less than 50% of the wild-type encoded FG content. While a 2xEGFP tandem moves similarly in WT and *fg-nup98a/b* mutant. In summary, this thesis proposes a novel PD transport mechanism in which NUPs were recruited to form a PD pore gating complex (PDPC), which enacts an FG-based phase separation that controls intercellular permeability. Simultaneously enabling facilitated passage of NTR-like cargo and exclusion of non-specific molecules.

Eidesstattliche Erklärung

Ich versichere an Eides Statt, dass die Dissertation von mir selbständig und ohne unzulässige fremde Hilfe unter Beachtung der „Grundsätze zur Sicherung guter wissenschaftlicher Praxis an der Heinrich-Heine-Universität Düsseldorf“ erstellt worden ist.

18.12.2024, Jona Obinna Ejike

Table of contents

List of abbreviations

Name	Abbreviation
GENE	*ITALICS*
Mutant	*italics*
PROTEIN	REGULAR
abscisic acid	ABA
AGAMOUS-LIKE	AGL
ALLY OF AML-1 AND LEF-1	ALY
amino acid	AA
APETALA1	AP1
armadillo repeat	ARM
AUXIN/INDOLE-3-ACETIC ACID INDUCIBLE 12	IAA12
brassinosteroid	BR
bundle sheath	BS
C. maxima PHLOEM PROTEIN16	CmPP16
CALLOSE SYNTHASES	CALS
CAPRICE	CPC
classical NLS	cNLS
coarse-grained molecular dynamics	CGMD
companion cells	CC
CONSTITUTIVE EXPRESSION OF PATHOGENESIS-RELATED GENE 5	CPR5
Cowpea mosaic virus	CPMV
CROWDED NUCLEI1	CRWN
Cucurbita maxima NON-CELL-AUTONOMOUS PROTEIN	CmNCAP
DNA BINDING WITH ONE FINGER	DOF
DOUBLE GENE BLOCK PROTEIN	DGBp
effector triggered immunity	ETI
electron tomography	ET
endoplasmic reticulum	ER
EXPORTIN5	XPO5
FLOWERING LOCUS T	FT
focused ion beam	FIB
gibberellin	GA
GLYCOPROTEIN 210	GP210
GLYCOSYL HYDROLASE 17 family	GHL17
Grapevine fanleaf virus	GFLV
GUANYLATE-BINDING PROTEIN-LIKE	GBPL3
HASTY	HST
HIGH EXPRESSION OF OSMOTICALLY RESPONSIVE GENES1	HOS1

Homeodomain	HD
immunoglobulin	IG
importin-α	IMPα
importin-β	IMPβ
INCREASED SIZE EXCLUSION LIMIT 1	ISE1
inner nuclear membrane	INM
intercellular transport motif	ITM
intermediary cells	IC
intrinsically disorder region	IDR
karyopherin-β	KAP
KNOTTED1	KN1
KNOTTED1-LIKE HOMEOBOX	KNOX
last common eukaryotic ancestor	LECA
LEAFY	LFY
liquid-liquid phase separated	LLPS
membrane contact sites	MCS
micro RNAs	miRNAs
MOVEMENT PROTEINs	MPs
MULTIPLE C2-AND TRANSMEMBRANE-DOMAIN CONTAINING PROTEINS	MCTPs
NON-CELL AUTONOMOUS PATHWAY PROTEIN1	NtNCAPP1
non-cell-autonomous proteins	NCAP
Nuclear envelope	NE
nuclear export signal	NES
nuclear localization signal	NLS
Nuclear pore complex	NPC
NUCLEAR TRANSPORT FACTOR2	NTF2
nuclear transport receptors	NTRs
nucleoporin	NUPs
one-bead-per-amino-acid	1BPA
outer nuclear membrane	ONM
pattern triggered immunity	PTI
pear WUSCHEL-RELATED HOMEOBOX	PbWOX
PHABULOSA	PHB
phenylalanine-glycine-rich nucleoporins	FG-NUPs
phloem pole pericycle	PPE
phosphatidylinositol-4-phosphate	PIP4
PLANT NE TRANSMEMBRANE1	PNET1
plasma membrane	PM
PLASMODESMATA LOCALIZED PROTEINs	PDLPs
programmed cell death	PCD
proto-sieve element	PSE

RAN guanine nucleotide exchange factor	RCC1
RAN-BINDING PROTEIN	RANBP
RAN-GTPase activating protein	RANGAP
RAS RELATED NUCLEAR PROTEIN	RAN
RETICULONS	RTN
Ribonucleoprotein	RNP
RNA-binding proteins	RBPs
rotamase cyclophilins	ROCs
salicylic acid	SA
SHOOTMERISTEM-LESS	STM
short linear motifs	SLMs
SHORTROOT	SHR
SHR INTERACTING EMBRYONIC LETHAL	SIEL
sieve-elements	SE
size exclusion limit	SEL
small interfering RNAs	siRNAs
small noncoding RNAs	sRNAs
TARGET OF MONOPTEROUS 7	TMO7
Tobacco mosaic virus	TMV
TOPLESS	TPL
transcription export complex	TREX
TRANSFORMER2	TRA2
Translocon complexes on the inner plastid membranes	TIC
Translocon complexes on the outer plastid membranes	TOC
tyrosine-glycine repeat	YG

List of Figures

Chapter I

2. General Introduction

2.1. Plasmodesmata

Plants are considered to function as supracellular organisms, in which cells form an interconnected continuum that allows processes like nutrient exchange, development, and immunity. Central to the plant's entity of interconnected cells (symplasm) are cell-cell pores termed plasmodesmata (PD) [1]. Historically, multiple botanists discovered open communication between certain cells in higher plants in the 19th century (namely Hartig, von Mohl, Nägeli, Hanstein, de Bary, Dippel, Wilhelm, Janczewski, Russow, and Tangl) [2]. Contextualizing their work, Eduard Strasburger defined the concept of '*plasmodesmen*' in 1901 [3]. PD are reported to transport proteins, peptides, RNAs, small molecules (e.g., sugars, phytohormones), and ions. PD are complex cell-cell connections that traverse the cell wall between adjacent plant cells. They harbor specialized cell wall components, multiple membranes [the plasma membrane (PM) and the endoplasmic reticulum (ER)-derived desmotubule], membrane proteins, and a cytosolic compartment in the intermembrane space of PM and desmotubule, which is termed the cytoplasmic sleeve. The cytoplasmic sleeve can vary in its diameter throughout development. In newly established PD of meristematic tissues, cytoplasmic sleeves are non-visible, as PM and ER are tightly appressed. In more differentiated cells, PD harbor up to 2.5-10 nm wide cytoplasmic sleeves, with presumably proteinaceous "spokes" that connect the PM and ER membrane [4] (Figure 1A) [2.5 nm 'presumed transport channel' in tobacco leaf PD [5], non-visible sleeve ("type I") to 10 nm sleeve ("type II") in Arabidopsis root tip [4]]. The cytoplasmic sleeve is postulated to be the main cargo passageway for PD-mediated transport. Contradictory, simple PD in tobacco leaves (2.5 nm cytoplasmic sleeve [5]) and even sleeveless PD allow non-targeted transport of the green fluorescent protein GFP (27 kDa, Stokes radius 2.8 nm [6]) [4,7], highlighting that the PD mediated transport mechanism remains elusive [1,8–11]. PD-mediated transport is described to be size-dependent, and the maximum size of diffusively passing cargo is considered as the size exclusion limit (SEL) (Figure 1B). While in some cases, non-specific molecules larger than the SEL diffuse to adjoining cells after extended time periods >24 h, effective transport of larger cargos requires active transport mechanisms [7]. PD are dynamic structures, as their SEL can be highly variable between different types of PD (simple PD SEL: 50 kDa in tobacco sink tissues vs branched PD SEL: ~1 kDa in tobacco source tissues [7]) or in different biotic or abiotic conditions (pathogen infection [12,13], diurnal cycles [14]). Additionally, PD substructure and distribution, and thereby symplasmic connectivity, can highly vary between tissues and developmental states (e.g., root cell files are symplasmically connected, in between root cell files, symplasmic connection is reduced [15,16] and root-hairs are symplasmically isolated [17]). Besides the SEL, the PD proteome is also dynamic in different conditions and mutants [18–20]. While proteomic changes in PD were reported in many mutants, evidences of direct effects of PD proteins on PD transport mechanisms are scarce. Current models of PD transport are mainly based around the β-1,3-glucan callose, which is part of the PD-derived cell wall and can accumulate in the PD neck region. Callose accumulations were shown to be accompanied by reductions in cell-cell transport rates and can even cause symplasmic isolation of tissues (e.g., in bud dormancy [21,22]), which led to a common model in which callose turnover at PD regulates the PD pore size and thereby, the SEL [23,24] (Figure 1B). Historically, it was postulated that callose deposition renders PD-associated cell walls more rigid, but recent experiments indicate the opposite: *in vitro* enrichment of callose in cellulose hydrogels increases their flexibility [25]. How those changes in cellulose flexibility translate to *in situ* transport rates remains to be revealed.

Recently, MULTIPLE C2-AND TRANSMEMBRANE-DOMAIN CONTAINING PROTEINS (MCTPs) were described as membrane tethers between the PM and desmotubule in PD [26]. MCTPs are key proteins in the formation of PDs after cell division [27] and affect PD-mediated transport in a callose-independent manner. MCTPs regulate the distance between ER and PM by binding phosphatidylinositol-4-phosphate (PIP4) in the PM via their N-terminal

C2-domains. Thus, PD were discussed as unconventional membrane contact sites (MCS) [28], which indicates that a solely callose-based model of PD-mediated transport is oversimplified. Callose-associated PD closure requires at least 30 minutes [29,30], but experiments utilizing a micropressure probe demonstrated that inducing turgor pressure differentials between *Nicotiana clevelandii* trichome cells caused a reduction of PD permeability in a time frame of 5 min [31]. Accordingly, a biophysical model was developed in which pressure-induced movement of the ER-desmotubule complex restricts passage into and throughout the cytoplasmic sleeve. The model predicts slow permeability decreases at low intercellular pressure differentials and complete PD closure at pressure differentials of Δ >150 kPa, which intriguingly matches experimental data [32]. There are also reports of rapid PD closure followed by increases of intracellular calcium concentrations, which happens in <10 s [33,34], indicating that regulation of PD permeability is multi-faceted and involves other pathways beyond callose turnover. The cytoplasmic sleeve is mostly discussed as the common cargo passageway, but elegant microinjection and particle bombardment experiments revealed that the desmotubule can also allow the size-dependent (<10kDa) passage of fluorescent dextrans and a fragment of the endogenous luminal BINDING PROTEIN (AtBIP)1 from cell-to-cell [35]. While the cytoplasmic sleeve, as well as the lumen of the desmotubule, allow cell-to-cell diffusion of cargo, FRAP experiments with fluorescent lipid analogs indicated that lateral lipid cell-to-cell diffusion is only possible via the ER membrane of the desmotubule and not the PM [36]. These findings indicate a lateral diffusion barrier in the plasmodesmal PM.
In summary, PD are highly complex and dynamic conduits that are essential for the maintenance and regulation of the multicellular plant body. Despite their importance, their ultrastructure, composition, and transport mechanism remains elusive.

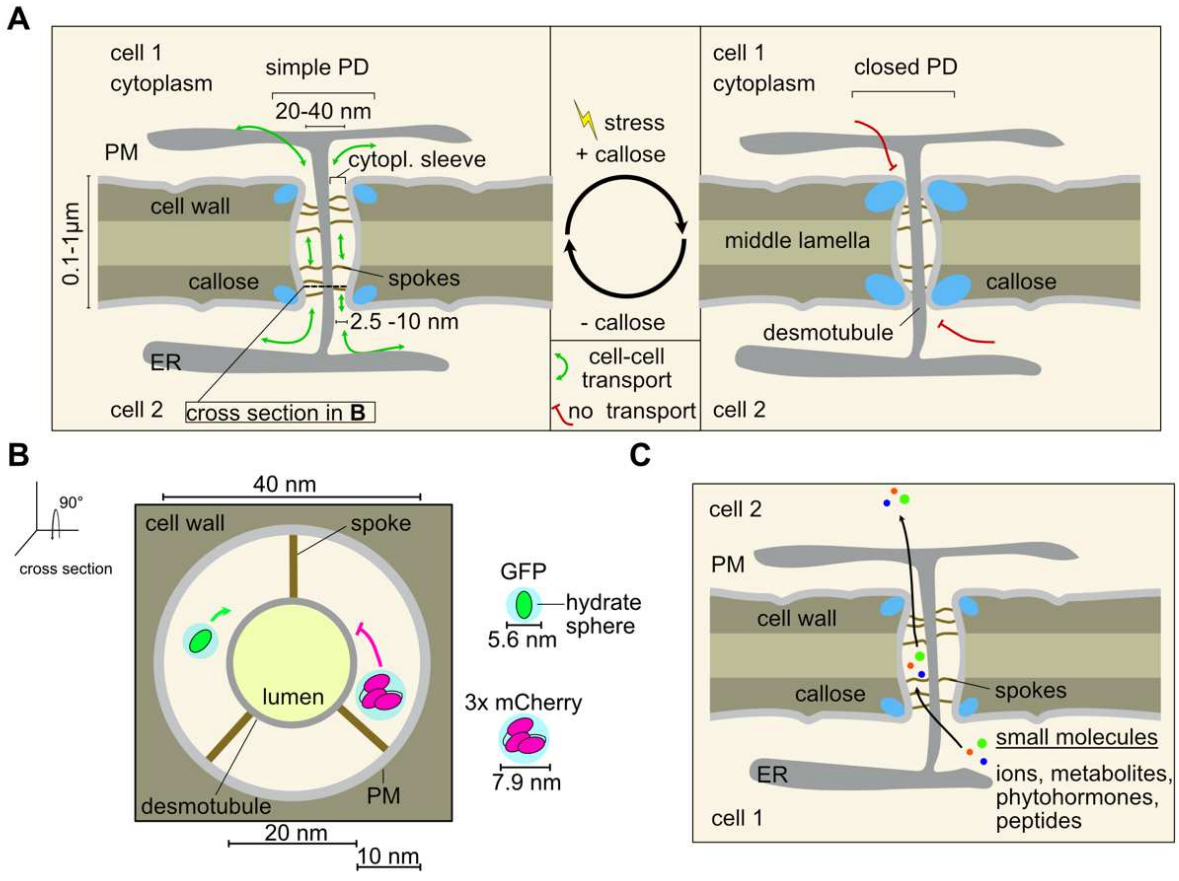

Figure 1: Plasmodesmata are cell wall-located nano-scale pores
A Illustration of a simple plasmodesmos [plural: plasmodesmata (PD)] connecting the cytoplasm of two adjacent cells. Published sizes of cell wall 0.1-1 µm, PD pore 20-40 µm and cytoplasmic sleeve 2.5-10 µm are indicated. Open PD enable intercellular transport of molecules (green arrows). Stress-induced callose accumulation can lead to changes in PD aperture, which results in reduced transport or even symplasmic isolation of cells (red arrows). **B** Illustration of the plasmodesmal cross-section. Sizes of cell-mobile (green arrow) GFP (hydrodynamic diameter 5.6 nm) and non-mobile (magenta arrow) 3xmCherry (hydrodynamic diameter 7.9 nm) are drawn to scale. Sizes of PD pore (~40 nm), desmotubule (~20 nm), and cytoplasmic sleeve (~10 nm) are based on Nicolas *et al.,* 2017 [4]. **C** Illustration depicts intercellular diffusion of small molecules, like ions, metabolites, phytohormones and peptides via PD.

2.2. Plasmodesmata formation and diversity

Throughout species, tissues, developmental stages, and environmental conditions, PD morphology is highly diverse. Depending on their developmental origin, PD are categorized into two groups. Primary PD are established after the cell division during cytokinesis by ER invagination in the forming cell plate [37] (also: "incomplete cytokinesis" [27]). During cytokinesis, the forming cell plate is punctured by numerous fenestrae, which gradually shrink and are either traversed by ER to form into primary PD or completely seal off if there is no ER present or after the traversing ER is abscised [27]. Arabidopsis RETICULONS (RTN3/ 6) are ER-tubulating proteins that are recruited to the cell plate during the late telophase. RTN3 and RTN6 transiently localize to PD in *Nicotiana benthamiana*. RTNs are less mobile at PD-proximal ER strands, which indicates an oligomerization that would result in tighter ER tubulation. Hence, it was postulated that RTNs constrict the ER into desmotubules during primary PD formation [38]. More recently, it was demonstrated that MCTPs (MCTP3, MCTP4, and MCTP6) are recruited to the cell plate in Arabidopsis root meristems and that their transmembrane region confers ER shaping functions similar to RTNs. MCTPs form higher-order oligomers that hold the ER in position and shape during primary PD formation and protect the ER from abscission during fenestrae constriction. MCTPs remain in the post-cytokinetic PD channel, while RTNs are excluded from it [27]. Primary PD are further classified into sleeveless "type I" and sleeve- and spoke-containing" type II" PD [4]. It seems likely that the spokes in type II PD observed in electron-micrographs are MCTP oligomers. Type II PD should not be confused with secondary PD, which develop in differentiated cells during cell wall extension. Secondary PD are described to "insert" at the cell wall proximal to primary PD to form twinned PD, which accumulate close to each other in so-called pit fields (in contrast to primary PD insertion, which is located randomly across the developing cell plate) [39]. In cells that develop secondary cell walls, lack of cellulose deposition at pit fields can lead to the formation of cellulose-depleted pit membranes. Pit membrane degradation can form open wall pits that enable water transport during xylem development [1,11]. Independent of their initiation (primary or secondary) PD are also classified into the categories of simple PD, which are cylindric and non-branched (type I and type II), and complex PD, which can be found in H-, Y-, and X-shapes [1,8,11]. In tobacco leaves, only simple PD allow non-targeted passage of GFP, and during the sink-source transition of the tissue, complex branched PD are established, which decreases intercellular conduit rates in the source tissues [7]. Some cell interfaces harbor unique PD morphologies that accompany specific transport phenomena. Pore-PD units are located in shoots between the phloem's companion cells (CC) and sieve-elements (SE). Pore-PD units are the last check-point before symplasmic phloem loading and harbor smaller channels towards the CC and a large pore facing the SE [11]. Funnel PD are located in roots at cell interfaces in the phloem unloading zone and harbor large entrances at the proto-sieve element (PSE) and narrower openings towards the phloem pole pericycle (PPE), which is hypothesized to assist phloem bulk flow and constitutes a larger than usual SEL (up to 112 kDa) [40]. Sugars and small molecules can pass undisturbed through funnel PD by a combination of bulk flow and

diffusion, while macromolecules were observed to traverse in discrete pulses. The pulsed unloading of macromolecules was referred to as 'batch unloading' [40]. A unique PD transport feature was found in the *N. tobacco* epidermis-trichome interface, in which the epidermis allows transport towards the basal trichome cells, but the basal trichome cells only allow transport towards distal trichome cells and not towards the epidermis [41]. It remains obscure how this unidirectional flow is established, as the PD in the basal trichome cell wall have no unique ultrastructure when observed in field emission electron microscopy [39] that might support such flow.

The mechanism of secondary PD initiation is mostly elusive. Primary and secondary PD are often difficult to distinguish. Interfaces at non-division cell walls, like between the angiosperm shoot meristems L1 layer (which divides only anticlinal and gives rise to the epidermis) and the L2/ 3 layers (which divides in all planes and gives rise to the subepidermal cells), are used to reliably examine secondary PD formation [42]. Through genetic screens, it was shown that loss of INCREASED SIZE EXCLUSION LIMIT 1 (ISE1) (mitochondrial RNA helicase) and ISE2 (chloroplastic RNA helicase) have increased SEL in the embryos mid-torpedo stage. *ise1/ 2* mutants are embryo-lethal, as they fail to retain symplasmic isolation, which is required for completing embryogenesis [43,44]. Controversially to established models in which complex PD restrict symplasmic connectivity, ISE1/ 2 silencing increases intercellular transport but also increases complex secondary PD formation, as demonstrated between epidermis and mesophyll cells [45]. Later, it was demonstrated that in ISE2 and other chloroplast genes that influence SEL, callose deposition at PD is decreased, which can explain the discrepancies to previously reported transport rates of complex PD [46]. Other interfaces that ensure definite secondary PD investigation are graft junctions and interspecies contact sites with parasitic plants [e.g., in the genus *Cuscuta* (dodder)] [42]. In Arabidopsis hypocotyl homograft junctions, secondary PD were mainly observed in thin cell walls of <100 nm, which indicates that secondary PD formation requires cell wall thinning (average Arabidopsis hypocotyl cell wall 150-200 nm). In thicker cell walls, "hemi-PD" U-formed ER invaginations that do not span the entire length of the cell wall were observed. Interestingly, the penetration depth of hemi-PD was also ~100 nm. Therefore, it was postulated that thicker cell walls require synchronized cell wall thinning and ER-invagination from both sides of the interface [47]. In some instances, it was observed that the pores that form between graft junctions can allow the cell-to-cell movement of whole organelles (amoeboid plastids – small, highly motile dedifferentiated plastids). But these events likely happen before ER invagination and initiation of mature PD [48]. Secondary PD at the host-parasitic plant interface of Arabidopsis and *Cuscuta australis* were shown to permit extensive bidirectional protein transport. Further, there is evidence of thousands of mRNAs that are transported from host to parasite, as well as microRNAs that target host gene expression and even plant viruses that move from parasite to host [49]. In concert with the results from homografts, especially junctions in heterografts indicate that secondary PD formation likely requires coordination of cell wall thinning from both sides of the interface. Yet the molecular mechanism behind secondary PD formation that enables coordinated initiation of cell wall thinning and directed ER invagination at cell wall fenestrae remains largely elusive. While the molecular basis of PD formation remains to be investigated, it can be summarized that PD substructure is highly diverse, which enables differential transport capacities in different tissues and cell types. Further, PD can constitute a selective barrier at certain cell interfaces that enables directional transport and spatially controlled initiation of developmental programs into different cell identities.

2.3. Plasmodesmata evolution

Most multicellular organisms evolved intercellular connections for molecular exchange. Filamentous cyanobacteria evolved septal junctions [50], animals gap junctions [51], and fungi

septal pores [52]. PD-like pores were proposed to have evolved independently between brown algae and the green lineage [53,54], while red algae evolved pit plugs [55]. PD in brown algae lack the ER-derived desmotubule and are unbranched and cylindric [53]. Brown algal PD form during cytokinesis in which they are pre-assembled as pores in a membranous sac that later is filled with cell wall material [53]. Strictly speaking, brown algal PD and green lineage PD are likely convergent structures, and their terminology as PD is rather historical than phylogenetically based. In the green lineage, the phragmoplast, an early stage of the cell plate (crucial in establishing cytokinesis), and PD first appeared within the Streptophyte algae. As there are reports of differing PD ultrastructures in different clades of the green lineage, there are diverging hypotheses for the evolution of PD. Within the green lineage, land plants evolved from a common ancestor with the Zygnematales, a clade of freshwater algae that are unicellular or form unbranched filaments but contain no PD. The next close relatives to land plants are the Coleochaetales, which contain PD but no desmotubule, and the Charales, which contain PD with a desmotubule that is not connected to the ER. As the Zygnematales contain no PD but are closer related to land plants than Streptophytes, it is hypothesized that PD evolved independently in freshwater algae and land plants [56]. An alternative hypothesis is that PD in Zygnematales were lost during evolution, in a secondary morphological simplification, which could be in line with the loss of branching and the absence of motile cilia in the clade [57] (Figure 2). Due to the high diversity in PD ultrastructure, phylogenetic analyses of PD proteins can give an alternative glimpse into the evolution of PD.

PD-located CALLOSE SYNTHASES (CALS) accumulate callose at PD neck regions, which in turn constricts PD aperture. But in higher plants, CALS are involved in multiple processes, like cell plate formation, male gamete development, and stress responses. CALS first appeared within the Streptophyte algae, presumably in an ancestor of the Klebsormidiales, which predates the evolution of the phragmoplast. Klebsormidiales employ a basal form of cytokinesis, which involves the formation of callose-containing cross-cell walls. Hence, early CALS emergence likely contributed to the evolution of cytokinesis [58]. GLYCOSYL HYDROLASE 17 family (GHL17) proteins are membrane-bound callose degrading enzymes with roles in plant immunity and development. Some GHL17 proteins are PD-localized and in concert with CALS contribute to callose balancing at PD. Phylogenetic analysis and fluorescence microscopy demonstrated that all PD-localized GHL17 proteins belong to the embryophyte specific α-clade, while β- and γ -clade GHL17 proteins are not PD-localized [59].

PLASMODESMATA LOCALIZED PROTEINs (PDLPs) are highly specific PD proteins that are involved in defense signal perception and regulate PD permeability in a callose-depended manner [60]. They contain two N-terminal extracellular carbohydrate-binding DUF26 domains and a C-terminal transmembrane domain. Interestingly, bryophytes and likely lycophytes harbor no PDLPs indicating, that they emerged in a common ancestor of seed plants [61].

MCTPs are key proteins in the ER stabilization during primary PD formation. Interestingly, MCTPs are highly conserved throughout the multicellular eukarya. While most metazoa encode for one or two MCTPs, the bryophyte *Physcomitrium patens* encodes 6 MCTPs. In seed plants, MCTPs diversified even more extensively, with some species carrying over 20 MCTPs [62,63]. The extensive diversification of MCTPs in the green lineage implies diverse functions in plant development and physiology and might be an indicator for the diversification of desmotubule-containing PD.

The emergence of PDLPs and the GHL17 α-clade in the embryophyta indicates that callose balancing at PD evolved after land colonization, despite the early emergence of CALS (Figure 2). Similarly, MCTPs seem to have diversified within the embryophyta and especially within seed plants. The selective pressure plants experienced in the terrestrial environment likely facilitated an expansion of their plasmodesmal proteome that broadened the regulation mechanisms that control PD permeability. This raises the question, of how Streptohphyte algae

regulate their PD permeability. Hence, it remains to be elucidated which molecular components are required to constitute an originator "blueprint" PD of an algal last common ancestor.

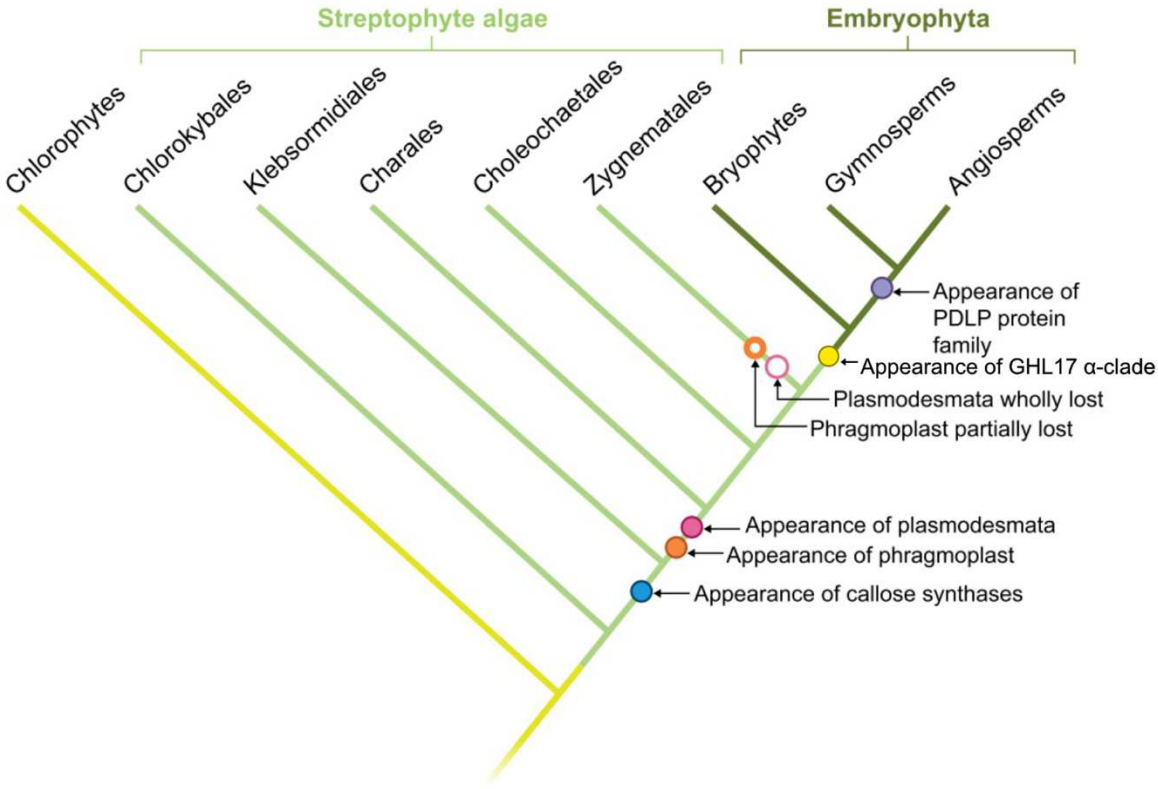

Figure 2: Plasmodesmal evolution (modified from Tee and Faulkner, 2024 [64])
The phylogenetic tree depicts the evolutionary origin of PD in the green lineage, likely evolved in a common ancestor of the Charales and Choleochaetales. Closed circles indicate the appearance of morphological structures, like the phragmoplast (orange) or PD (red) or protein families, like the GLYCOSYL HYDROLASE 17 (GHL17) α-clade (yellow) or the PD localized PLASMODESMATA-LOCATED PROTEIN (PDLP) family (purple). This tree hypothesizes a potential secondary loss of PD (thick ring) and the phragmoplast (thin ring) in the Zygnematales.

2.4. Plasmodesmata passage of small cargo

PD form a passageway for a diversity of cargo species, from smaller molecules like metabolites, phytohormones, and ions to macromolecules like proteins, mRNAs, and small RNAs. Cargo smaller than the SEL mostly moves through passive diffusion or bulk flow [65,66] (Figure 1C). Sugars belong to the most extensively studied small molecules that move via PD. In symplasmic phloem loaders sugars are translocated from the CCs into the phloem SEs to be redistributed from source to sink tissues. In some species sugar phloem loading is assisted by pore-PD units, while funnel PD alleviate hydraulic resistance in the phloem unloading zone. Some families (e.g., Cucurbitaceae) contain specified CCs, also termed intermediary cells (IC), that contain abundant and structurally distinct PD [11]. In those species, the predominantly phloem-transported sugars are the polymers stachyose (667 Da) and raffinose (504 Da) instead of the usual sucrose (342 Da) [1]. The polymer trap model postulates that sucrose is transported from the bundle sheath (BS) cells to the intermediate cells, actively metabolized to larger polymers (stachyose and raffinose), and thereby trapped, which enacts directionality of the phloem loading. Plants, like the Cucurbitaceae, that possess ICs are hence also referred to as active symplasmic phloem loaders. Nevertheless, there remains doubt if a separation of compounds through such small size differences is feasible [1,11] (for a detailed description of sugar loading mechanisms refer to Chapter II). By measuring diffusion coefficients of the

fluorescent dye fluorescin, which has a similar size to symplasmically loaded sugars, PD hindrance at the BS-IC interface was quantified (hydrodynamic radii: fluorescin 4.9 Å, sucrose 4.2 Å, stachyose 5.2 Å, raffinose 6 Å). The measured hindrance matched PD substructure models with a slit aperture of ~1 nm, several nanochannels of 0.7 nm, or a ~50 % saturated hydrogel [67]. While the proposed models explained the diffusion coefficients of fluorescin, none of them matched actual *in vivo* sugar fluxes that had been previously reported. Hence, it was postulated that the actual mechanism of sugar flux at BS-IC interfaces cannot be purely diffusive [67]. Implications of the polymer trap model usually postulate very tight cytoplasmic sleeves that should also restrict movement of other cargos (larger than 1 nm). In contrast, however, it was demonstrated that in heterografts of pumpkin and cucumber, transport of *Cucurbita maxima NON-CELL-AUTONOMOUS PROTEIN (CmNCAP)* mRNA from the pumpkin rootstock into the cucumber shoot apex is possible [68]. Both plants are members of the Cucurbitaceae (active symplasmic phloem loaders), meaning that *CmNCAP* mRNA should pass a BS-IC interface to reach the shoot apex. *CmNCAP* mRNA is 610 base pairs long [68], which, when estimated with the average size of a base pair (height 20 Å, width 3.4 Å), results in a height of 2 nm and length of 207.4 nm. Additionally, mRNAs are always accompanied by RNA-binding proteins (RBPs) that increase the size of the transported ribonucleoprotein (RNP)-complex. These indications hint that size differences are unlikely the cause for stachyose and raffinose exclusion at the BS-IC interface.

Ions have long been accepted as non-cell autonomous species, as one of the widely used symplasmic diffusive dyes, carboxyfluorescein is an anion (charge -3 at pH_{cyt} [69]). While testing cell-cell transport of endogenous ions remains challenging. Microinjection experiments with FITC-labeled amino acids demonstrated that preferentially anionic hydrophilic amino acids diffuse symplasmically, while aromatic amino acids were excluded [70]. Recent discoveries indicate that PD-mediated transport is permselective for anionic cargo. Permselectivity is the preferential transport of cargo of a specific charge. Microinjection experiments with small (<1kDa) cationic and anionic dyes of comparable sizes showed retention of cationic dyes, while anionic dyes were transported symplasmically. Selective diffusion of anionic dyes was even maintained when anionic and cationic dyes were co-injected [71]. In contrast to those findings, the net charge of the PM is negative and should in theory result in permselectivity for cationic cargo at PD. The data indicates that yet to be discovered positively charged compounds have to be concentrated at PD, to facilitate the permselectivity for anionic cargo [71]. Due to their size, phytohormones were hypothesized to be cell-cell transported species. Several phytohormones affect PD permeability during stress responses [e.g., salicylic acid (SA) can reduce PD permeability during infection [72], abscisic acid (ABA) closes PD in *Physcomitrium patens* [73], gibberellin (GA) is involved in reopening after bud dormancy [21]]. Recently, it was demonstrated that a brassinosteroid (BR) precursor is short-range transported via PD, which is required for BR synthesis. Further, BR accumulation can reduce PD permeability, which allows a feedback loop in which BR modulates its own biosynthesis [74]. It is well established that auxin is transported actively via transporters and the apoplasm, but recent modeling indicates that *in vivo* root tip auxin dynamics can only be explained by integrating a subfraction of symplasmically diffusing auxin [75]. Further PD-derived changes in auxin dynamics were reported, e.g., in lateral root patterning [76]. Similar to sugars and phytohormones, proteins that are smaller than the SEL can move through PD in a diffusive, non-targeted manner. The transcription factor LEAFY (LFY) (47 kDa) is important for the initiation of floral identity and diffuses from the L1 layer to L3 layer of floral primordia [77]. The transcription factor APETALA1 (AP1) is unrelated to LFY, slightly smaller in size (30 kDa), and also functions in floral identity. Despite being smaller than LFY, AP1 remains cell-autonomous, which was linked to its more pronounced nuclear localization than LFY. Hence, it was postulated that cytoplasmic localization is a prerequisite for diffusive cell-cell movement of proteins [78]. Later,

it was observed that nucleoplasmic sequestration via nuclear localization signal (NLS) or histone fusion reduced movement, while high protein levels enhanced movement, highlighting that cytoplasmic protein levels indeed affect intercellular passage [79].
Notably, in a screen for intercellular mobility of TFs in Arabidopsis roots (SEL 60 kDa) > 40 cell-autonomous TFs that even when fused to mCherry, were smaller than the PD SEL were identified (Table 4, appendix). Like, AGAMOUS-LIKE (AGL) 26 (14 kDa, fused to mCherry 41 kDa), which had a partially cytoplasmic localization and still remained cell-autonomous [79]. Conclusively, while cytoplasmic protein levels do affect intercellular mobility, there seem to be additional size-independent mechanisms in state that retain cell-autonomous localization of small cytoplasmic proteins. In the same screen, 22 non-cell autonomous TFs were identified, of which several were larger the 60 kDa SEL, indicating an active selective transport mechanism [79]. While callose turnover can regulate PD constriction and dilation [23], it does not describe how active transport of large cargoes is mediated, while simultaneously, smaller species remain cell-autonomous.

2.5. Intercellular transport of macromolecular cargo

Transport of cargo larger than the SEL has to be facilitated by carrier proteins/ transport receptors, which assist the intercellular transport of non-cell-autonomous proteins (NCAP) in an active manner. The maize homeobox transcription factor KNOTTED1 (KN1) was the first protein identified to be selectively transported via PD. KN1 protein is transported together with its mRNA into the shoot apical meristem to maintain stem cell identity [80]. KN1 might require partial unfolding to pass PD [81]. In line with this is the presence of a chaperonin complex in the recipient cell layers, which is essential for KN1 transport, indicating that it has a role in refolding partially unfolded transported KN1 protein [82]. Further, an RNA exosome subunit is required for the transport of *KN1* mRNA and its Arabidopsis homolog *SHOOTMERISTEM-LESS* (*STM*) mRNA [83] (Figure 3A). Analogous to KN1, SHORTROOT (SHR) is a transcription factor that contributes to the orientation of the cell division plane in the stem cell niche of Arabidopsis roots [84]. SHR is expressed in the stele of the root and moves to the endodermis via PD [85]. Interestingly, KN1 and SHR both require nuclear localization for their capacity to be intercellularly transported [86,87]. SHR transport is partly facilitated by SHR INTERACTING EMBRYONIC LETHAL (SIEL), which mediates endosome association of SHR via microtubules, which subsequently affects SHR cell-cell transport (Figure 3B). SIEL also interacts with other root non-cell autonomous transcription factors like CAPRICE (CPC), TARGET OF MONOPTEROUS 7 (TMO7), and AGL21 [88–90]. SIEL, as well as *Nicotiana tabacum* NON-CELL AUTONOMOUS PATHWAY PROTEIN1 (*Nt*NCAPP1), could be considered as transport receptors that mediate the transport of cargo to PD. *Nt*NCAPP1 is an ER-bound carrier protein that enables the transport of a subset of *N. tabacum* NCAPs towards PD. Deletion of the ER transmembrane domain of *Nt*NCAPP1 (*Nt*NCAPP1Δ $_{1–22}$) blocks the transport of its cargo [91]. *C. maxima* PHLOEM PROTEIN16 (*Cm*PP16) is an NCAP from pumpkin phloem sap that interacts with *Nt*CAPP1. Post-translational glycosylation and phosphorylation of both *Cm*PP16 and *Nt*NCAPP1 are essential for their interaction and subsequent *Cm*PP16 transport [92]. A homologous transport receptor in Arabidopsis has not been identified yet.
Plant viruses encode MOVEMENT PROTEINs (MPs) that facilitate the intercellular spread of viral particles by increasing PD SEL [93]. The mechanisms for different MPs are variable and can include direct PD targeting or trafficking towards PD along the cytoskeleton or secretory pathway [94]. *Tobacco mosaic virus* (*TMV*) MP moves in complex with *TMV* RNA as viral RNP particles (vRNP), which accumulate at PD, likely by trafficking along the ER membrane [95]. Interestingly, *Nt*NCAPP1Δ $_{1–22}$ blocks *TMV* MP and *Cm*PP16 mediated SEL increase, but not *Cucumber mosaic virus* MP or KN1 mediated SEL increase [91].

MPs of *Cowpea mosaic virus* (*CPMV*) and *Grapevine fanleaf virus* (*GFLV*) encode multi-subunit-tubule-forming MPs that replace the ER traversing PD and form conduits for viral movement. *GFLV* MP requires the presence of PDLPs to facilitate viral spread [94]. In a few MPs, motifs necessary for PD targeting or for intercellular transport were identified. The first 50 N-terminal amino acids of *TMV* MP are sufficient for PD targeting. Despite its smaller size, *TMV* MP 1-50 (~5 kDa) has only a fraction of the intercellular mobility of full-length *TMV* MP (30 kDa) [96]. While, DOUBLE GENE BLOCK PROTEIN (DGBp)1, the MPs of α-, β-, and γ-Carmoviruses share a conserved C-terminal aromatic motif that is required for homo- and heteromerization and consequently viral cell-cell movement [97]. In some endogenous plant proteins, further transport motifs were identified. Like the KNOTTED1-LIKE HOMEOBOX (KNOX) homeodomain (HD), composed of a NLS and three α-helices, which is necessary and sufficient for intercellular transport of KN1 and its mRNA [98–100] . Similarly, the Arabidopsis DNA BINDING WITH ONE FINGER (DOF) transcription factor *At*DOF4.1 was shown to harbor an N-terminal intercellular transport motif (ITM) that spans over the DOFs characteristic zinc-finger motif and the first motif of its bipartite NLS. The DOF-ITM is conserved in the plant kingdom, and even the ancestral DOF-ITM of the unicellular algae *Chlamydomonas reinhardtii* is functional when expressed in Arabidopsis. Indicating that the evolution of the DOF-ITM predates the evolution of PD [99].
Whether the DOF-ITM facilitates transport by itself or whether it recruits interactors that facilitate its intercellular transport (which evolved after the establishment of multicellularity) remains speculative.
Besides small molecules and proteins, RNAs are also transported symplasmically. Especially the transport of regulatory small noncoding RNAs (sRNAs) [e.g., micro RNAs (miRNAs), small interfering RNAs (siRNAs)] was extensively studied. The non-cell autonomous miRNA165/166 is involved in cell fate determination in primordia. miRNA165/166 form a gradient from the abaxial (high abundance) to the adaxial (low abundance) cells of the primordia, which affects the abundance of the transcription factor PHABULOSA (PHB) that specifies leaf polarity [101]. Recently, it was reported that symplasmic transport of endogenous miRNAs (including miRNA165/166) is cell-autonomously mediated by the nuclear transport receptor HASTY (HST), a homolog of the mammalian EXPORTIN5 (XPO5). While mammalian XPO5 facilitates the nuclear export of pre-miRNAs, Arabidopsis HST is mostly involved in miRNA biogenesis and is expendable for the nuclear export of miRNAs. HST seems to have evolved a symplasmic miRNA transport function independently [102]. It is possible that in plants, HST was repurposed to facilitate symplasmic miRNA transport, while other XPOs facilitate nuclear miRNA export. Regulation of plant development does not only require intercellular transport of transcription factors and sRNAs but also short- as well as long-distance mRNA transport. Transport of mRNAs might allow amplification of protein levels in recipient tissues, as a single mRNA can code for multiple protein copies. Recently, it was shown that tRNA-like structure [103] and m^5C-mRNA-methylation facilitate systemic mRNA transport from shoot to root and vice versa [103,104]. Nuclear mRNA export factors ALLY OF AML-1 AND LEF-1 (ALY)2 and ALY4 were reported to be required for long-distance mRNA transport from shoot to root tissues via the phloem. ALYs bind mRNAs and travel via the bulk flow of the phloem [105]. Phloem-mediated mRNA transport would likely require symplasmic phloem loading of RNP-complexes of ALYs and mobile mRNAs. Systemic mobile mRNAs can easily be identified by grafting experiments, which allowed the identification of several thousand candidates. Observation of short-range cell-cell movement of mRNAs, however, proves more complicated, as it requires mRNA tracking, which only was established recently and is not applicable in high-throughput [106]. Hence, there is limited knowledge of cell-to-cell mobile mRNAs, namely *KN1*/ *AtSTM*, pear *WUSCHEL-RELATED HOMEOBOX* (*PbWOX*)*T1*, *FLOWERING LOCUS T* (*FT*), and *AtAGL24*. All those mobile mRNAs form

RNP-complexes with RBPs that facilitate cell-to-cell transport [106], similar to vRNPs of plant viruses [95]. A recent mRNA-tracking-enabled discovery are the Arabidopsis rotamase cyclophilins (ROCs), which enable *FT* mRNA transport towards PD via organellar hitchhiking. ROCs are RNA-binding proteins that bind *FT* mRNA and locate it to the cytoplasmic face of multivesicular bodies and the trans-Golgi network, facilitating its intracellular transport [107]. Notably, mRNAs are much larger than the proteins they encode (e.g., KN1 protein ~40 kDa, *KN1* mRNA ~580 kDa), and *in vivo* they often form tertiary structures and are rarely free but in RNP-complexes, indicating that PD-mediated mRNA transport would require enormous dilation or an unfolding prior to transport [64]. PD seem to be capable of transporting cargo that is larger than the cytoplasmic sleeve, which is highlighted by PD-mediated mRNA transport (up to 2 nm x 1367 nm, for *Cas9* mRNA [64]), but also by the capability of sleeveless PD to transport GFP (5.6 nm hydrodynamic diameter). Moreover, PD are permselective for anions. These instances challenge the conventional models that link the plasmodesmal selectivity to the size of the cytoplasmic sleeve.
This raises the question of how PD exclude cell-autonomous species and at the same time, dilate their aperture for macromolecular cargo. As without an active exclusion mechanism, cell-autonomous species should be transported by pure chance.

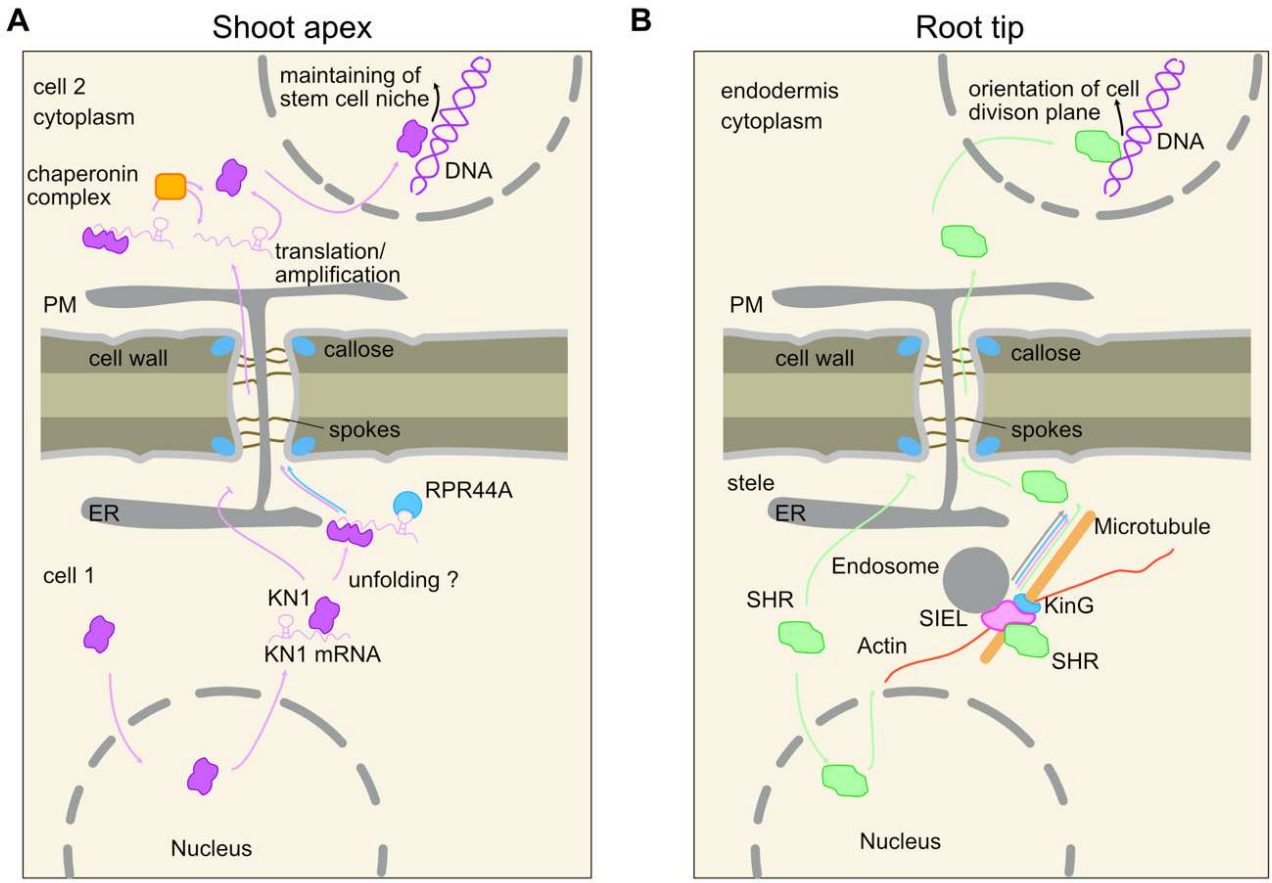

Figure 3: Facilitated transport across PD
A Illustration of KN1 and *KN1* mRNA transport in shoot apex. For its intercellular mobility KN1 requires its NLS, partial unfolding, RPR44A (an RNA exosome subunit protein) and a chaperonin complex for refolding in the recipient cell layer. **B** Illustration of SHR transport from stele to endodermis in roots. For its intercellular mobility SHR requires its nuclear localization, and the transport receptor SIEL. SIEL associates SHR with endosomes. KinG is required with cytoskeletal association of SIEL, which is required for SIEL to mediate SHR towards PD.

3. Aims of this thesis

3.1. The PD transport mechanism / Learning from analogous pores

PD transport larger cargoes than their cytoplasmic sleeve via a yet to be discovered mechanism [4]. As observed for KN1, partially un- and refolding is required for its intercellular transport [82] (Figure 3A). Un- and refolding might be a possible mechanism for active transport across PD. While unfolding might decrease the size of a protein in one dimension, an unfolded polypeptide will certainly be longer than its folded protein. It is questionable if an unfolded polypeptide will show enhanced intercellular diffusion, as the most efficient diffusion is observed for spherical particles [108]. Therefore, such a mechanism would likely require active shuttling of unfolded polypeptides throughout PD.

The presence of intercellular shuttles (carriers or transport receptors) was discussed as facilitators of PD passage for over 20 years [81,98,109]. But opposed to viral MPs, identified plant transport receptors (like *Nt*NCAPP1 and SIEL) seem to remain cell-autonomous, while only their cargo is cell-mobile [89,98].

The ability to exclude cargo is reminiscent of a sieve, but as even sleeveless PD seem to allow macromolecular diffusion [4], it is unclear which components enact those sieve-like properties. The elusiveness of the plasmodesmal transport mechanism raises the question, how analogous pores gate inter-compartment fluxes.

Plastids require an active protein import machinery, as 90% of their proteins are synthesized as precursors in the cytoplasm. Plastidial protein import is facilitated by translocon complexes on the outer and inner plastid membranes (TOC and TIC), which recognize cargos via cleavable transit peptides [110]. Similarly, mitochondrial import is mediated by analogous translocon complexes (TOM and TIM respectively), as well as cleavable transit peptides [111]. Plastidial and mitochondrial translocon complexes facilitate the efficient import of compartment-specific precursor proteins and potentially even nucleic acids [112,113]. However, opposed to PD their import capacity is likely limited by their pore size (~3 nm) [114,115].

In a perspective article published in 2000, Lee *et al*. discussed the similarities between plasmodesmal and nucleocytoplasmic transport, gated by PD and nuclear pore complexes (NPCs), respectively [116]. Both are nanometer-sized pores that enable passive diffusion and facilitated transport of small molecules, proteins, and RNAs [116]. NPCs traverse the nuclear envelope (NE) and concentrate phenylalanine-glycine-rich nucleoporins (FG-NUPs) in their central channel. The FG-NUPs enact a phase-separation-based permeability barrier that excludes inert molecules while simultaneously enabling the transport of cargo. Cargo passage is facilitated by nuclear transport receptors (NTRs), which recognize cargos via NLS or nuclear export signals (NES) [117]. Similar FG-NUP-based permeability barriers have been implied in gating the ciliary basal zone and thus controlling the transport between cytoplasm and cilia [118]. Meanwhile, import into peroxisomes was demonstrated to be mediated by an analogous phase-separation, based on tyrosine-glycine (YG)-rich repeats and recognition sequences in peroxisomal transport proteins, allowing import of cargos up to 10 nm [119,120].

While nuclear sequestration via NLSs was described to limit intercellular diffusion of non-specific cargos like mCherry and GFP [78,79], in the case of endogenous cargos, NLSs seem to play an important role in facilitating intercellular mobility, as seen in the DOF ITM and KNOX HD [99,100]. While not mediated by a canonical NLS, SHR also requires nuclear localization for its intercellular mobility [86].

Accordingly, we hypothesized that the transport mechanism of PD might be based on NTR-like transport receptors and an NPC-like phase separation domain.

3.2. Research questions and hypothesis

PD remain enigmatic structures. As outlined above, PD composition, regulation, transport mechanism, and evolution are yet to be deciphered.
Compared to the NPC, PD are not fully structurally resolved. Missing PD structures as well as their cell wall embedded, multimembrane composition, complicate the identification of novel PD components. This thesis was set on identifying novel components and molecular mechanisms that contribute to PD transport, by addressing the following main questions:

- What are the key components of PD?
- Are molecular mechanisms underlying PD transport similar to mechanisms underlying NPC transport?

After giving a general introduction on PD in Chapter I (see above), in Chapter II of my thesis, I detail and discuss the important role of PD in assimilate transport.
In Chapter III, I contributed to identifying new PD components by validating subcellular localizations of candidates found in a *Physcomitrium* PD proteome.

The hypothesis in Chapter III of the thesis was that:
Large-scale identification of novel PD components will grant novel insights into PD composition, transport mechanism, and evolution.

In Chapter IV, I review the well-characterized nano-sized NPC and the role of phase separation in its transport mechanism.
In Chapter V, I tested the localization of NPC components at PD and assessed their involvement in PD-mediated transport.

The hypothesis in Chapter V of the thesis was that:
NPC proteins are structural components at PD and functionally affect intercellular transport.

And in Chapter VI, I investigated the effect of NTR-like surface properties on intercellular movement.

The hypothesis in Chapter VI was, that:
Intercellular transport across PD is facilitated by similar features as nuclear transport.

Lastly, I summarize and discuss the thesis in Chapter VII.

This thesis provides a new perspective on the PD transport mechanism, by identifying novel components that functionally contribute to intercellular transport. To this end, I extensively reviewed current progress on PD, as well as NPCs, to establish a theoretic framework for my hypotheses. To test my hypotheses, I applied extensive molecular techniques, CRISPR-Cas9 and prime editing, transient and stable expression, confocal microscopy, and various *in planta* transport assays.

Chapter II

4. Plasmodesmata and their role in assimilate translocation

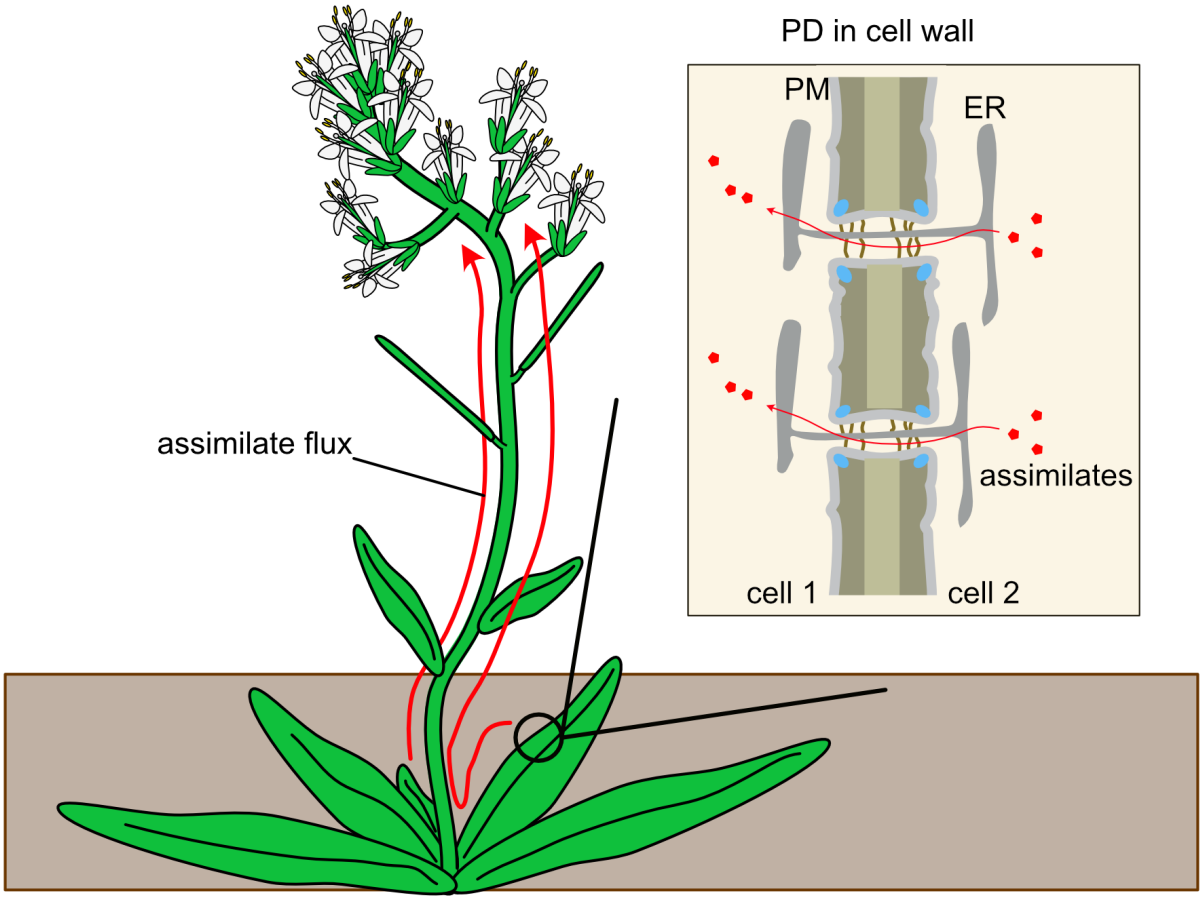

Status: Published
Journal: Journal of Plant Physiology
Impact factor: 4.3 (2022)
Contribution: 15% (specified in **Appendix**)

4.1. Aim of this chapter

4.1.1. Objective

Reviewing PD and their role in assimilate transport .

Journal of Plant Physiology 270 (2022) 153633

Contents lists available at ScienceDirect

Journal of Plant Physiology

journal homepage: www.elsevier.com/locate/jplph

Review

Plasmodesmata and their role in assimilate translocation

Manuel Miras [a,**], Mathieu Pottier [b], T. Moritz Schladt [c], J. Obinna Ejike [d], Laura Redzich [e], Wolf B. Frommer [f,g,*], Ji-Yun Kim [h,***]

[a] Institute for Molecular Physiology, Heinrich-Heine-University Düsseldorf, Düsseldorf, 40225, Germany
[b] Institute for Molecular Physiology, Heinrich-Heine-University Düsseldorf, Düsseldorf, 40225, Germany
[c] Institute for Molecular Physiology, Heinrich-Heine-University Düsseldorf, Düsseldorf, 40225, Germany
[d] Institute for Molecular Physiology and Cluster of Excellence on Plant Sciences (CEPLAS), Heinrich-Heine-University Düsseldorf, Düsseldorf, 40225, Germany
[e] Institute for Molecular Physiology and Cluster of Excellence on Plant Sciences (CEPLAS), Heinrich-Heine-University Düsseldorf, Düsseldorf, 40225, Germany
[f] Institute for Molecular Physiology and Cluster of Excellence on Plant Sciences (CEPLAS), Heinrich-Heine-University Düsseldorf, Düsseldorf, 40225, Germany
[g] Institute of Transformative Bio-Molecules (WPI-ITbM), Nagoya University, Chikusa, Nagoya, 464-8601, Japan
[h] Institute for Molecular Physiology and Cluster of Excellence on Plant Sciences (CEPLAS), Heinrich-Heine-University Düsseldorf, Düsseldorf, 40225, Germany

ARTICLE INFO

Keywords:
Plasmodesmata
Symplasm
Apoplasm
Transport
Transporters
Phloem loading
Seed filling
Plasmodesmogram

ABSTRACT

During multicellularization, plants evolved unique cell-cell connections, the plasmodesmata (PD). PD of angiosperms are complex cellular domains, embedded in the cell wall and consisting of multiple membranes and a large number of proteins. From the beginning, it had been assumed that PD provide passage for a wide range of molecules, from ions to metabolites and hormones, to RNAs and even proteins. In the context of assimilate allocation, it has been hypothesized that sucrose produced in mesophyll cells is transported via PD from cell to cell down a concentration gradient towards the phloem. Entry into the sieve element companion cell complex (SECCC) is then mediated on three potential routes, depending on the species and conditions, – either via diffusion across PD, after conversion to raffinose via PD using a polymer trap mechanism, or via a set of transporters which secrete sucrose from one cell and secondary active uptake into the SECCC. Multiple loading mechanisms can likely coexist. We here review the current knowledge regarding photoassimilate transport across PD between cells as a prerequisite for translocation from leaves to recipient organs, in particular roots and developing seeds. We summarize the state-of-the-art in protein composition, structure, transport mechanism and regulation of PD to apprehend their functions in carbohydrate allocation. Since many aspects of PD biology remain elusive, we highlight areas that require new approaches and technologies to advance our understanding of these enigmatic and important cell-cell connections.

1. Introduction

Assimilates produced in photosynthetically active source organs have to be delivered to supply sink organs that cannot produce their own. Translocation of sugar and organic nitrogen, as well as many other compounds, likely occurs on two routes: (i) transporter-mediated export from one cell, followed by diffusion across the cell wall and subsequent uptake into adjacent cells, or (ii) via cell-cell bridges, the so-called plasmodesmata (PD). During the evolution of multicellular organisms, all kingdoms developed unique cellular connections that serve as efficient pathways of exchanging nutrients and signals. Some fungi have septal pores, animals use gap junctions, and plants evolved PD. Gap junctions are made up of connexin (or pannexin or innexin) oligomers in the membranes of adjacent cells that connect two cells to produce gated channels that allow passage of ions and metabolites with a size exclusion limit (SEL) of 16–20 Å (Skerrett and Williams, 2017). In comparison, PD are far more complex and have to span the cell wall (typically 0.1–2 μm width). PD of early bryophytes and tracheophytes consist of cell walls, multiple membranes (plasma membrane and endoplasmic reticulum) separated by a cytosolic sleeve, and likely hundreds of proteins. PD are thought to mediate the translocation of ions, metabolites, RNAs and proteins; therefore, it has been hypothesized that plants function

* Corresponding author.
** Corresponding author.
*** Corresponding author.
E-mail address: frommew@hhu.de (W.B. Frommer).

https://doi.org/10.1016/j.jplph.2022.153633
Received 11 October 2021; Received in revised form 26 January 2022; Accepted 26 January 2022
Available online 3 February 2022

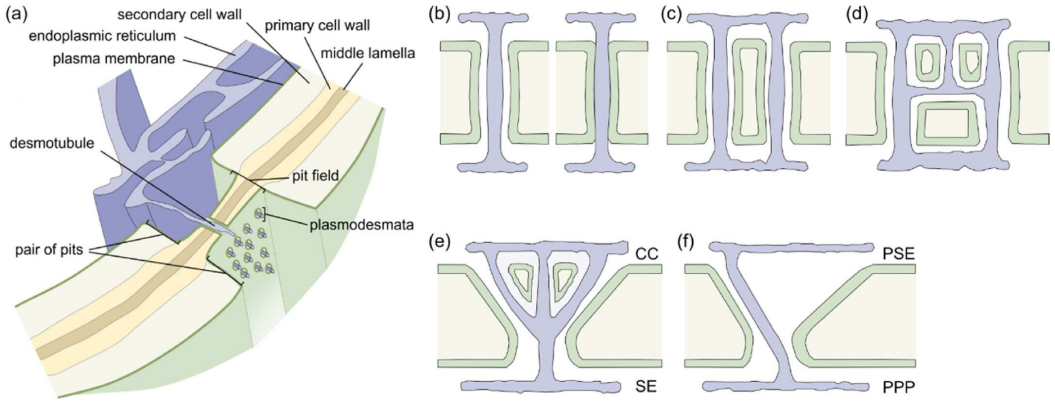

Fig. 1. Diversity of PD organization and morphology. (a) Plasmodesmata clustered into pit fields. PD can be found isolated or grouped in thinner areas of the primary cell wall that are called pit fields. In cells producing secondary wall layers (*e.g.*, sclerenchyma cells), poor cellulose microfibril deposition specifically at both sides of pit fields, might lead to the emergence of depressed area called pits, and primary cell wall located at pit fields might evolve into pit membranes. (b) Simple PD with single cytoplasmic strand (left) and simple PD lacking cytoplasmic sleeves (right); (c) Twinned PD consisting of two closely paired simple PD; (d) Branched PD containing a central cavity; (e) PD pore unit formed between sieve elements and companion cells; (f) Funnel PD formed between proto-sieve element and phloem pole pericycle cell in the root.

essentially as a large synthicium.

2. Types of PD and cell specific roles

Ontogenetically, PD can be classified into primary and secondary PD. Primary PD are produced in the cell plate during cell division, trapping the endoplasmic reticulum (ER) to form the desmotubule (Hepler, 1982). These primary PD develop between mother and daughter cells. Secondary PD are generated *de novo* in existing cell walls requiring cell wall-degrading enzymes and insertion of the endoplasmic reticulum (ER) (Ehlers and Kollmann, 2001). In grafting experiments, it was shown that secondary PD formation involves thinning of the cell wall and tethering of ER and the plasma membrane (PM) (Chambaud et al., 2021). Secondary PD are often generated in close proximity to existing PD, resulting in clusters of PD, called pit fields, located in thinner areas of the primary cell wall (Fig. 1a) (Carr, 1976; Faulkner, 2018). In cells producing secondary wall layers, the primary cell wall located at pit fields may then be converted into pit membranes separated by a pair of pits (Robards, 1976; Peters et al., 2021).

PD are complex and diverse, with morphotypes ranging from unbranched sleeveless PD lacking a sleeve between ER and PM, unbranched simple PD, characterized by a single channel, to complex V-, Y-, X- or H-shaped PD, with branched and twinned structures (Fig. 1b–f). Unique PD types are specifically localized at interfaces between different cell types. PD morphology may be modified during development to acclimate to new requirements. In young and immature organs in embryos, sink leaves, and root meristems, PD are predominantly of the simple type with high basal SEL, allowing for diffusion of large molecules (Oparka et al., 1999). In contrast, branched PD of mature organs such as source leaves often have a decreased SEL (Oparka et al., 1999). However, PD type and SEL do not always correlate; *e.g.*, *ise1* mutants, which have an increased number of branched and twinned PD compared to wild-type, were characterized by a higher SEL (Stonebloom et al., 2009). Notably, PD are not static and exhibit dynamic changes in structure and function: in tobacco (*Nicotiana benthamiana*) and squash (*Cucurbita pepo*) leaves, many simple PD are replaced by complex forms during the sink-source transition indicating the need for altered conductivity and regulation in the 'source' state (Volk et al., 1996; Roberts et al., 2001). Moreover, specific cell types are characterized by unique PD morphologies (Fig. 1b–f), for example, plasmodesmata-pore units (PPU) are specialized PD that connect companion cells (CC) with sieve elements (SE). On the CC-side, PD become highly branched, with a cavity that connects to a wider aperture on the SE side. This asymmetry may imply asymmetry in the permeability of the PD, and, together with the larger size exclusion limit (SEL) of ~70 kDa, likely plays a role in the need of sustaining the enucleate SE by the CC and assimilate translocation (van Bel and Knoblauch, 2000). In roots, funnel-shaped PD are located at the interface between protophloem sieve elements (PSE) and phloem-pole pericycle cells (PPP), with wider apertures at the PSE entrance that are thought to mediate bulk flow for unloading (Ross-Elliott et al., 2017) (Fig. 1f). Sugars and other small solutes may move relatively freely through funnel PD, while macromolecules appear to pass through these pores in discrete pulses, termed batch unloading (Ross-Elliott et al., 2017) (see also section *Contribution of PD to unloading of the phloem*). Recent technical developments in electron tomography have enabled the generation of three-dimensional models of the PD structure in the Arabidopsis (*Arabidopsis thaliana*) root tip columella (Nicolas et al., 2017). Ultrastructural analyses revealed that, while the outermost cell layers of the columella had canonical PD structures (PD type II), mitotically active columella cell initials at the upper layer featured PD without a cytoplasmic sleeve (PD type I) (Nicolas et al., 2017). Remarkably, sleeveless PD type I can traffic synthetic dyes such as carboxyfluorescein diacetate (CFDA) as well as GFP, putting models that predict diffusion of molecules through the cytoplasmic sleeve into question. More recent models that could account for geometric fluctuations in PD shape predicted that particles larger than the diameter of the cytoplasmic sleeve can permeate through the PD pore (Christensen et al., 2021). Of note, calculations of symplasmic permeabilities based on geometrical descriptions of PD suggest that the permeation efficiency does not only depend on the diameter of the cytoplasmic sleeve but also on the length of the PD (and thus cell wall thickness) (Deinum et al., 2019). Larger cytoplasmic sleeves were predicted to be more favorable for permeation efficiency through PD in thicker cell walls (200 nm) (Deinum et al., 2019). This hypothesis is in line with the observations in Arabidopsis columella, where PD type II with a larger cytosolic sleeve mostly appeared in thick cell walls (average 200 nm), and PD type I in thinner cell walls (average 100 nm) (Nicolas et al., 2017).

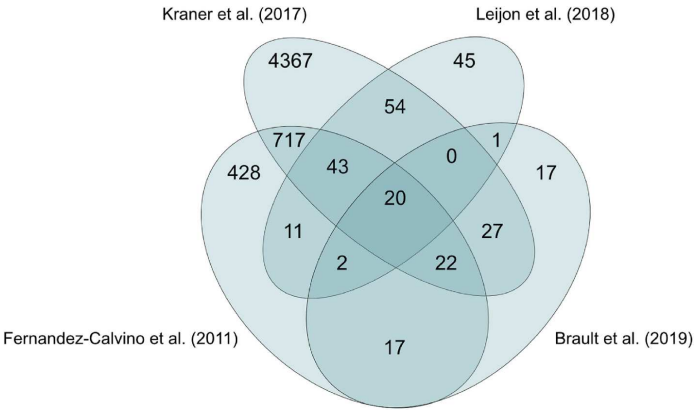

Fig. 2. PD proteome comparison. Venn diagram displaying the number of proteins overlapping between four previously published PD proteomes (Fernandez-Calvino et al., 2011; Kraner et al., 2017b; Leijon et al., 2018; Brault et al., 2019). Twenty core proteins common to all four proteomes were identified. For PD proteins identified from *P. trichocarpa* (Leijon et al., 2018), accessions for the closest Arabidopsis homologs were retrieved before PD proteome comparison. Protein list is available at www.molecular-physiology.hhu.de/summary-of-the-resources/core-plasmodesmatal-proteome.

3. PD protein composition

As PD are embedded in the cell wall, composed of multiple membranes, soluble and membrane proteins, they pose a major challenge in purification for compositional analyses. To date, putative PD proteomes have been established by three principal approaches: by chance through imaging of fluorescently tagged proteins, by proteomics-based approaches using cell wall fractions enriched for PD, and comparative analysis of the proteomes of mutants with reduced PD number (Fernandez-Calvino et al., 2011; Kraner et al., 2017b; Park et al., 2017; Leijon et al., 2018; Brault et al., 2019). Published PD proteomes include 1341 candidate proteins from Arabidopsis, 1113 from *Populus trichocarpa*, and 1070 from tobacco (Fernandez-Calvino et al., 2011; Park et al., 2017; Leijon et al., 2018). However, cell wall fractions are contaminated with non-PD proteins, *e.g.*, derived from ER and plasma membrane. Thus, it is necessary to assess in each case whether the candidates localize to PD. One typical approach is to generate fluorescent protein (FP) fusions and determine the localization by confocal microscopy. Localization studies are often performed by transiently expressing FP fusions driven by strong promoters in heterologous systems such as *N. benthamiana*. However, this experimental system is prone to artefacts as ectopic overexpression can lead to mistargeting or accumulation in the ER and Golgi. Generation of stable transformants with native promoters and all introns followed by analysis in the native cell types is more challenging and time-consuming, but likely essential for reliable validation. Notably, many PD proteins are not specific to PD but localize also to other sites such as PM, ER, etc. In an attempt to obtain a set of candidates, a refined dataset called 'core PD proteome' with 115 candidates from Arabidopsis was established (Brault et al., 2019). This 'core proteome' contains *bona fide* PD components, and does not mean that many of these candidates are PD-associated. Of note, only 22 proteins from the 'core PD proteome' have been validated by localization of FP fusions; moreover, this 'core PD proteome' lacks some of the well-characterized PD receptor-like kinases such as BAM1, CLAVATA1 and CRINKLY4 (Stahl et al., 2013; Rosas-Diaz et al., 2018). To compile a list of putatively PD localized proteins that are commonly found in PD preparations, we compared published PD proteomes and identified twenty common candidates in the four PD proteomes (Fernandez-Calvino et al., 2011; Kraner et al., 2017b; Leijon et al., 2018; Brault et al., 2019) (Fig. 2). Among the 20 candidates were three previously described PD proteins: CALLOSE SYNTHASE 3 (CALS3; AT5G13000), INFLORESCENCE MERISTEM RECEPTOR-LIKE KINASE 2 (IMK2; AT3G51740), MULTIPLE C2 DOMAINS AND TRANSMEMBRANE REGION PROTEIN 3 (MCTP3; AT3G57880). CALS3 co-localized with the RxLR3 effector of *Phytophthora brassicae*, PLAMODESMATA-LOCATED PROTEIN 5 (PDLP5) and callose (Tomczynska et al., 2020). IMK2, present at the plasma membrane, was shown to re-localize to PD in response to osmotic stress (Grison et al., 2019). MCTP3 was shown to be present at PD and interacted with SHOOTMERISTEMLESS (STM), a class I KNOTTED1 (KN1)-like homeobox (KNOX) protein. STM is presumably capable of trafficking through PD (Balkunde et al., 2017; Liu et al., 2018; Brault et al., 2019). Two members of the Tetraspanin family (AT2G23810, AT3G45600), two nucleobase ascorbate transporters (AT2G26510, AT2G27810), and PDLP6 (AT2G01660) were also part of the 'core PD proteome'. An additional twelve proteins were encountered in all four proteomes and have not been described as PD proteins so far (Supplemental Table S1). Notably, this list is not comprehensive, and proteins found in one species but not another may still be *bona fide* PD proteins. Systematic analysis of the localization of all candidates and new technologies such as proximity labeling may help researcher to build an even more comprehensive PD-type-specific parts list and a blueprint.

Different cell types are characterized by unique PD morphologies (*e.g.*, PPU connecting CC-SE). However, little is known about unique composition of distinct PD (Fig. 1). A well-characterized cell-type-specific PD component is MCTP1, which localizes to PD at the CC-SE interface (Liu et al., 2012). MCTP1 interacts with the florigen protein FLOWERING LOCUS T (FT) and is required for the trafficking of FT (Liu et al., 2012; Song et al., 2017). Consistent with these data, a recently published single-cell transcriptome of Arabidopsis leaves showed that *MCTP1* transcripts were specifically enriched in CC (Kim et al., 2021). Among members of the PDLP family, PDLP8 was shown to interact with the PD-located phloem-specific acyl-CoA-binding protein AtACBP6, which might mediate the transport of AtACBP6 from CC to SE (Ye et al., 2017). Additionally, PDLP6-GFP fusions driven by its native promoter, localized in the vasculature of leaves and roots (Li and Aung, 2021, BioRxiv). Overexpression of PDLP6 triggered callose deposition in the vasculature, as well as accumulation of starch granules in the bundle sheath (BS), which might be the result of restrictions of PD permeability between BS and PP (Li and Aung, 2021, BioRxiv). PDLP5 overexpression promoted callose deposition in PD between mesophyll cells. These results intimate a cell-type specific regulation based on the PD composition. In rice (*Oryza sativa*), the remorin protein GRAIN SETTING DEFECT1 (OsGSD1) specifically localized to the plasma membrane and PD in CC. OsGSD1 overexpression led to compromised grain setting and assimilate retention in leaves, possibly caused by reduced PD permeability in CC due to increased callose deposition. Additionally split-FP experiments and coimmunoprecipitation assays provided evidence

that OsGSD1 interacts with the desmotubule associated OsACT1, a protein that may play a role in regulating the CC PD-aperture (Gui et al., 2014). With the increasing number of identified PD proteins and single-cell transcriptome data, it will be possible to identify both proteins common to all PD as well as additional proteins specific for unique PD types (Denyer et al., 2019; Kim et al., 2021; Seyfferth et al., 2021).

4. PD transport mechanisms

Perspectives on the role of PD from Tangl, Pfeffer and Strasburger, to name some of the most prominent scientists who studied PD in the late 18th century, were based on the hypothesis that the 'holes' observed in the cell walls would enable cellular exchange of molecules (Tangl, 1879; von Hanstein, 1880; Strasburger, 1901). This 'hole-model' still dominates the current view. PD-mediated cell-to-cell movement of ions and other molecules is assumed to occur through the cytosolic sleeve of PD and is driven by diffusion, pressure differences between neighboring cells, and/or bulk flow. If movement occurs, it is not clear whether the channels allow free diffusion. Movement was found to be limited by molecule size, an SEL specific to different types of PD. The hypothesis that movement is subject to a SEL is affirmed by tracer movement studies (Goodwin et al., 1990; Barton et al., 2011; Rutschow et al., 2011; Liesche and Schulz, 2012a; Gerlitz et al., 2018; Wang et al., 2020). The SEL was shown to be cell-type specific but also depended on the physiological and developmental states of the tissue (Erwee and Goodwin, 1985; Wolf et al., 1989; Oparka et al., 1999) (see also section *Regulation of PD conductance*). SEL appears to be dynamic, with adaptive capabilities to acclimate to altered flux requirements, for example under stress conditions (Rutschow et al., 2011; O'Lexy et al., 2018). Differences in SEL have been attributed to differences in PD geometry (Deinum et al., 2019; Ostermeyer et al., 2021, BioRxiv).

Alternative models for PD transport assume that SEL and, thus, PD conductivity are more complex and might also depend on other features, in addition to PD geometry. SEL is determined by the Stokes radius of molecules, the flexibility of molecules, the folding state of RNAs and proteins; moreover, it is conceivable that molecules that pass require chaperones or carriers to enable permeation. In the nanometer-sized PD pores, negative electrostatic charges of the plasma membrane throughout the cytosolic sleeve might enable faster permeation for cations and positively charged molecules relative to anions and negatively charged molecules (Peters et al., 2021). Direct quantitative transport studies will be needed to assess permeation rates of differently charged ions to clarify the impact of electrostatic charges on the permeation of ions and molecules.

Some evidence implicated different mechanisms for cell-to-cell movement of small (<1 kDa) and large molecules (>27 kDa). During phloem unloading in Arabidopsis, small molecules (0.34–0.38 Da) permeated from SE into PPP at constant rates, whereas large molecules (27–112 kDa) permeated in discrete pulses, termed 'batch unloading' (Ross-Elliott et al., 2017). Batch unloading of large molecules might depend on thermal motion of structural PD components such as the desmotubule or the spokes (Peters et al., 2021). Peters et al. (2021) recently hypothesized that the desmotubule could be displaced from the center of the pore, thereby creating asymmetry which allows larger molecules to pass. While small molecules would permeate unhindered, independently of the position of the desmotubule, large molecules would be able to permeate only when the desmotubule is in the periphery of the PD. Once having entered the pore, large molecules could lock PD in a wide-open state, thus being cargo-gated (Christensen et al., 2021; Peters et al., 2021).

Specific mechanisms for targeting PD components and cargo proteins to PD must exist. One might speculate that N-terminal signal sequences are required, similar as for nuclear or organellar import (Kim and Hwang, 2013). Indeed, some proteins contain N-terminal sequences that are likely involved in PD targeting. The first 50 amino acids of TMV MP, a signal peptide of PDGLP1, and a zinc finger binding motif with the N-terminal part of the nuclear localization sequence (NLS) of INTERCELLULAR TRAFFICKING DOF1 (ITD), were found to be necessary and sufficient for PD targeting of TMV MP, PDGLP1, and ITD, respectively (Ham et al., 2012; Chen et al., 2013; Yuan et al., 2016). By contrast, C-terminal regions such as a transmembrane domain of PDLP1 and a sequence comprising the NLS and the homeodomain of KN1, have been found to be involved in PD targeting of PDLP1 and KN1, respectively (Kim et al., 2005c; Thomas et al., 2008). Yet so far, PD-targeting signal sequences or -peptides have been identified only in this subset of proteins and no universal code for PD targeting could be inferred from the already identified signal sequences (Li et al., 2020). Interestingly, different posttranscriptional modifications, such as glycosylation, phosphorylation and GPI modification seem to be involved in PD trafficking (Taoka et al., 2007; Zavaliev et al., 2016). Alternatively, PD targeting might not only depend on specific peptide sequences but also on less obvious features (*e.g.*, mitochondrial targeting signals contain an alternating pattern of hydrophobic and positively charged amino acids), for example interaction with PD localized proteins.

In summary, evolution generated an energy-efficient and versatile system, whose transport properties can be adjusted to communication and nutritional needs, with specific adjustments depending on the cell type, developmental stage and environmental conditions. No doubt, the systematic identification of PD components and direct transport assays will help to identify common features responsible for PD targeting.

5. Regulation of PD conductance

Principally, two major modes of gating PD have been proposed – rapid gating as observed in response to pressure changes (Oparka and Prior, 1992), and slow modes that involve deposition of callose, a β-1, 3-glucan (Zavaliev et al., 2011). The mechanism for pressure-mediated closure has remained elusive. Callose levels in the neck regions are mainly affected by two groups of PD-localized enzymes, callose synthases and β-1,3-glucanases. PD-LOCALIZED β-1,3-GLUCANASE (PdBG) 1 and 2 are both expressed in lateral root primordia. The *pdbg1,2* double mutant accumulated more callose relative to wild type and displayed reduced cell-to-cell trafficking of macromolecules in roots (Benitez-Alfonso et al., 2013). Overexpression of the PD-associated REVERSIBLY GLYCOSYLATED POLYPEPTIDES 2 (RGP2) protein, led to higher callose levels, likely interfering with conductance since elevated callose levels were correlated with reduced intercellular assimilate transport (Sagi et al., 2005). Members of the CALLOSE SYNTHASE (CALS) family are responsible for callose production at PD orifices. *Cals7* mutants failed to accumulate callose in PD of early sieve plates, resulting in reduced sieve pore number (Xie et al., 2011). Other members, such as CALS3 have similar roles in different cell types, *e.g.*, *cals3s* mutants showed elevated callose levels at PD and impaired GFP movement in Arabidopsis root tips (Vaten et al., 2011). By contrast, PD in maize callose synthase *tie-dyed2* mutants appeared to be unaffected, displaying normal callose deposition (Slewinski et al., 2012). However, *tie-dyed2* mutants hyperaccumulated starch and soluble sugars in leaves due to a defect in the cell-to-cell solute movement at the SE-CC interface. Furthermore, since the TD2 protein did not localize to PD but to the ER, its role is likely indirect (Baker and Braun, 2008; Slewinski et al., 2012). Remorins, were also shown to affect PD conductance. NDR1/HIN1-like26 (NHL26), a vasculature-specific protein that localizes to both PD and ER may be another protein important for PD function (Vilaine et al., 2013). Plants that ectopically overexpressed NHL26 displayed various phenotypes such as delayed flowering and senescence, reduced seed yield and increased fresh weight of rosette leaves (Vilaine et al., 2013). *nhl26* mutants accumulated sugars in mature source leaves which correlated with a reduction in sugar content in phloem sap exudates and seeds. At the same time, the raffinose concentration of phloem sap exudate increased in the mutant. NHL26 may thus play a role in modulating sugar export between CC and SE by affecting PD permeability.

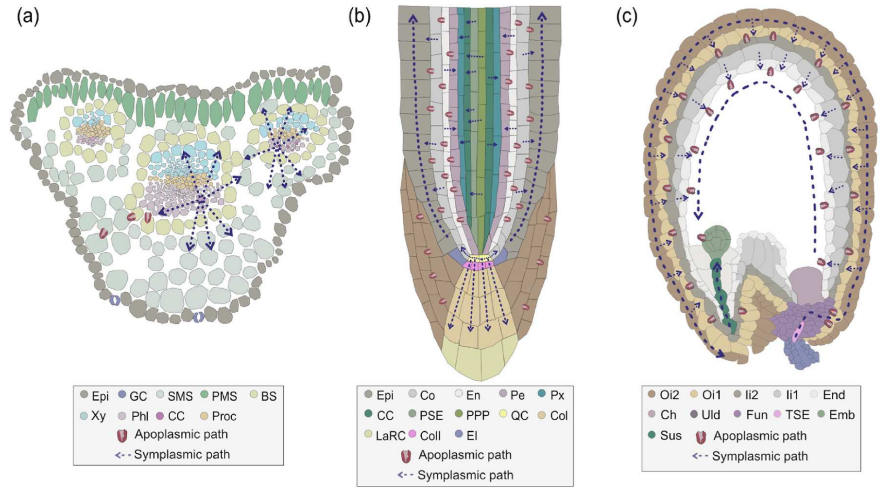

Fig. 3. Overview of the symplasmic domains in Arabidopsis tissues. Symplasmic and apoplasmic domains within the Arabidopsis leaf (a), root (b), and seed at the early globular stage (c). Symplasmic domains were identified by imaging the diffusion of GFP synthesized in specific cell types in studies from different labs. (a) In the leaf, GFP moves out of the companion cell (CC) only during the sink stage (Imlau et al., 1999; Skopelitis et al., 2018). (b) In the root, GFP is efficiently off-loaded from the phloem into primary meristems and from quiescent center (QC) into the columella (Col) (Imlau et al., 1999; Vaten et al., 2011; Liu et al., 2017; Skopelitis et al., 2018). Non-cell-autonomous transcription factors move from the cortex (Co)/endodermis (En) into epidermis (Epi) and pericycle (Pe) (Rim et al., 2011). (c) After fertilization, new branched PD are formed in the unloading zone (Uld) of seeds contributing to the formation of the symplasmically unloading unit (Stadler et al., 2005b; Werner et al., 2011). Efflux transporters are also localized in this zone, indicating the involvement of apoplasmic unloading step from the unloading domain to the integuments (Chen et al., 2015; Müller et al., 2015). The cells of the outer and inner integument of the seed form a symplasmic continuum (Stadler et al., 2005a). Arrows indicate the direction of the cell-to-cell movement in the symplasmic pathway. SE: sieve element. Oi: outer integument, Ii: inner integument. Epi: epidermis, Col: columella, Co: cortex, En: endodermis, Px: protoxylem, PSE: protophloem sieve element, Pe: pericycle, QC: quiescent center, Li: lateral root initials, EI: epidermis initials, LaRC: lateral root cap, ColI: columella initials, PPP: phloem pole pericycle, CC: companion cell, GC: guard cell, MS: mesophyll, PMS: palisade mesophyll, BS: bundle sheath, Xy: xylem, Phl: phloem, Proc: procambium, Pa: parenchyma.

PD are characterized by unique lipid composition. In particular, they share features with detergent-resistant microdomains enriched for sterols and sphingolipids (Grison et al., 2015; Liu et al., 2020). In Arabidopsis, the sphingolipid profiles affected PD permeability (Yan et al., 2019; Iswanto et al., 2020; Liu et al., 2020). Loss-of-function mutants of *PHLOEM UNLOADING MODULATOR* (*PLM*), which affects sphingolipid biosynthesis, caused an increase in phloem unloading at the interface between PPP and root endodermis independently of callose deposition (Yan et al., 2019). In contrast, Arabidopsis double mutants of *SPHINGOID LCB DENATURASE 1* and *2*, which showed a higher content of the long-chain sphingolipid phytosphinganine, displayed reduced PD permeability which correlated with an increase in callose accumulation (Liu et al., 2020). Similarly, Arabidopsis hypocotyls treated with inhibitors of the sphingolipid metabolism displayed reduced PD permeability which was associated with an higher level of callose deposition (Iswanto et al., 2020). A systematic characterization of the PD lipid composition is hampered by the difficulties in purifying PD, but would allow identification of the molecular mechanisms that contribute to lipid-mediated callose deposition and its role in PD transport.

So far, PD conductance was mainly studied by tracking the distribution of fluorescent dyes or by monitoring complex phenomena such as the distribution of ^{14}C-labeled sucrose or accumulation of starch in gain- or loss-of-function mutants. However, in several cases, the differences could be due to indirect effects (*e.g.*, reduction in PD number) rather than PD conductance. For example, maize mutants in *Carbohydrate partitioning defective33* showed decreased sucrose export yet had lower PD numbers at the SE-CC interface (Julius et al., 2018; Tran et al., 2019). The development of direct assays to monitor transport would help boosting our understanding of the mechanisms and regulation of PD conductance.

6. Viral movement proteins affect carbon allocation

A group of proteins that are not native plant components but target PD are the viral movement proteins (MPs), which are required for cell-to-cell movement of viral genomes and virus. MPs accumulate at PD where they gate PD at the infection front, increasing the SEL and enabling the spread of infectious components (Wolf et al., 1989; Benitez-Alfonso et al., 2010). Notably, MPs impact also carbohydrate metabolism and allocation. For instance, transgenic tobacco plants expressing the tobacco mosaic virus (TMV) MP under constitutive or phloem-restricted promoters caused a reduction in assimilate translocation to roots and an accumulation of starch in source leaves (Lucas et al., 1993; Balachandran et al., 1995; Olesinski et al., 1995). In contrast, expression of TMV MP under a green tissue-specific promoter in potato resulted in lower carbohydrate content and higher sucrose export (Olesinski et al., 1996). Tobacco plants expressing a MP from the phloem-limited potato leafroll virus (PLRV MP17) accumulated more sugars in source leaves (Herbers et al., 1997). Starch accumulation depended on MP17 dosage; low levels of MP17 caused a decrease in sugar content, possibly due to increased PD SEL, while carbohydrate excess seemed to be a consequence of indirect effects of high MP17 levels (Hofius et al., 2001). Deletion mutants in an MP domain of TMV that affected the SEL indicated that the effects on carbohydrates were SEL-independent (Balachandran et al., 1995). These findings imply complex roles that may be tissue- or even species-specific and an emerging model where carbon allocation might be regulated by MPs in subtle manners by interference of MPs endogenous signals involved in supracellular communication (Balachandran et al., 1995; Lucas and Wolf, 1999). This effect could be simply a side effect of alterations of the PD to allow the virus to spread, or may serve in providing zones that

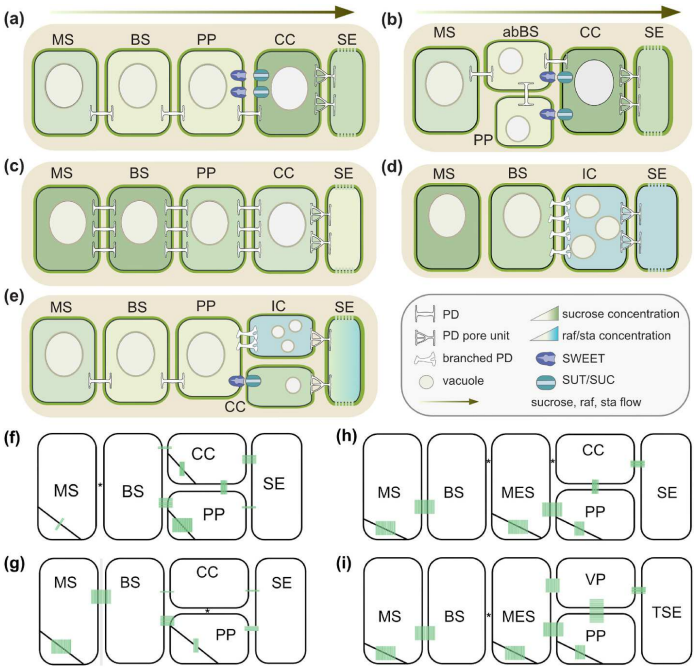

Fig. 4. Plasmodesmatal connectivity in relation to phloem loading. (a–d) Sucrose produced in mesophyll cells flows towards sieve elements for phloem loading by distinct mechanisms. Arrows indicate the direction of flow of sucrose and raffinose/stachyose from MS to SE as indicated in the legend of the schematics (right panel of Fig. 4e). Note that relative cell size depicted in the schematics does not reflect actual sizes. (a) Apoplasmic phloem loading in Arabidopsis. (b) Apoplasmic phloem loading in maize (c) Passive symplasmic loading. (d) Polymer trap symplasmic loading. (e) Mixed loading. (f–i) Plasmodesmograms indicating the density of plasmodesmata at the cellular interfaces of leaves in Arabidopsis (f), maize (g), and rice (h, i). Likely, different mechanisms may coexist in a single species and contribution may depend on environmental condition or developmental state. Two potential routes for phloem loading in rice: an apoplasmic (h) and a symplasmic route (i). Asterisks indicate data not found in the corresponding interface. The number of green lines denotes PD density at cellular interfaces. MS: mesophyll cell, BS: bundle sheath cell, PP: phloem parenchyma, CC: companion cell, SE: sieve element, IC: intermediary cell, VP: vascular parenchyma, MES: mestome sheath. raf: raffinose, sta: stachyose. (For interpretation of the references to colour in this figure legend, the reader is referred to the Web version of this article.)

have sufficient energy to allow for effective virus replication. No doubt, MPs are highly useful tools to study PD function and their contribution to carbon allocation. In summary, a better understanding of PD composition and function would be important also for developing new ways to engineer virus resistance.

7. Symplasmic domains may enable exchange of communication and sugars in zones

During differentiation, dynamic control over PD distribution and permeability leads to changes in the formation of "symplasmic domains", where exchange occurs through PD between specific cell groups while being restricted in others (Rinne and van der Schoot, 1998). These functional domains allow specific developmental programs to take place in restricted areas. Although not equivalent to native components of plant cells, GFP and dye loading have been used as a proxy for symplasmic translocation of small molecules (Duckett et al., 1994; Oparka et al., 1999; Kim et al., 2005b; Stadler et al., 2005a). By tracing GFP expression driven by the phloem specific *SUC2* promoter, different sink tissues such as the seed coat, the anther connective tissue, cells of the root tip and sink leaf mesophyll cells were identified as symplasmic domains connected to the phloem (Imlau et al., 1999). Free GFP expressed from the *SUC2* promoter diffused throughout sink leaves (Fig. 3a), while it was restricted to the vasculature after maturation (Imlau et al., 1999; Skopelitis et al., 2018). Notably, microRNAs like miRGFP could move across sink and mature source leaves (Skopelitis et al., 2018).

Symplasmic domains can be regulated in a spatio-temporal manner. For instance, during the vegetative phase, Arabidopsis shoot apices are symplasmically isolated in the meristematic corpus while shortly before and during the floral transition the symplasmic domain is extended throughout the whole shoot apex (Gisel et al., 1999). In poplar and birch, the shoot apical meristem is symplasmically isolated during dormancy (Rinne et al., 2001, 2011). In Arabidopsis, root hair cells gradually become symplasmically isolated during differentiation (Duckett et al., 1994), while cotton fiber cells are temporarily symplasmically isolated during fiber cell elongation (Ruan et al., 2001).

In the Arabidopsis root apex, mCherry expressed from cortical epidermal cells moved throughout all root tissues (Rim et al., 2011). By using differently sized mCherry reporters *i.e.,* 2xmCherry or mCherry-NLS, high SELs (~60 kDa) between the stellar-endodermal and the cortical-epidermal cell boundaries were observed, while the SEL between QC and cortex cells to root cap cells was lower (27 and 54 kDa, respectively) (Fig. 3b). Notably, several non-cell-autonomous transcription factor FP-fusions were shown to move across the stellar-endodermal and cortical-epidermal cell borders, despite surpassing the proposed SEL of 60 kDa, possibly implying other mechanisms (Rim et al., 2011).

During stomatal development, the stomata identity factor SPEECHLESS (SPCH) is symplasmically restricted to stomatal initials. After differentiation, stomata become fully symplasmically isolated by losing their PD (Lee et al., 2005). Callose synthase GLUCAN SYNTHASE-LIKE 8 mutants failed to accumulate callose in PD. As the result, stomatal initials were symplasmically connected and formed clustered stomata (Guseman et al., 2010).

During seed filling Arabidopsis seeds are provided with assimilates through the funicular phloem, which is symplasmically extended by the outer integument of the seed, while transport to the inner integument, a separate symplasmic domain, occurs apoplasmically (see also section *Contribution of PD to unloading of the phloem*). The suspensor, which connects embryo with maternal tissues and endosperm, forms a symplasmic domain with the embryo in early embryogenesis (Fig. 3c). At later stages of embryogenesis, the suspensor becomes symplasmically isolated and degenerates (Stadler et al., 2005a; Lafon-Placette and

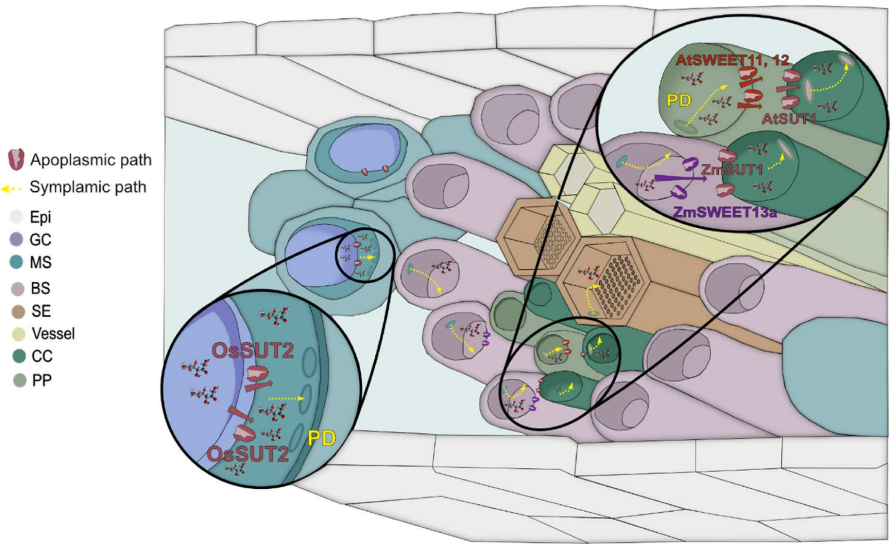

Fig. 5. A hypothetical model for phloem loading combining mechanisms identified in Arabidopsis, maize, and rice. Sucrose is primarily synthesized in leaf mesophyll cells. In Arabidopsis, sucrose is thought to move cell to cell via PD down a concentration gradient until it reaches the PP. At the PP-SECC interface, AtSWEET11 and AtSWEET12 mediate the efflux of sucrose into the apoplasm of Arabidopsis leaves, from where it is actively loaded into the SECC via SUT1 sucrose/H^+ symporters. In maize, ZmSWEET13s are found in the abaxial bundle sheath cells of minor veins where they mediate the efflux of sucrose towards the phloem, then following a symplasmic path to the SECCC. In rice, high levels of sucrose are stored in vacuoles of mesophyll cells where the vacuolar sucrose/H^+ symporter OsSUT2 mediates its export to the cytosol against a concentration gradient. OsSUT2-mediated transport, as a consequence of the large cytosol/vacuolar proton gradient, should lead to sucrose concentrations in the cytosol that exceed that of phloem sap (600 mM) to enable passive phloem loading via PD down the concentration gradient. Epi: epidermis, GC: guard cell, MS: mesophyll, BS: bundle sheath, SE: sieve element, CC: companion cell, PP: phloem parenchyma. Illustration modified from an unpublished cartoon developed by Guido Grossmann (HHU, Düsseldorf).

Köhler, 2014). Throughout embryogenesis the embryo's PD permeability is downregulated, to establish four symplasmic subdomains. These subdomains align with the axial body pattern: cotyledons, shoot apex, hypocotyl, and roots (Kim et al., 2005b). Symplasmic domains also are formed in certain plant-microbe interactions, *e.g.*, during nodule development in rhizobia-colonized tissues of *Medicago truncatula*, symplasmic domains are created while PD deposited callose levels decrease. The ß-glucanase MtBG2 seems to play an active role in callose degradation during nodule development (Gaudioso-Pedraza et al., 2018).

While symplasmic isolation is one option for controlling trafficking during development, multiple lines of evidence implicate other transport mechanisms, such as unidirectional PD flow in trichomes (Christensen et al., 2009), dilation of PD during protein trafficking across PD (Wolf et al., 1989; Xoconostle-Cázares et al., 1999), and cargo-gating dependent transport mechanism (Peters et al., 2021) (see also *PD transport mechanism*).

8. A focus on cell-to-cell translocation of carbohydrates

The translocation of carbohydrates between organs occurs via the phloem. The angiosperm leaf phloem is made up of three major cell types: the phloem parenchyma, CC and SE (van Bel and Knoblauch, 2000; Kim et al., 2021). SEs are the actual conduits, but since mature SE does not contain a nucleus and are assumed to not participate in major ways in metabolism of assimilates, these must be supplied from the neighboring CC via PD. It is generally assumed that sucrose, produced in the mesophyll, moves via PD towards the phloem (Fig. 4). The subsequent path then involves PD in the bundle sheath, phloem parenchyma and in what has been defined as symplasmic species, even into the SECCC (described in the *Symplasmic phloem loading* section below). Plasmodesmograms were generated to map PD frequencies in route between mesophyll and sieve tubes in different species (van Bel et al., 1992) (Fig. 4f–i). However, the presence of high frequencies of PD does not fully reflect the existence of a symplasmic communication, even more for a specific compound since PD could be obstructed or at least non-permeable for the studied compounds. Direct evidence for the contribution of the symplasmic pathway to carbohydrate transport is still awaited. In apoplasmic species, there is a sparsity of PD between PP and the SECCC, requiring apoplasmic steps that make use of plasma membrane sucrose transporter pairs (described in the *Apoplasmic phloem loading* section below). Notably, mixed translocation may occur. Unloading of carbohydrates in sink tissues is also achieved either symplasmic or apoplasmically, sometimes requiring transporters at post-phloem unloading steps.

9. Apoplasmic and symplasmic pathways for phloem loading

The phloem sap distributes a wide range of ions, metabolites, RNAs and proteins between plant organs. According to Münch's hypothesis, the flow of the phloem sap is generated by osmotically driven pressure gradients between the loading sites (typically leaves, also defined as source organs, high pressure) to the unloading sites (diverse organs like roots, flowers or developing seeds, together defined as sink organs; lower pressure) (Knoblauch and Peters, 2010). In many plant species, sucrose is the dominant osmolyte contributing to the osmotic driving force for phloem translocation. The sucrose concentration in the phloem sap varies between species. The SECCC of sugar beet leaves contains 80% of the total leaf sucrose (45 μg cm^{-2} leaf blade) and has a sucrose concentration of 0.8 M (Geiger et al., 1974). Sucrose concentrations of 0.8, 1.0 and 1.0 M have been measured in spinach, barley and maize

leaves, respectively (Lohaus et al., 1994). In maize, the data on sucrose concentration in the phloem sap vary between 0.9 and 1.4 M (Ohshima et al., 1990; Weiner et al., 1991). By comparison, the phloem sap of rice contains 0.5–0.6 M sucrose (Kawabe et al., 1980; Hayashi and Chino, 1986). Lower concentrations of sucrose of ~250 mM have been measured in the phloem sap of wheat. Interestingly, in wheat, sucrose does not appear to be the dominant osmolyte since the phloem sap contains higher levels of K^+ (~300 mM) and amino acids (~260 mM) (Hayashi and Chino, 1986).

Besides the role in generating the osmotic driving force for phloem transport, sucrose serves as the primary carbon and energy source for diverse sink organs. To be exported from the source leaf, sucrose must be translocated from the mesophyll where it is produced, across several cell types before it can be loaded into the SE (Figs. 4 and 5). Thus, appropriate sucrose gradients are required for translocation. Results from incipient plasmolysis support the existence of such gradients in a variety of species (Geiger et al., 1974) (Fig. 4a–e). The export rate for sucrose per leaf has been estimated to $\sim 5 \times 10^{-13}$ mole sec^{-1} mm^{-2} and the average flux of sucrose per plasmodesma to 7×10^{-19} mole sec^{-1} for mesophyll cells, 2.4×10^{-19} mole sec^{-1} for bundle sheath, and 8.1×10^{-19} mole sec^{-1} for the SE-CC interface (Gunning, 1976). More recently, mathematical models based on structural features of specific PD have been generated to predict solute flux through PD (Deinum et al., 2019). The frequency of PD along the route from mesophyll and sieve tubes varies between different species, as illustrated in plasmodesmograms (van Bel et al., 1992) (Fig. 4f–i). For instance, C_4 species were shown to have twice the number of PD per pit field area compared with their C_3 counterparts, and the pit field area per mesophyll-bundle sheath interface area is five times higher in C_4 species (Danila et al., 2016). However, as the density of PD at cell wall interfaces alone does not fully represent the actual symplasmic transport capacity or symplasmic continuity, how far these differences in density influence symplasmic flux remains to be elucidated (Liesche et al., 2019).

So far, two major modes of phloem loading have been described based on the plasmodesmatal connectivity and presence of transporters: apoplasmic loading, mediated by membrane transporters, and symplasmic loading via the PD. The symplasmic loading pathway can occur in an active or passive manner. Some species adopt a mixture of both apoplasmic and symplasmic pathways and are therefore referred to as mixed loaders. Various substrates are loaded into the phloem other than assimilates (*i.e.*, amino acids and secondary metabolites), yet here we focus on the process of phloem loading of sucrose. A detailed description of the phloem loading process of other substrates than sucrose can be found elsewhere (Eom et al., 2015; Tegeder and Hammes, 2018; Kim et al., 2021).

10. Phloem loading with the help of an apoplasmic step

Based on the connectivity of CC with the adjacent phloem parenchyma, plant species were categorized into different 'loading types' by counting the relative frequency of PD at the PP-CC interface using electron microscopy or confocal microscopy of fluorescently tagged PD. Type 1 (or "open phloem") plants are characterized by a high, Type 1–2a with intermediate, and Type 2 (or "closed phloem") by low PD abundance at the PP-CC interfaces (Turgeon and Webb, 1976; Gamalei, 1989, 1991). This classification was further refined as Type 1, Type 1–2a, Type 2a, Type 2b (transfer cells), Type 2c (Kranz anatomy) and a new type called "intermediary cells" (Turgeon et al., 2001). Species with "closed phloem" are assumed to load sucrose from the apoplasm. in Type 2 species, a pair of sucrose transporters is required for phloem loading: (i) SWEET-uniporters for efflux of sucrose from PP into the apoplasm, and (ii) SUT/SUC H^+/sucrose symporters for energized import into the SECCC. The mechanism of apoplasmic phloem loading has been studied most extensively in Arabidopsis and maize (Fig. 4a and b). In Arabidopsis, SWEET11, SWEET12 (and possibly SWEET13) mediate cellular efflux of sucrose into the apoplasm inside the phloem that had been synthesized in mesophyll cells and was translocated to the phloem parenchyma via the PD (Chen et al., 2012). Sucrose from the apoplasm is then taken up into the adjacent SECCC by H^+/sucrose symporters (SUT/SUC) (Figs. 4a and 5). In maize, a similar pair of transporters is required for transfer to the sieve elements, yet SWEETs are present in a distinct cell type. *Zm*SWEET13a,b,c are specifically produced in the two abaxial BS cells of minor veins (rank-2 intermediate veins) from where they efflux sucrose into the general apoplasmic space of the phloem. The SECCC then uses the H^+/sucrose symporter SUT1 (different clade than SUT1 in dicots) to actively import sucrose (Figs. 4b and 5). Notably, none of the sucrose transport mutants characterized today fully blocked sucrose delivery, indicating that there are parallel pathways that may differ in their relative importance (see section *Mixed Loading Mechanisms*).

11. Phloem loading along symplasmic paths

It has been suggested that symplasmic phloem loaders are independent of plasma membrane SWEET and SUT activities by movement of sugars exclusively in the symplasm. Notably however, the SWEET and SUT gene families are present in all genomes, implying that they may be required under certain conditions also in these species. Two types of symplasmic phloem loading mechanisms have been described: passive symplasmic loading and active symplasmic loading, also known as the polymer trap mechanism.

1. Passive symplasmic loading. As postulated by the pressure-flow hypothesis (Münch, 1930), passive loading is only thermodynamically feasible if the sucrose concentration in mesophyll cells is higher relative to that in the phloem sap. Indeed, in many woody and several herbaceous species, the concentration of sucrose in the cytosol of mesophyll cells was found to be higher as compared to the concentration in the phloem sap (Turgeon and Medville, 1998; Fu et al., 2011) (Fig. 4c). These species accumulated less starch in minor veins when treated with exogenous sucrose compared with plants that load sucrose actively and were rich in PD along the path from mesophyll to the SE (Turgeon and Ayre, 2005; Reidel et al., 2009; Rennie and Turgeon, 2009; Fu et al., 2011). However, although these factors fulfill the prerequisites for passive loading, there was a fundamental question of whether the pressure generated in passive loaders is sufficient to drive long-distance transport in large plants, such as tress. Modeling studies using anatomical data and experimental observations using synthetic tree-on-a-chip system indicated that small pressure differences may be sufficient to drive long-distance sugar translocation in tress (Jensen et al., 2012; Comtet et al., 2017). Furthermore, anatomical studies of the sieve tube and sieve plate in trees revealed a shift in SE structure that scales the sieve tube resistance along the path from leaf to root and, thus reduces the pressure required for sugar transport (Savage et al., 2017). These results indicate that tall trees can also rely on pressure-flow for symplasmic sugar transport.

2. Active symplasmic loading. The 'polymer trap' hypothesis for active symplasmic loading was based by the observation that species with specialized companion cells (referred to as intermediary cells) translocate raffinose family oligosaccharides (RFOs; raffinose; stachyose (Turgeon and Gowan, 1990). According to the 'polymer trap' model, sucrose (342 Da) diffuses down the concentration gradient across PD from the mesophyll across bundle sheath into intermediary cells. Intermediary cells convert a portion of sucrose into raffinose (594 Da) and stachyose (667 Da). The SEL of PDs at the interface is predicted to be so small, that it only allows sucrose to enter intermediary cells, while RFOs are too large to diffuse back (Fisher, 1986; Turgeon et al., 1993) (Fig. 4d). This way RFOs are trapped in the intermediary cell (polymer trap) (Fisher, 1986; Turgeon and Medville, 1998; Botha and Murugan, 2021). Thus, symplasmic translocation is energized by the enzymatic conversion of sucrose to raffinose by galactinol synthases in the intermediary cells (McCaskill and Turgeon, 2007). At present, it is not yet clear how much the cytoplasmic sleeve space would have to be reduced

to prevent back leakage of sucrose from the intermediary cells to the bundle sheath cells. Assuming that the hydrodynamic radius governs the mobility of sugars through PD (Terry and Robards, 1987), the cytoplasmic sleeve space in the plasmodesmata within the IC-side needs to be reduced to < 10.4 Å (hydrodynamic diameter of sucrose) to prevent leakage of sucrose back to the bundle sheath (Botha et al., 1993; Botha, 2005; Botha and Murugan, 2021). Recent high-resolution TEM analyses in *T. capensis* leaf veins revealed that the radius of the open cytoplasmic sleeve within the sphincter zone (physical constriction) on the IC side of the bundle sheath-intermediary cell PD was reduced to 1.5 nm (Botha et al., 1993; Botha, 2005; Botha and Murugan, 2021). If these PD have such a small SEL, then likely larger molecules such as RNAS and proteins, should not be able to move across this interface. We note, however, that formally, neither the transport of sucrose through PD, nor an SEL that allows sucrose to pass, - but prevents raffinose to back-diffuse through PD, have experimentally been demonstrated. As direct evidence is still lacking, there are still controversial views on whether additional factors are involved for active symplasmic loading (Dölger et al., 2014).

12. Mixed loading mechanisms

Species were generally classified as falling into one of the phloem loading strategies. However, multiple lines of evidence indicate that a single species can use more than one strategy, or mixed loading. All species, no matter how they have been classified maintain the SWEET and SUT sucrose transporter genes. Thus, parallel use of multiple phloem loading strategies may be beneficial under specific environmental conditions. In line with this notion, an 'ecophysiological hypothesis' has been proposed. According to this hypothesis, the relative activity of apoplasmic/symplasmic modes depends on environmental conditions and this heterogeneity allows plants to rapidly adapt to biotic and abiotic stresses (van Bel and Gamalei, 1992). Whether all species are generally mixed loaders, and/or whether there is an unexplored mechanism that species use to load sugars (*i.e.*, regulation of PD during symplasmic loading) remains to be elucidated.

Indirect evidence for mixed loading comes from anatomical features of polymer trap species. In various polymer trap species, such as cucurbits, CC have few symplasmic connections to surrounding cells (resembling ordinary companion cells of apoplasmic loading species) in addition to intermediary cells (Turgeon and Webb, 1976) (Fig. 4e). In other species such as *Asarina scandens* and *Acanthus mollis*, cell wall ingrowths were observed in the companion cells (van Bel and Gamalei, 1992; Rennie and Turgeon, 2009). Cell wall ingrowths are typical features of cells involved in apoplasmic loading that are thought to magnify the plasma membrane surface area, allowing deployment of more transporters and effectively increasing the flux. Analyses in polymer trapping species such as *Alonsoa meridionalis* (*A. meridionalis*) showed that the sucrose concentration in the phloem sap can be as high as in mesophyll cells, indicating the absence of the required sucrose gradient. Furthermore, *Am*SUT1 was shown to be present in the plasma membrane of SE and CC supporting the claim that apoplasmic loading through ordinary CC is also a mechanism that *A. meridionalis* uses for phloem loading (Knop et al., 2004; Voitsekhovskaja et al., 2006).

Other evidence for the coexistence of phloem loading mechanism can be derived from the analysis of mutants that either disrupt key pathways critical for polymer trapping or apoplasmic sucrose transporters. The majority of mutants with impaired RFO production in species using active symplasmic loading strategies did not display severe phenotypic symptoms or still transported sucrose (McCaskill and Turgeon, 2007). Furthermore, mutants of sucrose transporters in species considered as apoplasmic loaders, including *sut1/suc2* or *sweet11;12* in Arabidopsis or *zmsweet13a,b,c* and *sut1* in maize, were able to produced seeds, indicative of a remnant alternative loading mechanism (Riesmeier et al., 1994; Gottwald et al., 2000; Slewinski et al., 2009; Srivastava et al., 2009; Chen et al., 2012; Bezrutczyk et al., 2018). Although we can neither rule out that the mutants are not null, nor that compensatory mechanisms exist, these observations are consistent with mixed loading (McCaskill and Turgeon, 2007).

Notably, rice, which like maize belongs to the *Poaceae*, seems to use a symplasmic loading pathway, despite the high concentration of sucrose in the phloem sap. The presence of numerous PD connections between the CC and the parenchyma cells and the movement of the low molecular weight dye CFDA led to an assumption that sucrose loading occurs symplasmically (Kanako et al., 1980; Chonan et al., 1981; Scofield et al., 2007). Later, multiple members of OsSUT and SWEET families and proton pumping pyrophosphatases (H^+-PPases) were shown to be expressed in the phloem (Scofield et al., 2007; Regmi et al., 2016; Wang et al., 2021). More recently, the OsDOF11 transcription factor was shown to affect phloem loading by promoting the expression of OsSUTs and OsSWEETs (Wu et al., 2018). Together, these results served as strong evidence for claiming that rice employs apoplasmic loading as a major phloem loading strategy. However, *sweet13,14* double mutants had no obvious defect in phloem loading, and *ossut1* mutants and RNAi lines grown in growth chambers did not show measurable defects, yet field-grown mutants showed a mild decrease in height (Ishimaru et al., 2001; Scofield et al., 2002; Eom et al., 2012). By contrast mutants in the vacuolar SUT2, present in mesophyll cells, were lethal, possibly providing a mechanism for generating a steep sucrose gradient between the mesophyll cytosol and the phloem via active sucrose efflux from the vacuole into the mesophyll cytosol (Eom et al., 2012, 2019).

13. Contribution of PD to unloading of the phloem

Following phloem loading, assimilates are distributed through the sieve tubes to sink organs. The transfer of assimilates from the phloem cells to sink cells is called phloem unloading. The most widely accepted model describing phloem unloading is the high-pressure manifold model (Fisher et al., 2000). Based on this model, a high hydrostatic pressure is maintained throughout the flow in the sieve tube with low-pressure gradients from source to sink, but high-pressure gradients between the SE and the neighboring cells where the unloading occurs (unloading zone). Recent turgor measurements in some species such as morning glory however, did not support this model as low pressures were generated for flow but high-pressure differentials sufficient for unloading were not maintained in the unloading zone (Christensen et al., 2009; Knoblauch et al., 2016; Milne et al., 2018). These observations raised the possibility that the PD conductance in the unloading zone is high or/and an alternative strategy, such as active unloading processes, are being used. Indeed, as for phloem loading, phloem unloading can occur along sym- or apoplasmic pathways, and the relative contribution seems to vary depending on species, sink organs, and the sugars that are transported (sucrose, RFOs, or sugar alcohols).

In various species and tissues such as sink leaves of dicots, tubers, stem zones of herbaceous crop plants, developing fruit and seeds, phloem unloading occurs predominantly via the symplasmic route (Oparka et al., 1994; Ruan and Patrick, 1995; Wright and Oparka, 1997; Imlau et al., 1999; Imlau et al., 1999, 1999; Fisher and Cash-Clark, 2000; Patrick and Offler, 2001; Ruan et al., 2001; Viola et al., 2001; Wu et al., 2004; Kim and Zambryski, 2005; Rae et al., 2005; Nardozza et al., 2013; Milne et al., 2017; Skopelitis et al., 2018; Mehdi et al., 2019; Ko et al., 2021; Pan et al., 2021) (Fig. 3). For symplasmic unloading to occur, functional PD connections between the phloem cell types and neighboring cells must be present. Indeed, numerous PD are observed between SECCC and neighboring cells at sink organs as described in the section *Symplasmic domains may enable exchange of communication and sugars in zones*.

Phloem unloading has been studied most extensively in roots and seeds of Arabidopsis (Fig. 3b and c). A recent study that combined microscopy and mathematical modeling provided evidence for a mechanism in which small solutes (0.34–0.38 kDa) (suitable for sucrose translocation) freely move across PD, and are unloaded from the SE into

the PPP by funnel-shaped PD by a combination of mass flow and diffusion (Ross-Elliott et al., 2017) (Fig. 3b) (see also *PD transport mechanisms*). SUT sucrose transporters (*e.g.*, AtSUC1) may function in sucrose retrieval to maintain high turgor pressure necessary for symplasmic unloading by bulk flow (Milne et al., 2017, 2018). At the PPP, PLM, a putative enzyme necessary for sphingolipid metabolism was shown to play a role in symplasmic unloading by affecting PD ultrastructure at the interface between the PPP and endodermis (Yan et al., 2019). Similar as in Arabidopsis, phloem unloading in cassava (Manihot esculenta) was shown to occur via the symplasmic pathway into the phloem parenchyma cells of tuberous roots (Mehdi et al., 2019).

In seeds of Arabidopsis, phloem unloading takes place in the so-called unloading domain (ULD). The ULD emerges after fertilization when secondary PDs are formed *de novo* between the terminal SE and surrounding cells (Fig. 3c). Studies using fluorescent tracers revealed symplasmic continuity between terminal SE and the neighboring cells in the ULD, which extends to the outer integument (Patrick and Offler, 2001; Werner et al., 2011; Müller et al., 2015). SWEET efflux transporters were not detected at the ULD, in line with the notion that symplasmic routes are the dominant paths for unloading sugars in Arabidopsis seeds. After sugars have been unloaded into the ULD, post-phloem transport occurs likely both on sym- and apoplasmic paths. Multiple SWEETs (AtSWEET11, 12, and 15) are positioned at different cell layers to mediate a cascade of sucrose transport from the maternal tissue to the developing seed (Chen et al., 2015). So far, the mechanism of how sucrose enters the embryo is not resolved, Two possible routes have been proposed. The first route involves sucrose uptake in the suspensor (likely mediated by SWEET12) (Chen et al., 2015). The suspensor and the embryo are symplasmically connected at the globular stage. PD connecting the suspensor and embryo were shown to have a SEL of >2.6 nm (Stadler et al., 2005a). The second route requires the export of sucrose from the endothelium and uptake in the endosperm. Hexoses are the most abundant sugars accumulating in the endosperm during the early embryogenesis stage (Baud et al., 2002; Morley-Smith et al., 2008). Therefore, hexose transporters and invertases might play a major role in this path. Following import into the embryo, sugars likely move symplasmically throughout the embryo (Kim et al., 2005a, 2005b). As in Arabidopsis, phloem unloading and post-phloem transport occur via both sym- and apoplasmic routes in various species (Gisel et al., 2002; Kim et al., 2002a). In rice, sucrose is unloaded into the parenchyma cells and then to the nucellar layers symplasmically, while at later stages (export from the nucellar layer and import into the endosperm) occurs on an apoplasmic path (Oparka and Gates, 1981; Oparka and Gates, 1981; Yang et al., 2018). Here SWEETs and SUTs likely play roles at different places in the nucellar projection and at the interface to the endosperm (Yang et al., 2018).

In some species, phloem unloading pathways change during development. Unloading processes shift in Arabidopsis (Chen et al., 2015). In several legumes, apoplasmic pathways change during seed development by switching from a mechanism also involving invertases and hexose importers during the cell division phase to a sucrose transport pathway during the storage phase (Patrick and Offler, 2001; Borisjuk et al., 2002). In tobacco leaves, dye coupling from CC to PP it discontinued in the transition from sink to source, which correlates with dynamic changes from simple to complex PD (Oparka et al., 1999; Roberts et al., 2001). A correlation between onset of flowering and decreased leaf-to-shoot trafficking of symplasmic tracers was observed, which suggests a selective transport mechanism of signaling molecules during floral induction (Gisel et al., 1999, 2002; Ruan et al., 2001).

Due to the importance of fruit development in food production, phloem unloading during fruit development were studied in much detail. In some species, there is a shift from the apoplasmic to the symplasmic pathway. For instance, in potato plants (*Solanum tuberosum*), the apoplasmic unloading pathway is considered to be the major route for sugar transport in stolon undergoing extension growth while symplasmic unloading becomes the dominant path after tuberization (Viola et al., 2001). There are also species in which the process is different. In grape *Vitis vinifera* berries, symplasmic post-phloem unloading predominates in the early and middle stages in fruit development as shown with symplasmic tracers that were released from the phloem strands. However during ripening, the movement of symplasmic tracers was blocked, indicating a transition to an apoplasmic path (Zhang et al., 2006). TEM micrographs showed a higher electron-density in the PD at the late stage of fruit development which might be the cause of the blocking of the PD and the shift in the unloading pathways (Zhang et al., 2006).

Similar to grape berries, at the early stage of tomato (*Solanum lycopersium*) fruit development, photoassimilates are predominantly unloaded from the SECCC to surrounding parenchyma cells via PD. Yet, at later stages, apoplasmic routes seem to be the dominant path for sucrose unloading, indicted by a reduction in the mobility of symplasmic tracers and reduced abundance of PD connections (Ruan and Patrick, 1995). A recently identified sucrose transporter SISSWEET15 accumulated in vascular tissues of developing fruits. Fruits of *slsweet15* mutants were smaller in size, implicating SISWEET15 in mediating apoplasmic sucrose unloading during fruit development (Ruan and Patrick, 1995; Ko et al., 2021). Understanding phloem unloading mechanisms in fruits may allow scientists to develop strategies to improve fruit quality and yield.

14. Dynamic regulation of symplasmic connectivity

Although primary and secondary PD differ in their ontogeny, to our knowledge, no structural and functional differences have been reported yet. In contrast, simple and branched PD have been considerably investigated with the aim to identify differences in functions during plant development. Their obvious structural features allows identification and determination of spatial and temporal distribution; for instance in the sink-source transition of *Nicotiana tabacum* leaves (Roberts et al., 2001). The frequency of simple PD declines substantially during the sink-to-source transition between all examined cell types. At the same time branched PD increase in number (Oparka et al., 1999). As shown by analyses of the cell-to-cell movement of GFP fusions, the rise of branched PD frequency is associated with a substantial decrease of the PD SEL (Oparka et al., 1999; Crawford and Zambryski, 2001). In immature sink tissues, the steady state SEL of PD was shown to be around 50 kDa, allowing basal transport of large components such as proteins (average molecular mass of Arabidopsis proteins: 43 kDa) (Oparka et al., 1999; Tiessen et al., 2012). By contrast, in mature source tissues of tobacco, the SEL was determined to lie between 0.7 and 4 kDa, excluding the possibility of transport for the majority proteins, provided that the SEL determined is relevant for the transport of native proteins (Wolf et al., 1989). Since cellular differentiation requires the exchange of positional information with neighboring cells, in particular via non-cell-autonomous proteins and RNA (Marzec and Kurczynska, 2014; Otero et al., 2016), this decrease in SEL and/or PD branching could be a mechanism to restrict signaling to a specific cell cluster, without impairing the transport of sucrose (Ehlers and Kollmann, 2001). Roberts et al., also highlighted that branched PD appear asynchronously in the different leaf cell layers (Roberts et al., 2001). Branched PD develop first at the junction between epidermal cells and trichomes, between stalk cells of the trichome and in vascular tissues. They then emerge in sequential order in the upper epidermis, the lower epidermis, the spongy mesophyll and the anticlinal walls between palisade cells. At the end of the leaf development, only glandular cells of trichomes retain simple PD. Interestingly, this sequence of emergence coincides with that of tobacco leaf development (Poethig and Sussex, 1985). This is consistent with the general observation that immature tissues typically contain predominantly simple PD (Burch-Smith et al., 2011b), and indicates that PD branching is somehow linked to tissue differentiation. The sink-source transition was also found to be associated with an increase in leaf thickness by 40–50%, and the formation of large intercellular spaces in the mesophyll, leading to a decrease in shared-cell-wall interface area (Roberts et al., 2001). It has been suggested that during cell enlargement

and separation occurring during the sink-source transition, many simple PD are ripped apart, and that others are converted into branched PD. Although the roles of branched PD are still unclear, it has been hypothesized that they could represent solid junctions aiming at preserving cell adhesion, thereby contributing to cell shape formation and cell positioning during cell expansion and differentiation (Roberts et al., 2001).

15. Tools for studying and modifying PD transport

Our current understanding of PD conductance is based mainly on the use of tools that track cell-to-cell movement of molecules (Table 1) and our limited ability to manipulate PD gating and the analysis of the resulting alterations in distribution of the molecules, *e.g.*, accumulation or depletion in defined zones (Table 2). Actual translocation via PD has rarely been shown (Table 1). For instance, there are no data on the actual transport of K^+, Ca^+, glucose, and limited data regarding RNAs, proteins and sucrose. Most of the approaches undertaken with these tools are based on the assumption that cell-to-cell movement occurred through PD, and provide only indirect evidence since apoplasmic pathways could not be excluded. Unambiguous evidence can only come from studies that monitor the actual translocation through PD. One such method applicable to proteins is single molecule tracking, which has

Table 1
Tools available to study PD permeability.

TOOLS		MAIN STRENGTHS	MAIN WEAKNESSES	EXAMPLES	REF.
Indirect	**Dyes**	- Fast and easy to implement - High spatial specificity by photobleaching or photoactivation	- Only relative to the employed dye; do not provide information regarding endogenous molecules - No direct evidence	Assaying PD permeability using CFDA and the Drop-And-See (DANS) quantitative approach in Arabidopsis leaves	Cui et al. (2015)
				3D photoactivation microscopy using CMNB-caged fluorescein to study PD permeability between single cells in *Cucurbita maxima* mesophyll	Liesche and Schulz (2012b)
				Fluorescence loss in photobleaching using CFDA to study PD permeability along the phloem loading pathway in nine species	Liesche et al. (2019)
	Fluorescent proteins (FP)	- High spatial specificity using tissue-specific promoters, photobleaching, bombardment, or using photoactivable FP - To study PD SEL by fusion to *FP* sequence - For specific non-cell-autonomous proteins/RNA by fusion to *FP* sequence	- Fusion to *FP* sequence might affect permeability of non-cell-autonomous molecules - No direct evidence	Expression of GFP 1X, 2X and 3X under *STM* promoter to study cell-to-cell communication and SEL in Arabidopsis embryos	Kim and Zambryski (2005)
				Bombardment with vectors encoding GFP in Arabidopsis epidermal cells to compare PD permeability between WT and β-1,3-glucanase deficient mutant	Levy et al. (2007)
				DRONPA-s photoactivable FP to compare symplasmic connection of single cells in Arabidopsis roots	Gerlitz et al. (2018)
				Fusion of maize KN1 to *GFP* to study the non-cell-autonomous protein KN1 specific PD diffusion in Arabidopsis leaves	Kim et al. (2002b)
				RNA-SL/MS2-GFP system to track *FT* mRNA in *N. benthamiana* leaves	Luo et al. (2018)
	Sucrose analogue	Real-time imaging of sucrose analogue in living plant cells	- No direct evidence	Alkyne-tagged compound as a sucrose analogue is recognized by sucrose transporters and allow to visualize real-time uptake of sucrose	de Moliner et al. (2021)
	RNA interference	- For non-tagged RNA - High spatial specificity using tissue-specific promoters	- Possible off-targets - No direct evidence	miRGFP sensor system to study miRNA mobility in Arabidopsis	Skopelitis et al. (2018)
				GFP sensor system in which *GFP* sequence is fused to miR171 target sequence to study miR171 mobility in *N. benthamiana*	Parizotto et al. (2004)
				Expression of *SUL* inverted repeat sequence under *SUC2* promoter to study RNAi spreading in Arabidopsis	Rosas-Diaz et al. (2018)
	Sensors	- For endogenous molecules - In native conditions	- Specific sensors with compatible affinities are rarely available - Might affect the homeostasis of investigated molecules - No direct evidence	GCaMP3 fluorescent protein cytosolic calcium sensor to monitor calcium propagation in response to wounding in Arabidopsis	Toyota et al. (2018)
				Cameleon (NES-YC3.6) fluorescent protein cytosolic calcium sensor to study the calcium signal emerging at the root tip in response to a water potential gradient in Arabidopsis	Shkolnik et al. (2018)
	Electro-physiology	- Inducible by wounding - Endogenous signal - In native conditions	- Chemical nature of the current is unknown - No direct	Propagation of slow wave potentials depending on GLRs in response to wounding in Arabidopsis	Mousavi et al. (2013); Moe-Lange et al. (2021)
Direct	**Single molecule microscopy**	- Direct evidence of transport through PD	- Requires fusion to FP which might affect permeability	Single molecule tracking of mobile transcription factors in roots	Clark et al. (2016)

SEL: size exclusion limit; CFDA: 5-(and-6)-carboxyfluorescein diacetate; STM: SHOOT MERISTEMLESS; CMNB-caged fluorescein: Fluorescein bis-(5-Carboxymethoxy-2-Nitrobenzyl) ether, dipotassium salt; WT: wild type; KN1: KNOTTED1; MS2: a bacteriophage coat protein; SL: RNA stem loop; FT: Flowering locus T; SUC2: SUCROSE TRANSPORTER2; SUL: SULFUR; GLR: GLUTAMATE RECEPTOR-LIKE.

Table 2
Tools available to manipulate PD permeability.

TOOLS	EXAMPLES	MAIN STRENGTHS	MAIN WEAKNESSES	REF.
Related to callose metabolism	*iCALS3m* system spatiotemporally regulates the expression of a recombinant AtCALS3. Its induction allowed to inhibit SHR and *MIR165a* movement of from the stele to the endodermis and from the ground tissue to the vascular tissues, respectively.	- Decrease the SEL - Inducible - Reversible	- Pleiotropic effects *e.g.,* callose may cover cell wall and thus may affect apoplasmic pathways	Zuo et al. (2000); Vaten et al. (2011)
Related to other PD proteins	Overexpression of *AtPDLP5* is associated to callose accumulation at PD and a limitation of the PD permeability for several molecules including Ca^{2+} in Arabidopsis.	- Decrease the SEL - Inducible - Reversible	- Pleiotropic effects *e.g.,* callose may cover cell wall and thus may affect apoplasmic pathways	Lee et al. (2011); Toyota et al. (2018)
Related to non-PD proteins	*CHER1* encodes for a TGN located choline transporter. Its corresponding defective mutant exhibits a reduced pore density and an altered pore structure in sieve areas.	Enable to study PD protein composition by comparison with WT	- Defect in both PD number and structure - Pleiotropic effects *e.g.,* starch excess	Dettmer et al. (2014); Kraner et al. (2017a)
	ISE1 or *ISE2* encode for mitochondria and chloroplast RNA helicases, respectively. Silencing of one of them increases secondary PD formation in immature sink leaves and MP30-2xGFP cell-to-cell movement in *N. benthamiana* leaves.	Inducible	Pleiotropic effects, *e.g.,* - Alteration of organelle redox state - Defect in plastid structure (ISE2)	Stonebloom et al. (2009); Burch-Smith and Zambryski (2010); Burch-Smith et al. (2011a)
	GAT1 encodes for a plastid thioredoxin. Its ectopic expression increases GFP diffusion through PD while its corresponding mutant is affected in GFP unloading from the phloem into the meristem in Arabidopsis.	- Inducible - Increase/decrease the SEL	Pleiotropic effects *e.g.,* ROS accumulation in *gat1* mutant	Benitez-Alfonso et al. (2009)
	Maize KN1 is a non-cell-autonomous protein involved in development. Its expression in tobacco mesophyll cells increases PD SEL leading to its diffusion complexed with its corresponding anti-sense RNA.	- Increase the SEL - Inducible - Reversible	Pleiotropic effects *e.g.,* abnormal plant development	Lucas et al. (1995); Kragler et al. (1998)
Related to viral MPs	Expression of some viral MPs or of their plant orthologs increases PD SEL at least in part by regulating callose deposition at PD, leading to MP-RNA complexes diffusion.	- Increase the SEL - Can be inducible	No reversibility	Xoconostle-Cázares et al. (1999); Epel (2009); Zavaliev et al. (2011)
Obstruction or alteration of PD structure	Viral MP protein or non-cell-autonomous proteins such as KN1 complexed to 15nm gold particles prevent the increase of the PD SEL in *N. benthamiana* mesophyll cells.	Enable to study - PD permeability at steady-state SEL - SEL increase mechanism	- Need to generate gold-protein complexes - Microinjection is invasive	Kragler et al. (1998)
Pressure changes	The increase of turgor pressure differential between two cells impedes PD permeability: differentials of 200 kPa are sufficient to block PD permeability for LYCH (444 Da) in trichome cells of *Nicotiana clevelandii.*	- Instantaneous - Reversible - Almost absolute closure	- Microinjection is invasive - Pleiotropic effects *e.g.,* wounding response	Oparka and Prior (1992); Park et al. (2019)
ABA	ABA treatment triggers restriction of DENDRA2 (26 kDa) trafficking by decreasing PD SEL in *Physcomitrium patens.* Traffic of macromolecules increased in *P. patens* ABA-synthesis defective mutant, confirming the role of ABA in PD aperture, even at endogenous level.	- Fast (within 1hr) - Reversible (within 24 hrs) - Decrease/increase the SEL	ABA treatment might lead to pleiotropic effects, *e.g.,* stomata closure	Kitagawa et al. (2019)

CALS: CALLOSE SYNTHASE; PDLP: PLASMODESMAL-LOCALIZED PROTEIN; SHR: SHORT-ROOT; CHER1: CHOLINE TRANSPORTER-LIKE1; TGN: trans-Golgi network; *ISE: INCREASED SIZE EXCLUSION LIMIT*; MP: movement protein; GAT1: GFP ARRESTED TRAFFICKING; KN1: KNOTTED 1; LYCH: Lucifer yellow CH; ABA: Abscisic acid.

successfully been used to track movement of mobile transcription factors in roots (Clark et al., 2016). Recently, a minimally modified alkyne-tagged sucrose analog was shown to diffuse between BY2 cells (de Moliner et al., 2021). The synthesis of minimally modified sucrose analogs that can be used in Raman microscopy represents a major advance. However, since sucrose transporters mediate cellular uptake of the analogs it will be challenging to differentiate between flux through transporters versus PD. While it is conceivable that the observed differences in the timing of accumulation of the analog could be due to differences in PD connectivity between adjacent cells, more work will be required to evaluate this hypothesis (de Moliner et al., 2021). There is thus a need to develop new tools that allow tracking of cell-to-cell movement directly at the PD. Targeting of sensors to PD, for example sensors for sucrose, might be a potential means to detect sucrose movement across PD (Sadoine et al., 2021).

Investigating PD function and PD permeability requires approaches for manipulation (Table 2). Not surprisingly, mutants for PD located proteins or more generally for proteins involved in PD permeability often exhibit strong phenotypes and are embryolethal (Benitez-Alfonso et al., 2009; Stonebloom et al., 2009; Saatian et al., 2018). Although, several tools to spatiotemporally control the decrease of PD permeability by pressure changes or by callose deposition exist (Table 2), they require invasive approaches such as microinjection or the use of tissue specific inducible systems, which are not available for all species and tissues. Thus, the current adaptation of optogenetic tools to plants to control promoters of ion fluxes by light with a high spatiotemporal resolution offers new perspectives (Papanatsiou et al., 2019; Ochoa-Fernandez et al., 2020; Zhou et al., 2021).

Box 1
Nomenclature: Plasm or Plast

There are various forms used for components of cells and for cellular domains. Most will likely agree that a protoplast is a plant cell from which the cell wall has been removed by cell wall digesting enzymes. Similarly, when cell walls of yeast cells are removed, we use the term spheroplast. The protoplast contains the protoplasm (protoplasma; 1839 Johannes Evangelista Purkinje; 1787–1869; gelatinous fluid in living tissue; *Urschleim* in German), also called cytoplasm. These terms are over 100 years old (von Hanstein, 1880). Thus, unitary entities such as a plasma membrane-encapsulated unit rend on a 't', as in protoplast. Chloroplasts are entities ending on 't'. The cytoplasm consists of the cytosol, which had also been called hyaloplasm, plus the particles (named Kleinkörperchen by von Hanstein, 1880) or microsomata (microsomes, or better cell organelles and vesicles). PD connect the cytoplasm of most plant cells, creating a symplasm, as opposed to the continuous extracellular space (cell walls, xylem), which forms the apoplasm, in both cases not entities but both a plasm(a), a continuous liquid domain either inside or outside of plant cells. There is also some confusion regarding the term tonoplast. According to the definitions above, the vacuole is equivalent to the tonoplast, while its content would be a -plasm, *i.e.*, the vacuolar protoplasm. However, the term tonoplast has, already early on, also been used for the membrane that encapsulates the vacuole (Weber, 1932).

Eduard Tangl is considered the first to recognize the importance of the structures underlying the cell-cell connections that we now call PD. Tangl had named them Protoplasmafortsätze (protoplasm extensions), Eduard Strasburger originally used the German term *Plasmafäden* (plasma threads). In 1901, he coined the German term *Plasmodesmen* (Strasburger, 1901). Based on the ethymology, a single one is called plasmodesma (sometimes plasmodesmos), plural plasmodesmata.

Note that much of the original literature was in German, nevertheless you will frequently find that the word symplast and apoplast are used, also historically.

16. Summary and outlook

While extensive progress has been made regarding composition, structure and function of PD, our understanding of most aspects including composition of PD is in its beginnings, a blueprint is missing, and we have no reliable structural model of PD. Also, the transport mechanisms remain elusive, in part since the assays often just identify accumulation of a substrate in an adjacent cell, not an actual passage through PD. Thus there is a lot to be learned with novel approaches and technologies; single cell transcriptomes may help to target PD more specifically (Kim et al., 2021), base editing may enable finer tuning of PD activities with the help of *knock down* approaches (Monsur et al., 2020), biosensors may help to measure transport through PD in a more direct way (Okumoto, 2012) and cryo-electron tomography as used for example for resolving the structure of nuclear pores is among the most promising tools (Beck et al., 2007; Mosalaganti et al., 2018).

Greek (and New Latin) etymology (www.etymonline.com/)

protos: first
plásma: moldable substance, the liquid part of blood, etc., as distinguished from the corpuscles
hyalos: glass, clear alabaster, crystal lens used as a burning glass (as in hyaloplasma)
kytos: a hollow, receptacle, basket (as in cytoplasm)
desmá: band, bond, ligament (as in plasmodesmata)
apo-: word-forming element meaning "from, away from; after; in descent from" (apoplasm)
syn-; sym-: word-forming element meaning "together with, jointly; alike; at the same time' (symplasm)

CRediT authorship contribution statement

Manuel Miras: conceived of the review, wrote and edited large sections. **Mathieu Pottier:** analyzed literature, wrote and edited sections. **T. Moritz Schladt:** analyzed literature, wrote and edited sections. **J. Obinna Ejike:** analyzed literature, wrote and edited sections. **Laura Redzich:** performed the analysis of the PD proteome and generated the database. **Wolf B. Frommer:** conceived of the review, wrote and edited large sections. **Ji-Yun Kim:** conceived of the review, wrote and edited large sections. MM, JYK and WBF did most of the editing during the revision process. All authors contributed to the generation of the Tables and Figures.

Conflict of interest

The authors declare no conflict of interest.

Acknowledgements

This work has received funding from the European Research Council (ERC) and the Marie Skłodowska-Curie under the European Union's Horizon 2020 research and innovation programme (Grant agreements "SymPore" No. 951292 to WBF and "PDgate" No. 101023981 to MM, respectively). This research has also been supported by the Deutsche Forschungsgemeinschaft (DFG, German Research Foundation) under Germany's Excellence Strategy – EXC-2048/1 – project ID 390686111, the National Science Foundation (SECRETome Project: Systematic Evaluation of CellulaR ExporT from plant cells, IOS-1546879), and the Alexander von Humboldt Professorship, to WBF.

Appendix A. Supplementary data

Supplementary data to this article can be found online at https://doi.org/10.1016/j.jplph.2022.153633.

References

Baker, R.F., Braun, D.M., 2008. *Tie-dyed2* functions with *Tie-dyed1* to promote carbohydrate export from maize leaves. Plant Physiol. 146, 1085–1097.
Balachandran, S., Hull, R.J., Vaadia, Y., Wolf, S., Lucas, W.J., 1995. Alteration in carbon partitioning induced by the movement protein of tobacco mosaic virus originates in the mesophyll and is independent of change in the plasmodesmal size exclusion limit. Plant Cell Environ. 18, 1301–1310.
Balkunde, R., Kitagawa, M., Xu, X.M., Wang, J., Jackson, D., 2017. SHOOT MERISTEMLESS trafficking controls axillary meristem formation, meristem size and organ boundaries in Arabidopsis. Plant J. 90, 435–446.
Barton, D.A., Cole, L., Collings, D.A., Liu, D.Y.T., Smith, P.M.C., Day, D.A., Overall, R.L., 2011. Cell-to-cell transport via the lumen of the endoplasmic reticulum. Plant J. 66, 806–817.
Baud, S., Boutin, J.-P., Miquel, M., Lepiniec, L., Rochat, C., 2002. An integrated overview of seed development in *Arabidopsis thaliana* ecotype WS. Plant Physiol. Biochem. 40, 151–160.
Beck, M., Lucić, V., Förster, F., Baumeister, W., Medalia, O., 2007. Snapshots of nuclear pore complexes in action captured by cryo-electron tomography. Nature 449, 611–615.
van Bel, A.J.E., Gamalei, Y.V., 1992. Ecophysiology of phloem loading in source leaves. Plant Cell Environ. 15, 265–270.

van Bel, A.J.E., Gamalei, Y.V., Ammerlaan, A., Bik, L.P.M., 1992. Dissimilar phloem loading in leaves with symplasmic or apoplasmic minor-vein configurations. Planta 186, 518–525.

van Bel, A.J.E., Knoblauch, M., 2000. Sieve element and companion cell: the story of the comatose patient and the hyperactive nurse. Funct. Plant Biol. 27, 477–487.

Benitez-Alfonso, Y., Cilia, M., Roman, A.S., Thomas, C., Maule, A.J., Hearn, S., Jackson, D., 2009. Control of Arabidopsis meristem development by thioredoxin-dependent regulation of intercellular transport. Proc. Natl. Acad. Sci. U.S.A. 106, 3615–3620.

Benitez-Alfonso, Y., Faulkner, C., Pendle, A., Miyashima, S., Helariutta, Y., Maule, A.J., 2013. Symplastic intercellular connectivity regulates lateral root patterning. Dev. Cell 26, 136–147.

Benitez-Alfonso, Y., Faulkner, C., Ritzenthaler, C., Maule, A.J., 2010. Plasmodesmata: gateways to local and systemic virus infection. Mol. Plant Microbe Interact. 23, 1403–1412.

Bezrutczyk, M., Hartwig, T., Horschman, M., Char, S.N., Yang, J., Yang, B., Frommer, W. B., Sosso, D., 2018. Impaired phloem loading in *zmsweet13a,b,c* sucrose transporter triple knock-out mutants in *Zea mays*. New Phytol. 218, 594–603.

Borisjuk, L., Walenta, S., Rolletschek, H., Mueller-Klieser, W., Wobus, U., Weber, H., 2002. Spatial analysis of plant metabolism: sucrose imaging within *Vicia faba* cotyledons reveals specific developmental patterns. Plant J. 29, 521–530.

Botha, C.E.J., 2005. Interaction of phloem and xylem during phloem loading: functional symplasmic roles for thin- and thick-walled sieve tubes in monocotyledons. In: Vascular Transport in Plants. Elsevier, pp. 115–130.

Botha, C.E.J., Hartley, B.J., Cross, R.H.M., 1993. The ultrastructure and computer-enhanced digital image analysis of plasmodesmata at the Kranz mesophyll-bundle sheath Interface of *Themeda triandra var. imberbis* (Retz) A. Camus in conventionally-fixed blades. Ann. Bot. 72, 255–261.

Botha, C.E.J., Murugan, N., 2021. Changes in structure and dimension of plasmodesmata in the phloem loading pathway in *Tecoma capensis* (Bignoniaceae) - locating the polymer trap. South Afr. J. Bot. 140, 76–86.

Brault, M.L., Petit, J.D., Immel, F., Nicolas, W.J., Glavier, M., Brocard, L., Gaston, A., Fouché, M., Hawkins, T.J., Crowet, J.-M., et al., 2019. Multiple C2 domains and transmembrane region proteins (MCTPs) tether membranes at plasmodesmata. EMBO Rep. 20, e47182.

Burch-Smith, T.M., Brunkard, J.O., Choi, Y.G., Zambryski, P.C., 2011a. Organelle–nucleus cross-talk regulates plant intercellular communication via plasmodesmata. Proc. Natl. Acad. Sci. U.S.A. 108, E1451.

Burch-Smith, T.M., Stonebloom, S., Xu, M., Zambryski, P.C., 2011b. Plasmodesmata during development: re-examination of the importance of primary, secondary, and branched plasmodesmata structure versus function. Protoplasma 248, 61–74.

Burch-Smith, T.M., Zambryski, P.C., 2010. Loss of INCREASED SIZE EXCLUSION LIMIT (ISE)1 or ISE2 increases the formation of secondary plasmodesmata. Curr. Biol. 20, 989–993.

Carr, D.J., 1976. Plasmodesmata in growth and development. In: Gunning, B.E.S., Robards, A.W. (Eds.), Intercellular Communication in Plants: Studies on Plasmodesmata. Springer Berlin Heidelberg, Berlin, Heidelberg, pp. 243–289.

Chambaud, C., Cookson, S.J., Ollat, N., Bayer, E.M., Brocard, L., 2021. A correlative light electron microscopy approach reveals plasmodesmata ultrastructure at the graft interface. Plant Physiol. 188 (1), 44–55. https://doi.org/10.1093/plphys/kiab485.

Chen, H., Ahmad, M., Rim, Y., Lucas, W.J., Kim, J.-Y., 2013. Evolutionary and molecular analysis of Dof transcription factors identified a conserved motif for intercellular protein trafficking. New Phytol. 198, 1250–1260.

Chen, L.Q., Lin, I.W., Qu, X.-Q., Sosso, D., McFarlane, H.E., Londoño, A., Samuels, A.L., Frommer, W.B., 2015. A cascade of sequentially expressed sucrose transporters in the seed coat and endosperm provides nutrition for the Arabidopsis embryo. Plant Cell 27, 607–619.

Chen, L.Q., Qu, X.-Q., Hou, B.-H., Sosso, D., Osorio, S., Fernie, A.R., Frommer, W.B., 2012. Sucrose efflux mediated by SWEET proteins as a key step for phloem transport. Science 335, 207–211.

Chonan, N., Kanako, M., Kawahara, H., Matsuda, T., 1981. Ultrastructure of the large vascular bundles in the leaves of rice plant. Jpn. J. Crop Sci. 50, 323–331.

Christensen, A.H., Stone, H.A., Jensen, K.H., 2021. Diffusion and flow across shape-perturbed plasmodesmata nanopores in plants. Eur. Phys. J. Plus 136, 872.

Christensen, N.M., Faulkner, C., Oparka, K.J., 2009. Evidence for unidirectional flow through plasmodesmata. Plant Physiol. 150, 96–104.

Clark, N.M., Hinde, E., Winter, C.M., Fisher, A.P., Crosti, G., Blilou, I., Gratton, E., Benfey, P.N., Sozzani, R., 2016. Tracking transcription factor mobility and interaction in Arabidopsis roots with fluorescence correlation spectroscopy. eLife 5, e14770.

Comtet, J., Jensen, K.H., Turgeon, R., Stroock, A.D., Hosoi, A.E., 2017. Passive phloem loading and long-distance transport in a synthetic tree-on-a-chip. Nat. Plants 3, 17032.

Crawford, K.M., Zambryski, P.C., 2001. Non-targeted and targeted protein movement through plasmodesmata in leaves in different developmental and physiological states. Plant Physiol. 125, 1802–1812.

Cui, W., Wang, X., Lee, J.-Y., 2015. Drop-ANd-See: a simple, real-time, and noninvasive technique for assaying plasmodesmal permeability. Methods Mol. Biol. 1217, 149–156.

Danila, F.R., Quick, W.P., White, R.G., Furbank, R.T., von Caemmerer, S., 2016. The metabolite pathway between bundle sheath and mesophyll: quantification of plasmodesmata in leaves of C3 and C4 monocots. Plant Cell 28, 1461–1471.

Deinum, E.E., Mulder, B.M., Benitez-Alfonso, Y., 2019. From plasmodesma geometry to effective symplasmic permeability through biophysical modelling. eLife 8, e49000.

Denyer, T., Ma, X., Klesen, S., Scacchi, E., Nieselt, K., Timmermans, M.C.P., 2019. Spatiotemporal developmental trajectories in the Arabidopsis root revealed using high-throughput single-cell RNA sequencing. Dev. Cell 48, 840–852 e5.

Dettmer, J., Ursache, R., Campilho, A., Miyashima, S., Belevich, I., O'Regan, S., Mullendore, D.L., Yadav, S.R., Lanz, C., Beverina, L., et al., 2014. CHOLINE TRANSPORTER-LIKE1 is required for sieve plate development to mediate long-distance cell-to-cell communication. Nat. Commun. 5, 4276.

Dölger, J., Rademaker, H., Liesche, J., Schulz, A., Bohr, T., 2014. Diffusion and bulk flow in phloem loading: a theoretical analysis of the polymer trap mechanism for sugar transport in plants. Phys. Rev. E 90, 042704.

Duckett, C.M., Oparka, K.J., Prior, D.A.M., Dolan, L., Roberts, K., 1994. Dye-coupling in the root epidermis of Arabidopsis is progressively reduced during development. Development 120, 3247–3255.

Ehlers, K., Kollmann, R., 2001. Primary and secondary plasmodesmata: structure, origin, and functioning. Protoplasma 216, 1–30.

Eom, J.-S., Chen, L.-Q., Sosso, D., Julius, B.T., Lin, I.W., Qu, X.-Q., Braun, D.M., Frommer, W.B., 2015. SWEETs, transporters for intracellular and intercellular sugar translocation. Curr. Opin. Plant Biol. 25, 53–62.

Eom, J.-S., Choi, S.-B., Ward, J.M., Jeon, J.-S., 2012. The mechanism of phloem loading in rice (*Oryza sativa*). Mol. Cell. 33, 431–438.

Eom, J.-S., Luo, D., Atienza-Grande, G., Yang, J., Ji, C., Luu, V.T., Huguet-Tapia, J.C., Liu, B., Nguyen, H., Schmidt, S.M., et al., 2019. Diagnostic kit for rice blight resistance. Nat. Biotechnol. 37, 1372–1379.

Epel, B.L., 2009. Plant viruses spread by diffusion on ER-associated movement-protein-rafts through plasmodesmata gated by viral induced host β-1,3-glucanases. Semin. Cell Dev. Biol. 20, 1074–1081.

Erwee, M.G., Goodwin, P.B., 1985. Symplast domains in extrastelar tissues of *Egeria densa* Planch. Planta 163, 9–19.

Faulkner, C., 2018. Plasmodesmata and the symplast. Curr. Biol. 28, R1374–R1378.

Fernandez-Calvino, L., Faulkner, C., Walshaw, J., Saalbach, G., Bayer, E.M., Benitez-Alfonso, Y., Maule, A.J., 2011. Arabidopsis plasmodesmal proteome. PLoS One 6, e18880.

Fisher, D., Buchanan, B., Gruissem, W., Jones, R., 2000. Biochemistry and Molecular Biology of Plants. American Society of Plant Physiologists, Rockville, MD, pp. 730–778.

Fisher, D.B., Cash-Clark, C.E., 2000. Gradients in water potential and turgor pressure along the translocation pathway during grain filling in normally watered and water-stressed wheat plants. Plant Physiol. 123, 139–147.

Fisher, D.G., 1986. Ultrastructure, plasmodesmatal frequency, and solute concentration in green areas of variegated *Coleus blumei* Benth. leaves. Planta 169, 141–152.

Fu, Q., Cheng, L., Guo, Y., Turgeon, R., 2011. Phloem loading strategies and water relations in trees and herbaceous plants. Plant Physiol. 157, 1518.

Gamalei, Y., 1989. Structure and function of leaf minor veins in trees and herbs. A taxonomic review. Trees 3, 96–110.

Gamalei, Y., 1991. Phloem loading and its development related to plant evolution from trees to herbs. Trees 5, 50–64.

Gaudioso-Pedraza, R., Beck, M., Frances, L., Kirk, P., Ripodas, C., Niebel, A., Oldroyd, G. E.D., Benitez-Alfonso, Y., de Carvalho-Niebel, F., 2018. Callose-regulated symplastic communication coordinates symbiotic root nodule development. Curr. Biol. 28, 3562–3577.

Geiger, D.R., Sovonick, S.A., Shock, T.L., Fellows, R.J., 1974. Role of free space in translocation in sugar beet. Plant Physiol. 54, 892–898.

Gerlitz, N., Gerum, R., Sauer, N., Stadler, R., 2018. Photoinducible DRONPA-s: a new tool for investigating cell–cell connectivity. Plant J. 94, 751–766.

Gisel, A., Barella, S., Hempel, F.D., Zambryski, P.C., 1999. Temporal and spatial regulation of symplastic trafficking during development in *Arabidopsis thaliana* apices. Development 126, 1879–1889.

Gisel, A., Hempel, F.D., Barella, S., Zambryski, P.C., 2002. Leaf-to-shoot apex movement of symplastic tracer is restricted coincident with flowering in Arabidopsis. Proc. Natl. Acad. Sci. U.S.A. 99, 1713–1717.

Goodwin, P.B., Shepherd, V., Erwee, M.G., 1990. Compartmentation of fluorescent tracers injected into the epidermal cells of *Egeria densa* leaves. Planta 181, 129–136.

Gottwald, J.R., Krysan, P.J., Young, J.C., Evert, R.F., Sussman, M.R., 2000. Genetic evidence for the *in planta* role of phloem-specific plasma membrane sucrose transporters. Proc. Natl. Acad. Sci. U.S.A. 97, 13979–13984.

Grison, M.S., Brocard, L., Fouillen, L., Nicolas, W., Wewer, V., Dormann, P., Nacir, H., Benitez-Alfonso, Y., Claverol, S., Germain, V., et al., 2015. Specific membrane lipid composition is important for plasmodesmata function in Arabidopsis. Plant Cell 27, 1228–1250.

Grison, M.S., Kirk, P., Brault, M.L., Wu, X.N., Schulze, W.X., Benitez-Alfonso, Y., Immel, F., Bayer, E.M., 2019. Plasma membrane-associated receptor-like kinases relocalize to plasmodesmata in response to osmotic stress. Plant Physiol. 181, 142–160.

Gui, J., Liu, C., Shen, J., Li, L., 2014. Grain setting defect1, encoding a remorin protein, affects the grain setting in rice through regulating plasmodesmatal conductance. Plant Physiol. 166, 1463–1478.

Gunning, B.E.S., 1976. The role of plasmodesmata in short distance transport to and from the phloem. In: Gunning, B.E.S., Robards, A.W. (Eds.), Intercellular Communication in Plants: Studies on Plasmodesmata. Springer, Berlin, Heidelberg, pp. 203–227.

Guseman, J.M., Lee, J.S., Bogenschutz, N.L., Peterson, K.M., Virata, R.E., Xie, B., Kanaoka, M.M., Hong, Z., Torii, K.U., 2010. Dysregulation of cell-to-cell connectivity and stomatal patterning by loss-of-function mutation in Arabidopsis CHORUS (GLUCAN SYNTHASE-LIKE 8). Development 137, 1731–1741.

Ham, B.-K., Li, G., Kang, B.-H., Zeng, F., Lucas, W.J., 2012. Overexpression of Arabidopsis plasmodesmata Germin-like proteins disrupts root growth and development. Plant Cell 24, 3630–3648.

Chapter III

5. A high-confidence Physcomitrium patens plasmodesmata proteome by iterative scoring and validation reveals diversification of cell wall proteins during evolution

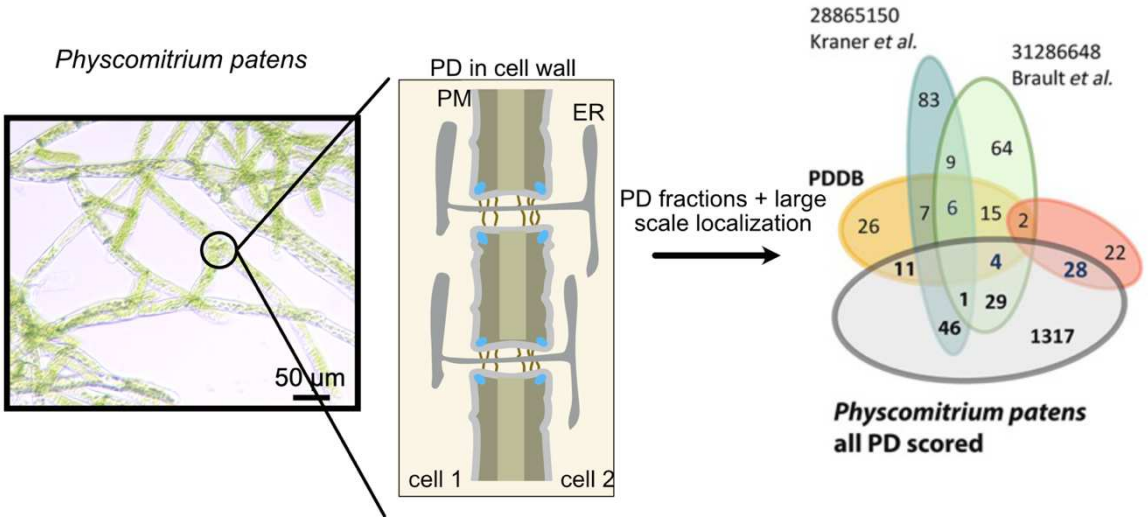

Status: Published
Journal: New Phytologist
Impact factor: 9.4 (2022)
Contribution: 15% (specified in Appendix)

5.1. Aim of this chapter

5.1.1. Research question:

- What are the key components of PD?

5.1.2. Objective

Identification of new PD components by validating subcellular localizations of candidates found in a *Physcomitrium* PD proteome.

5.1.3. Hypothesis

Large-scale identification of novel PD components will grant novel insights into PD composition, transport mechanism, and evolution.

Check for updates

New Phytologist

Research

A high-confidence *Physcomitrium patens* plasmodesmata proteome by iterative scoring and validation reveals diversification of cell wall proteins during evolution

Sven Gombos[1]*, Manuel Miras[2]*, Vicky Howe[3]*, Lin Xi[1], Mathieu Pottier[2], Neda S. Kazemein Jasemi[3], Moritz Schladt[2], J. Obinna Ejike[2], Ulla Neumann[4], Sebastian Hänsch[5], Franziska Kuttig[3], Zhaoxia Zhang[1], Marcel Dickmanns[2,6], Peng Xu[6], Thorsten Stefan[1], Wolfgang Baumeister[6], Wolf B. Frommer[2,7], Rüdiger Simon[3] and Waltraud X. Schulze[1]

[1]Department of Plant Systems Biology, University of Hohenheim, 70593 Stuttgart, Germany; [2]Department of Molecular Physiology, Heinrich Heine University of Düsseldorf, 40225 Düsseldorf, Germany; [3]Department of Developmental Genetics, Heinrich Heine University of Düsseldorf, 40225 Düsseldorf, Germany; [4]Central Microscopy, Max Planck Institute for Plant Breeding Research, 50829 Cologne, Germany; [5]Center for Advanced Imaging, Heinrich Heine University of Düsseldorf, 40225 Düsseldorf, Germany; [6]Department of Molecular Structural Biology, Max Planck Institute of Biochemistry, 82152 Martinsried, Germany; [7]Institute for Transformative Biomolecules, Nagoya University, Nagoya 464-0813, Japan

Author for correspondence:
Waltraud X. Schulze
Email: wschulze@uni-hohenheim.de

Received: *4 November 2022*
Accepted: *27 December 2022*

New Phytologist (2023) **238:** 637–653
doi: 10.1111/nph.18730

Key words: cell wall-modifying enzymes, cell-to-cell communication, evolution of multicellularity, plasmodesmata proteome, *Physcomitrium patens*.

Summary

- Plasmodesmata (PD) facilitate movement of molecules between plant cells. Regulation of this movement is still not understood. Plasmodesmata are hard to study, being deeply embedded within cell walls and incorporating several membrane types. Thus, structure and protein composition of PD remain enigmatic. Previous studies of PD protein composition identified protein lists with few validations, making functional conclusions difficult.
- We developed a PD scoring approach in iteration with large-scale systematic localization, defining a high-confidence PD proteome of *Physcomitrium patens* (HC300). HC300, together with *bona fide* PD proteins from literature, were placed in PDDB. About 65% of proteins in HC300 were not previously PD-localized.
- Callose-degrading glycolyl hydrolase family 17 (GHL17) is an abundant protein family with representatives across evolutionary scale. Among GHL17s, we exclusively found members of one phylogenetic clade with PD localization and orthologs occur only in species with developed PD. Phylogenetic comparison was expanded to xyloglucan endotransglucosylases/hydrolases and Exordium-like proteins, which also diversified into PD-localized and non-PD-localized members on distinct phylogenetic clades.
- Our high-confidence PD proteome HC300 provides insights into diversification of large protein families. Iterative and systematic large-scale localization across plant species strengthens the reliability of HC300 as basis for exploring structure, function, and evolution of this important organelle.

Introduction

Plasmodesmata (PD) are important and complex structures present in all land plants, providing connections between plant cells that are otherwise separated by a thick cell wall. During the evolution of multicellular life forms, the exchange of nutrients and information was required to coordinate development and distinct cellular differentiation. The cellular structures and mechanisms facilitating intercellular communication evolved along different paths. In animals, different types of gap junctions mediate the exchange of small molecules between cells, while primary cilia coordinate cell-to-cell signaling (Bangs & Anderson, 2017; Song *et al.*, 2018; Anvarian *et al.*, 2019). In plants, PD evolved to facilitate translocation of both nutrients and signaling molecules in the presence of a cell wall. While the structure and function of gap junctions and primary cilia are rather well understood, PD structure and function remain somewhat enigmatic.

Plasmodesmata were serendipitously discovered in the 1800s by the botanist Eduard Tangl while staining cell wall cellulose using organic pigments. To his surprise, he observed cytoplasmic connections between plant cells in the endosperm (Tangle, 1879). Similar structures were subsequently identified in many other plant species. Notably, analogous structures likely evolved independently at least six times, underlining their necessity for multicellularity (Raven, 2007).

*These authors contributed equally to this work.

Plasmodesmata connect neighboring cells by forming sophisticated channels lined by a contiguous plasma membrane. A special feature of land plant PD is the desmotubule, a strand of apparently tightly appressed ER that extends through the cytoplasmic sleeve (Ding *et al.*, 1992a,b, 1996). Since their discovery, PD are considered as pores between cells, enabling diffusion of small molecules below a certain size (Wolf *et al.*, 1989). They also seem to enable passage of macromolecules, such as RNAs, peptides, and proteins that are vital for plant development and physiological processes (Lucas *et al.*, 1995, 2009; Kim *et al.*, 2005). Recently, tethering between the plasma membrane and the desmotubule was suggested as a mechanism to control PD pore size and multiple C2 domains and transmembrane region proteins (MCTP) were shown to play a major role in this process (Brault *et al.*, 2019). However, mechanisms of transport through PD are still unclear, as is their precise structural composition.

Proteomic analyses of PD enrichments provide a glimpse of the protein composition of these complex channels. To date, PD proteomes have largely been derived through biochemical enrichment of cell wall preparations, for example in Arabidopsis (Bayer *et al.*, 2006; Fernandez-Calvino *et al.*, 2011; Kraner *et al.*, 2017), *Populus trichocarpa* (Leijon *et al.*, 2018), or *Nicotiana benthamiana* (Park *et al.*, 2017). Some of these proposed PD proteins were also found enriched in detergent-resistant membrane fractions. This may be due to the plasma membrane in PD being characterized by a distinct lipid and sterol composition (Grison *et al.*, 2015a; Yan *et al.*, 2019). Out of several thousand candidates identified in such proteomics analyses, only a small subset has actually been validated with PD localization *in planta*, and the fraction of false positives and contaminants in such lists is expected rather high.

Biochemical preparations of PD obtained, for example, through cell wall enrichment or differential centrifugations contain a large proportion of copurifying proteins from cellular domains other than PD. Therefore, quantitative methods distinguishing PD proteins from non-PD proteins are required. In previous studies, comparative quantitative assessments of PD proteomes were performed, for example, by determining an enrichment ratio of proteins identified in PD compared with cell walls to define a 'core PD proteome' (Brault *et al.*, 2019). In another study, a reduced abundance of PD proteins was observed in the loss of function mutant of Choline Transporter 1 (*cher1-1*) and this observation was used to rank PD components (Kraner *et al.*, 2017). A further approach characterizing PD proteomes explored protein recruitment to PD in response to viral infection (Park *et al.*, 2017). Viral movement between cells occurs through PD and thus proteins recruited or depleted from PD in response to viral infection were considered as candidate PD proteins. However, due to limited validation and limited number of species that have been used in PD studies, a reliable PD proteome with the probabilistic classification of core PD components and copurifying proteins remains to be resolved.

Here, we used the bryophyte *Physcomitrium patens* as a model organism to establish a PD proteome by an iterative discovery-verification workflow using experimental protein enrichment and a feature scoring algorithm in iteration with *in planta* localization. Bryophytes were among the first evolving land plants (Coudert *et al.*, 2019), thus requiring transport and communication between cells despite rigid cell walls. Our results give insights into the large PD protein families, such as cell-wall-modifying enzymes and Exordium (EXO) proteins. These protein families are evolutionarily conserved across species, indicating their importance in the evolution of multicellularity.

Materials and Methods

Plant material and culture conditions

Physcomitrium patens (Hedw.) ecotype Gransden cultures were obtained from the International Moss Stock Center (IMSC, Freiburg, Germany). *Physcomitrium patens* was cultured on modified BCD medium containing 5 mM diammonium tartrate (Cove *et al.*, 2009; Supporting Information Methods S1). *Nicotiana benthamiana* seeds were soaked in water for 24 h at 20°C and then grown on peat moss substrate in a glasshouse for 3 wk under long-day conditions (Methods S1).

Preparation of plasmodesmata

The PD preparation workflow (Fig. S1A) was based on two previously published methods (Faulkner & Bayer, 2017; Kraner *et al.*, 2017) and optimized for *P. patens* tissue. First step in PD (Fig. S1B) preparation workflow was disruption of plant tissue with a Potter-Elvehjem Homogenizer in presence of high detergent concentrations (150 mM NaCl, 10 mM EDTA, 1 mM DTT, 1% (v/v) Triton X-100, 0.5% (v/v) sodium deoxycholate, 0.1% (w/v) SDS, 10% (v/v) glycerol, and 100 mM Tris–HCl, pH 8). This gently perforated cell walls and removed organelles while leaving cell walls mostly intact to preserve PD structures (Fig. S1C). Two subsequent rounds of grinding cell wall fractions in liquid nitrogen efficiently removed additional soluble protein contaminants and prepared cell walls for digestion by breaking up cell clusters (Fig. S1D). Washing with lower concentrations of detergents (150 mM NaCl, 10 mM EDTA, 0.1% (v/v) Triton X-100, 10% (v/v) glycerol, and 100 mM Tris–HCl, pH 8) prevented premature solubilization of PD membranes at this point. Cell wall fragments were digested using driselase. After ultracentrifugation, the resulting PD pellet contained small membranous components and protein aggregates with very little remains of cell walls (Fig. S1E). Along the PD preparation workflow, four protein fractions were collected as input for later PD scoring: cell wall proteins (CW), total of microsomal membranes (Mic), final pellet of PD-enriched proteins (PD), and a total cell extract (TC).

Protein isolation from other sources

Total protein was extracted in a urea thiourea environment (He *et al.*, 2021). Microsomal fraction isolation followed established protocols (Pertl *et al.*, 2001). Cell wall extracts were obtained after cell homogenization with a Potter-Elvehjem PTFE tissue grinder in a high-detergent environment and centrifugation at 1000 ***g*** (Kraner *et al.*, 2017).

LC–MS/MS analysis of peptides

Proteins were trypsin-digested and desalted (Hughes *et al.*, 2019), and peptide mixtures were analyzed on a nanoflow UPLC-coupled Orbitrap hybrid mass spectrometer (Q-Exactive HF; Thermo Scientific, Waltham, MA, USA; Methods S1). Spectra were matched against *P. patens* proteome (Ppatens_318_v.3.3.-protein.fasta, 87 533 entries) using MaxQuant v.2.0.3.0 (Cox & Mann, 2008). Mass spectrometry proteomics data were deposited to ProteomeXchange Consortium via the PRIDE partner repository (Deutsch *et al.*, 2017) with identifier PXD032820.

PD score

The PD score is the sum of two components, enrichment score (Eqn 1) and feature score (Eqns 2, 3; Fig. S2A). LFQ values from the TC, MIC, CW, and PD fractions derived from MaxQuant (Tyanova *et al.*, 2016) were $\log_2$-transformed before further calculations. Fraction means were calculated and normalized using z-score (Fig. S2B):

$$\text{Enrichment Score}: \sum_{x \in X} z\,\text{Score}\big(\log_2(\text{LFQ intensity PD})\big) - z\,\text{Score}\big(\log_2(\text{LFQ intensity } x)\big) \quad \text{Eqn 1}$$

$X = \{\text{MIC, TC, CW}\}$.

Feature scores were based on frequency of protein functions, and Pfam domains (https://pfam.xfam.org/) found in the reference data set and validated PD candidates. The feature score is the sum of feature frequencies of PD protein-associated features found in the scored protein (Fig. S2C):

$$\text{Feature Frequency}: \sum_{i=1}^{n} \frac{\text{count}(\text{feature}_i)}{\max(\text{count}(\text{feature}_i))} \quad \text{Eqn 2}$$

$$\text{Feature Score}: \sum_{i=1}^{n} \text{feature}_i \text{ frequency} \quad \text{Eqn 3}$$

Quantification of PD candidate localization

Confocal images were screened visually for colocalization of proteins of interest and aniline blue. Candidates showing colocalization with aniline blue were quantitatively scored by the so-called PD index (Grison *et al.*, 2019). To minimize bias in quantification, we used a semi-automated approach of an in-house-generated macro for Fiji software package (Schindelin *et al.*, 2012; Methods S1).

Phylogenetic analysis

GHL17s, XTHs, and EXOs protein sequences were retrieved from Phytozome, Ensembl, Phycocosm, and http://genome.microbedb.jp/klebsormidium databases (Goodstein *et al.*, 2012; Hori *et al.*, 2014; Howe *et al.*, 2020; Grigoriev *et al.*, 2021). All protein sequences were subjected to protein domain prediction at InterPro server (Hunter *et al.*, 2009). Maximum likelihood trees were generated using the NGPhylogeny.fr tool (Lemoine *et al.*, 2019) and visualized and edited in iTol (Letunic & Bork, 2019).

Results

Detection of PD in *P. patens*

To evaluate the presence and type of PD in *Physcomitrium*, transmission electron micrographs of longitudinal and cross sections were generated from protonemata, in which PD were randomly distributed along the cell-to-cell interface (Fig. 1a,b). Simple PD morphotypes were found at interfaces between protonema cells at a relatively high density of 11.3 (±1.4) PD μm^{-2} (Fig. 1c) compared with PD densities in Arabidopsis roots, which ranged from 2.5 to 12.5 PD μm^{-2}, depending on the cell-type interface (Zhu & Lucas, 1998). Plasmodesmata averaged to 362.6 nm (±119.2 nm) in length and 29.7 nm (±4.9) in diameter. *Physcomitrium* protonema PD were clearly longer than what has been published for Arabidopsis suspension cells or roots (Grison *et al.*, 2015b; Nicolas *et al.*, 2017) because of thicker cell walls in measured *Physcomitrium* protonema. The diameter was in a similar range as described previously for Arabidopsis. (Fig. 1d) We achieved an enrichment of common PD proteins from *Physcomitrium* with concurrent depletion of typical contaminants. Proteins expected in PD, such as C2-domain-containing proteins (Brault *et al.*, 2019), were found with increased abundance in PD fractions compared with TC or CW fractions (Fig. 1e). Photosynthetic proteins in PD pellets were found in reduced abundance, while non-PD membrane proteins, such as plasma membrane ATPases, were most abundant in the microsomal fraction (Fig. 1e), and not in PD.

Our PD preparation workflow (Fig. S1) identified a total of 870 proteins in the final PD pellet. A comparison of published PD pellet proteomes from Arabidopsis (Bayer *et al.*, 2006; Fernandez-Calvino *et al.*, 2011; Kraner *et al.*, 2017; Brault *et al.*, 2019), *P. trichocarpa* (Leijon *et al.*, 2018), and *N. benthamiana* (Park *et al.*, 2017) revealed large overlap of 422 Arabidopsis orthologs in PD pellets of *Physcomitrium* and Arabidopsis (Fig. 1f). Besides typical PD protein functions in cell wall modification or C2-domain-containing proteins, there was a high fraction (22%; $n = 38$) of typical contaminants, such as ribosomes and photosynthetic proteins from light-harvesting complexes and Calvin-Benson Cycle among orthologs found in at least three species. The fact that such nontarget proteins made up of a high percentage of the overlap in PD protein lists, suggesting that definition of PD proteins, solely based on discovery in multiple proteomics data sets, lacks specificity and requires additional criteria for a robust definition of PD composition. Therefore, to identify high-confidence PD protein candidates, a data-driven proteomics-based approach was used in iteration with systematic verification of PD localization.

New Phytologist

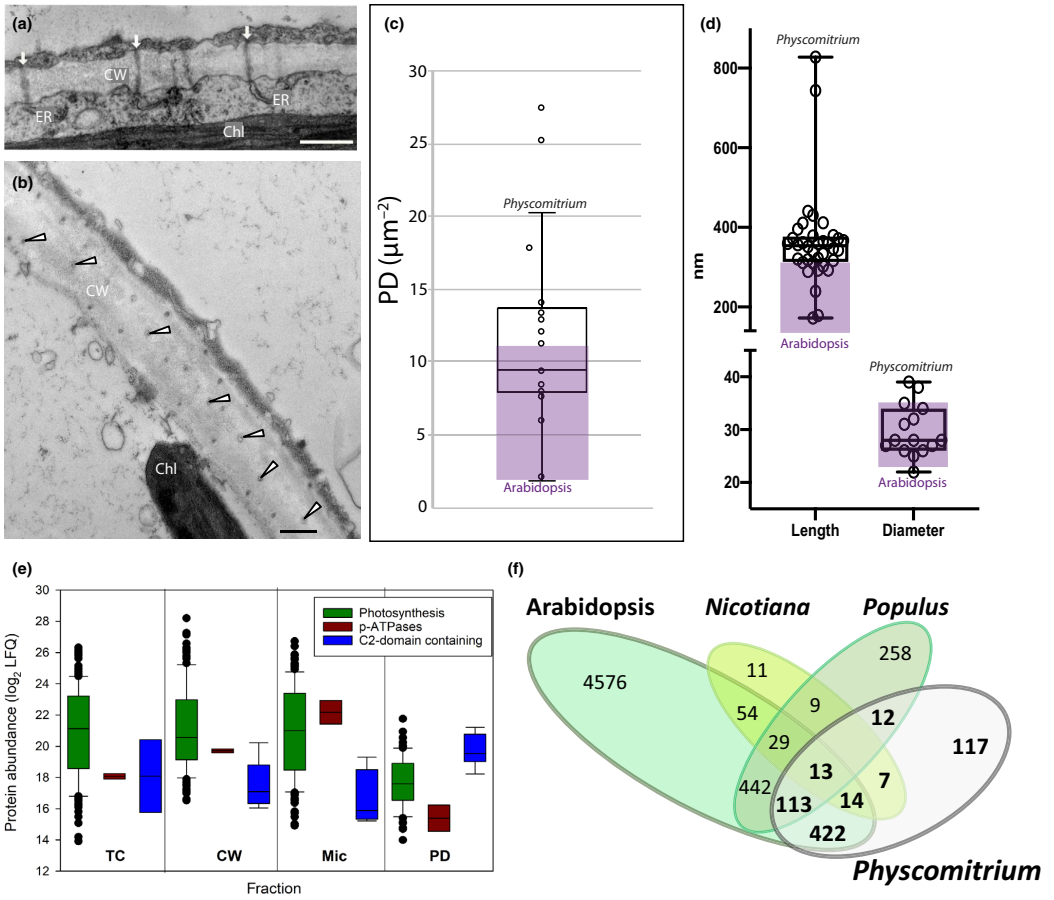

Fig. 1 Plasmodesmata (PD) from *Physcomitrium patens*. (a) Longitudinal section through simple PD between two protonema cells. Desmotubule (pointed with arrows) is visible in the central part of the lumen as a higher electron density. Bar, 500 nm. (b) Cross-section through PD between two protonema cells. Desmotubule (pointed with arrowheads) is visible in the central part of the lumen as a higher electron density. Bar, 500 nm. (c) PD density in protonema cell-to-cell interface as determined by TEM analysis. (d) Measurements of PD length and density based on TEM images. In (c) and (d), purple boxes indicate the ranges of respective values as found in the literature for Arabidopsis. The boxes and whiskers represent the 25th to 75th percentiles and minimum–maximum distributions of the data, respectively. Horizontal lines represent the median and open circles represent individual values. (e) Depletion of nontarget proteins (e.g. photosynthetic proteins) and enrichment of target proteins (e.g. C2-domain-containing proteins) in PD preparations. The family of plasma membrane H^+-ATPases (p-ATPases) was used as control for non-PD plasma membrane. The boxes and whiskers represent the 25th to 75th percentiles and minimum–maximum distributions of the data, respectively. Horizontal lines represent the median and open circles represent individual values. CW, cell wall; Mic, microsomal membranes; PD, plasmodesmata pellet; TC, total cell extract. (f) Overlap of identified protein in PD pellets from *Physcomitrium* and published data sets from *Arabidopsis* (Bayer *et al*., 2006; Fernandez-Calvino *et al*., 2011; Kraner *et al*., 2017; Brault *et al*., 2019), *Populus trichocarpa* (Leijon *et al*., 2018) and *Nicotiana benthamiana* (Park *et al*., 2017). For Arabidopsis, the protein lists from four different studies were combined. For this comparison, Arabidopsis orthologs from respective species were used based on mappings available from PHYTOZOME (Goodstein *et al*., 2012).

Definition of a high-confidence PD proteome using an iterative scoring system

To reliably distinguish actual PD proteins from non-PD proteins in biochemical PD preparations, we developed a PD score (Fig. S2), which is based on protein abundance data along the PD preparation workflow and on annotated features of a reference data set containing confirmed PD proteins from public sources. We compiled published proteome data sets in a relational database (PDDB http://pddb.uni-hohenheim.de, Fig. S3)

and complemented this with 70 individual protein entries with literature evidence of experimental PD localization (Table S1). These proteins were used as *bona fide* confirmed PD proteins and were further expanded by 115 proteins published as the PD core proteome (Brault *et al.*, 2019) based on their high enrichment in PD fractions compared with cell wall or membrane fractions. Additional reliable PD proteins from published sources included 152 proteins with greater than twofold depletion in the *cher1-1* mutant (Kraner *et al.*, 2017), and 56 proteins (52 unique Arabidopsis orthologs) with more than fivefold enrichment or depletion in PD in response to viral infection (Park *et al.*, 2017). Respective threshold values were chosen upon re-evaluation and by applying a two-standard deviation width to histograms of published quantitative data (Table S1). The list of 201 proteins published as PD-enriched from *P. trichocarpa* (Leijon *et al.*, 2018) was not included, since no enrichment ratios were published, making a quantitative re-evaluation difficult. Thus, the first PD scoring training data set comprised 338 unique Arabidopsis orthologs (Table S1) coming from complementary data sources (Fig. 2a).

The PD score was then calculated for each identified protein as the sum of an enrichment score and a feature score (Fig. S2). The enrichment score was derived from the abundance of proteins identified in PD fractions compared with the corresponding abundance in CW, MIC, and TC. The feature score was calculated from frequencies of PFAM domains (http://www.pantherdb.org) and functional classifications by MAPMAN (Thimm *et al.*, 2004) in the reference data set of 338 *bona fide* PD proteins. Consequently, proteins received higher PD scores when they were enriched in the PD fraction and in addition shared features with reference PD proteins.

For 863 proteins found in the *Physcomitrium* PD pellet, we were able to calculate an enrichment score, and for 200 proteins the enrichment score was > 1 (Fig. 2b). The full PD score was calculated for 2053 out of the 4996 identified proteins (Table S2). There were more proteins with a PD score (Fig. 2c) than with an enrichment score because also proteins not quantified by an enrichment score were awarded a PD score based on their features, and thus potentially qualified as part of the PD proteome. Out of this first PD score distribution, 147 proteins were selected and the corresponding cDNAs were cloned to validate PD localization by transient expression in *N. benthamiana* (Fig. 2d). Proteins which localized to PD were added to the reference data set in PDDB for PD scoring. As a result of an iterative second PD scoring based on the updated PD protein list, most of the experimentally localized PD proteins increased in PD score, as did other proteins with similar features (Fig. 2e). This visualizes the key concept of iterative PD scoring consisting of (1) protein abundance enrichment in PD fractions, (2) identification of proteins with similar features as known reference proteins, and (3) re-evaluating their PD score based on features of experimentally validated new PD-localized proteins.

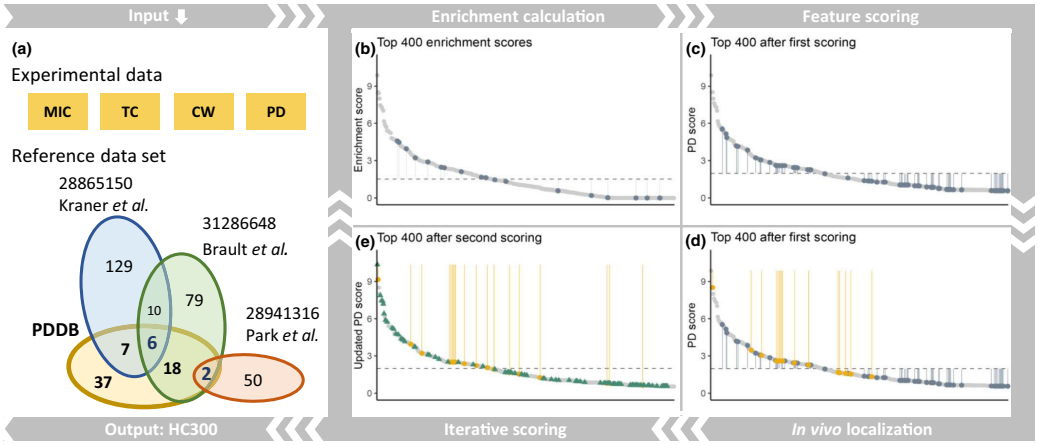

Fig. 2 Plasmodesmata (PD) scoring process visualized with the top 400 best-scoring proteins. (a) Input data consisting of protein abundances in microsomal (MIC), total cell (TC), cell wall (CW), and PD fractions and the *bona fide* PD reference data set of PD proteins characterized by quantitative proteomics (Kraner *et al.*, 2017; Park *et al.*, 2017; Brault *et al.*, 2019) (blue, green, red) and the additional PD-localized proteins in PDDB from different literature sources (yellow). This data set was used as a PD positive set in the first round of PD scoring. (b–e) The components of the PD scoring process. The *y*-axes show enrichment score or PD score. Each of the top 400 scoring proteins is represented by a light gray dot. Proteins are ordered by score in descending order from left to right. Dark gray dots and vertical lines mark the scores of proteins from the reference data set. Yellow dots and vertical lines mark the scores of proteins that have been verified by *in vivo* localization. Gray dashed lines show mean scores. (b) Calculation of the enrichment score that is solely based on proteomics data. (c) PD scores after including a first round of feature scoring. Higher values represent higher likelihood for PD presence. (d) Scores of newly PD-localized proteins are highlighted (yellow dots with vertical yellow lines) before iterative scoring. (e) Iterative second PD scoring including proteins experimentally localized to PD across the full range of PD candidate proteins. Green triangles indicate proteins which were not part of the reference data set but increased in score after iterative scoring.

New Phytologist

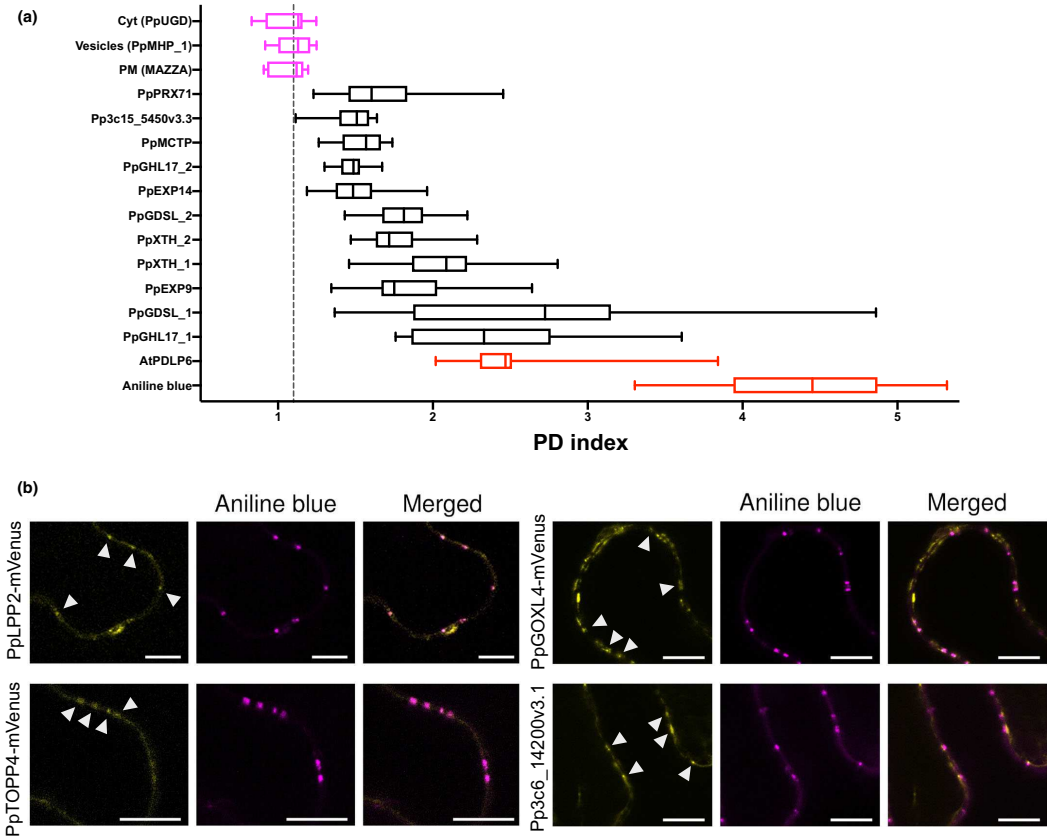

Fig. 3 Selected candidate proteins from *Physcomitrium patens* plasmodesmata (PD) proteome located at PD. Proteins were C-terminally fused to mVenus and transiently expressed under a β-estradiol inducible promoter. Subcellular localization was observed in epidermal cells of *Nicotiana benthamiana* at the confocal microscope. (a) Plasmodesmata index (PD index) of selected candidates, mainly known PD proteins, showed an enrichment at PD similar to well-established PD marker Arabidopsis Plasmodesmata Located Protein 6 (PDLP6). Plasmodesmata markers aniline blue and PDLP6, and non-PD-localized proteins Arabidopsis MAZZA (PM), PpMHP_1 (Pp3c16_460v3.7; vesicles), and PpUGD (cytoplasm) are shown as red and magenta boxplots, respectively. In the boxplots, the median value is denoted by a line and the boxes and whiskers represent the 25th to 75th percentiles, and minimum to maximum distribution. Dashed lines represent the threshold at which a protein is considered PD-enriched and was set at 1.1 corresponding to the highest mean score of the non-PD-localized proteins PpMHP_1. (b) Examples of single optical sections at cell-to-cell interface showing the colocalization of four novel PD protein candidates with PD marker aniline blue (white arrowheads). Bars, 10 μm.

Validation of PD localization using confocal microscopy

Putative PD-localized proteins were systematically screened for colocalization with the callose-staining dye aniline blue as a marker of PD pit fields. Candidates were initially screened for PD localization and given a preliminary validation score (Table S3). Proteins not colocalizing with aniline blue (112 candidates) were considered non-PD proteins for the purpose of PD scoring iteration. For the 36 proteins colocalizing with aniline blue, the degree of enrichment at PD compared with PM was calculated using a semi-automated PD indexing script. Proteins with a PD index > 1.1 (the highest mean score of the negative controls, Figs 3a, S4) were considered enriched at PD compared with bulk PM. For comparison, aniline blue and the Arabidopsis protein Plasmodesmata Located Protein 6 (PDLP6), a protein known to localize exclusively to PD (Thomas *et al.*, 2008), were used as positive controls (Fig. S4). Aniline blue had a PD index of 4.4, while PDLP6 had a PD index of 2.5. Similarly, three proteins from the initial screen that did not show any obvious colocalization with aniline blue, localizing to either PM, vesicles, or cytoplasm, were used as negative controls and had PD indices of *c.* 1.

Due to deficiencies in image quality, the PD index could not be calculated for all candidates deemed PD-localized by qualitative means. We calculated PD indices (range: 1.4–2.7) for 30 of

the 36 candidates that colocalized with aniline blue (Fig. 3b). For the purposes of iterating the PD scoring, all 36 candidates, including those not assigned a PD index, were treated as PD-localized proteins. Among this set of proteins were 20 proteins (56%) that had not previously been considered as PD proteins in other species (Table S4). Five members of the glyoxal oxidase family (Pp3c12_15000; Pp3c3_25264; Pp3c4_20120; Pp3c2_25840; Pp3c22_8310, and pPGOXL4, Fig. 3b), a serine–threonine phosphatase (Pp3c1_370, TOPP4, Fig. 3b), an uncharacterized transmembrane proteins (e.g. Pp3c6_14200, Fig. 3b), and members of the EXO protein family are examples of novel PD-localized proteins, which ranked among the top 10% proteins in the PD scoring (Table S2). For iterative scoring, the feature score component was modified by the contribution of these PD-localized proteins.

Refinement of a *Physcomitrium* high-confidence PD proteome

The iterative PD scores of proteins confirmed as PD localized in *N. benthamiana* clearly separated from PD scores of proteins that could not be localized to PD (Figs 4a, S5A). The PD score was then used to separate high-confidence PD proteins from other proteins (Figs 4a, S5A). A threshold PD score of 0.7 was chosen by carefully balancing the numbers of proteins not found with PD localization among the top-ranking proteins against proteins found with PD localization among lower ranking proteins. Among those 335 PD protein candidates with PD scores > 0.7 (Table S2) were 16 of the cloned and tested proteins, which did not show PD localization in *N. benthamiana*. Although there may be many valid reasons for failed PD localization of these proteins, we termed these as false positives and they made up 3.9% of the top 335 ranking PD protein subset. In turn, 28 proteins (1.6%) localizing to PD in *N. benthamiana* were found among the 1718 proteins with a calculated PD score of < 0.7, which were considered as false negatives.

The 335 PD protein candidates were further refined by considering the PD score difference between the second and the first round of PD scoring, thus taking advantage of the iterative improvement of PD scores by the contribution of novel PD protein functions after experimental localization. For protein functions expected among PD proteins, such as cell wall modifying proteins and C2-domain-containing proteins, but also for proteins with functions not thus far associated with typical PD proteins, the PD score improved throughout the iterative scoring process leading to high average PD score differences (Fig. S5B). In turn, for typical contaminant proteins, such as ribosomes, catalases, and photosynthetic proteins, the PD score was downgraded by the iterative process resulting in large negative PD score differences (Fig. S5B). By applying the PD score difference as further refinement, we excluded proteins that had a negative PD score difference (PD score difference < −0.13; Fig. 4b), resulting in *P. patens* high-confidence PD Proteome (HC300).

Arabidopsis orthologs were used to compare *Physcomitrium* PD proteomes with previously published PD proteomes of other species (Fig. 4c,d). The whole PD proteome dataset contained 1436 Arabidopsis orthologs (Fig. 4c). Of the 292 proteins contained in the HC300, 273 proteins were annotated with Arabidopsis orthologs. After exclusion of photosynthetic proteins as typical contaminants, HC300 contained 39 proteins annotated to 17 orthologs of confirmed PD proteins in other species and 249 other proteins mapping to 191 orthologous proteins which were previously not considered as high-confidence PD proteins (Fig. 4d,e). Upon stepwise refinement of the *Physcomitrium* HC300 PD proteome based on PD score and PD score difference, the overlap with other quantitative PD proteomes (Kraner *et al.*, 2017; Park *et al.*, 2017; Brault *et al.*, 2019) became smaller at each refinement step (Fig. 4c,d). The refinement steps efficiently removed typical contaminants, such as photosynthetic proteins and ribosomes. The proportion of contaminant proteins was rather high (25%) among the proteins not considered high-confidence PD proteins while in HC300 the fraction of putative contaminants was reduced to 16% (Fig. 4e). Among the novel proteins in HC300 were five out of 17 EXO/Exordium-Like (EXL) proteins, whose Arabidopsis orthologs were previously shown to be located in cell walls (Schröder *et al.*, 2009). HC300 contained five out of seven MCTP protein family members (Pp3c27_520, Pp3c14_25200, and Pp3c10_11080 in Fig. S4, Pp3c16_9250 and Pp3c27_540) as well as two other C2-domain-containing proteins (Pp3c9_16970 and Pp3c9_12510). Three receptor kinases (Pp3c25_12800, Pp3c1_10970, and Pp3c19_8660), a phosphatase (Pp3c1_370), and a transmembrane scaffold protein (Pp3c4_1550) were further top-ranking proteins of HC300 (Table S2).

Within HC300, 62% of the proteins were found to have a signal peptide, 76% had at least one transmembrane domain, and 57% of the proteins were predicted to have intrinsically disordered regions (IDR). Cell wall proteins (84 proteins; bins 10; $P = 5.5 \times 10^{-26}$) were highly over-represented, as were glyoxal oxidases (bin 24; $P = 8.9 \times 10^{-13}$; Fig. S5C). In agreement with the overall high content of cell wall-related proteins, HC300 was significantly enriched with PFAM domains of glycosyl hydrolase family 17 (GHL17) proteins (PF00332 and GHL17s), xyloglucan endotransglucosylases/hydrolases (PF06955, XTHs), and pectin esterase (PF1095). The PFAM X8 domain (PF07983), proposed with a role in protein targeting to PD through its signal sequences for a glycosylphosphatidylinositol (GPI) linkage, was found 14 times (5%; Fig. S5D; Simpson *et al.*, 2009).

Phylogenetic distribution of glycosyl hydrolase family 17

Cell wall proteins made up the largest functional group in HC300. We identified 16 proteins annotated as β-1,3-glucanases containing a GHL17 domain (Table S2). GHL17s are callose-degrading enzymes located at the cell wall and associated with PD (Levy *et al.*, 2007; Zavaliev *et al.*, 2013; Benitez-Alfonso, 2014). Members of the GHL17 family were previously identified in PD proteome lists from Arabidopsis, *P. trichocarpa*, and *N. benthamiana*, and 10 of them overlapped in at least two species. PpGHL17_16 (Pp3c16_16680) was the only member of the GHL17 family, for which orthologs were found in PD proteome lists of all four species. *Physcomitrium patens* HC300

New Phytologist

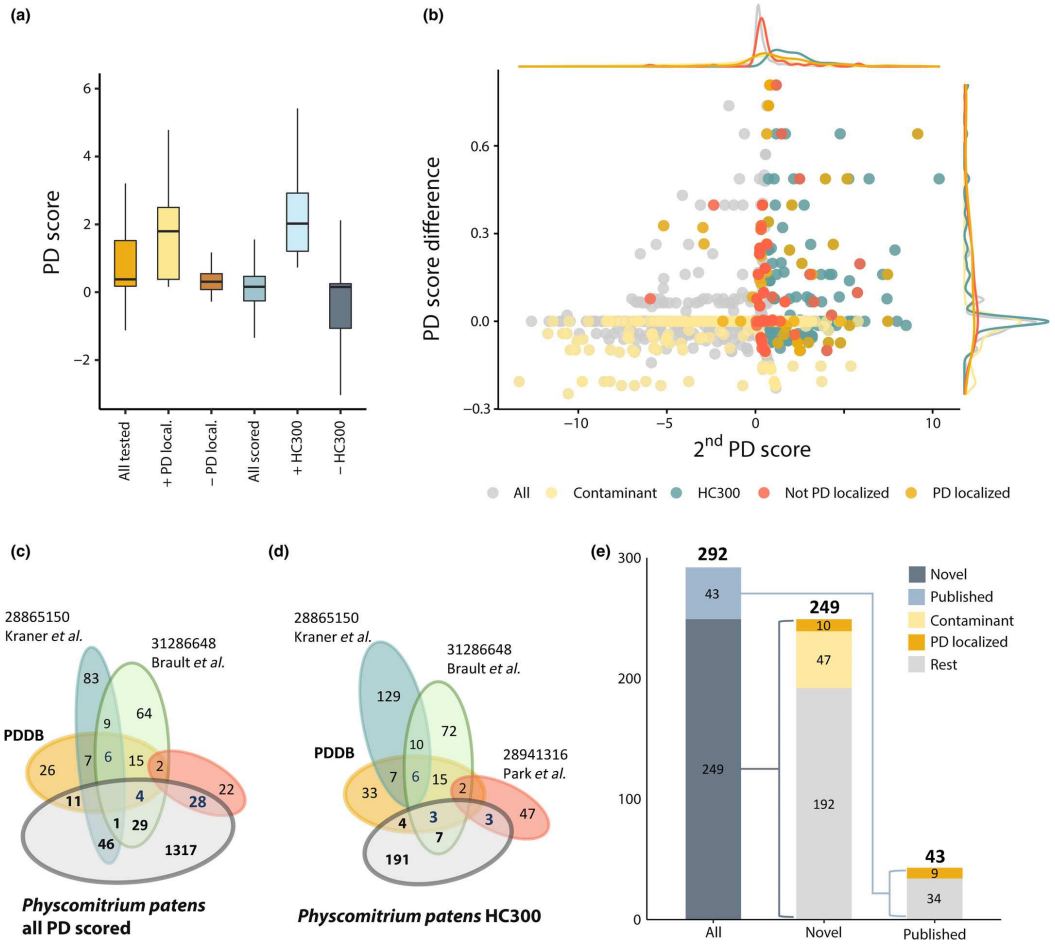

Fig. 4 Characterization of *Physcomitrium* plasmodesmata (PD) scored proteome. (a) Boxplots of PD scores (2nd scoring) of all proteins that were tested for localization at PD in *Nicotiana benthamiana* combined ('All tested') and separated into the proteins localized ('+ PD local.') and nonlocalized to PD ('– PD local.') and boxplots of PD scores (2nd scoring) of all scored proteins combined ('All scored') and separated into proteins that were included into the refined HC300 proteome ('+ HC300)') and excluded of the HC300 proteome ('- HC300'). Outliers were removed to improve clarity. See Supporting Information (Fig. S5A) for a comprehensive version of the plot. Horizontal lines represent the median value, whiskers indicate 25th and 75th percentiles. (b) PD score (> 0.7) and PD score difference (> –0.13) as criteria to define the high-confidence *Physcomitrium* PD proteome. Light gray: proteins not included in the refined HC300 proteome. Light yellow: photosynthetic proteins and ribosomal proteins as typical contaminants. Blue, refined HC300 proteome; red, proteins that did not localize at PD in *N. benthamiana*; yellow, proteins with PD localization in *N. benthamiana*. (c) Venn diagram containing the nonrefined set of Arabidopsis orthologs of all PD-scored proteins and the *bona fide* PD reference data set. (d) Venn diagram containing the Arabidopsis orthologs of the refined high-confidence PD proteome HC300 and the *bona fide* PD reference data set. (e) Overview of the HC300 based on *Physcomitrium* protein identifiers classified as 'published' and novel' proteins. For each group, contaminants (e.g. plastidial proteins) and experimentally PD-localized proteins were specifically highlighted.

contained three GHL17 orthologs (PpGHL17_2, PpGHL17_7, and PpGHL17_9; Table S5), which showed no overlap with PD proteomes from angiosperms (Fig. 5a).

Based on sequence similarity, GHL17 proteins of representative species from charophytic algae and embryophytes, including *P. patens*, were classified into three major clades (Doxey *et al.*, 2007; Gaudioso-Pedraza & Benitez-Alfonso, 2014). To get insights into their role in the evolution of multicellularity, a new phylogenetic analysis of the GHL17 family was performed including *P. patens*, Arabidopsis, *P. trichocarpa*, *Oryza sativa*, and

representative species from green algae (Figs 5b, S6A). Unexpectedly, no GHL17 orthologs could be identified in the unicellular algae *Mesostigma viride* and *Chlamydomonas reinhardtii*, which belong to the *Streptophyta* and *Chlorophyta* clades and thus are ancestors to embryophytes. This suggests that the GHL17 family emerged in multicellular organisms.

GHL17s from charophytic algae (*Klebsormidium nitens*, *Chara braunii*, and *Nepenthes mirabilis*) were present only near the base of the gamma clade, likely representing the ancestral type of GHL17 proteins (Fig. 5b). The alpha clade only contained GHL17s from embryophytes, suggesting that this group appeared during land colonization. Three of the Arabidopsis GHL17 proteins from the alpha clade were previously described to localize at PD, suggesting that phylogenetic distribution might correlate with the subcellular localization either at PD or apoplasm (Levy *et al.*, 2007; Benitez-Alfonso *et al.*, 2013). To further test this hypothesis, we studied the subcellular localization of six *P. patens* GHL17 representatives, four from the alpha clade and two from the beta clade by transient expression in *N. benthamiana*.

Transient expression of beta clustered PpGHL17_28-mVenus and PpGHL17_30-mVenus showed apoplasmic localization (Fig. S6B), whereas PpGHL17_1-mVenus, PpGHL17_7-mVenus, PpGHL17_8-mVenus, and PpGHL17_15-mVenus from the alpha clades were found with a punctate pattern at the cell periphery and overlaid with aniline blue (Fig. 5c). Since transient expression assays can lead to mislocalization, and PD targeting mechanisms might not be conserved between *N. benthamiana* and *P. patens*, we obtained a *P. patens* stable transgenic line expressing UBQ:PpGHL17_1-mVenus to further validate PD localization. The subcellular localization of PpGHL17_1-mVenus in the stable line confirmed PD localization found in transient expression assays (Fig. 5d,e). In addition, when overexpressing PD-localized PpGHL17_1 in *Physcomitrium*, diffusion of the PD mobile dye carboxyfluorescein diacetate (CFDA) increased compared with wild-type ecotype (Fig. 5f,g) suggesting GHL17s play a role in regulating PD opening through the degradation of callose. Interestingly, expressing beta-clade PpGHL17_30, which did not localize to PD (Fig. S6), did not enhance CFDA diffusion between neighboring protonema cells (Fig. 5f,g). This points to a functional diversification of PD and non-PD-localized members of the GHL17 family or that only PD-localized PpGHL17s can degrade callose at PD. In recent parallel work, GHL17_4 (Pp3c11_25840) and GHL17_18 (Ppc16_15860), also members of the GHL17 alpha clade, were localized to PD in *P. patens* (Johnston *et al.*, 2023), thus adding further evidence for PD localization of alpha clade GHL17s.

In search of a potential PD localization signal, we modeled structures of alpha-clade PpGHL17s (Fig. 5h). The sequence motif IFALFENE(N) was over-represented among this group of GHL17s and was absent in the members of the beta clade. However, this motif was predicted to be only partially surface-exposed as part of the 40 Å cleft of the glycosyl hydrolase domain and is therefore more likely to be related to enzyme function rather than localization (Fig. 5g). Another interesting observation was that all GHL17s from the alpha clade contained a beta tunnel and cleft domain, while the distribution of other structural features, such as an X8 domain and GPI-anchor signal, was not equally present (Table S5).

Xyloglucan endotransglucosylases/hydrolases

XTHs are enzymes involved in xyloglucan metabolism and are important for the control of cell wall strength as well as extensibility during growth and development. In Arabidopsis, XTHs were shown to be upregulated in the *ise2* mutants, which displayed an increase in cell-to-cell transport of fluorescent probes (Burch-Smith *et al.*, 2011). We found 12 members of the XTH family in HC300, six of which were confirmed as PD-localized in *N. benthamiana* (Fig. S7A). The molecular phylogeny of XTH genes was previously shown to segregate into three major groups (I, II, and III), and an isolated small group named 'ancestral' (Baumann *et al.*, 2007; Eklöf & Brumer, 2010; Shinohara & Nishitani, 2021). All *Physcomitrium* XTH genes, except Pp3c13_11910 and Pp3c3_9730, clustered in group I. The PpXTHs identified in HC300 were exclusively from group I (Fig. S7B), indicating a correlation between PD localization and phylogenetic distribution to group I.

Exordium and exordium-like proteins

Five members of the Arabidopsis EXO and EXL protein family were identified in HC300: Pp3c19_8770 (PpEXO1), Pp3c10_8680, and Pp3c14_6120 (AtEXO ortholog by protein BLAST), Pp3c18_22500 (AtPHI1/EXL7 ortholog), and Pp3c22_12550 (AtEXL2 ortholog). EXL2 was previously found in Arabidopsis and *P. trichocarpa* PD proteomes, but their PD localization was not confirmed (Fernandez-Calvino *et al.*, 2011; Leijon *et al.*, 2018). Several members of this family were also found in Arabidopsis cell wall proteomes (AtEXO, AtEXL1, AtEXL2, AtEXL3, and AtEXO4) and membrane proteomes (AtEXL4) (Bayer *et al.*, 2006; Feiz *et al.*, 2006; Jamet *et al.*, 2006; Mitra *et al.*, 2007). Here, PpEXO1 and Pp3c22_12550 were found among the top 10 PD score ranks in HC300 (Table S2) and PpEXO1 localized to PD in transient expression assays in *N. benthamiana* (Fig. 6a). The members of the EXO protein family share structural similarity in an N-terminal tail with a transmembrane domain and a globular C-terminal part (Fig. 6b). The globular part of the EXO proteins contains a distinct 'nose' with two clefts, which could serve as scaffolding or binding sites (Fig. 6b).

A phylogenetic analysis was undertaken to study sequence divergence along the EXO family evolution. Exordium proteins from representative species of the embryophytes (17 from *P. patens*, 8 from Arabidopsis, 12 from *O. sativa*, and 17 from *P. trichocarpa*) as well as all EXO proteins identified in algae were therefore included in this analysis (Fig. 6b). We found that EXOs are distributed between three clades. While clade I contained only EXO sequences from algae including both Chlorophyta and Charaphyta, clade II contained EXO sequences from all the investigated species, distributed between two subclades. Subclade II-a exclusively included EXOs from the algae *Spirogloea*

New Phytologist

muscicola, and subclade II-b contained embryophyte sequences. This clustering shows that embryophyte EXOs found in clade II are more similar to the EXOs of algae *S. muscicola* of subclade II-b than to embryophyte EXOs found in clade III. Clade III contained EXO sequences from all investigated embryophyte species but none from the investigated algae species. The four *P. patens*

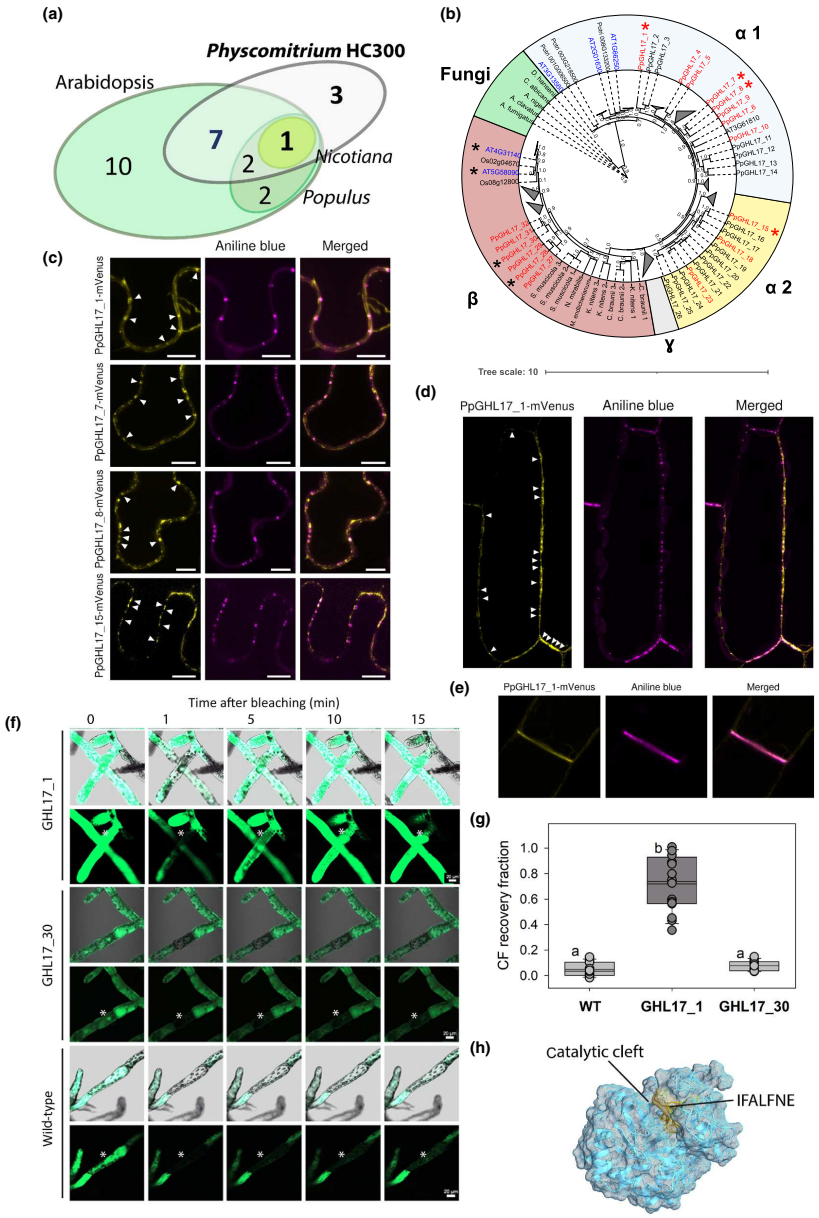

New Phytologist

Fig. 5 Plasmodesmata (PD) localization of glycolyl hydrolase 17 (GHL17) proteins correlates with phylogenetic distribution. (a) Members of the GHL17 family identified in PD proteomes from angiosperms (Arabidopsis, *Populus trichocarpa*, *Nicotiana benthamiana*) and the moss *Physcomitrium*. (b) Phylogenetic analysis of GHL17 sequences showed three major clades: α (yellow), β (blue), and γ (red), as defined by Gaudioso-Pedraza & Benitez-Alfonso (2014). *Physcomitrium patens* GHL17 proteins identified in the PD proteome are labeled in red and Arabidopsis orthologs previously assayed for localization colored in blue (Benitez-Alfonso, 2014; Gaudioso-Pedraza & Benitez-Alfonso, 2014). Red asterisks indicate *P. patens* and Arabidopsis PD-localized GHL17 proteins and group in clade α, whereas non-PD-localized proteins are marked with black asterisks and cluster in either β or γ clades. Charophyta green algae grouped in clade β. Fungi GHL17 sequences clustered separately (in green). The phylogenetic tree was generated with the maximum likelihood method implemented in PhyML (Lemoine *et al*., 2019). Support values from 1000 bootstrap samples are shown at the nodes. Clades which do not contain *P. patens* or Arabidopsis sequences were collapsed. (c) Subcellular localization in *N. benthamiana* epidermis cells of PpGHL17_1 (Pp3c17_13760V3.2), PpGHL17_7 (Pp3c10_5480V3.1), PpGHL17_8 (Pp3c14_5200V3.2), and PpGHL17_15 (Pp3c12_13470V3.5) mVenus fusion proteins belonging to α clades. Bars, 20 μm. (d) Localization of PpGHL17_1-mVenus at PD pit fields (white arrowheads) in *P. patens* gametophore cells (Supporting Information Methods S1). (e) Protonema cells of *P. patens* expressing PpGHL17_1-mVenus (Pp3c17_13760v3.2) showed an enrichment at the cell-to-cell interface. Due to the high density of PD at the cell–cell interface, individual PD cannot be resolved in the image. (f) Images of CFDA/FRAP transport assays of *Physcomitrium* ecotype Grandsen chloronema cells for wild-type, overexpressing PpGHL17_1 or PpGHL17_30. Bars, 20 μm. Asterisks indicate the cell which was bleached. (g) Quantification of CFDA transport rates in *P. patens* ecotype Grandsen wild-type and genotypes overexpressing GHL17_1 or GHL17_30 presented as fraction of CF recovery in the photo-bleached protonema cells within 15 min (Methods S1). Values represent the mean ± SE of 16 experiments for each line; small letters indicate significant ($P < 0.05$) differences (one-way ANOVA, Holm-Sidak correction). (h) Alpha-Fold model of *Pp*GHL17 α clade glycoside hydrolase domains (cyan) with the conserved IFALFNE(N) motif (yellow).

EXO proteins identified in HC300 were all found in a subclade of clade III which seems to correspond to a cluster of EXO orthologs from seedless plants previously defined by the EXO sequences of *P. patens* and *Selaginella moellendorffii* (Li *et al*., 2021). Interestingly, EXOs from Arabidopsis and *P. trichocarpa* previously identified in PD proteome lists were also found in clade III (Fig. 6b). The EXO protein family is yet the third example of a protein family in which PD-localized members group in a distinct phylogenetic clade.

Discussion

A PD scoring algorithm to define PD proteomes

Plasmodesmata are nanometer-scale structures of high complexity. They contain different types of cellular membranes, and their protein composition depends on environmental cues, tissue, and/or developmental stage. Thus, in order to understand the protein composition of PD, we require *in silico* approaches which tag likely PD-localized proteins and separate them from likely non-PD proteins. No biochemical method yields pure PD. Therefore, highly abundant proteins such as photosynthetic proteins or ribosomes will always be detected in PD preparations. We found that the overlap between unweighted PD proteome lists contains a high proportion of contaminant proteins and mere identification of a protein in biochemically enriched PD preparations is not sufficient to conclude its PD localization without additional information. We demonstrated the improvement of the scoring algorithm after extensive protein localization and used this information to refine a high-confidence PD proteome of *Physcomitrium* (HC300) (Fig. 4). A previous approach (Kirk *et al*., 2021) also applied a bioinformatic strategy to predict PD proteins based on protein features found in a subset of the published proteomes (Fernandez-Calvino *et al*., 2011; Park *et al*., 2017; Brault *et al*., 2019). However, these authors did not consider biochemical aspects (i.e. enrichment in biochemical PD fractions) and they did not benchmark the predictions against experimental protein localization.

Here, we used strict scoring thresholds to define the high-confidence set of proteins likely present in PD of *P. patens*. However, the drawback of stringent thresholding lies in accepting potential losses of loosely associated proteins or proteins dynamically associated with PD. Similar effects were discussed previously for interactome data: proteins identified with high reproducibility and high-confidence tended to make up stable protein complexes, such as ribosomes, respiratory chain, or photosynthetic complexes (Gilbert *et al*., 2021). In turn, proteins with higher variability among replicates and lower confidence values tended to contain more protein functions for which dynamic or conditional interactions are expected, such as for example signaling proteins (Gilbert *et al*., 2021).

A trade-off between accuracy and coverage has also been discussed for yeast interactome data (von Mering *et al*., 2002). In analogy, HC300 is rich in cell wall proteins and structural elements (e.g. the C2-domain-containing proteins and putative scaffolds) but contains a rather low fraction of signaling elements such as receptor kinases. We found only one member of the GDSL-motif lipase/hydrolase family proteins in HC300, while nine other identified family members were not considered part of the high-confidence proteome based on their PD score rank, although two of them were experimentally localized to PD. Similarly, dynamins and RAN-GTPases were not classified among the HC300 after PD score ranking (Table S2). However, members of these protein families also showed a PD score difference > 0.3, indicating highly improved ranking based on features of experimental localizations. We therefore considered these protein families part of an extended PD proteome (Table S2).

Besides cell wall modifying proteins, our approach identified several members of the EXO protein family (Fig. 6) and several members of the glyoxal oxidase family (Fig. 3) as prominent novel protein families with PD localization. In general, since protein composition, structure, and molecular functioning of PD still remain largely enigmatic, a high-confidence 'parts list' will be a valuable basis for future work on PD structure and function. In that sense, the HC300 defined here presents the community with a set of potentially rewarding targets for in-depth functional studies.

New Phytologist

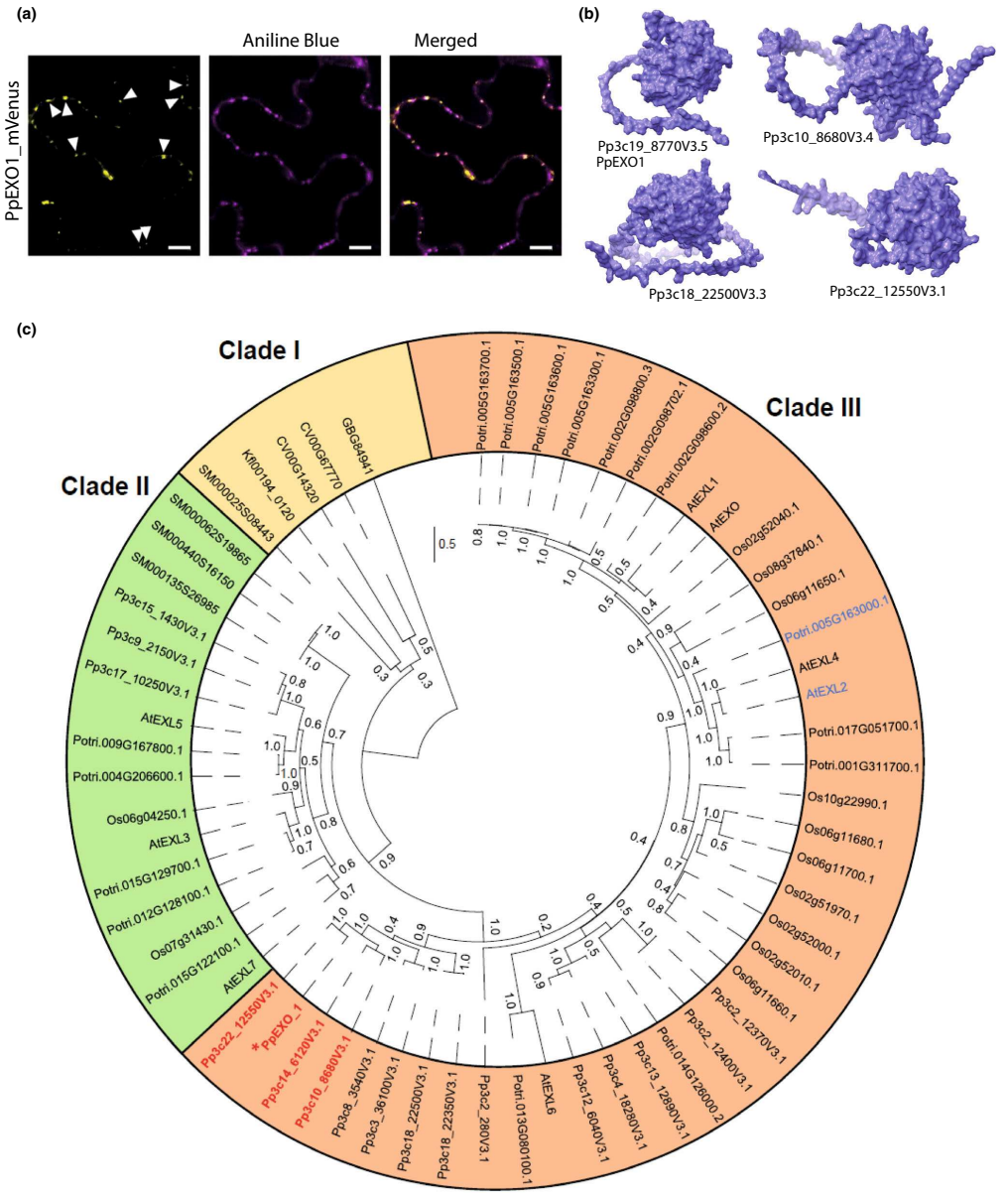

Fig. 6 Exo/Exordium-Like (EXO/EXL) family members. (a) Subcellular localization of PpEXO_1 (Pp3c19_8770V3.5) in *Nicotiana benthamiana* leaf epidermis cells showing overlay with aniline blue. Bars, 10 μm. (b) AlphaFold model of the four top-ranking EXO family members in HC300. (c) Phylogenetic tree of EXO/EXL family members from representative species of the embryophytes (17 from *Physcomitrium patens*, 8 from Arabidopsis, 12 from *Oryza sativa*, and 17 from *Populus trichocarpa*) and all algae for which EXO orthologs could be identified (*Coccomyxa subellipsoidea*, *Klebsormidium nitens*, *Chara braunii*, *Spirogloea muscicola*). *Physcomitrium patens* EXO/EXL members identified in the HC300 plasmodesmata (PD) proteome are labeled in red and clustered in clade III in which EXO identified in other PD proteomes are grouped (labeled in blue). Numbers indicate fraction of bootstrapping rounds supporting this node.

Large-scale PD localization in *N. benthamiana*

Despite improvement in distinguishing likely PD proteins from likely non-PD proteins by the PD scoring, experimental localization remains important. For example, we tested five members of the GHL17 family of glycosyl hydrolases from the whole PD proteome for PD localization with positive results for three proteins and no PD localization in *N. benthamiana* for two family members. Overall, the transient localization of *Physcomitrium* proteins in the *N. benthamiana* system proved efficient and applicable also on a larger scale. Most importantly, our approach showed that targeting mechanisms to PD are conserved between bryophytes and vascular plants. However, we cannot exclude the possibility that false negatives occurred, either due to the absence of required chaperones or misinterpretation of sorting signals in this heterologous system. In turn, false positives could have resulted from overexpression or mislocalization. To address such caveats, we used an inducible promoter and appropriate induction times to minimize overexpression artifacts.

Major protein families of *P. patens* PD

Plasmodesmata in land plants evolved to have more complex structures compared with their counterparts found in *Characeae* algae (Brunkard & Zambryski, 2017). This might reflect adaptations to regulate PD conductance and the emergence of specialized metabolic enzymes. Deposition of callose at the neck region of PD is one of the major modes to gate PD (Zavaliev *et al.*, 2011). The maintenance of callose associated with PD is affected mainly by callose synthases and β-1,3-glucanases. Thus, it comes as no surprise that our high-confidence subset of the *P. patens* PD proteome contains a high number ($n = 84$) of cell wall and cell wall-modifying proteins. Among these, the largest group comprised glycosyl hydrolases from the GHL17 subfamily. The GHL17 family is an excellent example of a large protein family which throughout evolution diversified in its subcellular localization, with one clade becoming PD-localized. This subfamily can also be taken as an example highlighting the two components of the PD scoring, namely biochemical enrichment in PD, and a feature scoring component. The feature scoring component alone would not have been able to differentiate proteins from the two clades of GHL17 proteins. However, the whole PD score revealed an important means to differentiate PD-localized and non-PD-localized GHL17s.

GHL17s and XTHs are considered important in controlling PD gating by affecting callose formation. GHL17s as callose-degrading enzymes are considered to be involved in keeping PD in an open state (Levy *et al.*, 2007; Zavaliev *et al.*, 2013; Benitez-Alfonso, 2014; Fig. 5e,f), while for XTHs, a role in cell wall remodeling during formation of secondary PD was proposed (Ehlers & Kollmann, 2001). Similarly, a callose synthase ortholog has been characterized with critical functions in enabling sucrose transport in rice (Wang *et al.*, 2009). The large numbers of proteins involved in cell wall synthesis and remodeling in the *Physcomitrium* PD proteome may reflect the need to dynamically modify the composition of the PD associated cell wall regions independently of other regions.

We identified four out of the 17 *P. patens* EXO/EXL proteins in HC300. The Arabidopsis ortholog to Pp3c18_22500 is Phosphate induced 1 (PHI-1) and was initially identified in tobacco BY-2 cell suspension cultures among genes induced after recovery from phosphate-induced starvation (Sano *et al.*, 1999). In Arabidopsis, EXO/EXLs were proposed as potential mediators of brassinosteroid-promoted growth (Coll-Garcia *et al.*, 2004; Schröder *et al.*, 2011). Indeed, *AtEXO* and *AtEXL1* expression is induced by brassinosteroids, and *AtEXO* regulates other brassinosteroid-responsive genes (Coll-Garcia *et al.*, 2004; Schröder *et al.*, 2011). While overexpression of *AtEXO* promotes shoot and root growth, its loss of function leads to a reduction in growth resulting from a defect in cell expansion (Schröder *et al.*, 2009). The expression of several *AtEXLs* is also controlled by carbon metabolism and energy status and is required during adaptation to carbon and energy-limiting growth conditions (Schröder *et al.*, 2011). Although physiological functions of EXO proteins are still unclear, it was proposed that AtEXO could connect extracellular carbon status to growth responses (Schröder *et al.*, 2009, 2011; Lisso *et al.*, 2013).

Bud dormancy was shown to be associated with a molecular carbon starvation response which includes an increase in *EXL2* and *EXL4* RNA levels (Tarancon *et al.*, 2017). During bud dormancy, meristematic cells are symplasmically isolated through callose-dependent PD obstruction (Rinne *et al.*, 2001; Ruonala *et al.*, 2008; Cooke *et al.*, 2012; Tylewicz *et al.*, 2018). Photoperiod and gibberellic acid mediate opening of PD by inducing the expression of GHL17s. GHL17s then promote callose hydrolysis at PD and thereby contribute to dormancy release (Rinne *et al.*, 2011). Because of increasing evidence of EXO/EXL localization at PD, the involvement of these proteins in sensing of carbon status and regulation of growth response might need to be revisited in the context of symplasmic communication. Indeed, mechanisms by which these proteins mediate their physiological functions remain to be elucidated. Structural features of the EXO proteins suggest they can interact with other proteins through their C-terminal globular domain and thus may have functions in stabilizing protein complexes as scaffolds and/or in presenting signaling components or substrates.

The Arabidopsis homolog to phosphatase Pp3c1_370, TOPP4, was shown to regulate PIN1 polarity and trafficking (Guo *et al.*, 2015). This, together with receptor kinases identified in HC300, indicates that also in *Physcomitrium* PD, posttranslational modification of proteins could be an important mechanism defining protein localization or gating of PD. Indeed, phosphorylation-dependent recruitment to PD was described for coreceptor QSK1 in Arabidopsis (Grison *et al.*, 2019).

Evolution of PD localization within large protein families

Here, we present a thorough characterization of the PD proteome of *P. patens*, a member of the bryophytes, which were among the evolutionary early land plants. It is now possible to compare PD proteomes of an early embryophyte to PD

proteomes of vascular plants to obtain insights into evolution of PD itself and also into evolution of processes that involve PD. Symplasmic transport is highly regulated and involved in numerous processes in plant development, for example, bud dormancy and meristem activity. Thus, some of the PD proteins are involved in transport of signaling molecules and resource sharing and/or regulation thereof. These functions must have evolved and diversified during evolution of multicellularity. The *P. patens* HC300 contains multiple members of larger protein families, exemplified by GHL17s, XTHs, and EXO/EXLs, each of which diverged into several phylogenetic clades. Interestingly, in all cases, PD-localized members grouped in a distinct clade, often – as in the GHL17s – separating PD-localized and non-PD-localized family members. Contrary to what has been previously reported (Li *et al.*, 2021), we also found EXO/EXL orthologs in algae. However, EXO/EXL identified in the PD proteome do not cluster with algae members, suggesting that EXO/EXL PD localization might have emerged later during evolution of embryophytes. The EXLs are not predicted to have GPI anchors, but they contain an N-terminal alpha-helix, which is predicted to contain an ER/secretory pathway targeting signal. We hypothesize that a co-evolution of PD functions and respective protein localization took place, leading to diversification in these protein families.

Acknowledgements

We thank Elmehdi Bahafid for excellent assistance during *Physcomitrium* transformation, Jan Weber for excellent assistance during protein preparations of PD fractions, and Ronja Lange for excellent assistance in cloning of *Physcomitrium* genes. pTH UbiGate plasmid was a kind gift from Prof. Bezanilla, Dartmourth, USA. This work received funding from the European Research Council (ERC) and the Marie Skłodowska-Curie under the European Union's Horizon 2020 research and innovation program (Grant agreements 'SymPore' no. 951292 to WBF, RS, WXS, and WB, 'PDgate' no. 101023981 to MM, and 'CLAVHUB' no. 101023589 to VH, respectively). This research was supported by the Deutsche Forschungsgemeinschaft (DFG, German Research Foundation) under Germany's Excellence Strategy – EXC-2048/1 – project ID 390686111 (RS, SH and WF), and the Alexander von Humboldt Professorship (WBF). Open Access funding enabled and organized by Projekt DEAL.

Author contributions

SG performed proteomics experiments, developed the PD scoring and prepared figures, and wrote the manuscript. MM contributed to cloning and localization of PD candidates in *N. benthamiana*, image analysis, figure preparation, phylogenetic analysis, and wrote the manuscript. VH contributed to cloning and localization of PD candidates in *N. benthamiana*, and image analysis, and contributed to writing of the manuscript. LX contributed to development of the PD scoring and PDDB structure and participated in writing of the manuscript. MP contributed to cloning and localization of PD candidates in *N. benthamiana*, image analysis, and phylogenetic analysis. NSKJ contributed to cloning and localization of PD candidates in *N. benthamiana*, transformation of PD-localized candidates in *P. patens*, transport assay of CFDA in *P. patens*, and figure preparation. MS contributed to cloning and localization of PD candidates in *N. benthamiana*, and image analysis. JOE contributed to cloning and localization of PD candidates in *N. benthamiana*, image analysis, and transformation of PD-localized candidates in *P. patens*. UN performed transmission electron microscopy. SH wrote PD indexing Fiji macro. FK contributed to cloning and localization of PD candidates in *N. benthamiana*. ZZ contributed to the implementation of PDDB database structure and design. MD performed Cryo transmission electron microscopy of PD fraction preparation and structural analysis of *Pp*GHL17s. PX performed Cryo transmission electron microscopy of PD fraction preparation. TS performed sequence motif analysis of the GHL17 proteins. WB developed the concept and designed experiments. WBF and RS developed the concept, designed experiments, and contributed to writing. WXS developed the concept, designed experiments, performed data analysis, and wrote the manuscript. SG, MM and VH contributed equally to this work.

ORCID

Wolfgang Baumeister https://orcid.org/0000-0001-8154-8809
Marcel Dickmanns https://orcid.org/0000-0003-4001-707X
J. Obinna Ejike https://orcid.org/0000-0002-4601-8551
Wolf B. Frommer https://orcid.org/0000-0001-6465-0115
Sven Gombos https://orcid.org/0000-0003-4177-526X
Sebastian Hänsch https://orcid.org/0000-0002-7762-2516
Vicky Howe https://orcid.org/0000-0002-7319-0664
Neda S. Kazemein Jasemi https://orcid.org/0000-0002-7842-6998
Manuel Miras https://orcid.org/0000-0002-3636-0265
Ulla Neumann https://orcid.org/0000-0001-9200-4209
Mathieu Pottier https://orcid.org/0000-0003-1551-4699
Moritz Schladt https://orcid.org/0000-0002-9160-4664
Waltraud X. Schulze https://orcid.org/0000-0001-9957-7245
Rüdiger Simon https://orcid.org/0000-0002-1317-7716
Lin Xi https://orcid.org/0000-0002-6811-9505

Data availability

Proteomics data sets: Mass spectrometry proteomics data were deposited to the ProteomeXchange Consortium via the PRIDE partner repository (Deutsch *et al.*, 2017) with the dataset identifier PXD032820.

Image data sets: Images of PD-localized proteins were made public within the PDDB (pddb.uni-hohenheim.de). In addition, confocal images and the TEM micrographs were deposited at Bioimage Archive (https://www.ebi.ac.uk/bioimage-archive/) under accession no. S-BIAD466.

PD index quantification scripts: A script was developed aiding assessment of PD localization based on the co-expression of

mVenus fusion proteins with aniline blue. Code of the FIJI macro can be accessed at: https://github.com/SHaensch/2022_PD-index-quantification.

PD scoring: The formulas underlying PD scoring are described in the Materials and Methods section of the manuscript.

References

Anvarian Z, Mykytyn K, Mukhopadhyay S, Pedersen LB, Christensen ST. 2019. Cellular signalling by primary cilia in development, organ function and disease. *Nature Reviews. Nephrology* **15**: 199–219.

Bangs F, Anderson KV. 2017. Primary cilia and mammalian hedgehog signaling. *Cold Spring Harbor Perspectives in Biology* **9**: a028175.

Baumann MJ, Eklof JM, Michel G, Kallas AM, Teeri TT, Czjzek M, Brumer H 3rd. 2007. Structural evidence for the evolution of xyloglucanase activity from xyloglucan endo-transglycosylases: biological implications for cell wall metabolism. *Plant Cell* **19**: 1947–1963.

Bayer EM, Bottrill AR, Walshaw J, Vigouroux M, Naldrett MJ, Thomas CL, Maule AJ. 2006. Arabidopsis cell wall proteome defined using multidimensional protein identification technology. *Proteomics* **6**: 301–311.

Benitez-Alfonso Y. 2014. Symplastic intercellular transport from a developmental perspective. *Journal of Experimental Botany* **65**: 1857–1863.

Benitez-Alfonso Y, Faulkner C, Pendle A, Miyashima S, Helariutta Y, Maule A. 2013. Symplastic intercellular connectivity regulates lateral root patterning. *Developmental Cell* **26**: 136–147.

Brault ML, Petit JD, Immel F, Nicolas WJ, Glavier M, Brocard L, Gaston A, Fouche M, Hawkins TJ, Crowet JM *et al.* 2019. Multiple C2 domains and transmembrane region proteins (MCTPs) tether membranes at plasmodesmata. *EMBO Reports* **20**: e47182.

Brunkard JO, Zambryski PC. 2017. Plasmodesmata enable multicellularity: new insights into their evolution, biogenesis, and functions in development and immunity. *Current Opinion in Plant Biology* **35**: 76–83.

Burch-Smith TM, Brunkard JO, Choi YG, Zambryski PC. 2011. Organelle-nucleus cross-talk regulates plant intercellular communication via plasmodesmata. *Proceedings of the National Academy of Sciences, USA* **108**: E1451–E1460.

Coll-Garcia D, Mazuch J, Altmann T, Müssig C. 2004. EXORDIUM regulates brassinosteroid-responsive genes. *FEBS Letters* **563**: 82–86.

Cooke JE, Eriksson ME, Junttila O. 2012. The dynamic nature of bud dormancy in trees: environmental control and molecular mechanisms. *Plant, Cell & Environment* **35**: 1707–1728.

Coudert Y, Harris S, Charrier B. 2019. Design principles of branching morphogenesis in filamentous organisms. *Current Biology* **29**: R1149–R1162.

Cove JD, Perroud P-F, Charron AJ, McDaniel SF, Khandelwal A, Quatrano RS. 2009. Culturing the moss *Physcomitrella patens. Cold Spring Harbor Protocols.* doi: 10.1101/pdb.prot5136.

Cox J, Mann M. 2008. MAXQUANT enables high peptide identification rates, individualized p.p.b.-range mass accuracies and proteome-wide protein quantification. *Nature Biotechnology* **26**: 1367–1372.

Deutsch EW, Csordas A, Sun Z, Jarnuczak A, Perez-Riverol Y, Ternent T, Campbell DS, Bernal-Llinares M, Okuda S, Kawano S *et al.* 2017. The ProteomeXchange consortium in 2017: supporting the cultural change in proteomics public data deposition. *Nucleic Acids Research* **45**: D1100–D1106.

Ding B, Haudenshield JS, Hull RJ, Wolf S, Beachy RN, Lucas WJ. 1992a. Secondary plasmodesmata are specific sites of localization of the tobacco mosaic virus movement protein in transgenic tobacco plants. *Plant Cell* **4**: 915–928.

Ding B, Kwon MO, Warnberg L. 1996. Evidence that actin filaments are involved in controlling the permeability of plasmodesmata in tobacco mesophyll. *The Plant Journal* **10**: 157–164.

Ding B, Turgeon R, Parthasarathy MV. 1992b. Substructure of freeze-substituted plasmodesmata. *Protoplasma* **169**: 28–41.

Doxey AC, Yaish MW, Moffatt BA, Griffith M, McConkey BJ. 2007. Functional divergence in the *Arabidopsis* β-1,3-glucanase gene family inferred by phylogenetic reconstruction of expression states. *Molecular Biology and Evolution* **24**: 1045–1055.

Ehlers K, Kollmann R. 2001. Primary and secondary plasmodesmata: structure, origin, and functioning. *Protoplasma* **216**: 1–30.

Eklöf JM, Brumer H. 2010. The *XTH* gene family: an update on enzyme structure, function, and phylogeny in xyloglucan remodeling. *Plant Physiology* **153**: 456–466.

Faulkner C, Bayer EM. 2017. Isolation of plasmodesmata. *Methods in Molecular Biology* **1511**: 187–198.

Feiz L, Irshad M, Pont-Lezica RF, Canut H, Jamet E. 2006. Evaluation of cell wall preparations for proteomics: a new procedure for purifying cell walls from Arabidopsis hypocotyls. *Plant Methods* **2**: 10.

Fernandez-Calvino L, Faulkner C, Walshaw J, Saalbach G, Bayer E, Benitez-Alfonso Y, Maule A. 2011. Arabidopsis plasmodesmal proteome. *PLoS ONE* **6**: e18880.

Gaudioso-Pedraza R, Benitez-Alfonso Y. 2014. A phylogenetic approach to study the origin and evolution of plasmodesmata-localized glycosyl hydrolases family 17. *Frontiers in Plant Science* **5**: 212.

Gilbert M, Li Z, Wu XN, Rohr L, Gombos S, Harter K, Schulze WX. 2021. Comparison of path-based centrality measures in protein–protein interaction networks revealed proteins with phenotypic relevance during adaptation to changing nitrogen environments. *Journal of Proteomics* **235**: 104114.

Goodstein DM, Shu S, Howson R, Neupane R, Hayes RD, Fazo J, Mitros T, Dirks W, Hellsten U, Putnam N *et al.* 2012. PHYTOZOME: a comparative platform for green plant genomics. *Nucleic Acids Research* **40**: D1178–D1186.

Grigoriev IV, Hayes RD, Calhoun S, Kamel B, Wang A, Ahrendt S, Dusheyko S, Nikitin R, Mondo SJ, Salamov A *et al.* 2021. PHYCOCOSM, a comparative algal genomics resource. *Nucleic Acids Research* **49**: D1004–D1011.

Grison MS, Brocard L, Fouillen L, Nicolas W, Wewer V, Dormann P, Nacir H, Benitez-Alfonso Y, Claverol S, Germain V *et al.* 2015a. Specific membrane lipid composition is important for plasmodesmata function in Arabidopsis. *Plant Cell* **27**: 1228–1250.

Grison MS, Fernandez-Calvino L, Mongrand S, Bayer EM. 2015b. Isolation of plasmodesmata from Arabidopsis suspension culture cells. *Methods in Molecular Biology* **1217**: 83–93.

Grison MS, Kirk P, Brault M, Wu XN, Schulze WX, Benitez-Alfonso Y, Immel F, Bayer EMF. 2019. Plasma membrane-associated receptor like kinases relocalize to plasmodesmata in response to osmotic stress. *Plant Physiology* **181**: 142–160.

Guo X, Qin Q, Yan J, Niu Y, Huang B, Guan L, Li Y, Ren D, Li J, Hou S. 2015. TYPE-ONE PROTEIN PHOSPHATASE4 regulates pavement cell interdigitation by modulating PIN-FORMED1 polarity and trafficking in Arabidopsis. *Plant Physiology* **167**: 1058–1075.

He M, Li X, Mang M, Li Z, Ludewig U, Schulze WX. 2021. A systems-biology approach identifies co-expression modules in response to low phosphate supply in maize lines of different breeding history. *The Plant Journal* **109**: 1249–1270.

Hori K, Maruyama F, Fujisawa T, Togashi T, Yamamoto N, Seo M, Sato S, Yamada T, Mori H, Tajima N *et al.* 2014. *Klebsormidium flaccidum* genome reveals primary factors for plant terrestrial adaptation. *Nature Communications* **5**: 3978.

Howe KL, Contreras-Moreira B, De Silva N, Maslen G, Akanni W, Allen J, Alvarez-Jarreta J, Barba M, Bolser DM, Cambell L *et al.* 2020. Ensembl Genomes 2020-enabling non-vertebrate genomic research. *Nucleic Acids Research* **48**: D689–D695.

Hughes CS, Moggridge S, Muller T, Sorensen PH, Morin GB, Krijgsveld J. 2019. Single-pot, solid-phase-enhanced sample preparation for proteomics experiments. *Nature Protocols* **14**: 68–85.

Hunter S, Apweiler R, Attwood TK, Bairoch A, Bateman A, Binns D, Bork P, Das U, Daugherty L, Duquenne L *et al.* 2009. INTERPRO: the integrative protein signature database. *Nucleic Acids Research* **37**: D211–D215.

Jamet E, Canut H, Boudart G, Pont-Lezica RF. 2006. Cell wall proteins: a new insight through proteomics. *Trends in Plant Science* **11**: 33–39.

Johnston MG, Breakspear A, Samwald S, Zhang D, Papp D, Faulkner C, de Keijzer J. 2023. Comparative phyloproteomics identifies conserved plasmodesmal proteins. *Journal of Experimental Botany.* doi: 10.1093/jxb/erad022.

Kim I, Kobayashi K, Cho E, Zambryski PC. 2005. Subdomains for transport via plasmodesmata corresponding to the apical-basal axis are established during

Arabidopsis embryogenesis. *Proceedings of the National Academy of Sciences, USA* **102**: 11945–11950.

Kirk P, Amsbury S, German L, Gaudioso-Peraza R, Benitez-Alfonso Y. 2021. Comparative meta-proteomic analysis for the identification of novel plasmodesmata proteins and regulatory cues. *bioRxiv*. doi: 10.1101/2021.05.04.442592.

Kraner ME, Muller C, Sonnewald U. 2017. Comparative proteomic profiling of the choline transporter-like1 (CHER1) mutant provides insights into plasmodesmata composition of fully developed *Arabidopsis thaliana* leaves. *The Plant Journal* **92**: 696–709.

Leijon F, Melzer M, Zhou Q, Srivastava V, Bulone V. 2018. Proteomic analysis of plasmodesmata from *Populus* cell suspension cultures in relation with callose biosynthesis. *Frontiers in Plant Science* **9**: 1681.

Lemoine F, Correia D, Lefort V, Doppelt-Azeroual O, Mareuil F, Cohen-Boulakia S, Gascuel O. 2019. NGPhylogeny.fr: new generation phylogenetic services for non-specialists. *Nucleic Acids Research* **47**: W260–W265.

Letunic I, Bork P. 2019. Interactive Tree Of Life (iTol) v.4: recent updates and new developments. *Nucleic Acids Research* **47**: W256–W259.

Levy A, Erlanger M, Rosenthal M, Epel BL. 2007. A plasmodesmata-associated beta-1,3-glucanase in Arabidopsis. *The Plant Journal* **49**: 669–682.

Li S, Liu Z, Chen G, Qanmber G, Lu L, Zhang J, Ma S, Yang Z, Li F. 2021. Identification and analysis of GhEXO gene family indicated that GhEXO7_At promotes plant growth and development through brassinosteroid signaling in cotton (*Gossypium hirsutum* L.). *Frontiers in Plant Science* **12**: 719889.

Lisso J, Schröder F, Müssig C. 2013. EXO modifies sucrose and trehalose responses and connects the extracellular carbon status to growth. *Frontiers in Plant Science* **4**: 219.

Lucas WJ, Bouche P-S, Jackson DP, Nguyen L, Baker L, Ding B, Hake S. 1995. Selective trafficking of KNOTTED1 homeodomain protein and its mRNA through plasmodesmata. *Science* **270**: 1980–1983.

Lucas WJ, Ham BK, Kim JY. 2009. Plasmodesmata – bridging the gap between neighboring plant cells. *Trends in Cell Biology* **19**: 495–503.

von Mering C, Krause R, Snel B, Cornell M, Oliver SG, Fields S, Bork P. 2002. Comparative assessment of large-scale data sets of protein–protein interactions. *Nature* **417**: 339–403.

Mitra SK, Gantt JA, Ruby JF, Clouse SD, Goshe MB. 2007. Membrane proteomic analysis of *Arabidopsis thaliana* using alternative solubilization techniques. *Journal of Proteome Research* **6**: 1933–1950.

Nicolas WJ, Grison MS, Trepout S, Gaston A, Fouche M, Cordelieres FP, Oparka K, Tilsner J, Brocard L, Bayer EM. 2017. Architecture and permeability of post-cytokinesis plasmodesmata lacking cytoplasmic sleeves. *Nature Plants* **3**: 17082.

Park SH, Li F, Renaud J, Shen W, Li Y, Guo L, Cui H, Sumarah M, Wang A. 2017. NbEXPA1, an alpha-expansin, is plasmodesmata-specific and a novel host factor for potyviral infection. *The Plant Journal* **92**: 846–861.

Pertl H, Himly M, Gehwolf R, Kriechbaumer R, Strasser D, Michalke W, Richter K, Ferreira F, Obermeyer G. 2001. Molecular and physiological characterisation of a 14-3-3 protein from lily pollen grains regulating the activity of the plasma membrane H+ ATPase during pollen grain germination and tube growth. *Planta* **213**: 132–141.

Raven JA. 2007. *Evolution of plasmodesmata*. Hoboken, NJ, USA: John Wiley and Sons.

Rinne PL, Kaikuranta PM, van der Schoot C. 2001. The shoot apical meristem restores its symplasmic organization during chilling-induced release from dormancy. *The Plant Journal* **26**: 249–264.

Rinne PL, Welling A, Vahala J, Ripel L, Ruonala R, Kangasjarvi J, van der Schoot C. 2011. Chilling of dormant buds hyperinduces FLOWERING LOCUS T and recruits GA-inducible 1,3-beta-glucanases to reopen signal conduits and release dormancy in *Populus*. *Plant Cell* **23**: 130–146.

Ruonala R, Rinne PL, Kangasjarvi J, van der Schoot C. 2008. CENL1 expression in the rib meristem affects stem elongation and the transition to dormancy in *Populus*. *Plant Cell* **20**: 59–74.

Sano T, Kuraya Y, Amino S, Nagata T. 1999. Phosphate as a limiting factor for the cell division of tobacco BY-2 cells. *Plant & Cell Physiology* **40**: 1–8.

Schindelin J, Arganda-Carreras I, Frise E, Kaynig V, Longair M, Pietzsch T, Preibisch S, Rueden C, Saalfeld S, Schmid B *et al.* 2012. Fiji: an open-source platform for biological-image analysis. *Nature Methods* **9**: 676–682.

Schröder F, Lisso J, Lange P, Müssig C. 2009. The extracellular EXO protein mediates cell expansion in Arabidopsis leaves. *BMC Plant Biology* **9**: 20.

Schröder F, Lisso J, Müssig C. 2011. EXORDIUM-LIKE1 promotes growth during low carbon availability in Arabidopsis. *Plant Physiology* **156**: 1620–1630.

Shinohara N, Nishitani K. 2021. Cryogenian origin and subsequent diversification of the plant cell-wall enzyme XTH family. *Plant & Cell Physiology* **62**: 1874–1889.

Simpson C, Thomas C, Findlay K, Bayer E, Maule AJ. 2009. An Arabidopsis GPI-anchor plasmodesmal neck protein with callose binding activity and potential to regulate cell-to-cell trafficking. *Plant Cell* **21**: 581–594.

Song DK, Choi JH, Kim MS. 2018. Primary cilia as a signaling platform for control of energy metabolism. *Diabetes and Metabolism Journal* **42**: 117–127.

Tangle E. 1879. Über offene Communicationen zwischen den Zellen des Endosperms einiger Samen. *Jahrbücher für Wissenschaftliche Botanik* **12**: 170–190.

Tarancon C, Gonzalez-Grandio E, Oliveros JC, Nicolas M, Cubas P. 2017. A conserved carbon starvation response underlies bud dormancy in woody and herbaceous species. *Frontiers in Plant Science* **8**: 788.

Thimm O, Bläsing O, Gibon Y, Nagel A, Meyer S, Kruger P, Selbig J, Muller LA, Rhee SY, Stitt M. 2004. Mapman: a user-driven tool to display genomics data sets onto diagrams of metabolic pathways and other biological processes. *The Plant Journal* **37**: 914–939.

Thomas CL, Bayer E, Ritzenthaler C, Fernandez-Calvino L, Maule AJ. 2008. Specific targeting of a plasmodesmal protein affecting cell-to-cell communication. *PLoS Biology* **6**: e7.

Tyanova S, Temu T, Sinitcyn P, Carlson A, Hein MY, Geiger T, Mann M, Cox J. 2016. The Perseus computational platform for comprehensive analysis of (prote)omics data. *Nature Methods* **13**: 731–740.

Tylewicz S, Petterle A, Marttila S, Miskolczi P, Azeez A, Singh RK, Immanen J, Mahler N, Hvidsten TR, Eklund DM *et al.* 2018. Photoperiodic control of seasonal growth is mediated by ABA acting on cell-cell communication. *Science* **360**: 212–215.

Wang R, Xing X, Wang Y, Tran A, Crawford NM. 2009. A genetic screen for nitrate regulatory mutants captures the nitrate transporter gene NRT1.1. *Plant Physiology* **151**: 472–478.

Wolf S, Deom CM, Beachy RN, Lucas WJ. 1989. Movement protein of tobacco mosaic virus modifies plasmodesmatal size exclusion limit. *Science* **246**: 377–379.

Yan D, Yadav SR, Paterlini A, Nicolas WJ, Petit JD, Brocard L, Belevich I, Grison MS, Vaten A, Karami L *et al.* 2019. Sphingolipid biosynthesis modulates plasmodesmal ultrastructure and phloem unloading. *Nature Plants* **5**: 604–615.

Zavaliev R, Levy A, Gera A, Epel BL. 2013. Subcellular dynamics and role of Arabidopsis β-1,3-glucanases in cell-to-cell movement of tobamoviruses. *Molecular Plant–Microbe Interactions* **26**: 1016–1030.

Zavaliev R, Ueki S, Epel BL, Citovsky V. 2011. Biology of callose (beta-1,3-glucan) turnover at plasmodesmata. *Protoplasma* **248**: 117–130.

Zhu T, Lucas WJ. 1998. Directional cell-to-cell communication in the Arabidopsis root apical meristem. I. An ultrastructural and functional analysis. *Protoplasma* **203**: 35–47.

Supporting Information

Additional Supporting Information may be found online in the Supporting Information section at the end of the article.

Fig. S1 Enrichment protocol of plasmodesmata from *Physcomitrium patens*.

Fig. S2 Details on the plasmodesmata score.

Fig. S3 Structure of the core PDDB database.

Fig. S4 Subcellular localization of control proteins from *Physcomitrium patens* plasmodesmata proteome in *Nicotiana benthamiana* leaf epidermis cells.

Fig. S5 Refinement of the *Physcomitrium* plasmodesmata proteome.

Fig. S6 Plasmodesmata localization of glycosyl hydrolase family 17 (GHL17) proteins correlates with phylogenetic distribution.

Fig. S7 Plasmodesmata-localized *Physcomitrium patens* XTHs grouped in cluster I.

Methods S1 Additional details of experimental procedures.

Table S1 Published plasmodesmata data sets.

Table S2 Plasmodesmata (PD) proteome list with PD scores.

Table S3 Plasmodesmata index validation scale.

Table S4 Verified proteins.

Table S5 List of protein family members GHLs, XTHs, and EXOs.

Please note: Wiley is not responsible for the content or functionality of any Supporting Information supplied by the authors. Any queries (other than missing material) should be directed to the *New Phytologist* Central Office.

5.2. Summary

Research question:

- What are the key components of PD?

Objective

Identification of new PD components by validating subcellular localizations of candidates found in a *Physcomitrium* PD proteome.

Hypothesis

Large-scale identification of novel PD components will grant novel insights into PD composition, transport mechanism, and evolution.

5.2.1. Result

The approach allowed the identification of novel PD proteins. Especially, cell wall residual protein families, like the callose-degrading GHL17s, XTHs, and EXO-like proteins, could be robustly separated in PD- and non-PD localized phylogenetic clades.

Chapter IV

6. The role of phase separation for transport through the nuclear pore complex

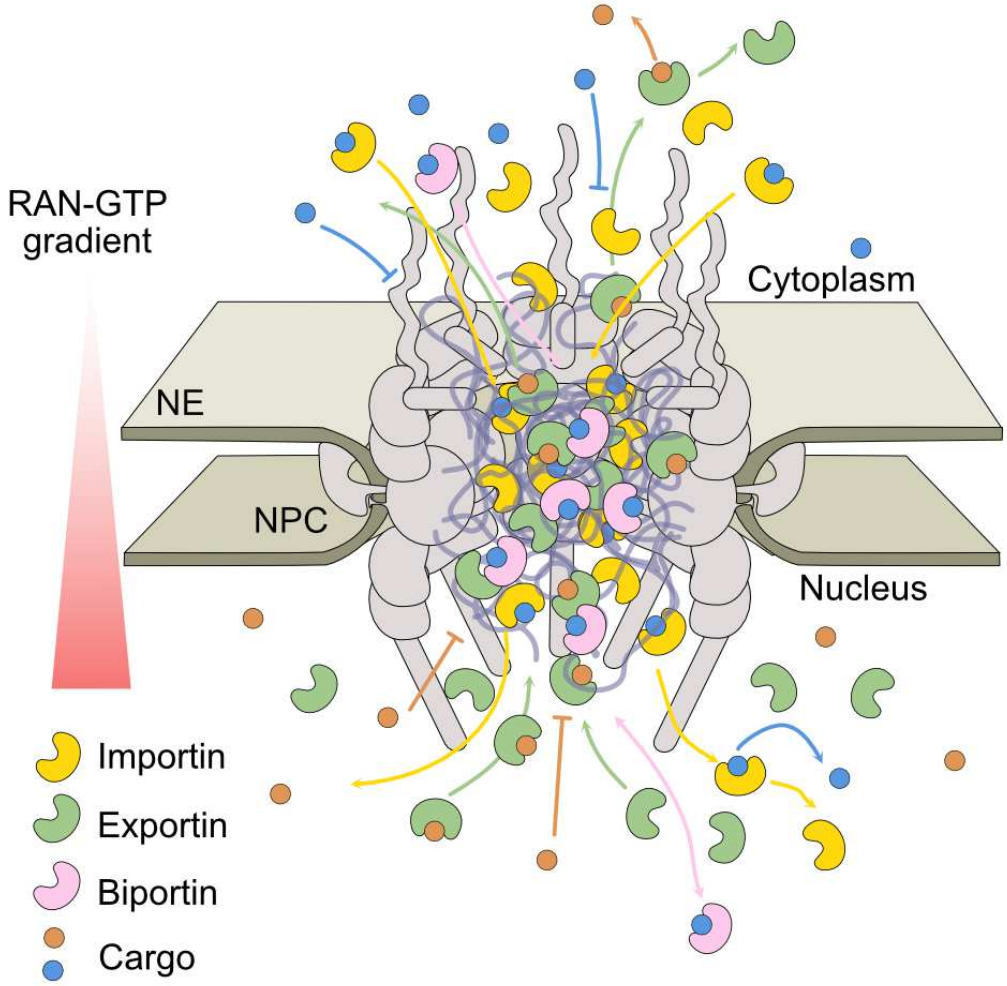

Status: In preparation (invited Review)
Journal: Journal of Experimental Botany
Impact factor: 6.9 (2022)
Contribution: 95% (specified in Appendix)
*Note as the manuscript is unpublished it is inserted into the thesis as Word file to enable cross-referencing with other Chapters. Hence, the references of this Chapter are included at the end of the thesis.

6.1. Aim of this chapter

6.1.1. Objective

Review the well-characterized nano-sized NPC and the role of phase separation in its transport mechanism.

The role of phase separation for macromolecular transport through the nuclear pore complex

Jona Obinna Ejike[1,2,*], Moritz Schladt[1,2,*], Wolf B. Frommer[1,2,3,*]

[1] Heinrich Heine University Düsseldorf, Faculty of Mathematics and Natural Sciences, Institute for Molecular Physiology, Düsseldorf, Germany
[2] Cluster of Excellence on Plant Sciences, Heinrich Heine University Düsseldorf, Germany
[3] Institute for Transformative Biomolecules (WPI-ITbM), Nagoya University, Nagoya, Japan

* corresponding author

Key words: Nuclear pore complex, Nuclear transport, nucleocytoplasmic transport, Nucleoporins, Karyopherins

Abstract
Eukaryotes developed a separate compartment for transcription, the nucleus (karyon) that gave them their name. The nucleus is protected by a double membrane that contains nanometer-sized nuclear pores that enable the exchange of solutes between cyto- and nucleoplasm, in particular, they enable the exchange of RNAs and proteins. Composition and structure of the nuclear pore have been resolved to the atomic level. The core of the transport mechanism is based on phase separation produced by a set of FG-(phenylalanine-glycine) repeat nucleoporins, the FG-NUPs. Nuclear transport receptors (NTRs) facilitate cargo transport throughout the FG-phase. Currently, several distinct models aim to describe the physical state of the FG-NUPs phase separation domain. We here provide an overview of the composition, structure, and transport mechanism of nuclear pore complexes. Further, we review recent research on the yet structurally unresolved plant NPC.

6.2. Nuclear Pore Complex

A key characteristic of the Eukarya is the development of the nucleus, in which the ER-derived nuclear envelope (NE) constitutes a compartment for eukaryotic cellular DNA. While the NE allows spatial separation of gene expression and protein biosynthesis, it also necessitates a mechanism for nucleocytoplasmic exchange [121]. The Nuclear Pore Complex (NPC) is an octagonally symmetric protein complex that traverses the NE and thereby forms a passageway for bi-directional transport between cytoplasm and nucleus. NPCs have a diameter of ~100 nm and a mass of 50–110 MDa (dependent on species) and comprise ~1000 proteins termed Nucleoporins (NUPs). The NPC´s core scaffold is anchored by one inner ring that is sandwiched between two outer rings facing cytoplasm and nucleoplasm. The luminal ring surrounds the core scaffold in the NE lumen. The rings of the core scaffold are rotationally symmetric in a co-planar axis to the NE. In the nucleocytoplasmic axis, the core scaffold comprises 8 symmetric spokes stabilized by a linker scaffold. The core scaffold anchors the central channel's phenylalanine-glycine repeat-rich (FG-)NUPs, which constitute the NPC's phase-separating permeability barrier. In addition to the central channel, 8 lateral channels traverse between the core scaffold's spokes [122–127]. Attached to the core scaffold, cytoplasmic filaments and a nuclear basket form extensions that assist cargo transport but also expand the NPC's roles. The cytoplasmic filaments are mainly involved in mRNA export directionality by irreversibly remodeling messenger ribonucleoprotein (mRNP)-complexes [128]. The nuclear basket connects the NPC to the nuclear periphery. It tethers the NPC to the nuclear lamina (in plants nucleoskeleton), a polymeric meshwork under the inner leaflet of the NE, and spatially organizes the transcription export (TREX) complex as well as transcriptionally active euchromatin [129]. The "gene-gating" hypothesis proposes that transcriptionally active genes tethered to the NPC can be efficiently transcribed, and the transcripts rapidly exported [130]. While it was demonstrated that the NPC is involved in transcription activation, it also can repress transcription in a target-specific manner. More specifically, NPC-mediated gene regulation shows high heterogeneity in different subdomains, even in single nuclei [131].

NPC structure differs between taxa but can even be variable in single nuclei. Three NPC subtypes coexist in yeast cells, the majority of NPCs have a single nuclear and cytoplasmic ring, while other NPCs contain double nuclear rings with/ or without nuclear basket [132]. Moreover, NPC structure confers plasticity. Cryo-electron tomography (ET) of focused ion beam (FIB)-generated lamellae of human and yeast cell revealed a larger inner ring and central and lateral channels compared to NPC structures from purified NEs. This demonstrated that NPC architecture and dimensions are shaped by the cellular environment [132,133]. While the luminal ring was suggested to limit the extent of pore extension [132], the relaxed connections between the spokes of the core scaffold grant plasticity that enables reversible constriction and dilation of the inner ring in response to differential NE tensions [134,135].

Conclusively, the NPC presents a multifaceted flexible platform that is assembled into ring modules and can occur in different variations. Furthermore, NPCs regulate nucleocytoplasmic transport and organize transcriptional and translational processes.

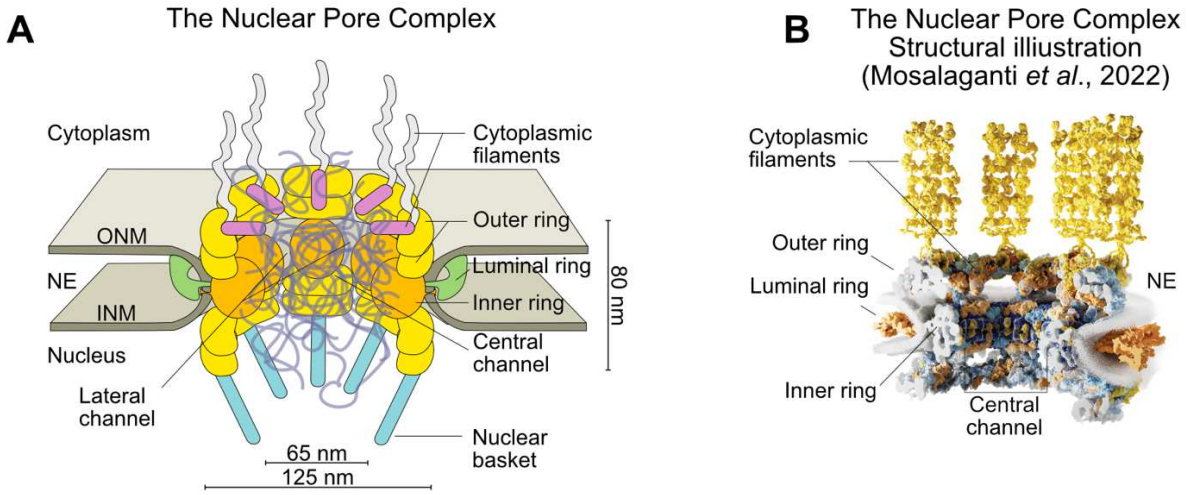

Figure 4: The human nuclear pore complex (NPC)
A Illustration of the radially symmetric human NPC, connecting cytoplasm and nucleoplasm. The different ring subunits of the NPC are depicted by 5 of its 8 symmetric spokes. In between the spoke units, the NPC's lateral channels are depicted. The luminal ring and inner ring anchor the NPC in the nuclear envelope (NE). The outer double rings attach at the outer- and inner nuclear membrane (ONM, INM), respectively. The cytoplasmic filaments and nuclear basket form the NPC's peripheral extensions. The central channel is filled by intrinsically disordered phenylalanine-glycine-rich nucleoporins (FG-NUPs), which are depicted as "spaghetti-like" domains (translucent purple). Notably, the central channel is not structurally resolved, and the *in vivo* conformational state of the FG-NUPs remains speculative. Their "spaghetti-like" depiction here only serves as an illustration. Also, the cytoplasmic filaments and nuclear basket contain intrinsically disordered FG-domains, too, which are not depicted for simplification. All depicted dimensions are based on the human NPC (central channel: 65 nm, core scaffold diameter: 125 nm, core scaffold nucleocytoplasmic axis: 80 nm) [124]. **B** Structural illustration based on near atomic-resolution models of human NPC (modified from Mosalaganti *et al.*, 2022 [136]). The illustration demonstrates the stark contrast between the well-resolved core scaffold and cytoplasmic filaments and the structural elusiveness of the central channel. The nuclear basket is not depicted here, as it was not resolved at the time point of the study.

6.3. Structural complexes of the NPC

NPCs contain ~30 distinct NUPs, which assemble several subcomplexes and constitute the rings and extensions of the NPC. The most extensively studied subcomplex is the Y-complex, named after its conformational "Y-shape". By binding head-to-tail 8 Y-complexes form a ring assembly. Two stacked Y-complex rings constitute the outer rings of the vertebrate NPC (cytoplasmic and nuclear). The Y-complex comprises seven conserved members, which are NUP85, NUP96, NUP107, NUP133, NUP160, SEC13, and SEH1. In vertebrates NUP37, NUP43, and ELYS (specific to nuclear ring) are additional NUPs of the Y-complex [123,125].
Compared to the outer rings, interactions in the inner ring's spokes are more loosely and mediated by short linear motifs (SLMs) of the linkers NUP35 (also referred to as NUP53), NUP93, and FG-NUP98. SLMs are often positioned inside intrinsically disordered regions (flexible linkers) and hence allow compositional flexibility as well as robustness against mechanical stress, which allows the establishment of lateral channels between the inner ring's spokes [123,135]. The inner ring can be divided into three layers: the outer, middle, and inner layers. In the outer layer, the transmembrane NUP NDC1 anchors the inner ring in the NE and heterodimerizes with ALADIN, which in turn is linked to the membrane-sensing NUP155 via the linkers FG-NUP98 and NUP35. NUP35 can stabilize spoke interconnections by dimerization. The N-terminus of NUP35 reaches into the inner ring's middle layer through interaction with the structured domains of NUP93 and NUP205. The N-terminal linker region of NUP93 interacts with NUP205 and NUP188, of which two symmetrically arranged copies form the inner ring spokes midplane. NUP93 further anchors the structured domains of the FG-

NUP62-complex composed of FG-NUP54, FG-NUP58, and FG-NUP62, which are considered as the inner layer of the inner ring. The FG-domains of FG-NUP98 and the FG-NUP62 complex occupy the central channel and form the NPC´s permeability barrier [124–126,136,137]. In human NPCs NUP155 copies bridge inner and outer ring [137], while NUP93 links NUP205 associated with adjacent Y-complexes, forming a *trans*-spoke staple. These features are missing in yeast and algal NPCs [124,135,136]. In human NPCs, 8 copies of the single pass-TM GLYCOPROTEIN 210 (GP210) (or NUP210) per spoke (yeast: two copies/ spoke) anchor in the NE. Each GP210 copy projects 15 immunoglobulin (IG)-like domains into the NE lumen. The IG-like domains in each spoke form a butterfly-shaped arrangement that constitutes the luminal ring [124,136,138].

The NUP214-complex forms the cytoplasmic filaments, which reach over the central channel at the cytoplasmic face of the NPC, where they contribute to the FG-meshwork and regulate mRNA export. It comprises FG-NUP62, NUP88, FG-NUP214, FG-NUP98, RAE1, and the ATP-dependent DEAD-box RNA helicase DDX19. Additionally, the GLE1-FG-NUP42 complex primes DDX19 for mRNP-remodeling, which ensures that mRNAs are only released from their mRNP complexes after NPC passage. Metazoan-specific NUP358 pentamers link the proximal and distal cytoplasmic rings (Y-complexes) via their N-termini, while their intrinsically disordered C-termini carry FG-repeats and form long extensions (up to ~60 nm) that present binding sites for the small GTPase RAN and the RAN-GTPase activating protein (RANGAP) [124,128]. The nuclear basket attaches to the nuclear ring and comprises ELYS, FG-NUP153, FG-NUP50, and TPR (also FG-NUP), which facilitate mRNP export by interacting with the TREX complex [124]. Attachment of the nuclear basket requires two nuclear rings, as TPR specifically connects to the distal Y-complex of the outer nuclear ring. TPRs coiled-coiled domains form the basket's struts, while the unstructured N- and C-termini likely dock mRNPs for nuclear export. Further, the nuclear basket is surrounded by a 20 nm exclusion zone, which is proposed to be involved in chromatin organization [139]. Interestingly, the directionality of nuclear and cytoplasmic ring assembly is defined by the RAN-GTP gradient, which previously was mainly studied regarding its effect on the directionality of nucleocytoplasmic transport [140]. While the scaffold, transmembrane rings, and peripheral extensions of the NPC, as well as several NTR-cargo complexes, were resolved in near-atomic resolution, the central channel, which mediates nucleocytoplasmic transport, remains elusive due to the highly flexible nature of the intrinsically disordered FG-domains.

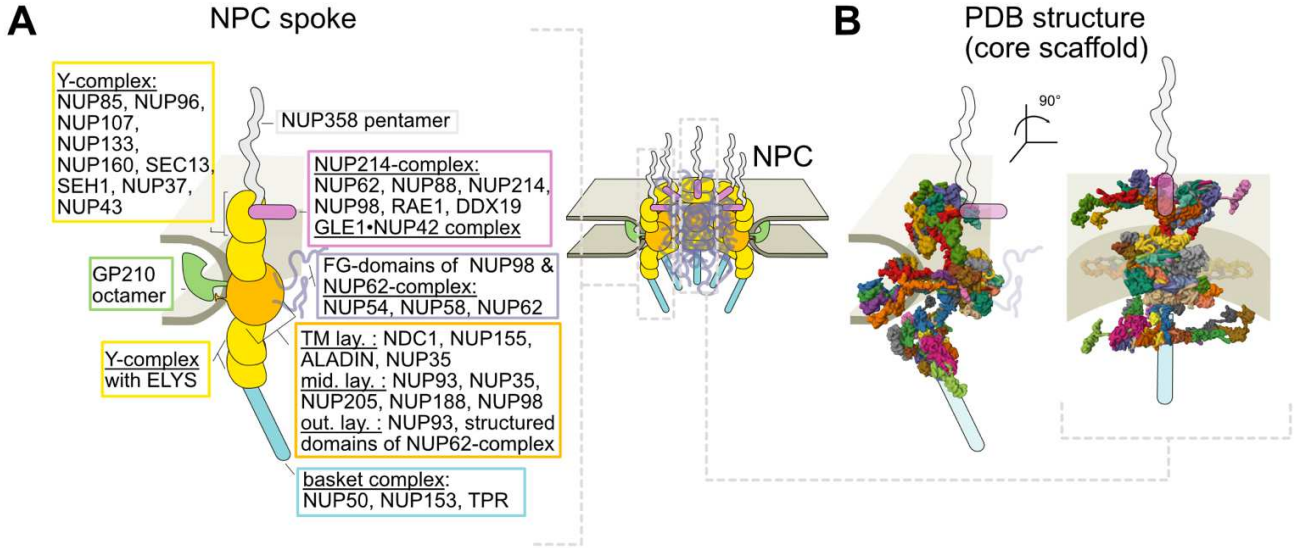

Figure 5: Structural complexes of the NPC

A Illustration of the different subcomplexes that comprise one NPC spoke. The luminal ring formed by GP210 octamers (green), anchors in the NE. On the other side of the NE the three-layered inner ring (IR) (orange). The

IR contains a transmembrane layer (TM), which anchors the IR in the NE via the TM-domains of NDC1 and additional membrane-binding NUPs like NUP155 and NUP35. The IR's middle layer is composed of scaffold NUPs and linked by linker NUP93 and NUP98 to the IR's outer layer composed of the structural domains of the FG-NUP62 complex. The FG-domains of the NUP62 complex and NUP98 fill the central channel (translucent purple). Each outer ring module is composed of a Y-complex (yellow). NUP358 pentamers comprise the long cytoplasmic extensions (grey) and the NUP214- and GLE1-NUP42-complex the mRNA processing machinery of the cytoplasmic filaments. The basket-complex comprises NUP50, Nup153, and TPR. **B** Structure of a NPC-core scaffold spoke. The structure was downloaded from RCSB PDB (7TBJ) and was deposited by Petrovic *et al.*, 2022 [135].

6.4. The central channel's FG-based permeability barrier

The central channel is enriched in FG-NUPs. FG-NUPs contain structured domains, which anchor them at the core scaffold, and intrinsically disordered FG-repeat-rich domains that reach into the central channel. FG-domains harbor a characteristic "stickers" and "spacers" architecture, in which numerous FG-motifs hydrophobically interact with each other as highly dynamic "stickers", while the inter-FG "spacers" mediate the contact of the "stickers". The "stickers" and "spacers" architecture allows the formation of a phase-separating FG-meshwork that functions as nucleocytoplasmic permeability barrier (or "smart sieve") [141–143]. Besides hydrophobic FG-FG interactions, interactions between the aromatic groups of the F residues, like π-π or T-stacking, were proposed to contribute to the FG-mediated phase separation [144]. Traditionally, it was described that cargo species smaller than 5 nm (40 kDa) can pass the mesh of FG-repeats passively (similar to a sieve), while larger cargo is transported in a facilitated fashion. Later, it was demonstrated that specific surface features can render molecules below the size limit inert: negative charges or lysines impede NPC passage, even of GFP monomers (sinGFP4a, 27 kDa), while hydrophobic surface properties as well as exposed arginines, histidines and cysteines accelerate passage, even for cargo larger than the proposed size-limit for passive diffusion (GFP^{NTR}_3B7C, homotetramer 108 kDa). Conclusively, nuclear transport happens in a continuum from passive to facilitated passage, dependent on the cargo´s surface properties [145]. Nuclear transport receptors (NTRs, also termed karyopherins) share passage-promoting surface features and can recognize their cargo by binding nuclear localization-/ nuclear export signals (NLS, NES) or cargo-specific domains to mediate nucleocytoplasmic transport in a RAS RELATED NUCLEAR PROTEIN (RAN)-GTP dependent manner [146]. NTRs contain hydrophobic binding pockets on their surface, which enable hydrophobic interaction with FG-motifs. Electrostatic interactions, cation-π and π −π stacking were also demonstrated to contribute to NTR-FG interactions [147]. The NTR-FG interactions are weak, reversible, ultrafast, and multivalent, and allow the NTR to pass throughout the FG-mesh. Further, not only the FG repeats but also the inter-FG-spacers, between each repeat, can interact with NTRs and hence affect passage rates [142,148]. Besides the surface properties of the cargo, the kinetics of NPC passage are also affected by the cohesiveness of the FG-mesh. FG-repeats can differ in their residues (e.g., GLFG, FSFG, FxFG, also referred to as flavors), which affect the cohesiveness of their interactions. FG-mesh cohesiveness is also dependent on the spacer length between each FG-repeat [148].

Many models describe the *in situ* conformational state of the FG-NUPs inside the NPC. Frey *et al.* demonstrated that *in vitro* purified FG-domains form biomolecular condensates termed hydrogels, which maintain NPC transport properties (e.g., NTR-mediated passage and exclusion of non-cargos) [149].

Based on the hydrogels, their "selective phase model" postulates that the NPC's permeability barrier is a three-dimensional FG-meshwork reversibly crosslinked by cohesive FG-FG interactions [117]. Hydrogel formation in *in vitro* purified FG-domains is time dependent and could be a consequence of aging. Hence, experiments in a microfluidic device that enabled rapid FG-phase separation could show that FG-phases also maintain nucleocytoplasmic

transport properties in a liquid-liquid phase separated (LLPS) state [150]. Strictly speaking, FG-NUPs in the NPC cannot be considered as liquids since they are tethered to the core scaffold. The "polymer brush"(or "virtual gating") model describes FG-domains, as non-interacting bristles of a brush, which dynamically move, maximally extend, and exclude non-cargo by 'entropic expulsion' [151]. To approximate the conformational state of NPC-localized FG-NUPs in live and permeabilized cells, small-molecule labeling and FLIM-FRET were used to quantify intramolecular distances in human FG-NUP98 inside NPCs. Mapping the molecular environment inside the NPC, the authors found that the NPC provides a "good solvent" environment, in line with the Flory-Huggins solution theory. In the NPC's "good solvent" environment, the conformation of the FG-domains is extended compared to their conformation in a simple aqueous solvent, but not as extensively extended as in polymer brushes. Hence, these results are not in line with the polymer brush model [152]. It remains to be elucidated if other FG-NUPs share these conformational properties. As it was deemed unlikely that all FG-NUPs co-phase due to their different anchor points and thereby orientations in the central channel and distinct cohesiveness [148]. Notably, it was discussed that liquid, gel, solid, and expanded conformations, as in polymer brushes, exist as close neighbors in a phase diagram of heteropolymers. Hence, in the central channel, more than one phase state could coexist [150]
While several previous models focused solely on the composition of the dynamic FG-mesh [117,151], recent findings highlight that *in vivo* NPCs are crowded by a constant flux of NTRs, which account for over three-quarters of the central channel´s density. This led to "NTR-centric" (or "KAP-centric") models, which postulate that NTR presence is an essential component of the NPC's selectivity barrier [151,153].

6.5. NTR-mediated NPC passage

Most NTRs belong to the karyopherin-β (KAP) family proteins, which can facilitate nuclear import (importins), export (exportins), and bi-directional transport (biportins).
KAPs are composed of 19-24 HEAT repeats, which result in convex and concave surfaces that constitute interaction interfaces for FG-NUPs, RAN-GTP, and cargo proteins. An extensively studied KAP is importin-β (IMPβ). IMPβ requires binding to an adaptor protein importin-α (IMPα) that enables binding to the classical NLS (cNLS) of the cargo protein. IMPα is a tandem armadillo (ARM)-repeat protein that increases its affinity to cNLS 100-fold upon IMPβ binding. Consequently, IMPβ facilitates nucleocytoplasmic import of the trimeric IMPβ/α/cNLS-cargo complex. While higher eukaryotes only possess one copy of IMPβ, they possess at least 7 isoforms of IMPα, which have different *in vivo* substrate specificities and thereby allow fine-tuned regulation of nuclear import. The IMPβ/α mediated nuclear import pathway is also referred to as "classical", nonetheless, other KAPs can bind their designated domain or NLS/NES directly [146,154]. The directionality of NTR transport is dependent on a RAN-GTP gradient. Nucleoplasmic RAN is predominantly bound by GTP due to its chromatin-anchored guanine nucleotide exchange factor (RCC1), which catalyzes the conversion of RAN-GDP + P_i to RAN-GTP. Depending on the NTR type, nucleoplasmic RAN-GTP can either compete, allosterically hinder, or facilitate cargo binding, which leads to cargo unloading from importins, or, in the case of exportins, facilitation of cargo binding on the nucleoplasmic side. Further, post-translational modifications can affect the binding affinities of NTRs and their cargoes [146]. NTR-bound RAN-GTP is released in the cytosol and hydrolyzed by the cytosolic RAN GTPase ACTIVATING PROTEIN (RANGAP) and RAN-BINDING PROTEIN (RANBP), to RAN-GDP + P_i [146]. Finally, inactive RAN-GDP is imported back into the nucleus by NUCLEAR TRANSPORT FACTOR (NTF)2, a small NTR that contains no HEAT-repeats and is not part of the KAP family [155,156].
The transport pathway of NTRs throughout the central channel was a topic of extensive study. Pioneering electron microscopy and cryo-electron tomography studies captured snapshots of

NTRs in transit throughout the NPC. Surprisingly, NTRs were depleted from the central region of the central channel that was postulated to be the main cargo passageway [157,158]. Later, high-speed super-resolution microscopy allowed tracking of real-time NTR passage and confirmed that NTR-facilitated cargo is transported at the periphery of the central channel [159–162]. NTR-cargo complexes pass the NPC in an hourglass-shaped transport pathway (Figure 7C) along the inner surface of the core scaffold [162], reminiscent of the "central transporter" that occupies the central channel in yeast NPCs structures from isolated NEs [132]. This transport pathway also applies to pre 60S ribosomal particles (up to 3 MDa, 25 nm), which belong to largest NPC-transported particles [163]. Interestingly, the NPCs lateral channels were shown to be the main passageway for inner nuclear membrane (INM) proteins, which laterally diffuse from the outer to the inner NE leaflet [164]. While small passively diffusing molecules (e.g., dextrans or GFP) pass throughout the center of the central channel [160,161]. These transport pathways align with the mapping of NTR-FG and FG-FG interactions that also predominantly occur along the core scaffold and are depleted in the central axis of the FG-barrier. Moreover, distinct NTRs possess distinct interaction zones in the FG-barrier, which results in 'personalized' transport pathways. As NTR transport pathways can change due to self- or inter-NTR competition, NTRs were postulated to enable a change in the FG-meshwork's tomography, possibly by competing with FG-FG interactions [161]. A novel yeast NPC one-bead-per-amino-acid (1BPA) coarse-grained molecular dynamics (CGMD) model permits simulation of the FG-meshwork's tomography during nuclear transport at amino acid resolution. Every amino acid of each yeast FG-NUP are represented by a single interacting bead that carries the residue-specific charge, hydrophobicity, and hydrodynamic radius. Further, the 1BPA CGMD model incorporates backbone stiffness as well as inter-residue cation-π interactions [143,165]. Molecular dynamics simulations revealed that GLFG-repeats (abundant in NUP98) form a high-density concentric ring at the core scaffold, in line with super-resolution studies. The high-density GLFG-ring is extensively cross-linked (40% of the FG-repeats) and has strikingly similar features to a phase condensate but remains dynamic, in line with the "spacers" and "stickers" architecture. While, the open space of the GLFG-ring is filled with a low-density percolated network of Nsp1 (homolog of human NUP62), which is the most abundant FG-NUP in yeast. Nsp1 forms an energetic barrier for passive diffusive transport, which is further increased by the addition of KAP95 (homolog of human IMPβ [165]. KAP95 does not compete with FG-FG interactions but rather binds unoccupied FG-repeats and moves in multiple steps throughout the FG-meshwork. FG interaction leads to retention while unbound KAP95 moves in transient FG-depleted "voids". This leads to "slow" GLFG-bound KAP95 that facilitates transport of "fast" KAP95 by shielding from the "sticky" GLFG-ring. Accumulation of "slow" KAP95 in the GLFG-ring additionally limits leakage of unspecific non-cargo along the core scaffold. Notably, the "slow" and "fast" modes are interchangeable, dependent on the FG binding and unbinding, which is in line with the "dirty velcro" effect. These results provide a molecular framework for "KAP-centric" models [153,165,166]. Intriguingly, in line with the results of the simulation of the FG-meshwork´s tomography, it was also experimentally demonstrated that NTR enrichment can increase the facilitated influx of cargos [167] while simultaneously fortifying the nucleocytoplasmic selectivity barrier against unspecific leakage [168]. Recently, mapping of the *in vivo* spatial distribution of all 11 human FG-NUPs revealed that the FG-domains of most core scaffold anchored FG-NUPs (NUP54, NUP58, NUP62, and POM121) are less extended in the central channel, except for FG-NUP98 which exhibited significant extensions throughout the NPCs core [169], which is in line with intramolecular FLIM-FRET experiments of NUP98 [152]. Together, the 5 FG-NUPs anchored in the core scaffold constitute a donut-shaped transport channel that harbors an FG-depleted central axis with a diameter of approximately 7 nm. The 6 peripheral FG-NUPs (Nup358, hCG1, Nup214, Nup153, Nup50, and TPR) show increased flexibility extending to the cytoplasmic and nucleoplasmic regions. Surprisingly, NUP214 and

NUP153 were observed to form cap-like structures on the cytoplasmic and nucleoplasmic sides, respectively, which could exist in open and closed states. Interestingly, the positions of the cap-like structures overlapped with transport pathways of facilitated cargo and posed obstruction sites for large passive diffusive molecules (>60 kDa) [169].
The yeast FG-NUP amino acid resolution model and the human *in vivo* NTR and FG-NUP mapping both predict NTR-FG interactions to accumulate at the central channels periphery along the core scaffold. It remains to be elucidated if NTRs move along the core scaffold, or rather follow a "dirty velcro" mechanism, where "slow" NTRs are retained in the GLFG-ring at the core scaffold to facilitate rapid transport of "fast" NTRs. The retention in the peripheral GLFG-phase of "slow" NTR fractions may lead to higher photon counts in super-resolution microscopy, while the passage rate of "fast" NTRs is not sufficiently enough resolved to pin down the passageway (0.4 ms timeframe for SPEED microscopy vs. single KAP95 transport throughout central channel in <10 µs in yeast NPC model). Yet another enigma is the FG-void central axis that is reported in super-resolution studies, while the amino acid-resolution model predicts that a low-density percolated network of Nsp1 occupies this region. It remains to be shown if these differences are species-specific (human vs. yeast) or derive from the limitations of the used approaches.

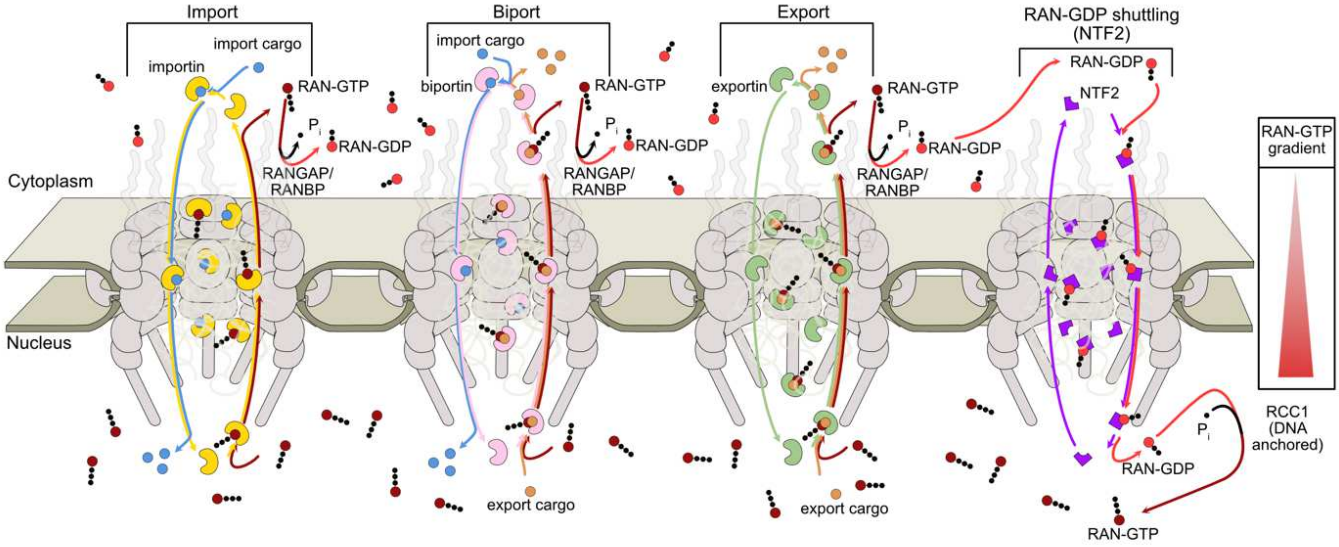

Figure 6: RAN-GTP directed nuclear transport receptor (NTR) transport
Most NTRs belong to the karyopherin-β (KAP) family, which comprises importins (yellow), biportins (pink), exportins (green). KAPs transport cargo along a RAN-GTP gradient (high in the nucleus, low in the cytoplasm). Importins unbind their cargo in RAN-GTP-dependently. Hence, they release cargo in the nucleus. Exportins bind cargo in a RAN-GTP-dependent manner and unbind it in the cytosol. Biportins can facilitate both import and export. The high nuclear RAN-GTP levels are maintained by the chromatin-anchored RAN nucleotide exchange factor (RCC1), which catalyzes the conversion of RAN-GDP to RAN-GTP, as well as the small NTR, NTF2, which shuttles RAN-GDP back into the nucleus.

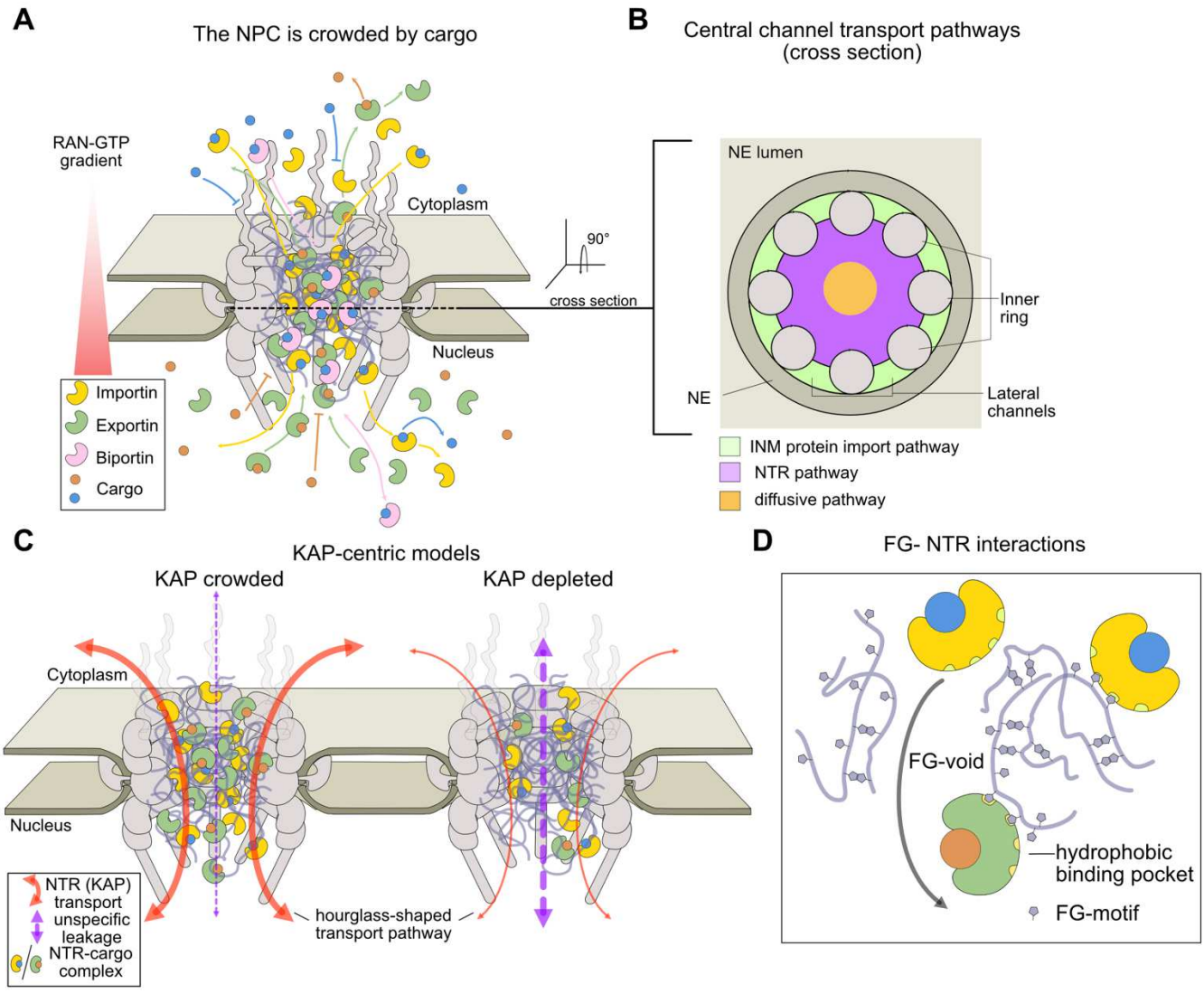

Figure 7: NTR pathways and KAP-centric models
A Illustration of the NTR and cargo crowded NPC. **B** Illustration of NPC cross section at the height of the central channel. Radially symmetric inner rings are depicted in grey. Between the inner ring, the lateral channels form the import pathway for inner nuclear membrane (INM) proteins (green). NTRs are most abundant in the central channel close to the core scaffold, indicated by the NTR pathway (purple). While diffusive transport occurs throughout the center of the pore (orange). **C** Mechanistic framework for KAP-centric models. NTR/KAP crowded NPCs show increased NTR flux (red) and decreased unspecific leakage (purple). While KAP reduction reduces NTR flux and increases unspecific leakage. NTR-fluxes are indicated in the hourglass-shape (red) along the core scaffold as indicated by super-resolution microscopy [162]. **D** Illustration of FG-NTR interaction as indicated by computational amino-acid resolution models of the NPC [165]. FG-mesh is crosslinked by FG-FG interactions. While NTRs bind free FG-motifs via their hydrophobic binding pockets, which causes retention. NTR movement occurs through FG voids. In NTR crowded conditions, less free FG-motifs are available, which shields mobile NTRs from forming decelerating FG-NTR interactions.

6.6. NPC assembly in higher eukaryotes

There are two distinct pathways of NPC formation in eukaryotes that perform open mitosis (which includes animals and plants [170]). NPCs can either be inserted postmitotically or during nuclear expansion in the interphase. Both pathways are different in order and kinetics. The postmitotic assembly is faster and occurs in a time frame of minutes, while interphase assembly requires about one hour in mammalian cells [171]. In mitosis, the NE is formed from highly fenestrated ER sheets, which contain progressively shrinking holes. Electron tomography revealed that postmitotic NPC assembly is initiated by the insertion of small prepores into NE

holes half the diameter of an NPC. The prepores contain nuclear rings and dense material of unknown molecular identity filling up the membrane hole. Upon recruitment of inner and cytoplasmic rings, the small membrane openings radially dilate [172]. Those relatively recent studies fit well with the molecular mechanism that was elucidated in isolated nuclei. At the onset of mitosis, several NUPs (starting with the SLM of NUP98 [123]), lamins, and INM proteins are phosphorylated via mitotic kinases, which triggers nuclear lamina and NPC disassembly, as well as the release of chromatin from the INM. At the exit of mitosis, the phosphorylation is removed via deactivation of mitotic kinases and the activation of phosphatases, which allows INM chromatin binding as well as reassembly of NPCs and nuclear lamina. KAPs can shield key mitotic protein complexes by interacting with them in the cytosol and target them towards chromatin in a RAN-GTP-dependent manner [173]. One of the targeted proteins is the nuclear ring NUP ELYS, which is described as an 'early assembler'. ELYS interacts with mitotic chromatin in mid-anaphase and recruits the nuclear and cytoplasmic ring components NUP107-160 complex (also Y-complex), which in turn allows the recruitment of the transmembrane NUPs NDC1 and POM121 and the membrane-associated NUP35. NUP35 recruits the inner ring NUP155, which induces the recruitment of further inner ring components and then of the central channel FG-NUP62 complex, resulting in a transport-capable pore. Lastly, in the late telophase, the nuclear basket NUP TPR and the cytoplasmic filament NUP214 are recruited [171,173]. Summarized, in postmitotic assembly, the Y-complex and central ring are rapidly assembled, which are lastly followed by cytoplasmic filaments and nuclear basket. This mechanism was later confirmed *in vivo* by a recent study that employed super-resolution imaging in combination with CRISPR-mediated fluorescent protein knock-in, to study NPC assembly at near-native protein levels. Conversely, this study also found that different to postmitotic assembly, in interphase assembly, the Y-complex is first combined with the nuclear basket NUP TPR and the base of the cytoplasmic filament NUP214, while the central ring complex is assembled later [171], highlighting the second pathway that is utilized in interphase NPC assembly. Interphase NPC assembly requires NPC insertion into the closed double membrane of the NE, which is mediated by an asymmetric inside-out fusion of the INM and the ONM. The INM evagination was accompanied by a mushroom-shaped protein density that likely facilitates the membrane deformation from the nuclear side [174]. While the molecular identity of the mushroom-shaped density is not discernable via electron tomography, its base was accompanied by an 8-fold rotationally symmetric ring. Also, super-resolution microscopy demonstrated that the outer ring component NUP107 was present from the initiation of the inside-out membrane invagination, indicating the involvement of a NUP complex in the process. It was demonstrated that ELYS, which is obligatory for postmitotic assembly, is dispensable for interphase/ *de novo* NPC assembly, while the membrane-deforming NUP35, ER-tubulating yeast RTNs, the membrane curvature-sensing domain of NUP133, POM121, and SUN1, as well as the nuclear import of NUP153 to recruit the Y-complex, seem to be required [173].

Conclusively, NPC assembly in organisms that perform open mitosis is mediated by two distinct pathways. Namely, postmitotic and interphase assembly. Both assembly pathways involve membrane curvature sensing and membrane deforming proteins, which likely also played a substantial role in the evolution of the NPC.

6.7. Evolution of the nucleus and the NPC

The nucleus is a key feature of the Eukarya, but eukaryogenesis is one of the biggest enigmas in biology, as roughly 2 billion years separate modern-day organisms and the last common eukaryotic ancestor (LECA). Researchers widely agree that eukaryogenesis involved endosymbiosis of an archaeal and an α-proteobacterial ancestor for the acquisition of mitochondria and a second endosymbiosis with a cyanobacterial ancestor for the acquisition of

chloroplasts [175]. The origin of the nucleus remains more obscure and might be more complex, as a majority of the nuclear replication-, transcription- and translation-machinery seems to be of archaeal origin, while eukaryotic membranes seem to be of bacterial origin[175]. Hence, there are several models for the origin of the nucleus. Many models postulated a *de novo* origin of the nucleus in which the nucleus is acquired in an "outside-in" mechanism. Where the nucleus is formed by a coalescence of membranes around the DNA, similar to NE reformation after exit of open mitosis. This would require the development of endocytosis before nuclear development, as well as extensive membrane remodeling to facilitate the development of the endomembrane system, the continuous inner and outer leaflets of the NE, and the NPC [176]. An alternative hypothesis, the "inside-out" model, postulates that an archaeal ancestor accomplished membranelles spatial separation of its DNA and cytoplasmic domains, while the ER as nucleocytoplasmic boundary developed as a relic of its membrane, essentially describing an autogenous origin of the nucleus [175]. Notably, many models of eukaryogenesis postulate an autogenous establishment of the nucleus in an archaeal ancestor and often only diverge in the sequence of the evolutionary steps towards a LECA, while this sequence ultimately remains enigmatic [177]. Asgard archaea are the closest known relatives to eukaryotes and are studied as models for eukaryogenesis. It was observed that in Loki- and Heimdallarchaeota (both Asgard) DNA, and ribosomal RNA are spatially separated, distinctive to other prokaryotes, which indicates separate locations for transcription and translation, reminiscent of nucleus and cytoplasm [178]. Further, it was reported that prerequisites for nucleocytoplasmic transport like NLS and small GTPase are of archaeal origin [175]. Archaea contain conserved ribosomal NLS-like sequences, which can functionally rescue the deletion of eukaryotic ribosomal NLS [179]. Archaeal NLS could be involved in transport between transcriptional and translational regions, which then evolved to nucleocytoplasmic transport during eukaryogenesis. Cryo-ET of *Candidatus* Lokiarchaeum ossiferum', a member of the Asgard phylum, revealed that it forms several branched spatially separated domains, protrusions that point away from their cell body. At the cell body-protrusion interface, electron-dense molecules were located, which are likely proteins that stabilize the highly curved membrane [180]. Such membrane protrusions with electron densities indicate that Asgard archaea likely possess membrane-deforming proteins, which are also central to the establishment of an endomembranous system. Eukaryotic organisms only possess a limited amount of membrane-deforming paralogous families that enable the formation and mechanism of the endomembrane system. The organellar paralogy hypothesis proposes that paralogous duplication and diversification of membrane-deforming proteins enabled the diversification of new organelles [181]. Likewise, all currently known eukaryotic membrane-deforming protein complexes fall into three structural classes, namely the ESCRT complex, the BAR domain-containing proteins, and the protocoatomer complexes. Protocoatomer complexes comprise the largest group of membrane-deforming complexes and are involved in a plethora of processes [181]. Protocoatomers share a characteristic β-propeller N-terminus and α-solenoid C-terminus (β-α) structure and can be structurally grouped into two distinct families. Type I coats comprise COPI coating complexes that mediate Golgi-to-ER trafficking, as well as clathrin-mediated exo- and endocytosis. Type II coats contain the COPII coating complex that mediates ER-to-Golgi trafficking. Similar β-propeller and α-solenoid proteins were discovered in archaea, but their function remains to be elucidated [182]. Interestingly, protocoatomer complexes are not only involved in short-lived membrane associations (vesicular trafficking: milliseconds-seconds) but also in the assembly of long-lived endomembrane complexes like the NE-located core scaffold NUPs of the NPC (NPC core scaffold lifetime: days-years) [181]. Hence, the outer ring´s Y-complexes are also referred to as "coat NUP complexes". NPC structures indicate that the multiple rings, eightfold symmetry, and diverse core scaffold NUPs likely evolved via oligomerization, stoichiometric duplication and paralogous duplication of a simple NPC protomer. Further, it was revealed that the core

scaffold is structurally unique as it comprises an intermixed arrangement of type I and II coats, which likely also applied to an ancient NPC protomer. These findings indicate that at least the NPCs core scaffold evolved after the establishment of membrane coating type I and II complexes, and might indicate a later nuclear establishment in eukaryogenesis than previously expected [182]. Still, NPCs are ubiquitous in the eukaryotic lineage and, hence, originated before eukaryotic diversification. It is therefore, postulated that "modern" NPCs were already present in the LECA [182,183]. While the origin of the core scaffold NUPs can be robustly traced back to protocoatomer complexes, the origin of FG-NUPs, transmembrane NUPs, filament and basket NUPs, as well as the mRNA export machinery remain to be discovered. Intriguingly, in artificial nanopores, a selectivity barrier can be generated by only using a truncated version of yeast FG-NUPs Nsp1 and NUP100 or a *de novo* designed FG-NUP [184,185]. Further, *in vitro* reconstitution in liposomes of yeast transmembrane NUPs NDC1 and FG-containing POM121 led to the formation of self-assembling ring-like complexes that constitute electrically conductive nanopores [186]. Conclusively, FG-NUPs and transmembrane NUPs seem to be able to constitute minimal nanopores, which indicates that ancient NPCs in the first eukaryotic common ancestor (FECA) could have had very simplistic designs and might not necessarily have required a LECA-like protocoatomer-derived core scaffold [183]. Which, in turn, leaves a lot of room for speculation over the origins of the nucleus and the NPC during eukaryogenesis.

6.8. NPCs in the green-lineage

In contrast to mammals and yeast, there is no high-resolution plant NPC structure published, as cryo-fixation of intact plant tissues proves difficult due to their thickness, cell wall, cell and organelle size [187]. Until now, the best-resolved plant NPCs were visualized by scanning electron microscopy in tobacco BY-2 cells, which revealed a vertebrate-like eightfold radial symmetric structure with a ~105 nm diameter, distinct developmental stage-dependent morphologies, and association with the nucleoskeleton [188]. While this has not yet been accomplished in the plant field, cryo-ET of FIB-generated lamellae allowed to resolve native *Chlamydomonas reinhardtii* NPCs, which revealed substantial differences in algal NPC architecture compared to human NPCs. Characteristically, algal NPCs harbor an asymmetric arrangement in which the cytoplasmic ring is smaller (8 Y-complexes) than the nuclear ring (16 Y-complexes as in human NPCs). Also, the ring complexes are in closer contact, hence more compactified in algal NPCs, leading to a smaller nucleocytoplasmic axis (human NPC ~80 nm, algal NPC ~60 nm) [189] (Figure 8A). Metazoan NUP358 connects the cytoplasmic inner and outer Y-complexes but is missing in the green lineage [190], which might account to the reduced number of Y-complexes in algal NPCs [189]. Hence, plant NPCs might also harbor an asymmetric ring arrangement, which is in line with only scarce sightings of single cytoplasmic projections in NPCs of tobacco BY-2 cells [188] (Figure 8A). While the structure of plant NPCs remains speculative, several proteomic studies revealed insight into the plant NPC´s interaction networks. The identification of most of the Arabidopsis NUPs revealed that plants lack homologs of 6 NUPs (NUP358, NUP188, NUP153, NUP45, NUP37, and POM121) that are present in vertebrates. However, plants harbor plant-specific NUPs like NUP136 [190] and its paralog NUP82 [191], as well as CONSTITUTIVE EXPRESSION OF PATHOGENESIS-RELATED GENE 5 (CPR5) [192], which might compensate for missing vertebrate NUPs or mediate plant-specific functions (Figure 8B). Higher plants also encode a plant-specific KAP of unknown function, termed PLANTKAP, while they lack a homolog of XPO6 [193].

The nuclear basket component NUP136 acts as a functional homolog of vertebrate NUP153 but misses two vertebrate-specific domains [190]. NUP136 is involved in miRNA export at the nuclear basket by physically linking the RNA-exporting TREX-2 complex. While in yeast, the TREX-2 complex is involved in mRNA transport, in Arabidopsis, it seems to export miRNA [194]. Interestingly, EXPORTIN5 is the miRNA exporting NTR in vertebrates, while its

Arabidopsis homolog HASTY (HST) has no apparent effect in miRNA export but rather acquired a new function in cell-autonomously facilitating symplasmic miRNA transport [102]. In contrast to Arabidopsis TREX-2, the Arabidopsis TREX-complex retained its involvement in mRNA export. Arabidopsis TREX interacts with RNA helicases and the mRNA export factors MODIFIER OF SNC1 (MOS)11 and ALYs to facilitate mRNA export [195]. Similar to HST, ALYs acquired a novel function *in planta*, as they facilitate the long-distance transport of mRNAs by recruiting them in the phloem [105]. In addition to the TREX-2 complex, NUP136 and NUP82 link the nuclear basket, to the nucleoskeleton via interaction with plant-unique KAKU4 and the lamin-like CROWDED NUCLEI1 (CRWN) proteins. Interestingly, NUP82/136 and KAKU4 carry a conserved protein motif that is required for localization to the nuclear periphery, self-interaction, and interaction with CRWNs. Phylogenetics indicate that KAKU4 and NUP82 duplicated from an ancestral NUP136. While NUP82 and NUP136 bridge the nuclear basket and nucleoskeleton, KAKU4 lost its NUP function and became an integral member of the nucleoskeleton [196]. A newly identified Arabidopsis nuclear basket component GUANYLATE-BINDING PROTEIN-LIKE (GBPL)3, physically interacts with both nuclear basket and the nucleoskeleton [197] and can promote the formation of biomolecular condensates. GBPL3-induced condensates are enriched in transcription- and post-transcriptional processing machinery and were demonstrated to promote gene-gating during plant immune responses [129,198].

HIGH EXPRESSION OF OSMOTICALLY RESPONSIVE GENES1 (HOS1) is the plant homolog of the nuclear ring NUP ELYS, but they only share a small region of homology that is required for NPC anchoring. Hence it is unclear if HOS1 has similar roles as ELYS in the NPC. Nonetheless, HOS1 regulates a wide range of genes via direct interactions with chromatin (similar to ELYS), epigenetic modification, involvement in mRNA export, and its plant-unique E3 ubiquitin ligase activity. Consequently, the *hos1* mutant phenotype is pleiotropic as interfering with *HOS1* gene function affects cold responses, flowering time, and the circadian clock [129,199]. Recently, it was demonstrated that NUP160 is required to localize HOS1 to the NPC, where HOS1 initiates the degradation of the key circadian flowering activator CONSTANS via ubiquitination, counteracting early-flowering [200]. This highlights HOS1 as a fortifier of the nucleocytoplasmic barrier that can repress NPC passage by initiating localized degradation. Plant FG-NUPs were demonstrated to enable phase separation (similar to vertebrate and yeast FG-NUPs), which in turn fortifies the nucleocytoplasmic barrier against pest invasion [201].

The Arabidopsis NE proteome was expanded by employing a combination of subtractive proteomics with nuclear fractions and proximity-labeling of NPC components. Proxiomes using the inner ring NUP93a and the outer ring NUP82 as baits helped to identify new NUPs like the transmembrane ring NUPs PLANT NE TRANSMEMBRANE1 (PNET1) (homolog of mammalian TMEM209) and PNET6, as well as novel NE components like PNET2-5 [202]. More recently, those efforts [203] were intensified, and NUP-proxiomes of the axillary ring complexes, namely cytoplasmic filament FG-NUP CG1 and nuclear basket FG-NUP50a shed insight into the additional functions of the NPC. The proxiome of the cytoplasmic filaments revealed the association of translation regulation machinery, while the nuclear basket, which is involved in mRNA export showed an association with chromatin remodeling complexes and the spliceosome. The collected proxiomes of the NPC core scaffold and its peripheral extensions (namely: NUP50a, CGI1, PNET1, NUP82, NUP93a, NUP54, NUP188, KAKU4, GBPL3) were combined into a NPC associated-proteome. Interestingly, the proteome was significantly overrepresented in intrinsically disorder region (IDR)-proteins (e.g FG-NUPs but also RBPs), indicating that the NPC coordinates diverse tasks like transport, transcription- and translation regulation by establishing phase-separated subdomains [204]

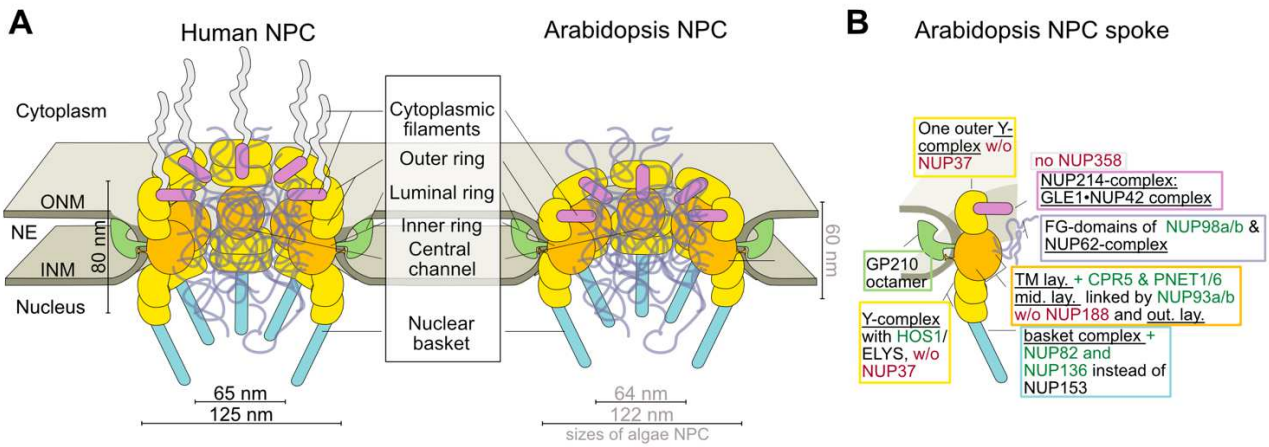

Figure 8: Human vs Arabidopsis NPC
A Comparison of human and Arabidopsis NPC structure. Animal-specific NUP358 links the inner and outer cytoplasmic rings and forms the long extensions (grey) characteristic in depictions of the cytoplasmic filaments**.** The green lineage does not contain NUP358, so Arabidopsis NPCs likely contain only a single outer ring and no symmetric cytoplasmic extensions, as indicated by scanning electron microscopy in tobacco BY-2 cells [188]. As *in vivo* dimensions for the Arabidopsis NPC remain unresolved, the dimensions of the *Chlamydomonas reinhardtii* NPC are depicted. The algal NPC has a 64 nm central channel and 122 nm core scaffold, similar to the human NPC. A structural difference is in the nucleocytoplasmic axis, which is compactified and only 60 nm instead of 80 nm (human NPC). **B** Structural complexes in Arabidopsis NPC spoke. Missing NUPs in Arabidopsis (NUP37, NUP358, and NUP188) are written in dark red. Plant-specific NUPs (or NUP domains) are written in green. Arabidopsis contains three plant-specific membrane NUPs, namely CPR5, PNET1 and PNET6. Two plant-specific basket NUPs, namely NUP136 and NUP82, and plant-specific domains fused to the nuclear ring NUP ELYS (HOS1/ELYS). Lastly, NUP98 and NUP93 were duplicated in Arabidopsis (NUP98a/b and NUP93a/b).

6.9. The plant-specific transmembrane NUP CPR5

CPR5 is a transmembrane NUP that is unique to the green lineage. CPR5 has a repressive role on effector triggered immunity (ETI) and programmed cell death (PCD) [192,205]. Recently, it was shown that CPR5 has additional roles as an activator of pattern triggered immunity (PTI) [206], which highlights CPR5 as an immune master regulator that balances between the PTI and ETI pathways at the nucleocytoplasmic barrier. Mutants of *CPR5* show a pleiotropic phenotype: they are dwarfed, have a reduced trichome development, and form spontaneous chlorotic lesions. Further, they accumulate salicylic acid (SA) and are resistant to multiple pathogens [207,208]. Other effects of *cpr5* mutants comprise changed cell wall composition [209], altered response to abscisic acid [210], ethylene [211], and sugars [212], altered unfolded protein response [213], defective cell proliferation [214], and accelerated leaf senescence [215]. The pleiotropic effects of *CPR5* mutation could be a consequence of its role as plant-specific transmembrane NUP. CPR5 homomers localize to the transmembrane ring of the NPC. In addition, CPR5 interacts with members of the core scaffold like NUP93a and NUP155. Upon ETI, activation of CPR5 homomerization is disrupted, which results in nucleocytoplasmic import of immune cargos and release of cyclin-dependent kinase inhibitors, resulting in a potentiated ETI signal transduction [192].The KAP *EXPORTIN4* (*XPO4*) was identified as a genetic interactor of *CPR5*. Knock-out of *XPO4* in a *cpr5* mutant background triggers extreme immune responses, which result in seedling lethality. Proximity-labelling of XPO4 revealed TOPLESS (TPL) and TPL-related (TPR) transcription co-repressors as its specific cargos. TPL/TPR are imported into the nucleus in response to SA accumulation and promote transcriptional co-repression of negative immune regulators. XPO4 exports TPL/TPR and thereby counteracts TPL/TPR-mediated immune potentiation. As immune markers only accumulate if *xpo4* is introduced in the *cpr5* mutant background, the XPO4-TPL/TPR mediated immune potentiation was hypothesized to be downstream of CPR5-mediated ETI repression [216]. Interestingly, CPR5 also affects

nucleocytoplasmic shuttling of non-immune-cargos. CPR5 specifically blocks nucleocytoplasmic import of the regulators of auxin signaling AUXIN/INDOLE-3-ACETIC ACID INDUCIBLE 12 (IAA12) and IAA19, which transmit auxin signaling output in the cytosol. In abiotic stress conditions, CPR5 levels are reduced, which results in IAA12/ 19 nuclear accumulation, reduced auxin signaling, and consequently reduced lateral root growth [210]. In addition to its role as transmembrane NUP, a recent publication highlighted that the CPR5 N-terminus contains RNA-binding motifs belonging to the TRANSFORMER2 (TRA2)-subfamily. Moreover, CPR5 seems to be involved in alternative splicing and alternative polyadenylation by physically interacting with RNA-processing proteins in nuclear speckles, which are RNA-processing organelles [217]. It remains unclear how CPR5 localizes to nuclear speckles despite its TM-domains one possibility is that the CPR5 N-terminus is cleaved and relocated into the nucleoplasm, which was proposed previously due to the observation of nucleoplasmic CPR5 localization in overexpression and the presence of a bipartite NLS in the N-terminus [213,214]. The *cpr5* mutant phenotypes are largely pleiotropic in Arabidopsis. The recent discoveries suggesting that CPR5 gates the NPC and affects cargo transport, as well as RNA-processing of large quantities of transcripts, could explain the many processes that are altered in the *cpr5* mutant background. Obscurely, knock-out of *CPR5.1* in rice confers resistance against rice yellow mottle virus, while even a double knock-out has no macroscopic phenotypes [218]. Highlighting that the molecular mechanism of CPR5 function still bears gaps that remain to be elucidated.

6.10. Conclusion

While the evolutionary mechanism behind karyogenesis and NPC formation remains elusive, FIB-enabled cryo-ET led to extensive breakthroughs in elucidating native NPC structures of multiple organisms at near-atomic resolution, which revealed precise NPC composition and even gave some indications on the evolutionary appearance of the NPCs core scaffold. While plant NPC structures are yet to be published, proteomic characterizations indicate association with nuclear and cytoplasmic complexes that expand the plant NPC-associated functions to gene expression and mRNA remodeling. While the structured NUP domains of the yeast, algae, and animal NPCs core scaffold and peripheral extensions have been visualized in great detail, the central channel and peripheral FG-domains conformational state remains enigmatic due to their intrinsic disorder. Several models describe the state of the NPC's FG-based phase separation, and recent computational models and experimental advances indicate that NTR crowding in the NPC likely contributes to the permeability barrier (KAP-centric model). Phase separation contributes to cellular organization by generating membrane-less subdomains, as seen in several novel studies on the multifaceted roles of FG-domains, LLPS, and biomolecular condensates [204,219]. Accordingly, it is conceivable that phase separation might be a mechanism involved in other transport processes, like indicated in cilia [118], peroxisomes[119,120], or intra-chloroplast cargo sorting [220]. The cellular environment is crowded. Single yeast cells for example contain ~42 million proteins [221]. Further, research on NPC phase separation and similar biomolecular condensates will be central to investigate how cells organize such crowded environments while simultaneously maintaining cellular integrity.

Chapter V

7. Identification of nuclear pore proteins at plasmodesmata

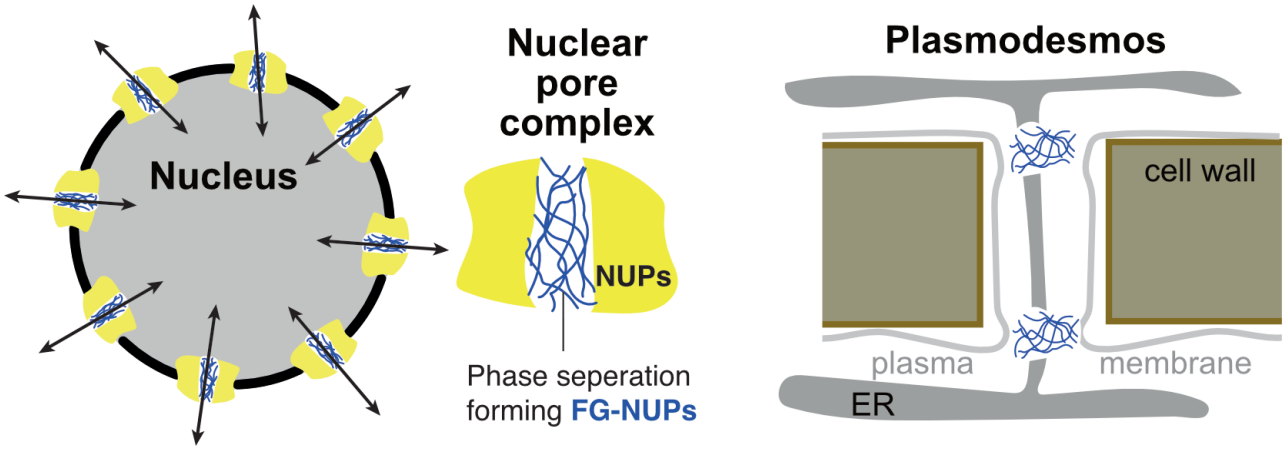

Status: Preprint
Journal: bioRxiv
Contribution: 25% (shared first author)
(specified in Appendix)

7.1. Aim of this chapter

7.1.1. Research question:

- What are the key components of PD?

- Are molecular mechanisms underlying PD transport similar to mechanisms underlying NPC transport?

7.1.2. Objective

Testing localization of NPC components at PD and assessing their involvement in PD-mediated transport.

7.1.3. Hypothesis

NPC proteins are structural components at PD and functionally affect intercellular transport.

Identification of nuclear pore proteins at plasmodesmata

T. Moritz Schladt[1,2,*], Manuel Miras[1,2,8,*], Jona Obinna Ejike[1,2,*], Mathieu Pottier[1,2,9,*], Lin Xi[3], Andrea Restrepo-Escobar[1,2], Masayoshi Nakamura[4], Niklas Pütz[1,2], Sebastian Hänsch[2,5], Chen Gao[1,2], Julia Engelhorn[1,2], Marcel Dickmanns[1,2,6], Gwendolyn V. Davis[1,2], Ahan Dalal[1,2], Sven Gombos[3], Ronja Lange[1,2], Rüdiger Simon[2,7], Waltraud X. Schulze[3] & Wolf B. Frommer[1,2,4,§]

[1] Heinrich Heine University Düsseldorf, Faculty of Mathematics and Natural Sciences, Institute for Molecular Physiology, Düsseldorf, Germany
[2] Cluster of Excellence on Plant Sciences, Heinrich Heine University Düsseldorf, Germany
[3] Department of Plant Systems Biology, University of Hohenheim, 70593 Stuttgart, Germany
[4] Institute for Transformative Biomolecules (WPI-ITbM), Nagoya University, Nagoya, Japan
[5] Center for Advanced Imaging; Heinrich Heine University Düsseldorf, Düsseldorf, Germany
[6] Department of Molecular Structural Biology, Max Planck Institute of Biochemistry, Martinsried, Germany
[7] Heinrich Heine University Düsseldorf, Faculty of Mathematics and Natural Sciences, Institute of Developmental Genetics, Germany
[8] New address: Department of Stress Biology and Plant Pathology, CEBAS-CSIC, Murcia, Spain
[9] New address: Université de Lorraine, INRAE, IAM, F-54000 Nancy, France

* Equal contribution
§ For correspondence: frommew@hhu.de

Summary

Plasmodesmata (PD) exchange small molecules, RNAs and proteins between plant cells with an exclusion limit for passive, non-specific transport. PD also facilitate the transport of specific cargo that may require chaperones or carriers for transport. The mechanisms underlying PD transport are not understood. PD and nuclear pore complexes (NPC), are nanometer size micropores with similar transport properties. The permeability barrier in NPCs is a phase separation domain formed by FG-nucleoporins (FG-NUP). Here we used bioinformatics, proteomics and fluorescence imaging to identify proteins with similarities to phase separating FG-NUPs at PD. We identified 20 NUPs in PD fractions, and validated dual localization to NPC and PD for 7 NUPs. Structured illumination microscopy detected the transmembrane anchor NUP CPR5 at both orifices of PD. *cpr5* mutants showed reduced intercellular transport of SHR from stele to endodermis. The identification of FG-NUPs at PD is consistent with the recruitment of NUPs in the green lineage to form a PD pore gating complex consistent with liquid phase separation domains as diffusion barriers at PD.

2

Introduction

Nutrient exchange and communication between cells are essential for multicellular organisms. Besides transporters and cell surface receptors, metazoa, fungi and plants independently evolved cell-cell bridges. The green lineage developed unique structures, called plasmodesmata (PD), composed of modified cell wall domains that form plasma membrane-lined channels and contain an ER-derived desmotubule to generate continuity between the cytoplasm of neighboring cells. Since PD are embedded into the cell wall and likely contain diverse membrane and soluble proteins, PD pose a major challenge for biochemical and cell biological analyses. Several studies obtained PD proteomes by enriching membrane proteins in cell wall fractions[1–4]. Genetic approaches have so far failed to identify genes that could fully explain the transport mechanism, possibly due to redundancy or lethality. Transport studies are also challenging since intact multicellular systems are required for analyses.

Key features of PD transport appear to be the ability to translocate highly diverse cargo (from ions to macromolecules), a size exclusion limit (which, depending of the type of PD, can reach 70 kDa, in funnel PD up to 120 kDa), and the ability to translocate specific cargo[5,6]. Lee et al. highlighted that transport through PD and the nuclear pore complex (NPC) share common features[7], namely both NPC and PD transport a similar spectrum of cargo species (ions, metabolites, proteins, and ribonucleoprotein complexes). For both NPC and PD, the ability for pore dilation has been described[8,9]. Both NPC and PD constitute selective barriers, allowing '*passive passage of molecules'* with an apparent size exclusion limit (term used in animal literature; named '*non-targeted movement*' for PD) and '*facilitated translocation of specific macromolecules'* ('*targeted movement*' for PD)[10,11]. Surface properties of cargo proteins appear to play an important role, thus at least for nuclei, there is no strict size exclusion limit[11]. The core of the permeability barrier of the NPC appears to be a separated phase or condensate formed by disordered phenylalanine–glycine (FG) repeat-containing proteins, which function as 'smart sieves' and produce phase-separated domains in a good Flory solvent-like environment *in situ*[11–14]. These smart sieves mediate passage of smaller molecules and proteins without interaction with the FG repeats, while larger molecules or specific cargo can pass with the help of nuclear transport receptors (NTR) that interact with the FG repeats[15]. As a shared structure among eukaryotes, the ultrastructure, function and transport mechanism of the NPC is well understood[16]. The human NPC, with about 1000 polypeptides, has a diameter of 120 nm, a pore size of ~43 nm and a height of 80 nm and is composed of a membrane-anchor, three stacked rings (a sandwich of two outer and an inner ring), cytoplasmic filaments, and a nucleocytoplasmic basket[17].

FG-NUPs and other NUPs in PD fractions of *Physcomitrium patens* and Arabidopsis

Based on similar features, we hypothesized that the PD transport mechanism could involve FG-repeat proteins that generate a liquid phase separation domain in PD with properties similar as the NPC. We thus explored whether the green lineage evolved a distinct set of FG-repeat containing proteins. The human genome encodes twelve FG-nucleoporins (NUPs): NUP42, NUP50, NUP54, NUP58 (aka NUP45), NUP62, NUP98, NUP153, NUP214, POM121, POM121B, POM121C, and NUP358[18], while plant genomes encode ten FG-NUPs: NUP42 (aka CG1), NUP50a & NUP50b, NUP54, NUP58, NUP62, NUP98a & NUP98b, NUP136 and NUP214[19,20]. The majority of the FG-NUPs were conserved, with only three FG-NUPs lost in the green lineage (NUP153, POM121, NUP358). A bioinformatic search for FG repeat-containing proteins in the genome of the moss *P. patens* revealed that 12 out of the 15 top-ranked FG-containing proteins were NUPs; the other three proteins were not considered candidates for a transport function (table S1; file S1; file S2 for Arabidopsis FG-containing proteins). An alternative hypothesis was that the PD permeability barrier is generated by NUPs derived by tandem gene duplications followed by differentiation into NPC and PD functions. However, phylogenetic analyses showed that the majority of NUPs are encoded by single genes (table S2)[20,21]. Notably, an analysis of the PD proteome from *P. patens* identified FG-NUP50a and two other NUPs, SEC13 and NUA[1]. Our previous work had indicated that moss PD proteins can be targeted to PD when expressed in tobacco leaves, indicating conservation of the targeting signals[1]. To test whether FG-NUPs localize exclusively to the NPC or can also be targeted to PD, the subcellular localization of fluorescent protein (FP) fusions of three *P. patens* FG-NUPs (NUP58, NUP62 and NUP98) was analyzed by confocal microscopy after estradiol-controlled transient expression in *Nicotiana benthamiana*. A substantial number of fluorescent puncta derived from C-terminal mVenus fusions of the three FG-NUPs overlaid with fluorescent puncta of aniline blue marking callose at PD (Fig.

1A; fig. S1). PD localization did not appear to be due to an FG-NUPs-specific mis-localization, since the inner ring linker NUP35, which connects the transmembrane interaction hub with the ALADIN-NDC1 core to NUP155, also localized to PD (Fig. 1A).

To obtain independent evidence, and to explore whether FG-NUPs may also be present in PD fractions from a vascular plant, we utilized established PD enrichment and data analysis pipelines to generate a PD proteome from Arabidopsis shoots[1]. This shoot PD proteome had an overlap of 80% with published PD proteomes and included ~43% of known high-confidence PD proteins, e.g., the well-established PDLP and MCTP PD markers (table S3, fig. S2, S3, file S3)[2,22]. Notably, seven Arabidopsis FG-NUPs were identified in the PD fraction (Fig. 1B). In addition, inner and outer ring and basket NUPs were found in the high-confidence PD protein list (Fig. 1B). In total, 20 proteins covering different domains of the NPC were identified, and 15 were enriched in PD fractions compared to cell wall and total Arabidopsis protein fractions (Fig. 1B, C, fig. S2, S3). Several of the identified nuclear pore components passed the threshold for consideration as high-confidence PD proteins, in particular proteins of the inner and outer rings, core and basket. Three FG-NUPs NUP62, NUP214, NUP50a, as well as CPR5, GP210, NUP35, NUP93a, NUP155, NUP205, NUP43, HOS1 (aka HOS1/ELYS), SEC13, and NUP82 were also found in proteomics data of cell wall/PD protein fractions from other studies (table S4)[1,3,4,23,24].

Localization of Arabidopsis FG-NUPs and other NUPs to PD

To explore whether Arabidopsis FG-NUP-mVenus fusions can be detected at PD by confocal microscopy, candidates were expressed from an estradiol-inducible promoter in *N. benthamiana* leaves, which can be used to limit overexpression. Fluorescence derived from FP-fusions of the FG-NUP58, FG-NUP62 and FG-NUP98b overlaid with aniline blue fluorescent puncta (with a significantly higher PD index relative to that for the non-specific cell wall dye propidium iodide, Fig. 2, fig S4, table S2), indicating that Arabidopsis FG-NUPs can also be targeted to PD in this system. Notably, 12 out of a total of the 16 NUPs tested here localized to puncta in the cell periphery that overlaid with aniline blue fluorescence at pit fields (Fig. 2, Fig. 3A, B; fig. S4)[25]. Overall, 12 NUPs showed significant enrichment at PD compared to the cell wall marker (Fig. 2B, Fig. 3B, table S2). Among them were two outer ring NUPs (NUP43, HOS1/ELYS) and two transmembrane NUPs (GP210, CPR5) (Fig. 1C, 3B). As expected, ten NUP fusions for various inner and outer ring and membrane anchor NUPs were also detected in nuclei (fig. S4, list of 16 tested NUPs: table S2). Fluorescent puncta of aniline blue and FP-fusions of PD protein typically do not provide a perfect colocalization since aniline blue staining does not mark all PD and typically, the overlay is partial since FP-fusions are not detected at all PD even for high confidence PD proteins[26]. As an independent measure, overlay of the PD marker PDLP5-mScarlet3 and an mCitrine fusion of the putative NUP107-160 complex recruitment factor HOS1/ELYS at PD was validated (Fig. 3C). To test for potential artifacts, caused possibly by mistargeting due to overexpression, both the concentration of the inducer estradiol and the induction time were reduced, leading to a drop in overall fluorescence intensity, however, without negatively affecting dual NUP localization (here NUP43-mCitrine) at NPC and PD (Fig. 3D). Single copy insertions of GFP-fusions are likely to avoid overexpression. Analysis of nine independent stably transformed homozygous single insertion Arabidopsis lines expressing a full-length genomic FG-NUP62-GFP fusion showed dual localization to nuclei and PD in cotyledons (Fig. 2 C, D). Arabidopsis FG-NUP62 had previously shown to form hydrogels that recapitulate the NPCs phase separation-like transport properties *in vitro*[27]. The results are in line with the hypothesis of FG-repeat based phase separation domains as a permeability barrier at PD[27]. Other components of the NPC located at PD could provide a scaffold that holds the FG-NUPs in place in a yet to be determined structure. Notably, in contrast to C-terminal FP fusions of the auto-cleavable NUP98a[28], here, a C-terminal NUP98b-mVenus fusion produced fluorescence at PD (Fig. 2, fig. S4), indicating that either the main fraction of NUP98b in the study by Gallemi et al. (2016) was unprocessed, or that the C-terminal peptide reassociated with the N-terminal domain of NUP98b, as previously described for the two splice forms of the human NUP98[29]. Out of 16 NUPs tested, four NUPs did not localize at PD, as indicated by *p*-values >0.08 (table S2). Out of 35 currently known Arabidopsis NUPs, 19 NUPs were not yet tested here (table S2). In summary, our data indicate that NUPs of the non-vascular moss *P. patens* and the vascular plant Arabidopsis can dually localize to NPC and PD, including the plant-specific membrane anchor CPR5 and FG-NUP NUP62. Components

of the inner ring, NUP93a and NUP155, and the basket, NUP82, were also detected at PD, although with lower confidence compared to, e.g., CPR5. Analysis of published data from other groups who had localized NUPs to nuclei also showed peripheral puncta, which had not been analyzed further (table S5). While it is conceivable that NUPs may contain distinct NPC and PD targeting sequences, alternatively they might be recruited to the two locations as preformed subcomplexes by a common receptor or anchor to assemble a pore that harbors a phase separation domain and constitutes a permeability barrier.

Topology of CPR5, a potential membrane anchor at both NPC and PD

Since the phase separation domain in the nuclear pore is produced by ten FG-NUPs and PD appear to contain multiple FG-NUPs, it may be necessary to mutate multiple *FG-NUP* genes before it is possible to observe intercellular transport defects. It is also conceivable that, *knock-out* mutants in multiple *FG-NUPs* may be lethal. We therefore focused on the green lineage-specific membrane anchor CPR5, a nuclear pore component with a PD index of 1.48 (Fig. 3, table S2). Four potential membrane proteins that anchor the human NPC in the nuclear membrane had been identified: GP210, POM121, NDC1 and TMEM33. Arabidopsis encodes genes for three anchors GP210, NDC1 and PNET1 (homologue of human TMEM209) (table S6), while CPR5 had been proposed to serve as an anchor in the equatorial plane of the NPC[30]. Since CPR5 was among the top 5 candidates based on the PD index, one may hypothesize that it contributes to anchoring an NPC-like structure at PD (Fig. 3A, B, fig. S4). CPR5, a polytopic membrane protein, is predicted to form a globular helix bundle domain at its N-terminus, flanked by disordered regions and connected to a 105 amino acid α-helix (fig. S5). The central helix contains a hydrophobic region, which, together with four shorter hydrophobic helices, forms an approximately 35 Å long transmembrane domain, consistent with the expected thickness of ER membranes. The C-terminus possibly extends into the ER lumen. CPR5 may play a specialized role in the plant NPC or serve as a replacement for the missing metazoan POM121[31]. CPR5 is encoded as a single gene in Arabidopsis and two in rice (fig. S6, table S6, table S7)[32].

Principal differences between the NPC and PD are the overall length (nuclear double membrane thickness at the pore ～30 nm; PD, length depends on cell wall thickness, between 100 nm and several μm), the presence of a nuclear double-membrane *vs*. two separate membranes at PD, i.e., an outer plasma membrane and an ER-like desmotubule in the center of the pore. In PD, CPR5 could either be embedded into the PD plasma membrane, with the C-terminus facing the apoplasm, or into the ER/desmotubule membrane, with its C-terminus facing the desmotubule lumen and the long N-terminal domain pointing into the intermembrane space of PD, analogous to the CPR5 topology in the ER-derived nuclear membrane at the NPC. A split-GFP system for topology studies of membrane proteins was used to determine whether the C-terminus of CPR5 faces the luminal side of the ER[33]. When an N-terminal GFP11 fusion to CPR5 was co-expressed with a free cytosolic GFP1-10, fluorescence was reconstituted, consistent with the N-terminus located in the cytosol sleeve of PD (Fig. 4A; fig. S7). A control using a GFP1-10 domain targeted to and retained in the ER lumen (GFP1-10-HDEL) did not show detectable fluorescence reconstitution (Fig. 4B). The complementary fusion of GFP11 to the C-terminus of CPR5 led to reconstitution of fluorescence when co-expressed with an ER lumen targeted GFP1-10-HDEL, but not when co-expressed with a cytosolic GFP1-10 (Fig. 4A, B; fig. S7). The topological data are consistent with a model in which the C-terminal five-helix-bundle of CPR5 traverses the ER/desmotubule membrane with the C-terminus inside the lumen of the ER/desmotubule, while the extended central α-helix, the predicted unstructured domains, and the smaller helical bundle of CPR5 are located in the intermembrane space between the ER/desmotubule and the plasma membrane (fig. S5).

Localization of CPR5 at the orifices of PD

A hypothetical NPC-like structure could serve as a micropore in the PD channel, or be present on PD entrance. To determine CPR5 localization in the PD at higher resolution, we performed structured illumination microscopy (SIM) with a CPR5-mCitrine fusion. CPR5 localized to the neck region of PD adjacent to aniline blue labeled callose deposition (Fig. 4C, D; fig. S8), but not in the central cavity of the PD, where PDLP5-mScarlet3 was localized[34]. These findings are consistent with a model in which NUPs are present at the PD orifices. We did not observe puncta at both paired neck regions in all cases (fig.

S8B, top), possibly due to mosaic-like expression in *N. benthamiana*, in which only one of the adjacent cells expressed the fusion protein (model: Fig. 4D).

Intercellular transport defects in *cpr5* mutants

If indeed NUPs form condensates at PD to control cell-to-cell transport, and given the defects of *cpr5* mutants in nuclear transport, one may expect that interference with CPR5 function might impair *facilitated and non-facilitated cell-to-cell translocation of specific macromolecules*. Particle bombardment of Arabidopsis leaves was performed to transiently express a tandem-GFP fusion (2xmEGFP; 54 kDa) in two independent *cpr5* loss-of-function mutants (EMS mutant *cpr5-1* (G420D) and T-DNA insertion mutant *cpr5-T3*[35,36];fig. S9C, D)[30,35–40] uncovered defects in cell-to-cell transport. Cell-to-cell movement of 2xmEGFP was significantly reduced in the *cpr5* mutants relative to WT (Fig. 5A, B; fig. S9A, B). Originally named for its *constitutive pathogen response* phenotype, loss of CPR5 activity can trigger constitutive defense responses that could cause callose deposition and closure of PD [41], however, callose levels were not significantly different (Fig. 5C). The transcription factor SHORT-ROOT (SHR), produced in cells of the stele, migrates into the endodermis by *facilitated cell-to-cell translocation,* followed by nuclear import[42]. Intercellular transport of SHR is crucial for tissue patterning[42–44]. To explore whether SHR-GFP (86.6 kDa) movement was impacted in a *cpr5* loss-of-function mutant*,* we compared the endodermis-to-stele ratio (E:S ratio) of GFP fluorescence intensity in roots of homozygous *shr* mutants expressing pSHR:SHR–GFP in wild type (WT) as well as in the *cpr5-1* mutant background. The E:S ratio was significantly reduced in *cpr5-1* compared to WT, consistent with a defect in facilitated SHR transport across PD (Fig. 5D, E). Fluorescence recovery after photobleaching (FRAP) of nuclei in the root endodermis of homozygous *shr*/pSHR:SHR lines in *cpr5-1* was significantly lower compared to WT, further supporting that targeted transport across PD is reduced in *cpr5-1* (Fig. 5F,G, fig. S9F). Notably, no significant difference in SHR–GFP fluorescence intensity was observed in the steles of WT versus *cpr5-1* lines (fig. S9E). The *cpr5* mutants showed no detectable defect in small molecule transport indicates WT-like PD density and retention of the capability to mediate small molecule transport as shown by Drop-ANd-See *trans*-leaf diffusion assays (DANS, carboxyfluorescein: 376 Da; control CaMV*35S:PDLP5*; Fig. 5H, I)[45]. Localization of CPR5 to PD, and the specific defects in macromolecular non-targeted and targeted transport may implicate a role of CPR5 in PD transport.

Potential roles for NUPs at PD

Based on the observations (i) that NUPs were identified in PD-enriched cell wall fractions, (ii) that 12/35 known plant NUPs, and in particular FG-NUPs, localized to PD, and (iii) that intercellular tandem-GFP and SHR transport was reduced in *cpr5* mutants may indicate that components of the NPC may generate a complex that can sustain a similar liquid phase separation domain at PD as found in the NPC, and that liquid phase separation generated by FG-NUPs may play a role in intercellular translocation[15]. The exact composition and structure of the predicted plasmodesmatal pore complex (PDPC), and how dual targeting is achieved, remains to be explored. The insights gained here may open new ways to understand the structure, function, transport mechanism and regulation of PD and how to engineer the permeability barrier between cells.

References

1. Gombos, S. *et al.* A high-confidence *Physcomitrium patens* plasmodesmata proteome by iterative scoring and validation reveals diversification of cell wall proteins during evolution. *New Phytol.* **238**, 637–653 (2023).
2. Brault, M. L. *et al.* Multiple C2 domains and transmembrane region proteins (MCTPs) tether membranes at plasmodesmata. *EMBO Rep.* **20**, e47182 (2019).
3. Fernandez-Calvino, L. *et al.* Arabidopsis plasmodesmal proteome. *PloS One* **6**, e18880 (2011).
4. Bayer, E. M. *et al.* Arabidopsis cell wall proteome defined using multidimensional protein identification technology. *PROTEOMICS* **6**, 301–311 (2006).

5. Paultre, D. S. G., Gustin, M.-P., Molnar, A. & Oparka, K. J. Lost in transit: long-distance trafficking and phloem unloading of protein signals in Arabidopsis homografts. *Plant Cell* **28**, 2016–2025 (2016).
6. Ross-Elliott, T. J. *et al.* Phloem unloading in Arabidopsis roots is convective and regulated by the phloem-pole pericycle. *eLife* **6**, e24125 (2017).
7. Lee, J. Y., Yoo, B. C. & Lucas, W. J. Parallels between nuclear-pore and plasmodesmal trafficking of information molecules. *Planta* **210**, 177–187 (2000).
8. Zimmerli, C. E. *et al.* Nuclear pores dilate and constrict in cellulo. *Science* **374**, eabd9776 (2021).
9. Kragler, F., Monzer, J., Shash, K., Xoconostle-Cázares, B. & Lucas, W. J. Cell-to-cell transport of proteins: requirement for unfolding and characterization of binding to a putative plasmodesmal receptor. *Plant J.* **15**, 367–381 (1998).
10. Crawford, K. M. & Zambryski, P. C. Non-targeted and targeted protein movement through plasmodesmata in leaves in different developmental and physiological states. *Plant Physiol.* **125**, 1802–1812 (2001).
11. Frey, S. *et al.* Surface properties determining passage rates of proteins through nuclear pores. *Cell* **174**, 202-217.e9 (2018).
12. Ng, S. C., Güttler, T. & Görlich, D. Recapitulation of selective nuclear import and export with a perfectly repeated 12mer GLFG peptide. *Nat. Commun.* **12**, 4047 (2021).
13. Hoogenboom, B. W. *et al.* Physics of the nuclear pore complex: Theory, modeling and experiment. *Phys. Rep.* **921**, 1–53 (2021).
14. Yu, M. *et al.* Visualizing the disordered nuclear transport machinery in situ. *Nature* **617**, 162–169 (2023).
15. Kehlenbach, R. H., Neumann, P., Ficner, R. & Dickmanns, A. Interaction of nucleoporins with nuclear transport receptors: a structural perspective. *Biol. Chem.* **404**, 791–805 (2023).
16. Mosalaganti, S. *et al.* AI-based structure prediction empowers integrative structural analysis of human nuclear pores. *Science* **376**, eabm9506 (2022).
17. Lin, D. H. & Hoelz, A. The structure of the nuclear pore complex (an update). *Annu. Rev. Biochem.* **88**, 725–783 (2019).
18. Terry, L. J. & Wente, S. R. Flexible gates: dynamic topologies and functions for FG nucleoporins in nucleocytoplasmic transport. *Eukaryot. Cell* **8**, 1814–1827 (2009).
19. Chopra, K., Bawaria, S. & Chauhan, R. Evolutionary divergence of the nuclear pore complex from fungi to metazoans. *Protein Sci.* **28**, 571–586 (2019).
20. Makarov, A. A., Padilla-Mejia, N. E. & Field, M. C. Evolution and diversification of the nuclear pore complex. *Biochem. Soc. Trans.* **49**, 1601–1619 (2021).
21. Zhang, C. *et al.* Genomic identification and expression analysis of nuclear pore proteins in *Malus domestica*. *Sci. Rep.* **10**, 17426 (2020).
22. Thomas, C. L., Bayer, E. M., Ritzenthaler, C., Fernandez-Calvino, L. & Maule, A. J. Specific targeting of a plasmodesmal protein affecting cell-to-cell communication. *PLoS Biol.* **6**, e7 (2008).
23. Kraner, M. E., Müller, C. & Sonnewald, U. Comparative proteomic profiling of the choline transporter-like1 (CHER1) mutant provides insights into plasmodesmata composition of fully developed *Arabidopsis thaliana* leaves. *Plant J. Cell Mol. Biol.* **92**, 696–709 (2017).
24. Kirk, P., Amsbury, S., German, L., Gaudioso-Pedraza, R. & Benitez-Alfonso, Y. A comparative meta-proteomic pipeline for the identification of plasmodesmata proteins and regulatory conditions in diverse plant species. *BMC Biol.* **20**, 128 (2022).

25. Zavaliev, R. & Epel, B. L. Imaging callose at plasmodesmata using aniline blue: quantitative confocal microscopy. *Methods Mol. Biol. Clifton NJ* **1217**, 105–119 (2015).
26. Pendle, A. & Benitez-Alfonso, Y. Immunofluorescence detection of callose deposition around plasmodesmata sites. *Methods Mol. Biol. Clifton NJ* **1217**, 95–104 (2015).
27. Wang, J. *et al.* Phase separation of the nuclear pore complex facilitates selective nuclear transport to regulate plant defense against pathogen and pest invasion. *Mol. Plant* **16**, 1016–1030 (2023).
28. Gallemí, M. *et al.* DRACULA2 is a dynamic nucleoporin with a role in regulating the shade avoidance syndrome in Arabidopsis. *Development* **143**, 1623–1631 (2016).
29. Hodel, A. E. *et al.* The three-dimensional structure of the autoproteolytic, nuclear pore-targeting domain of the human nucleoporin Nup98. *Mol. Cell* **10**, 347–358 (2002).
30. Gu, Y. *et al.* Nuclear pore permeabilization is a convergent signaling event in effector-triggered immunity. *Cell* **166**, 1526-1538.e11 (2016).
31. Apelt, L. *et al.* Systematic protein–protein interaction analysis reveals intersubcomplex contacts in the Nuclear Pore Complex. *Mol. Cell. Proteomics MCP* **15**, 2594–2606 (2016).
32. Arra, Y. *et al.* Rice Yellow Mottle Virus resistance by genome editing of the *Oryza sativa L. ssp. japonica* nucleoporin gene *OsCPR5.1* but not *OsCPR5.2*. *Plant Biotechnol. J.* **22**, 1299–1311 (2024).
33. Xie, W., Nielsen, M. E., Pedersen, C. & Thordal-Christensen, H. A split-GFP gateway cloning system for topology analyses of membrane proteins in plants. *PLOS ONE* **12**, e0170118 (2017).
34. Fitzgibbon, J., Bell, K., King, E. & Oparka, K. Super-resolution imaging of plasmodesmata using three-dimensional structured illumination microscopy. *Plant Physiol.* **153**, 1453–63 (2010).
35. Wang, F. *et al.* Arabidopsis CPR5 regulates ethylene signaling via molecular association with the ETR1 receptor. *J. Integr. Plant Biol.* **59**, 810–824 (2017).
36. Bowling, S. A., Clarke, J. D., Liu, Y., Klessig, D. F. & Dong, X. The cpr5 mutant of Arabidopsis expresses both NPR1-dependent and NPR1-independent resistance. *Plant Cell* **9**, 1573–84 (1997).
37. Crawford, K. M. & Zambryski, P. C. Subcellular localization determines the availability of non-targeted proteins to plasmodesmatal transport. *Curr. Biol.* **10**, 1032–1040 (2000).
38. Faulkner, C. *et al.* LYM2-dependent chitin perception limits molecular flux via plasmodesmata. *Proc. Natl. Acad. Sci.* **110**, 9166–9170 (2013).
39. Sakulkoo, W. *et al.* A single fungal MAP kinase controls plant cell-to-cell invasion by the rice blast fungus. *Science* **359**, 1399–1403 (2018).
40. Otero, S., Helariutta, Y. & Benitez-Alfonso, Y. Symplastic communication in organ formation and tissue patterning. *Curr. Opin. Plant Biol.* **29**, 21–28 (2016).
41. Kohler, A., Schwindling, S. & Conrath, U. Benzothiadiazole-induced priming for potentiated responses to pathogen infection, wounding, and infiltration of water into leaves requires the *NPR1/NIM1* gene in Arabidopsis. *Plant Physiol.* **128**, 1046–1056 (2002).
42. Nakajima, K., Sena, G., Nawy, T. & Benfey, P. N. Intercellular movement of the putative transcription factor SHR in root patterning. *Nature* **413**, 307–311 (2001).
43. Koizumi, K., Hayashi, T., Wu, S. & Gallagher, K. L. The SHORT-ROOT protein acts as a mobile, dose-dependent signal in patterning the ground tissue. *Proc. Natl. Acad. Sci. U. S. A.* **109**, 13010–13015 (2012).
44. Winter, C. M. *et al.* SHR and SCR coordinate root patterning and growth early in the cell cycle. *Nature* 1–6 (2024) doi:10.1038/s41586-023-06971-z.
45. Lee, J.-Y. *et al.* A plasmodesmata-localized protein mediates crosstalk between cell-to-cell communication and innate immunity in Arabidopsis. *Plant Cell* **23**, 3353–3373 (2011).

Acknowledgments

We would like to dedicate this manuscript to the 'champion of plasmodesmata', William J. (Bill) Lucas (UC Davis). We thank Madlen Somsich (HHU) for project coordination and management and Anita Snyder (www.anitaksnyder.com) for copyediting. This work has received funding from the European Research Council (ERC) and the Marie Skłodowska-Curie Actions under the European Union's Horizon 2020 research and innovation programme (Grant agreements 'SymPore' No. 951292 to WBF and "PDgate" No. 101023981 to MM, respectively). This research was also supported by the Deutsche Forschungsgemeinschaft (DFG, German Research Foundation) under Germany´s Excellence Strategy – EXC-2048/1 – project ID 390686111, and the Alexander von Humboldt Professorship, to WBF.

Data availability

Source data will be deposited at Dryad. Sequencing data for strains from this study have been deposited in the NCBI Sequence Read Archive (SRA) database under the accession codes will be provided at the time of publication. Materials will be made available under MTA; some materials were obtained from others as marked and require permission from the respective authors.

Contributions

WBF conceived of the study. J.E. performed the bioinformatic analyses; L.X., S.G. and W.S. performed proteomics and data analysis; M.D. analyzed the structure and generated fig. S4; S.H. helped to establish and advised on SIM. T.M.S, M.P., M.M., J.O.E., N.P., M.N., G.V.D, C.G. and A.D. performed imaging and/or transport studies; R.S. advised on imaging and data analyses; M.M. and A.R-E. performed split GFP studies, T.M.S, M.M., M.P., J.O.E., B.S., and W.B.F. analyzed the data; T.M.S., M.M., M.P., J.O.E., G.V.D, R.S. and W.B.F. wrote the manuscript.

Competing interests

We declare no competing interests.

Supplementary Materials

- Material and Methods
- 8 Supplementary Tables
- 10 Supplementary Figures
- 3 Supplementary files
- 2 Supplemental scripts
- Supplementary references

Figures and legends

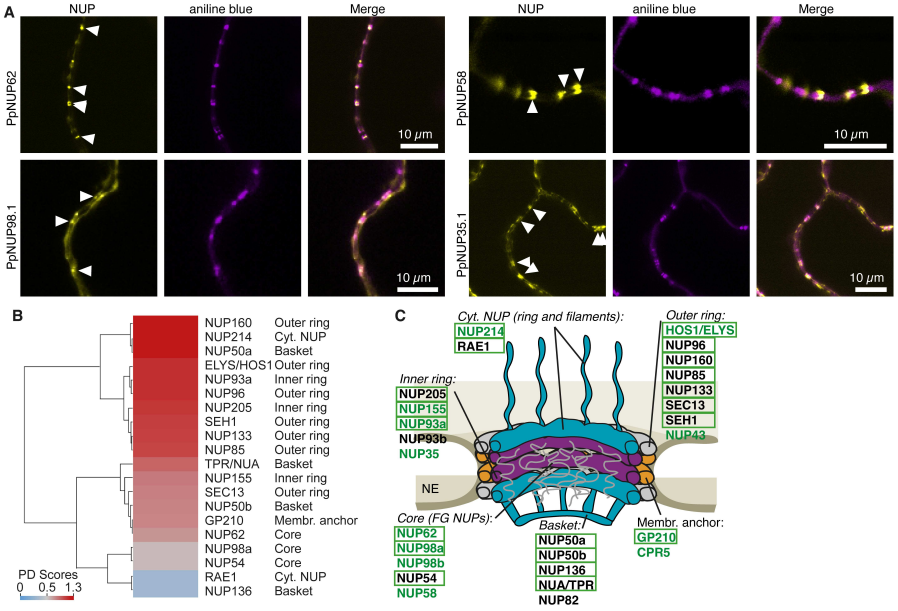

Figure 1. Identification of NUPs at plasmodesmata. (**A)** Localization of NUPs from *Physcomitrium patens* at PD. **(B)** Hierarchical clustering of PD scores of Arabidopsis NPC components found in PD proteome preparations from 5-week-old Arabidopsis shoot tissues. Clustering based on Euclidean distance of PD scores, which were averages of at least three replicate scores from separate tissue preparations. Color scale represents PD score values. PD scores above the high-confidence threshold of 0.5 are indicated in shades of red. (**C)** Scheme of an NPC embedded in the nuclear envelope with all NUPs studied in this work. NUPs listed in B are green boxed. NUPs found to be significantly enriched at PD in the transient localization assay (Fig. 2B, 3B) are written in green letters. Corresponding AGI locus identifiers in table S2. Cytoplasmic NUP is abbreviated as Cyt. NUP, and membrane anchor as Membr. anchor.

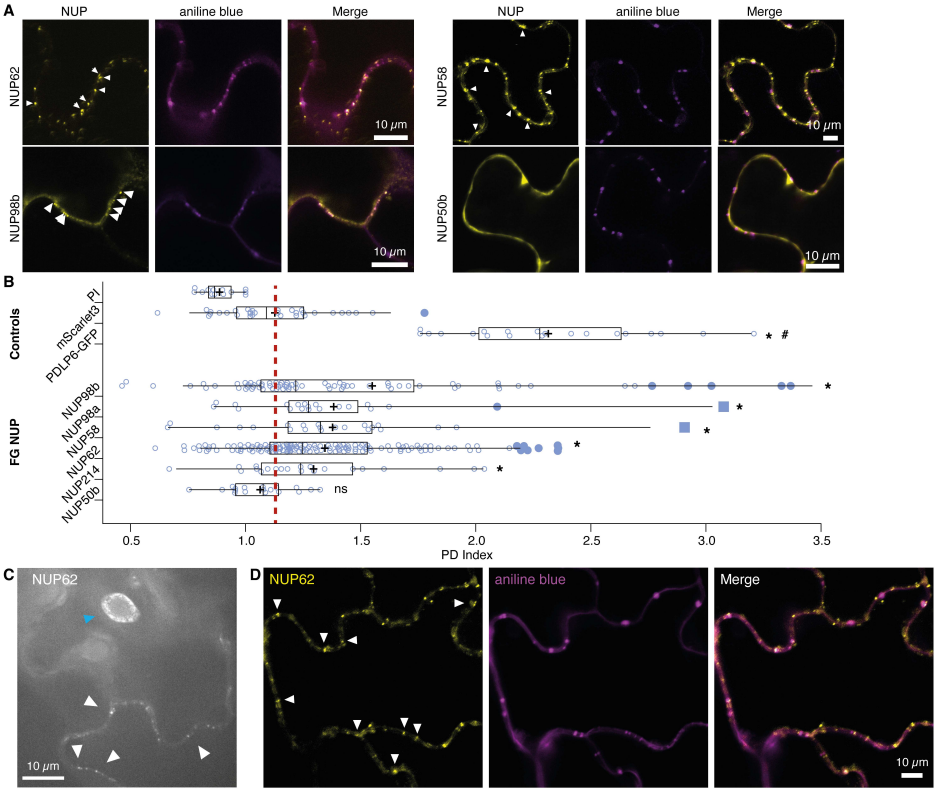

Figure 2. Analysis of the localization of Arabidopsis FG NUPs to PD. (A) Localization of selected Arabidopsis FG-NUPs after transient expression under the control of the estradiol-inducible XVE promotor in *N. benthamiana* epidermal cells using confocal microscopy. mVenus was fused to the C-terminus of different NUPs, except for Nup98a for which GFP was fused both N- and C-terminally (GFP-NUP98a-GFP). Aniline blue was infiltrated to detect callose in pit fields as an indicator of plasmodesmata. Localization was repeated in three independent experiments with similar results. (**B**) Quantification of the PD localization by PD index. Red dashed line indicates the mean PD index of mScarlet3 (cytoplasmic control). PI, propidium iodide ('membrane impermeant dye'). Significantly ($p < 0.05$) increased PD indices compared to the cell wall or cytoplasmic controls are indicated by * and #, respectively. Kruskal-Wallis Test $p = < 0.001$, p-values of Bonferroni corrected pairwise test are summarized in table S2. Median is represented by vertical line inside the box, mean is represented by the bold +. Values between quartiles 1 and 3 are represented by box ranges, and 5th and 95th percentile are represented by error bars. At least 15 images from 3 biological replicates were analyzed for each NUP. Independent localization data are shown in fig. S3. (**C and D**) Arabidopsis NUP62-GFP plant expressing NUP62 fused to GFP under its own promoter. (**C**) The localization of NUP62-GFP in 12-day-old cotyledon epidermal cells was visualized by confocal microscopy using a confocal unit CSU10 with a 100x oil-immersion lens. Blue arrowhead for nuclear localization, white arrowheads for peripheral localization of NUP-62-GFP. **(D)** Localization of NUP62-GFP in a 12-day-old cotyledon epidermal cell of stably transformed Arabidopsis line. The cotyledon was immersed in aniline blue to detect callose in pit fields as an indicator of plasmodesmata. White arrowheads in D indicate overlay of NUPs and aniline blue. Scale bar: 10 µm.

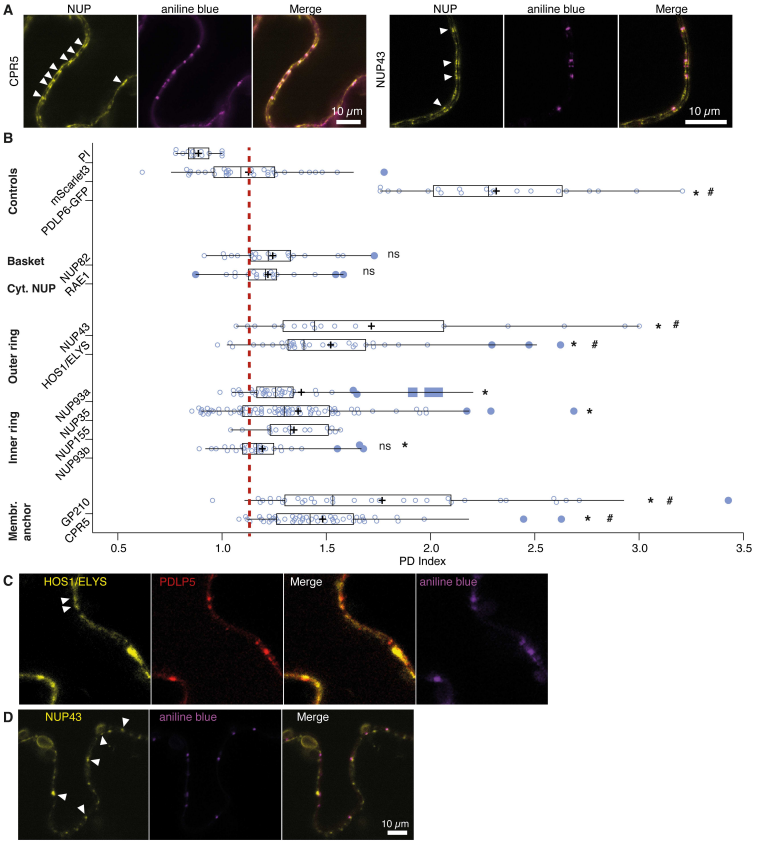

Figure 3. Dual localization of Arabidopsis scaffold and transmembrane NUPs. (A) Localization of Arabidopsis transmembrane (CPR5) and scaffold (NUP43) NUPs after transient expression under the control of the estradiol-inducible XVE promotor in *N. benthamiana* epidermal cells using confocal microscopy. mVenus was fused to the C-terminus of different NUPs. Aniline blue was infiltrated to detect callose in pit fields as an indicator of plasmodesmata. White arrowheads indicate overlay with aniline blue. Localization was repeated in three independent experiments with similar results. (**B**) Quantification of the PD localization by PD index. Red dashed line indicates the mean PD index of mScarlet3 (cytoplasmic control). PI, propidium iodide ('membrane impermeant dye'). Significantly ($p < 0.05$) increased PD indices compared to the cell wall or cytoplasmic controls are indicated by * and #, respectively. Kruskal-Wallis Test $p < 0.001$, p-values of Bonferroni corrected pairwise test are summarized in table S2. Median is represented by vertical line inside the box, mean is represented by the bold +. Values between quartiles 1 and 3 are represented by box ranges, and 5th and 95th percentile are represented by error bars. At least 15 images from 3 biological replicates were analyzed for each NUP. Independent localization data are shown in fig. S3. Control identical to Fig. 2B. (**C**) Localization of HOS1/ELYS-mCitrine and PDLP5-mScarlet3 expressed transiently under the control of the inducible XVE promotor in *N. benthamiana* epidermal cells. Aniline blue was infiltrated to stain callose that accumulates in pit fields. White arrowheads indicate overlay of HOS1/ELYS-mCitrine and PDLP5-mScarlet3 channel. The localization pattern has been repeated in three independent experiments with similar results. **(D)** NUP43-mCitrine localization at PD at 1/10 estradiol concentration and shortened induction time. White arrowheads indicate overlay with aniline blue.

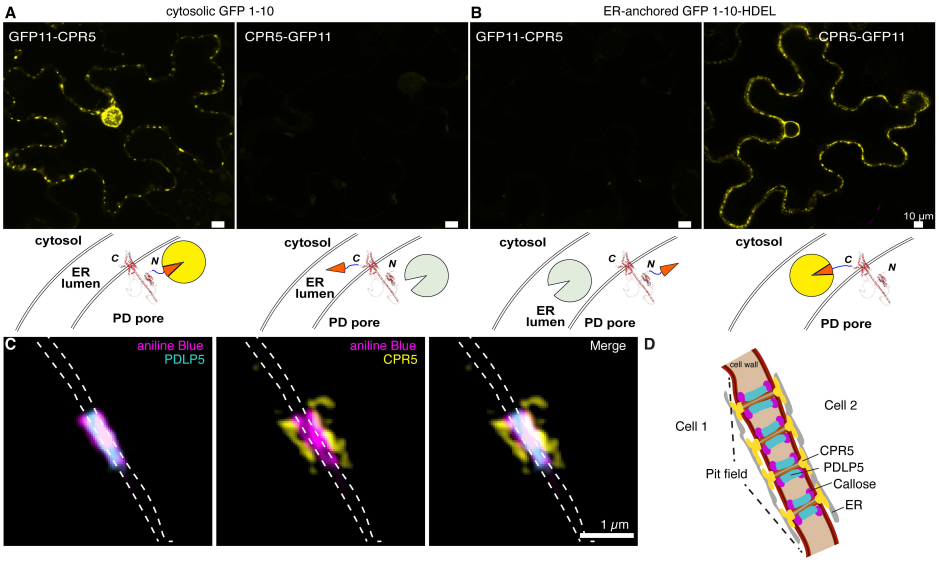

Figure 4. CPR5 topology and localization of CPR5 near PD orifices. Split-GFP membrane topology to test for the orientation of CPR5 in the nuclear pore membrane and the ER at PD. (**A)** *(left)* Fluorescence reconstitution at PD between a cytosolic non-fluorescent GFP domain lacking β-sheet 11 (GFP1-10; the circle missing a wedge) and a fusion of the GFP11 to the N-terminus of CPR5 (the red wedge). Since reconstitution occurs at PD, each cartoon indicates reconstitution in the intermembrane space between ER/desmotubule and plasma membrane. *(right)* Absence of fluorescence reconstitution between a cytosolic GFP1-10 and the fusion of the GFP11 to the C-terminus of CPR5. (**B)** *(left)* Absence of fluorescence reconstitution between an ER-retained GFP1-10-HDEL and a fusion of GFP11 to the N-terminus of CPR5. *(right)* Fluorescence reconstitution at PD between an ER-retained GFP1-10-HDEL and a fusion of the GFP11 to the C-terminus of CPR5. Repeated independently 3 times with comparable results. (**C)** Detection of CPR5-mCitrine close to the orifices of PD by Structured Illumination Microscopy (SIM) of *N. benthamiana* leaves co-infiltrated with XVE:PDLP5-mScarlet3 and XVE:CPR5-mCitrine. Prior to the imaging, leaves were infiltrated with aniline blue. PDLP5-mScarlet3 in turquoise, CPR5-mCitrine in yellow, and aniline blue in magenta. Repeated independently four times with comparable results. **(D)** Cartoon approximately to scale, illustrating plasmodesmata in a pitfield between two adjacent cells with callose marked in purple, PDLP5 in magenta and CPR5 in yellow.

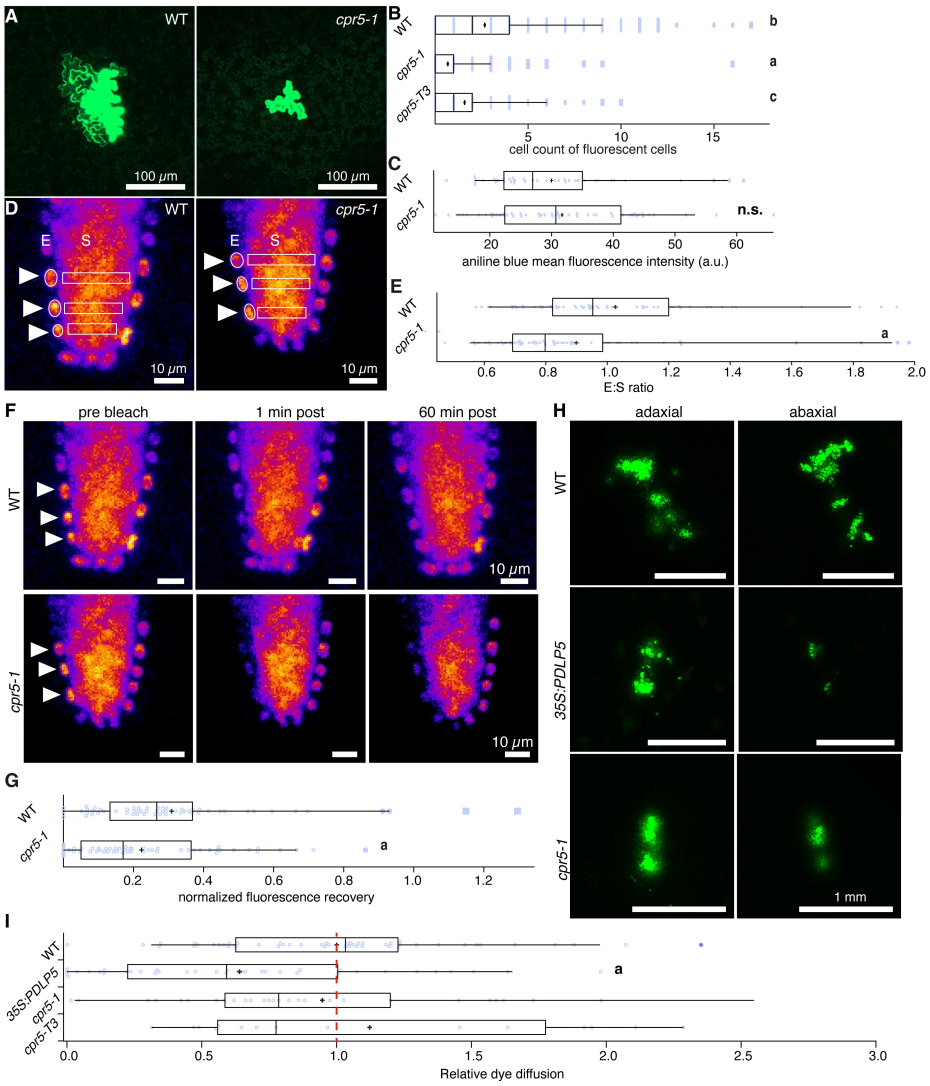

Figure 5. Defects in cell-to-cell transport of kDa-sized cargo in *cpr5* mutants. (A) Example images of intercellular 2xmEGFP movement in wild type (WT, *left*) and *cpr5-1* (*right*) Arabidopsis leaves. Leaves were bombarded with gold particles coated with p35S:mEGFP-mEGFP DNA plasmids 24 h prior to the experiment (fusion protein abbreviated as 2xmEGFP). **(B)** Quantification of the intercellular spread of mEGFP by counting fluorescent cells in the GFP channel. $n_{(WT)} = 594$ bombarded cells, 17 independent biological replicates. $n_{(cpr5\text{-}1)} = 278$ bombarded cells, 6 independent biological replicates. $n_{(cpr5\text{-}T3)} = 99$ bombarded cells, four independent biological replicates. **a** indicates significant difference to WT with $p_{(cpr5\text{-}T3)} = 0.0004$; **b** indicates significant difference to WT with $p_{(cpr5\text{-}1)} < 10^{-15}$; $p_{(cpr5\text{-}1 \text{ vs. } cpr5\text{-}T3)} = 0.0002$ (Kruskal-Wallis test with Bonferroni correction for pairwise comparison). **(C)** Callose quantification. $n_{(WT)} = 4$ independent experiments, $n_{(cpr5\text{-}1)} = 5$ independent experiments, graph summarizes all experiments. Student´s *t*-test $p = 0.48$. **(D)** Sum projections showing SHR–GFP distribution in WT (*left*) and *cpr5-1* mutant (*right*) root. White circles and boxes indicate positions of endodermis nuclei (E,

arrows) and corresponding regions in the stele (S, white boxes). **(E)** Quantification of SHR–GFP endodermis:stele ratio (E:S) for WT and *cpr5-1* mutant. $n_{(WT)}$ = 62 nuclei, $n_{(cpr5\text{-}1)}$ = 62 nuclei, with 3-4 nuclei analyzed per root. **a** indicates significantly decreased E:S in *cpr5-1* mutant, based on Mann-Whitney U test with p = 0.0006. **(F)**, Sum projections showing SHR–GFP distribution in WT (*top*) and *cpr5-1* (*bottom*) background. **(G)**, Quantification of relative SHR–GFP fluorescence recovery for WT and *cpr5-1* mutant after 1 h. Fluorescence recovery was normalized to a control nucleus in the endodermis (see Methods and fig. S9F). n(WT) = 59 bleached nuclei, n(*cpr5-1*) = 59, per root 3-4 nuclei were bleached. Student´s t-test p = 0.037 indicating significantly decreased fluorescence recovery after 60 min. **(H and I)** PD permeabilities examined by CFDA/CFSE-based DANS dye loading assays. **(H)** Epifluorescence reporting on CF diffusion in the epidermis of the adaxial (*left*) and abaxial (*right*) side of the leaf. WT *(top), 35S:PDLP5* (*middle*), and *cpr5-1* (*bottom*). Bars, 1 mm. **(I)** Quantification of CF diffusion in WT and mutant lines. $n_{(WT)}$ = 49 plants, 7 independent biological replicates; $n_{(35S:PDLP5)}$ = 38 plants, 5 independent biological replicates; $n_{(cpr5\text{-}1)}$ = 29 plants, 5 independent biological replicates; $n_{(cpr5\text{-}T3)}$ = 15 plants, 5 independent biological replicates. Fluorescent areas on the abaxial side were identified using auto threshold and Fiji YEN-algorithm with user modifications. The same threshold setting was used for the adaxial side. The extent of dye diffusion was quantified by the ratio between the areal spread of fluorescence on the abaxial side and the areal spread of fluorescence on the adaxial side. **a** indicates significantly different at the α = 0.032 level according to Bonferroni-corrected pair wise comparison following Kruskal-Wallis analysis.

15

7.2. Summary

Research question:

- What are the key components of PD?
- Are molecular mechanisms underlying PD transport similar to mechanisms underlying NPC transport?

Objective

Testing localization of NPC components at PD and assessing their involvement in PD-mediated transport.

Hypothesis

NPC proteins are structural components at PD and functionally affect intercellular transport.

7.2.1. Result

Identification of 7 NUPs that dual localized to NPC and PD. Also, mutants of transmembrane NUP CPR5 showed callose-independent reduced diffusive and selective intercellular transport for macromolecules. The results indicate the functional role of NUPs in intercellular transport. Accordingly, it was hypothesized that NUPs were recruited to form a PD pore gating complex (PDPC) in the green lineage.

8. Gene editing in *P. patens*

Status: Unpublished
Contribution: 100 % (specified in appendix)

8.1. Aim of this chapter

8.1.1. Research question:

- Are molecular mechanisms underlying PD transport similar to mechanisms underlying NPC transport?

8.1.2. Objective

Generating *nup* knock-outs and *NUP-FP knock-ins* in bryophyte *P. patens*, via CRISPR-Cas9 and prime editing.

8.2. Introduction

CRISPR-Cas9 enables targeted induction of DNA double-strand breaks (DBS), which allows full coding sequence knock-outs and targeted *fluorescent protein gene (FP)* knock-in. For full coding sequence knock-outs two single guide (sg)RNAs are targeted to the 5'- and 3'-UTR of the gene of interest. *FP* knock-ins require the addition of an exogenous template DNA that contains an *FP* flanked by homolog upstream and downstream regions of the CRISPR-targeted site. The internal DNA repair machinery uses the template DNA to repair the Cas9-induced DBS via homologous recombination, which results in *FP* integration in the native locus. While native *FP* knock-ins have low efficiencies in Arabidopsis, they are standardized in *P. patens* due to its high homologous recombination rate [222]. Prime editing allows targeted rewriting of DNA sequences via a prime editor (PE). The PE is a fusion of a Cas9 nickase (only generates single strand break) and an engineered reverse transcriptase. The corresponding prime editing guide (peg)RNA contains sgRNA as a target sequence, fused to a structural RNA scaffold, as well as a template for the reverse transcriptase [223,224]. Additionally, it was demonstrated that pegRNA fusion to RNA sequences with secondary structures shields the pegRNA from nucleases. This engineered pegRNA (epegRNA) results in higher prime editing efficiencies [225,226].

Here, CRISPR-Cas9 was employed to edit *P. patens NUP*s. *PpCPR5* knock-outs and several *NUP FP* knock-ins were generated. Additionally, both *PpCPR5* versions were prime edited to imitate the well-established Arabidopsis *CPR5* G420D (also *cpr5-1*) mutation [207], which showed a drastic decrease in intercellular transport in Schladt *et al.* 2024 (Chapter V) [227]. Currently, it is unknown why the single AA change affects CPR5 function so drastically, as localization of *At*CPR5 G420D showed a similar PD association as wild-type *At*CPR5 (Figure 12, appendix). *P. patens* is an ancestral land plant and a suitable model to test the evolution of NUP involvement at PD. Further, *P. patens* harbors thin tissues, with protonemata and leaflets that are only one cell layer thick, which allowed the establishment of FIB-enabled cryo-ET in *P. patens* (Marcel Dickmanns, personal communication). Employing cryo-ET in *Ppnup* mutants (e.g., *Ppcpr5* mutants) would allow to test their structural involvement at PD in native conditions.

8.3. Material and Methods

8.3.1. sgRNA design and DNA construction

Vectors for transient localization of PpCPR5 were constructed via GreenGate cloning or In-Fusion cloning, Takara Bio Europe. Primers for amplifications are listed in appendix (Table 5). The GreenGate plasmid kit used for generation of plant transformation constructs was a gift from Jan Lohmann (Addgene kit # 1000000036) [228]. Phusion Plus DNA Polymerase, BsaI-HF and T4 ligase, required for PCRs and GreenGate cloning steps were purchased from New England Biolabs. All sgRNAs were designed via CRISPOR [229] and ordered as overlapping primer sequences (Table 6, appendix). sgRNAs were designed for *PpCPR5.1* (Pp3c21_530), *PpCPR5.2* (Pp3c22_5670), *PpGp210* (Pp3c27_1470), *PpHOS1.1* (Pp3c24_4970), *PpIMB3* (Pp3c11_22120), *PpNUP62* (Pp3c15_14630), *PpNUP98* (Pp3c3_17910), *PpSec13.1* (Pp3c19_9370), and *PpTrp/NUA* (Pp3c8_8020). For gene knock-outs two sgRNAs targeting 3'-UTR and 5'-UTR were generated. Each sgRNA was cloned into pGB3α1_vector via BsaI-mediated GoldenBraid cloning. Final pGB3α1_target sgRNA vectors contained target sgRNA flanked by a *PpU6-1* promoter, *esgRNA_scaffold_SUP4* terminator. pGB_*PpU6-1* promoter, pGB_*esgRNA_scaffold_SUP4* terminator and pGB3α1_vector were kindly gifted from Fabien Nogué. For *FP* knock-ins one sgRNA, close to the respective insertion site was generated. *FP* knock-ins required an additional template vector, which contained homologous sequences ~400 bp upstream and downstream of the PAM, flanking in-frame linker region, and FP coding

sequences (pTwistAmp_FP template). The first batch of *PpCPR5* constructs contained GFP or mCherry, while the second batch of vectors contained a *P. patens*-codon-optimized mVenus (via VectorBuilder). The template vector functions as a template for homologous recombination and enables targeted insertion of the FP. PAM or sgRNA binding sites on the template were changed as silent mutations according to the codon usage of *P. patens* [230], to prevent Cas9 off-targeting on the template vector. Genotyping primers were designed upstream and downstream of the coding sequence (knock-out) or the flanking sequences (knock-in) in the template vector to ensure genomic integration of *FPs* (

Table 7, appendix). For prime editing pegRNA targets and reverse transcription templates were designed with PlantPegDesigner [231]. Final prime editing template vectors contained PpU6-1 promoter, pegRNA target, esgRNA_scaffold, reverse transcription template, peg-linker, structured RNA-motif, and SUP4 terminator (pTwistAmp_epegRNA). All template vectors were gene-synthesized by Twist Bioscience. BsaI-HF and T4 ligase, required for both cloning steps, were purchased from New England Biolabs. Target sgRNA vectors were Sanger-sequenced. All DNA sequencing was performed by Microsynth Seqlab. All primers were synthesized by Integrated DNA Technologies.

8.3.2. Plant growth conditions

Physcomitrium growth was performed as described in Gombos *et al.* 2022. Long-term storage of confirmed edited lines is maintained in 4 ml tubes containing 2 ml BN-media at 6° C with daily 30 min light pulses.

8.3.3. Protoplast transfection

Physcomitrium protoplast were transfected with pGB3α1_target sgRNA, pBRNF (carrying G418 resistance) and GB_pro*UBI*:*Cas9* respectively. For FP knock-ins pTwistAmp_*FP* template was included. For prime editing pBRNF, GB_pro*UBI:PPE* and respective pTwistAmp_*epegRNA* were cotransfected. Transfection was performed as described in Charlot *et al.* 2022 [232]. As I performed the transfections at INRAE Versailles-Saclay, and transferred the transfected plants back to HHU Düsseldorf, I performed all transfections minimum twice, to prevent losses from contaminations.

8.3.4. Selection of transfected *P. patens* lines and genotyping

Two days after transfection, protoplast were transferred on G418 (30 µg/µl) containing BN-plates and grown for one week to select for transfected plants. For each transfection 96 surviving plants were picked, transferred to BN-plates, and grown for two-three weeks. Afterwards, genotyping was performed, leaflets were picked in 96-well cluster tube plates (each tube containing two metal beads) and on BN-plates again for propagation. 96-well plates were frozen at -80° C. Frozen moss tissue was grinded in a Retsch MM400 ball mill for 2 min at 25 Hz. 150 µl Edwards Buffer (200 mM Tris pH 7.5, 250 mM NaCl, 25 mM EDTA, 0.5% SDS) [233], was added for gDNA extraction. Plates were incubated at 65° C for 10 min, moss tissue was pelleted by a 15 min centrifugation at 4000 g. 100 µl supernatant were transferred into fresh 96-well cluster tube plates, containing 80 µl isopropanol in each tube. Content was mixed and incubated 2 min at room temperature. DNA was pelleted by by15 min centrifugation at 4000 g, supernatant was discarded, and the pellet was washed with 70 % ethanol. After a 5 min centrifugation at 4000 g, ethanol was discarded and DNA pellet was dried at 65° C and resuspended in 100 µl TE-buffer at 4° C overnight. 1 µl of extracted DNA was used for genotyping PCRs. Leaflets of plants that were confirmed by genotyping were selected on G418 again. Only lines that lost the G418 resistance were long-term stored as “clean” edited lines.

8.4. Results and Discussion

To test the localization of *P. patens* CPR5.1 and CPR5.2, I generated C-terminal FP-fusions and transiently overexpressed them in *N. benthamiana.* In PCRs from cDNA, I amplified *CPR5.2* sequences that contained a 29 bp intronic insertion, which led to a frameshift and premature stop codon in the N-terminal part of the translated CPR5.2 protein (frame-shift after AA 456, stop codon at after AA 466). The intronic insertion matched *P. patens* expression profiles of RNAseq data (

Figure **9**A), which indicated that the intron insertion is abundant in *CPR5.2* mRNAs and possibly a result of alternative splicing. Hence, the CPR5.2 N-terminal truncation may have a physiological function in line with previously hypothesized proteolytic cleavage of Arabidopsis CPR5 N-terminus [213,214]. Accordingly, CPR5.1-mVenus, CPR5.2a-mVenus, and CPR5.2a N-terminus [1-456AA + intronic insert: (CPR5.2a-N)]-mCitrine were cloned and localized. All versions showed localization to the NE (data not shown) and overlay with PD-marker aniline blue (

Figure **9**B), indicating PD localization.

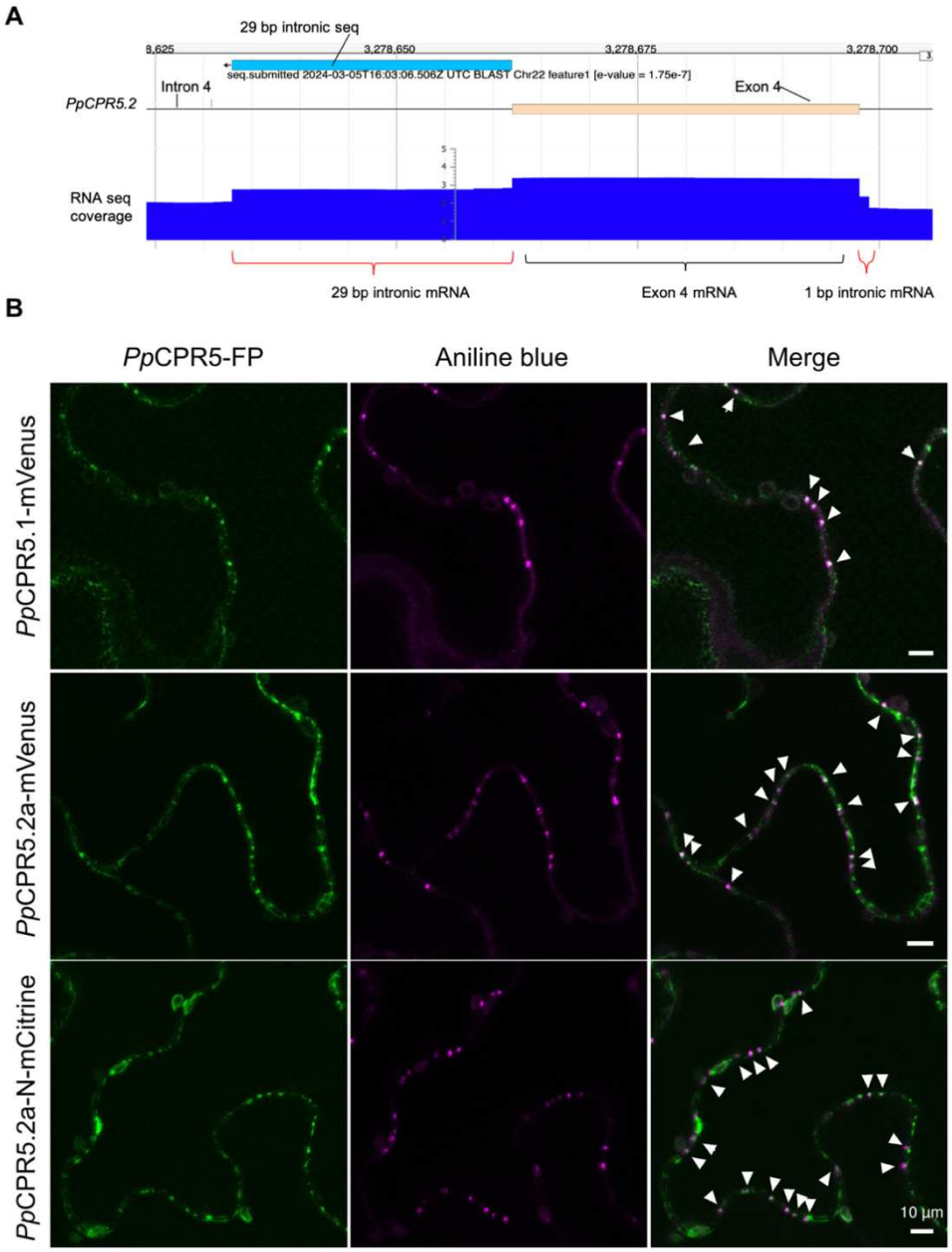

Figure 9: Analysis of *Pp*CPR5-FP PD localization
A RNAseq-coverage of 29 bp intronic insertion before Exon 4 of *PpCPR5.2a*. Comparison of the *P. patens* RNAseq-coverage and exon annotation indicates that 29 bp intronic insertion or 1 bp intronic insertions can be contained in the *PpCPR5.2a* mRNA. Both insertions lead to a premature stop codon. Genomic sequences and mRNA coverage were visualized with JBrowse [234]. **B** Localization of *Pp*CPR5.1-mVenus, *Pp*CPR5.2a-mVenus,

and *Pp*CPR5.2a-N-mCitrine (green) transiently expressed under the control of the estradiol-inducible XVE promoter in *N. benthamiana* epidermal cells using confocal microscopy. FP was fused to the C-terminus of PpCPR5. Aniline blue (magenta) was infiltrated to detect callose in pit fields as an indicator of plasmodesmata. Arrows indicate puncta with overlaying aniline blue and FP fluorescence. Localization was repeated in two independent experiments with similar results. Scale bars: 10 µm.

As PD localization appeared to be conserved between Arabidopsis and *P. patens* CPR5, I generated stable FP-fusion lines and *Ppcpr5* mutants via CRISPR-Cas9 and prime editing as the next step.

P. patens editing was performed in two batches. In the first CRISPR-Cas9 batch full coding sequence knock-outs for *PpCPR5.1* and *PpCPR5.2*, a double knock-out of both *PpCPR5s*, *PpCPR5.1-GFP*, PpCPR5*.2-GFP* and *PpCPR5.2-mCherry*, as well as a *PpCPR5.1-GFP_PpCPR5.2-mCherry* (double tag) line were generated. Further, via prime-editing *PpCPR5.1 At*G420D and *PpCPR5.2 At*G420D, as well as a double prime edited *PpCPR5 At*G420D line, was generated. Essentially, the *P. patens* Gly (G) residue homologous to the *AtCPR5* G420D was edited into an Asp (D) in both of *PpCPR5* homologs. CRISPR-Cas9 editing in *P. patens* is well established [232] and had efficiencies of ~10-70 %, hence per line only 48 plants were genotyped. Prime-editing, on the other hand, has lower efficiencies in *P. patens* (<5 %) [224,225]. Hence, 96 plants were genotyped for the double prime edit line. The *CPR5.1* prime edit resulted in 19/96 (19.8%) positive plants, and the *CPR5.2* prime edit in 5/96 (5.2 %) positive plants. Only one plant contained both edits, which aligns with the multiplied efficiency of both epegRNAs (1.0 %). To our knowledge, this is the first report of a double prime edit event *in P. patens* (personal communication Pierre-François Perroud and Fabien Nogué). Notably, this was likely possibly due to the comparably high efficiency for the *CPR5.1* epegRNA of nearly 20 %. In summary, for the first batch over 1600 plants were picked (duplicates, to prevent losses by contamination), and 432 plants were genotyped. All positive lines were verified by sequencing and long-term stored [Table 1, (Figure 13, Appendix)].

CRISPR-mediated *FP* knock-in allows observation of proteins of interest at close to native expression levels. Unfortunately, mostly no fluorescence could be observed in all *FP*-fusions lines of the first batch. Occasionally, single moss cells showed weak cytosolic fluorescence, which was not in line with the 5 TM-domains of *Pp*CPR5 and likely presented free FP fluorescence. Indicating that the C-terminal FP fusions were truncated. Similar observations were made for overexpression of CPR5-FP fusions in stable Arabidopsis lines by us (data not shown), as well as other groups [235]. Also, N-terminal FP fusions of rice CPR5.1 and CPR5.2 showed high fluorescence in transient expression in *N. benthamiana*, while C-terminal fusions could barely be detected (personal communication, Andrea Restrepo). This indicates a conserved feature in which the CPR5 C-terminus seems to complicate FP-fusions, especially in the native organism. Notably, *At*CPR5-mVenus and *Pp*CPR5-mVenus showed detectable fluorescence when transiently expressed in *N. benthamiana* (see above).

Accordingly, a second batch of CRISPR-Cas9 edited FP knock-ins was generated, tagging 9 *PpNUP*s with a *P. patens* codon-optimized *mVenus*. In summary the second batch contained, *mVenus-PpCPR5.1*, *PpCPR5.2-mVenus* insertion (as CPR5.2 contains a N-terminal signal peptide), *PpGp210-mVenus*, *PpHOS1.1-mVenus*, *mVenus-PpIMB3*, *mVenus-PpNUP62*, *mVenus-PpNUP98, PpSec13.1-mVenus* and *mVenus-PpTrp/NUA*. Again over 1700 plants were picked (in duplicates). Compared to the first batch, fluorescence could be confirmed in whole plants, via epifluorescence microscopy. While subcellular localization of the NUP-mVenus fusion will require confocal microscopy, the fluorescence indicates successful editing.

Table 1: Genotyped *P. patens* lines
Summary of first batch of *PpCPR5* lines, all lines were genotyped, sequenced and long-term stored.

Generated Lines	Line Number
1) Ppcpr5.1 .KO	49
1) Ppcpr5.1 .KO	54
1) Ppcpr5.1 KO	59
1) Ppcpr5.1 KO	66
4) *Ppcpr5.* double KO	15
4) *Ppcpr5.* double KO	18
4) *Ppcpr5.* double KO	28
4) *Ppcpr5.* double KO	38
5) PpCPR5.1-GFP	14
5) PpCPR5.1-GFP	19
5) PpCPR5.1-GFP	20
5) PpCPR5.1-GFP	41
6) PpCPR5.2-GFP	1
6) PpCPR5.2-GFP	31
7) PpCPR5.2-mCherry	33
7) PpCPR5.2-mCherry	36

Generated Lines	Line Number
7) PpCPR5.2-mCherry	40
7) PpCPR5.2-mCherry	46
8) *PpCPR5* Double Tag	36
11) Ppcpr5.2 KO	1
11) Ppcpr5.2 KO	7
11) Ppcpr5.2 KO	39
11) Ppcpr5.2 KO	43
13) *PpCPR5.1* prime edit G420D	8
13) *PpCPR5.1* prime edit G420D	11
13) *PpCPR5.1* prime edit G420D	35
13) *PpCPR5.1* prime edit G420D	46
13) *PpCPR5.2* prime edit G420D	27
13) *PpCPR5.2* prime edit G420D	68
13) *PpCPR5.2* prime edit G420D	81
13) *PpCPR5* double prime edit G420D	50

8.5. Outlook

The *NUP-mVenus* knock-in lines will be genotyped to ensure in-frame knock-in and analyzed for subcellular NUP localization by confocal microscopy. *Ppcpr5* knockouts and prime editing lines will be phenotyped for growth defects and can be used in transport assays, to test if CPR5's role in intercellular transport is conserved in land plants. If CPR5 displays conserved functions in PD-mediated transport, the *Ppcpr5* knock-outs lines could be used in FIB-enabled cryo-ET to study how CPR5 depletion affects PD structurally.

Chapter VI

9. PD transport has features of surface-dependent NPC transport

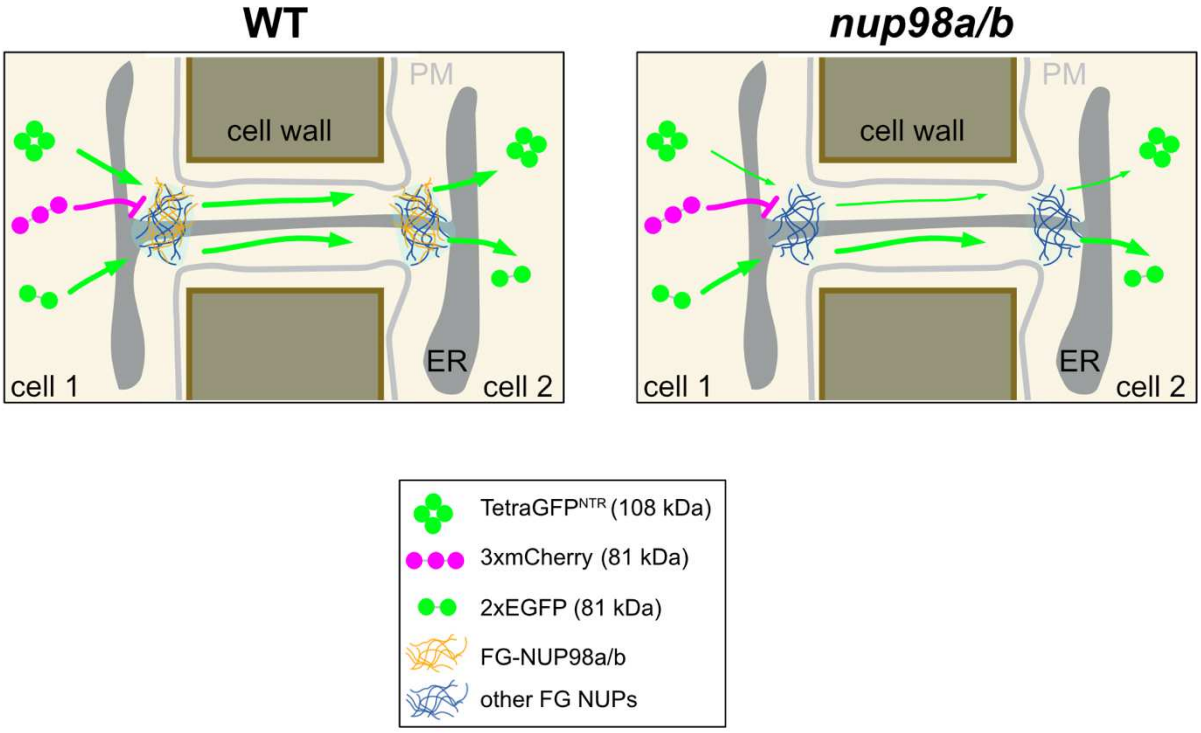

Status: Unpublished
Contribution: 100% (specified in appendix)

9.1. Aim of this chapter

9.1.1. Research question:

- Are molecular mechanisms underlying PD transport similar to mechanisms underlying NPC transport?

9.1.2. Objective

Investigating the effect of NTR-like surface properties on intercellular movement.

9.1.3. Hypothesis

Intercellular transport across PD is facilitated by similar features as nuclear transport.

9.2. Introduction

The NPC permeability barrier is a phase-separated domain constituted by FG-NUPs. Due to their hydrophobic surface features, NTRs can interact with FG-NUPs and thereby facilitate the transport of bound cargo molecules (for a detailed review of the mechanism see Chapter IV). Elegant experiments by Frey *et al.* and Ng *et al.*, employed engineered GFP variants that mimic surface features of NTRs to test NPC transport features [145,148]. The NTR-like GFP variant with the highest reported FG-specificity is TetraGFP^{NTR} , a tetrameric GFP variant that facilitates rapid FG-phase passage despite its size [148] (110 kDa, stokes diameter: 7.73 nm) (Figure 10A)
PD, on the other hand, have been described to be gated by the SEL. Molecules larger than the SEL remain cell-autonomous unless they are selectively transported. Generally, 3xFP-tandems are non-mobile in Arabidopsis shoots, leaves, and roots [11,227]. Hence, a 3xmCherry tandem, which is comprised of 3xmCherry subunits fused by flexible linkers (83 kDa, stokes diameter: 7.87 nm) (Figure 10A), was used as non-specific cell-autonomous proxy.
While TetraGFP^{NTR} was used to test the effect of NTR-like features on intercellular mobility. To assess the potential involvement of FG-NUPs at plasmodesmal gates, particle bombardment assays were performed in Arabidopsis WT and a *nup98a/b* mutant that is substantially reduced in encoded FG-repeats.

9.3. Material & Methods

9.3.1. Plant Growth

Arabidopsis seedlings were grown under light conditions as described in Schladt *et al*., 2024 [227] (see above). All seedlings described in the Result section were grown on ½ MS media supplemented with 2% sucrose, to rescue the early senescence phenotype of the *nup98a/b* double mutant [236]. Additionally, WT plants for mEGFP and 2xmEGFP tandem bombardment (Table 2) were grown on ½ MS supplemented with 1% sucrose, and are hence only described in the discussion section. In general, we observe significantly increased intercellular movement at 2% sucrose supplementation (observed in WT for 2xEGFP by Oliver Kraft, Master student).

9.3.2. Plasmid construction

TetraGFP^{NTR} coding sequence was taken Ng *et al*. 2023 and Frey *et al*. 2018 [145,148], codon optimized for Arabidopsis and gene synthesized as gBlock by Integrated DNA Technologies. TetraGFP^{NTR} gBlock was used as a template for amplification with Tetra GFP^{NTR} FW ggc (TTTGGTCTCAGGCTCTATGACTTCAAGAGGGGAAG) and Tetra GFP^{NTR} RV ggc (TTTGGTCTCACTGATCTAATAAGTTCGTCCATACC), to add overhangs for restriction-ligation cloning into the pGGC-000 GreenGate entry vector. The *Ubq10* pro: Ω-Element-*3xmCherry* cassette was amplified from a vector that was kindly gifted by Elmehdi Bahfid and cloned into the pGGF-000 GreenGate entry vector [amplified by 3xmCherry FW (TTTGGTCTCAactacgacgagtcagtaataaacggcgtc) and 3xmCherry RV (TTTGGTCTCAatactatgagcccatcttatctttaatcatattcc)]. The final *CaMV 35s* pro:T*etraGFP^{NTR}*/ *Ubq10* pro: Ω-Element-*3xmCherry* expression vector was generated via Greengate cloning. The GreenGate plasmid kit used for the generation of plant transformation constructs was a gift from Jan Lohmann (Addgene kit # 1000000036) [228]. Phusion Plus DNA Polymerase, BsaI-HF, and T4 ligase, required for both cloning steps were purchased from New England Biolabs. Entry vectors were Sanger-sequenced for coding sequence ,and the final expression vector was full plasmid sequenced. All DNA sequencing was performed by Microsynth Seqlab.

9.3.3. Particle bombardment

Particle bombardment experiments were performed as described in Schladt *et al*., 2024 [227] (Chapter V). 2xEGFP tandem bombardment (at 2% sucrose) was performed and counted by Oliver Kraft, (Master student) under my supervision. All other bombardments were performed and analyzed by me.

9.3.4. Bioinformatics and statistical analysis

Protein structures were modeled with AlphaFold3 [237] and visualized via PyMOL V3.1.1 Schrödinger, LLC [238]. Plots and statistics were calculated with OriginLab 2021. Hydrodynamic protein properties were predicted with HullRad V10 [239]. Figures and Plots were refined with Affinity Designer V1.10.8.

9.4. Results

9.4.1. PD transport has features of surface-dependent NPC transport

To test the effect of NTR-like surface properties on intercellular transport 3xmCherry tandem and TetraGFP^{NTR} were co-bombarded into leaves of Arabidopsis seedlings (Figure 10B). As expected, 24 h post bombardment, 3xmCherry tandem remained cell-autonomous (mean movement 0.0 cells). Surprisingly, TetraGFP^{NTR} moved intercellularly and was predominantly observed in nuclei of distal cells (Figure 10B). On average, TetraGFP^{NTR} moved to 2.9 cells (Figure 10C, Table 2). Structure-based prediction of the free diffusional coefficient of 3xmCherry tandem and TetraGFP^{NTR} indicated similar hydrodynamic diameter and diffusion coefficients for both FPs (Table 2). It is unlikely that the highly significant increase in movement of TetraGFP^{NTR} compared to 3xmCherry tandem (Kruskal-Wallis-ANOVA with post-hoc Dunn-test: *p*-Value=2.6x10^{-42}) was due to the minimal difference in stokes diameter (1.6 Å) or diffusion coefficient (1 µm^2/s) (Figure 10A, Table 2). Instead, as their hydrodynamic properties are similar, the increased TetraGFP^{NTR} movement may be a consequence of its NTR-like surface. This is in line with the hypothesis that PD might share NPC-like surface-dependent transport features.

TetraGFP^{NTR} was evolved to preferentially pass through FG-based permeability barriers [148]. Hence, TetraGFP^{NTR} and 3xmCherry tandem were co-bombarded into the Arabidopsis *nup98a/b* double mutant, which is substantially reduced in FG-repeats [*nup98a/b* contains 45.6% of WT encoded FG-motifs, (Table 3)]. Surprisingly, TetraGFP^{NTR} moved significantly less in the *nup98a/b* double mutant than in WT, with an average of 1.1 cells (and a median of 0 cells), while 3xmCherry tandem remained cell-autonomous (Figure 10B & C). Conversely, bombardment of a 2xEGFP tandem (55 kDa, stokes diameter: 6.49 nm) into WT and the *nup98a/b* mutant showed no significant differences of intercellular movement (Figure 10D). These results are in line with TetraGFP^{NTR}'s FG-specificity and indicate that FG-repeat depletion in Arabidopsis specifically reduces intercellular TetraGFP^{NTR} movement, while less FG-specific fluorescent proteins (2xEGFP tandem) can retain their intercellular passage. Of note, 2xEGFP tandem intercellular movement in Arabidopsis WT leaves is not significantly increased over TetraGFP^{NTR} movement (Figure 10D), although 2xEGFP tandem has only 50 % of TetraGFP^{NTR}'s mass and a 57 % higher translational diffusion coefficient (Table 2). Conclusively, TetraGFP^{NTR} is selectively transported via Arabidopsis leaf PD despite being larger than the SEL. Intercellular TetraGFP^{NTR} movement might be a consequence of its NTR-like surface properties, which is potentially facilitated by the presence of an FG-based mechanism, as FG-repeat reduction specifically reduces TetraGFP^{NTR} movement, and not 2XEGFP tandem movement (Figure 10E).

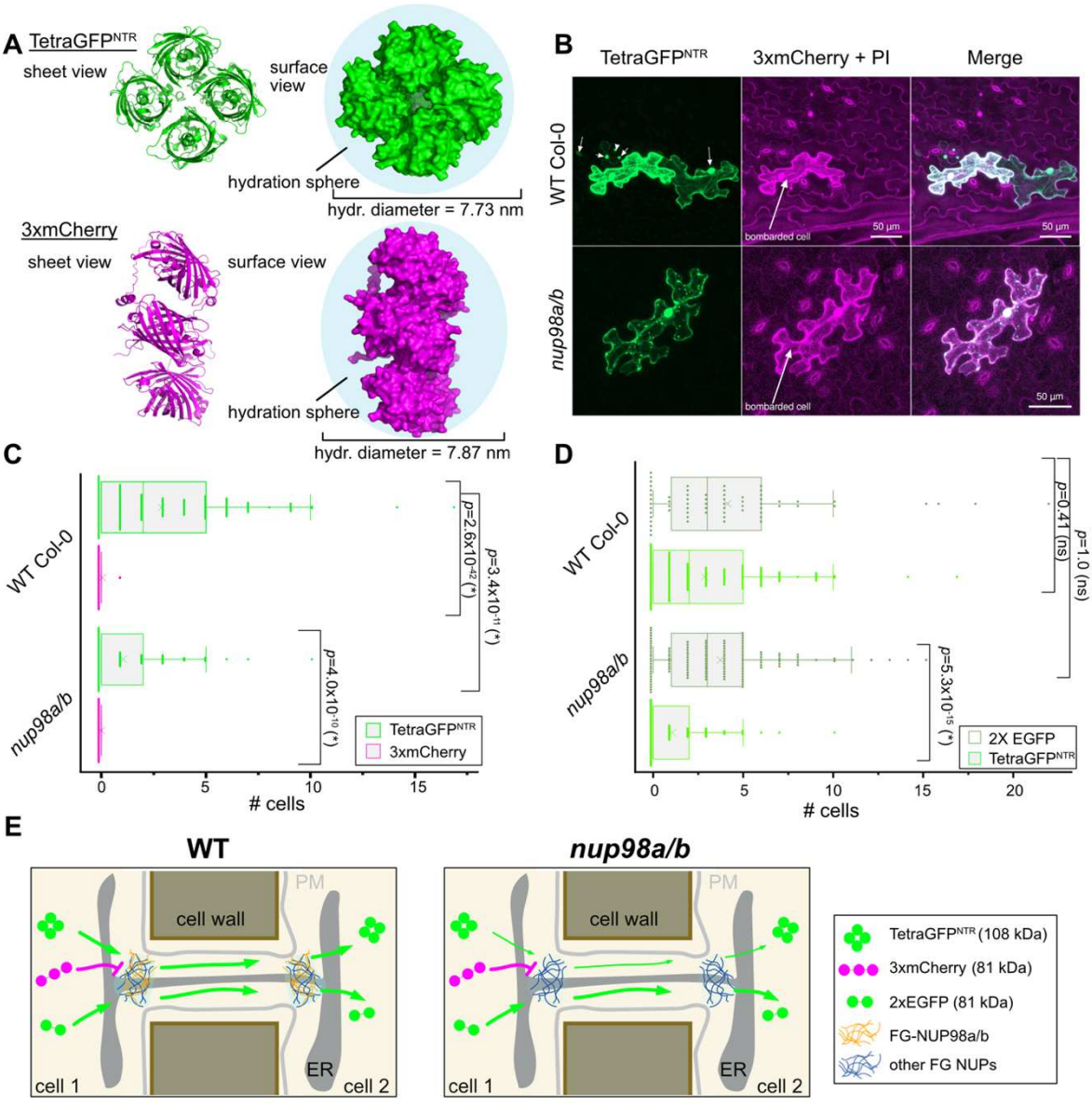

Figure 10: TetraGFP^{NTR} transport

A AlphaFold 3 prediction of TetraGFP^{NTR} and 3xmCherry tandem. Hydrodynamic diameters were predicted with HullRad V10 and are indicated in the figure. The hydration sphere of both proteins is indicated by a light blue hull **B** Confocal image of co-bombardment of TetraGFP^{NTR} (green) and 3xmCherry tandem (3xmCherry) (magenta) in WT and *nup98a/b* mutant background. Arabidopsis leaves were bombarded with gold particles coated with *CaMV 35s* pro:*TetraGFPNTR*/ *Ubq10* pro: Ω-Element-*3xmCherry* plasmids 24 h prior to the experiment. Cell walls were stained with propidium iodide (PI) to distinguish cells. White arrows in green channel indicate intercellular movement of TetraGFP^{NTR}. The bombarded cell is indicated by white arrow in magenta channel. Scale bar: 50 µm. **C** Quantification of the intercellular spread of TetraGFP^{NTR} and 3xmCherry tandem by counting fluorescent cells in each channel. $n_{(WT)} = 171$ bombarded cells, 3 independent biological replicates. $n_{(nup98a/b)} = 146$ bombarded cells, 3 independent biological replicates. $p_{(WT;\ Tetra\ vs\ 3xmCh)} = 2.6x10^{-42}$, $p_{(nup98a/b;\ Tetra\ vs\ 3xmCh)} = 4.0x10^{-10}$ and $p_{(WT\ vs\ nup98a/b;\ Tetra)} = 3.4x10^{-11}$ were all determined by Kruskal-Wallis test with post-hoc Dunn test. **D** Quantification of the intercellular spread of TetraGFP^{NTR} and 2xEGFP tandem by counting fluorescent cells in each channel. $n_{(WT;\ 2xEGFP)} = 73$ bombarded cells, 3 independent biological replicates. $n_{(nup98a/b;\ 2xEGFP)} = 145$ bombarded cells, 3 independent biological replicates. (*) indicates a significant difference to compared dataset, ns indicates no significance. $p_{(WT;\ Tetra\ vs\ 2xEGFP)} = 0.41$, $p_{(WT\ vs\ nup98a/b;\ 2xEGFP)} = 1$, were all determined by Kruskal-Wallis test with post-hoc Dunn test. TetraGFP^{NTR} data is the same as in B. Median is represented by vertical line inside the box, mean is represented by the bold X. Values between quartiles 1 and 3 are represented by box ranges, and 5th and 95th percentile are represented by error bars.**E** Illustration for FG-dependent TetraGFP^{NTR} intercellular movement in FG-reduced *nup98a/b* mutant.

Table 2: Movement and hydrodynamic properties of used FP variants
½ MS media sucrose supplementation indicated by: suc

Property	mEGFP	2xEGFP	3xmCherry	TetraGFP^{NTR}
#Amino Acids	239	497	750	956
Molecular Mass of the protein (M) [kDa]	26.998	55.465	83.354	110.21
mean cell # FP moved to in WT (2% suc)	NA	4.12	0.04	2.88
mean cell # FP moved to in WT (1% suc)	10.87	2.72	NA	NA
mean cell # FP moved to in *nup98a/b* (2% suc)	NA	3.73	0	1.05
median cell # FP moved to in WT (2% suc)	NA	3	0	2
median cell # FP moved to in *nup98a/b* (2% suc)	NA	3	0	0
Anhydr. Volume Sphere Radius (Ro(anhy.)) [Å]	19.89	25.25	28.87	31.70
Maximum Dimension (Dmax) [Å]	62.63	71.16	113.68	82.1
Translational Diffusion Coefficient (Dt) [µm^2/s]	87.3	66.2	54.5	55.5
Translational Stokes Radius (R(transl.)) [Å]	24.55	32.39	39.34	38.63
Translational Stokes Diameter (D(transl.)) [Å]	49.1	64.78	78.68	77.26

Table 3: Total FG-repeats in Arabidopsis FG-NUPs

GeneID	FG NUP	Max FG	GLFG
AT1G10390	NUP98a	65	0
AT1G59660	NUP98b	52	0
AT2G45000	NUP62	26	0
AT3G10650	NUP136	26	0
AT1G55540	NUP214	21	0
AT1G24310	NUP54	7	0
AT1G75340	CG1	6	0
AT4G37130	NUP58	6	0
AT1G52380	NUP50a	3	0
AT3G15970	Nup50b	3	0
AT1G79280	TPR/NUA	0	0
***At*FG WT**	100%	215	
AtFG nup98a/b	45.60%	98	

9.5. Discussion

While the subunits in the 3xmCherry tandem are covalently bound via linkers, the 4 subunits of TetraGFP^{NTR}, interact via two multimerization interfaces to form homotetramers [145]. The tetrameric GFP^{NTR} series of Frey *et al.* 2018 (predecessors of TetraGFP^{NTR}) was demonstrated to form monodisperse tetramers by crystallization and multi angle light scattering [145]. TetraGFP^{NTR} was designed for further interface stabilization by introducing a buried M225F mutation in its predecessor GFP^{NTR}_3B7C [148] and was demonstrated to form monodisperse tetramers via fluorescence correlation spectroscopy (personal communication, Dirk Görlich). Considering the abundant evidence that the GFP^{NTR} series form monodisperse tetramers, it is unlikely that they would not do so *in planta*. Yet I cannot definitely exclude that the intercellular TetraGFP^{NTR} movement I observed is from unassembled subunits. Hence, testing the oligomerization state of mobile TetraGFP^{NTR} *in planta* via fluorescence correlation spectroscopy or anisotropy measurement would be suitable control experiments. Assuming TetraGFP^{NTR} forms monodisperse tetramers *in planta*, it is peculiar that it moved significantly more than cell-autonomous 3xmCherry-tandem.

TetraGFP^{NTR} and 3xmCherry-tandem harbor similar predicted hydrodynamic radii and diffusion coefficients despite their 27 kDa mass difference. This might be attributed to the differential shape of both FPs. Rod-shaped particles diffuse slower than globular particles of identical size. In-solution diffusion coefficients of tandem EGFP oligomers (2x-, 3x-, 4xEGFP) matched with predicted diffusion coefficients for rod-shaped particles [108]. Hence, 3xmCherry tandem likely diffused like a rod-shaped particle, while TetraGFP^{NTR} is more globular, as indicated by AlphaFold3 protein structure prediction (Figure 10D). While the in-solution diffusion coefficients of both FPs are similar, the large maximal dimension of the rod-shaped 3xmCherry tandem (D_{max}=11.4 nm) may hinder its diffusion throughout the nanometer size cytoplasmic sleeve (in Arabidopsis root tip cells ~10 nm). In contrast, the more globular TetraGFP^{NTR} (D_{max}=8.2 nm) might still pass the cytoplasmic sleeve. The large differences between single EGFP movement and 2xEGFP tandem movement in WT [mean movement: mEGFP 10.87 cells, 2XEGFP tandem 2.72 cells at 1% sucrose supplementation (Table 2)], implicates that size indeed affects intercellular diffusion. Notably, even a single GFP would be hindered to 10% of its in-solution diffusion in a cylindric channel with a 14 nm diameter [1]. Hence, steric hindrance in the cytoplasmic sleeve is likely the reason for the comparably low intercellular movement observed for FPs like 2XEGFP tandem and larger (Table 2).

Nonetheless, 2xEGFP tandem and TetraGFP^{NTR} moved similarly in WT, while only TetraGFP^{NTR} showed reduced intercellular movement in the *nup98a/b* mutant (Figure 10D). The TetraGFP^{NTR}-specific movement reduction in FG-reduced background is likely independent of steric hindrance at PD. Otherwise, 2xEGFP should also have reduced movement in the *nup98a/b* mutant. Hence, it is likely that TetraGFP^{NTR}'s FG-specificity contributes to its increased intercellular movement in WT. TetraGFP^{NTR} has a high specificity for NUP98-typic GLFG-repeats. In *in vitro* experiments, TetraGFP^{NTR} partitions 15 times better into GLFG hydrogels than into those composed of GFLG repeats and even 25 times better than into FSFG hydrogels [148,240]. While *AtNUP98a/b* are annotated as GLFG-family NUPs [241] they do not contain any GLFG motifs. Together, they contain 2 SLFG and 3 PLFG motifs, which might have GLFG-like interaction properties, as Gly, Ser, and Pro are all abundant in natural linkers [242]. Notably, there is not a single GLFG repeat in any of the characterized Arabidopsis FG-NUPs (Table 3). Hence, it is possible that less GLFG-specific GFP^{NTR} variants, like tetrameric GFP^{NTR}_3B7C, might show enhanced intercellular movement compared to TetraGFP^{NTR}. Nonetheless, it was demonstrated that the FG-domains of Arabidopsis NUP98b and 9 other eukaryotic FG-NUP98 homologs (including mammals, insects, nematodes, and fungi, to name a few) spontaneously phase-separate into FG-particles in aqueous solution. All tested NUP98 FG-phases reproduced specific entry of large NTR-complexes, as well as the exclusion of smaller inert non-cargos [243].

Conclusively, the obtained results are in line with our hypothesis of a FG-based phase separation that contributes to the intercellular permeability barrier between plant cells. More controlled transport experiments, like fluorescence recovery after photobleaching (FRAP) of monomeric FG-phillic and FG-phobic GFPs [145], will allow determining precise intercellular diffusion rates, would allow quantifying surface-dependent hindrances at intercellular borders. Previously, similar hindrance quantifications were used to model the structural parameters of PD [67]. Hence, such experiments might help in elucidating the composition of the plasmodesmal permeability barrier.

9.6. Summary

Research question:

- Are molecular mechanisms underlying PD transport similar to mechanisms underlying NPC transport?

Objective

Investigating the effect of NTR-like surface properties on intercellular movement.

Hypothesis

Intercellular transport across PD is facilitated by similar features as nuclear transport.

9.6.1. Result

TetraGFP^{NTR}, an NTR-like GFP variant, but not 3xmCherry tandem, moved via PD despite being larger than the SEL, indicating selective transport of NTR-like proteins. Further, only TetraGFP^{NTR} movement was decreased in a *fg-nup98a/b* mutant, while 2xEGFP tandem movement was unaffected, which is the first evidence that FG-NTR interactions indeed play a role in PD-mediated intercellular transport.

Chapter VII

10. Discussion

10.1. Limitations of this study

This thesis summarizes the novel identification of NUPs as dual-localized NE and PD proteins that functionally contribute to PD transport. As highlighted in Chapter III, the generally high rate of false-positives in PD proteomes necessitates *in planta* localization for validation of PD candidates [244]. Most localizations in this study were performed with transient overexpression in the heterologous plant system *N. benthamiana*. While heterologous systems like *N. benthamiana* simplify transient protein expression and localization, PD localization of proteins is not always conserved across organisms as reported for Class 1 REVERSIBLY GLYCOSYLATED PROTEINs (^{C1}RGP). A ^{C1}RGP was enriched in cell-wall fractions, and antisera against it specifically stained PD and Golgi in *Zea mays* [245]. Further overexpression of *At*RGP2 (homolog of maize ^{C1}RGP) resulted in PD and Golgi localization [246] and reduced *TMV* spread and assimilate distribution in transgenic tobacco [247]. While silencing of *^{C1}RGP* mRNA led to increased *TMV* spread in *N. benthamiana* [248]. Conversely, immunolocalization of ^{C1}RGP as well as RGP1&2-YFP fusions only localized to Golgi and cytoplasm in Arabidopsis [249]. Highlighting that PD-association of ^{C1}RGP might be species-specific in maize and tobacco. Hence, PD localization in heterologous systems, like *N. benthamiana*, does not necessarily reflect the native localization. While we used an estradiol inducible expression system to limit overexpression, the expression levels observed in *N. benthamiana* were likely still higher than in native conditions. Overexpression can lead to the mislocalization of proteins [250,251]. ER-resident proteins like NE-localized NUPs might laterally diffuse along the ER and accumulate at the cortical ER in front of PD. It was quantitively assessed that higher expression levels of ER proteins can disrupt localization at the subdomain resolution, leading to spread throughout the entire ER. While CRISPR-mediated endogenous *FP* fusions could reproduce native expression levels and subdomain localization of several ER proteins [250].

Notably, NUPs that did not contain any membrane-binding or transmembrane domains, like nuclear ring NUP HOS1/ELYS and FG-NUPs like NUP62 [252], localized to PD in *N. benthamiana* too. Quantification of NUP PD localization in *N. benthamiana* via the PD index (PDI) indicated significantly increased indices over the membrane-impermeable dye propidium iodide for 12 NUPS. Still, even the best localized NUPs (NUP43-mVenus PDI=1.7 and GP210-mVenus PDI=1.8) localized less specific, as PD marker PDLP6-GFP (PDI≈2.2). NUP62-GFP fusions also localized to PD in stable transgenic Arabidopsis lines when the transgenic construct contained native promoter and terminator regions. Conversely, constructs that contained the *NUP62* coding sequence flanked by an *HSP18.2* terminator did not localize to PD (Figure 15, appendix). In the mammalian system it was demonstrated that alternative 3'-UTRs can differently affect the localization and function of membrane proteins. 3'-UTRs can recruit interactors during translation, which post-translationally affect protein targeting [253]. Indicating that native 3'-UTRs might be required for peripheral targeting of plant NUPs. Similar results in which the native terminator was required for PD targeting were observed for other PD proteins (personal communication, Neda S. Kazemein Jasemi). This highlights the importance of studying protein localization in the native context, which is why I generated the endogenous *PpNUP-FP* fusions via CRISPR/Cas9 (see Chapter V, Gene editing in *P. patens*). Further, NUP-specific anti- or nanobodies would also allow visualizing NUPs in native conditions of WT tissues.

The pleiotropy of plant *nup* mutants (see Chapter IV, NPCs in the green-lineage) complicates studying their role in intercellular transport. Also, it is not trivial to separate defects in nucleocytoplasmic transport and intercellular transport. In particle bombardment we cannot distinguish defects in nuclear mRNA export from defects in intercellular protein transport. Notably, we do observe cytoplasmic fluorescence in all *nup* mutants, indicating that *2xEGFP tandem* mRNA export is not fully defective. But still, we cannot exclude the possibility that a

reduced rate of mRNA export might contribute to reduced cytosolic FP levels and thereby, reduced intercellular transport.
We can exclude the effects of mRNA export in the SHR-GFP FRAP assay, as stele SHR-GFP levels between WT and *cpr5* mutants were not significantly different. Reduced mRNA export should lead to less SHR-GFP translation and thereby reduced stele SHR-GFP values. Also, the SHR-GFP assay is normalized to the SHR-GFP fluorescence levels. But as SHR-GFP transport involves nuclear import in the endodermis, we cannot fully exclude that a slower nuclear import rate is contributing to slower nuclear GFP recovery after photo-bleaching. Endodermal nuclear targeting of SHR-GFP seemed to be functional in the *cpr5-1* mutant, and we observed no fluorescence in the endodermal cytoplasm. Also, it was established that *cpr5* mutants increase the nuclear influx of TFs [192]. Hence, it is unlikely that the quantified reduction of SHR-GFP movement to the endodermal nucleus was attributed to defective nuclear import. Nonetheless, we cannot fully exclude the possibility of contributions through nucleocytoplasmic transport defects in *nup* mutants unless we find a way to specifically target PD-localized NUPs.
However, the experiments that indicated selective intercellular transport of NTR-like GFP variant TetraGFP^{NTR} were performed in WT. Also, the reduced intercellular movement in the FG-reduced *nup98a/b* mutant was only observed for NTR-like TetraGFP^{NTR} and not for FG-unspecific 2xEGFP tandem. The WT-like transport of 2xEGFP tandem in *nup98a/b* mutant background indicates that the *nup98a/b* mutant unlikely contains indirect cell-cell reducing features. Accordingly, TetraGFP^{NTR} movement is likely reduced as a direct effect of the FG-reduction in the *nup98a/b* mutant. This indicates the involvement of FG-NUPs in PD-mediated transport, in line with PD localizations of *At*NUP98a/b and *Pp*NUP98.1 in transient expression (Chapter V, Identification of nuclear pore proteins at plasmodesmata).

10.2. Novel components in plasmodesmal gating

PD are cell wall embedded channels that are affected by cell wall dynamics [24] as reflected in the HC300 *P .patens* PD proteome, which contains ~30 % cell wall-associated proteins. We identified GHL17s, EXOs, and XTHs as cell wall-associated protein families that, during the evolution of multicellularity, each diversified into non-PD- and PD-localizing clades. We demonstrated that overexpression of PD-localized *Pp*GHL17_1 increased intercellular connectivity between adjacent protonemata cells. Notably, carboxyfluorescein (CF) diffusion rates in WT *P. patens* protonemata were comparably slow. 15 min after bleaching, only a slight fraction of the CF fraction recovered (WT <10%, *Pp*GHL17_1 overexpression ~70 %). Similar slow rates were repeatedly reported for the photo-convertible GFP variant DENDRA2 (27 kDa), which can be detected in adjacent cells 15 min after photo-conversion [73,254,255]. For comparison, in WT Arabidopsis roots, CF fluorescence intensity recovers to ~70 % 100 s after bleaching, and photo-switchable DRONPA-s (27 kDa) becomes detectable in adjacent cells 2 min after photo-activation [28]. Intentionally, due to their single-cell nature, we considered protonemata as simple models for studying cell-cell transport. These results indicated that protonematal cell-cell transport likely is not comparable to that in higher plant tissues. Hence, later, we focused predominantly on characterizing novel PD components in Arabidopsis.
The enrichment of PD membrane fractions out of rigid cell walls requires multiple centrifugation steps, detergent washes, and enzymatic digestion to remove cell walls, organelles, and soluble proteins. In combination with stringent thresholding in data analysis, soluble proteins in transit through PD and loosely PD-associated proteins might be removed [244]. While the ‘feature score’ increases the chance of identifying novel PD proteins similar to already localized bona fide PD proteins, it also biases for identifying such. Hence, our proteomic analysis might have a blind spot for novel more loosely associated PD-components, like cytoplasmic cargo.

Notably, only one karyopherin (*Pp*IMB3) ranked in the HC300 *P. patens* PD proteome. The basket NUP *Pp*TRP/NUA and two homologs of *At*RAN3 were also enriched in *P. patens* PD membrane fractions and ranked in the HC600. Nonetheless, 19 nuclear transport-related proteins were enriched in cell wall fractions (Table 8, appendix). Two of those (*Pp*NUP62 and *Pp*NUP98.1) dual-localized to PD and NPC in transient expression in *N. benthamiana*. While *Pp*NUP58 and *Pp*NUP35.1 were not present in the cell wall fractions, they were still dual-localized to PD and NPC. These results indicate that proteomic fractions alone are not enough to confirm or exclude PD localization, as discussed above (Chapter III). While our iterative-scoring approach strengthened predictions for PD candidates, the candidates chosen for large-scale localization were still based on proteomic PD fractions. Hence, we cannot entirely exclude proteomic-derived biases in our approach. In comparison to the *P. patens* PD proteome, the Arabidopsis shoots proteome contained 40 nuclear transport-related proteins considered as high confidence (Table 9, appendix). Whether these differences are species-dependent or due to differential protocols in the PD fraction enrichment remains to be elucidated. Conclusively, we identified a wide range of PD proteins with our *P. patens* high-confidence proteome. Nonetheless, identifying an entire PD blueprint will require complementary methods.

10.3. Multifunctionality of NUPs

Here, we report the dual-localization of NUPs to PD and NPCs and propose that NUPs play a role in intercellular transport in plants, forming a potential PDPC. Interestingly, NUPs are involved in a plethora of cellular processes that do not necessitate their function in nucleocytoplasmic transport [219]. In line with the gene gating hypothesis (see Chapter IV), multiple NUPs were shown to be involved in gene regulation [129], but further have roles in DNA repair and mitosis [219]. In many of these instances, NUPs play functional roles outside of the nucleus. One prominent example of peripheral NUPs are annulate lamellae (ALs), which are stacked ER sheets that are penetrated by preassembled NPCs, that contain most NUPs. ALs are abundant in embryonic cells and gametes, where they are described as NPC storages for early development [219]. While less abundant ALs are also present in somatic cells, where they insert into the NE during nuclear growth [256]. Interestingly, ALs are also found in plant cells [257]. FG-NUPs specifically are involved in several cyto- and nucleoplasmic membranelles organelles, like P-bodies, P-granules, stress granules, and viral-associated organelles [219], in which they might contribute to establish phase separation. Further, NUPs seem to be able to constitute permeability barriers at other cellular interfaces than the nuclear pore, as seen between cytoplasm and cilia (ciliary transition zone). Cilia are sensory microtubule-containing projections that have roles in signaling, motility, and development. A ciliary pore complex (CPC), located at the ciliary transition zone, was proposed to maintain ciliary identity by selectively transporting ciliary cargo [258]. While several groups localized 7 distinct NUPs to the ciliary base, which includes the ciliary transition zone (namely cytoplasmic FG-NUP214, outer ring NUP37 & -85, inner ring NUP35 & -188, linker NUP93 and central FG-NUP62 & -98), other groups failed to localize some of these NUPs [118]. Hence, how exactly a potential CPC is composed and anchored remains elusive, as there are no cryo-ET structures of the ciliary base/ transition zone [118]. Recent, super-resolution microscopy at the ciliary base established that NUP188 forms two barrels-like structures, which are likely wrapped around the mother and daughter centriole. The authors stressed that the observed barrel-like structures are inherently different from NPCs and hence opposed the CPC model [259]. Still, diverse functional evidence underpins the involvement of NPC-related components in ciliary transport. Forced dimerization of FG-NUP62 inhibited nuclear transport, as well as ciliary import of cytosolic but not membrane proteins [260]. FG-NUP98 was implied to play a key role in upholding cilial SEL, as FG-NUP98 knockdown increased leakage of ciliary tubulin (>100 kDa), which

resulted in shorter cilia [261]. Similar to nuclei, the import of several ciliary components is facilitated by IMPβ2 along a RAN-GTP gradient and requires ciliary target signals that resemble NLSs [262–264]. Conclusively, it seems evident that a subset of NUPs and NTRs affect transport between the cytoplasm and cilia. Notably, the arrangement of the involved NUP/ CPC complex might drastically vary from the conventional NPC. In summary, NUPs have the capacity to function in compartments other than NPCs and can form a multitude of complexes, which can fulfill transport, but also transport-independent functions.
The multifunctionality of NUPs indicates a possibility for NUPs to contribute to PD gates *in planta*. But also highlights that a potential PDPC might harbor a different architecture and composition than the NPC, similar to NUPs at the ciliary base/ CPC. For the CPC it was proposed that it is assembled in parallel to NPCs, as both NPC and cilia are assembled *de novo* during cell division [118]. Similarly, PD are initiated during cell division (Chapter I, Plasmodesmata formation and diversity), which could indicate a pathway in which NUPs might migrate towards cortical ER tubules before the ER tubules insert into cell plate fenestrae and form primary PD [27].

10.4. Dimensional differences of PD and NPC

PD and NPCs both constitute nanometer-scale pores that are involved in gating molecular fluxes between distinct compartments [116]. The dimensions of both pores are similar but not equal. PD are PM-located pores that are variable in dimensions dependent on the type of PD. Electron tomography of Arabidopsis root tips revealed ~40 nm wide PD with a cytoplasmic sleeve of ~10 nm. If desmotubule displacement can occur, indicated by its dynamic positioning throughout several micrographs, the cytoplasmic sleeve could be up to 20 nm wide [4]. Notably, the tomograms from Nicolas *et al.*, do not depict membrane-associated proteins in the cytoplasmic sleeve [4]. PM or ER-associated proteins in PD would likely further limit the active transport channel. Electron micrographs generated by Ding *et al.* 1992*,* indicated structured densities at the PD membranes, which led to estimations of a only 2.5 nm transport channel [5]. Nonetheless, the capacity of sleeveless PD to transport macromolecular cargo indicates that PD likely have a flexible active transport channel. As callose increases the flexibility of cellulose hydrogels, PD cell walls might allow dilation of the cytoplasmic sleeve [25]. The channel length of PD is dependent on the cell wall thickness and can range from 80-1000 nm in meristematic root cells of Arabidopsis. Notably, electron microscopy of organic matter actually visualizes the heavy metal staining agents (used for contrast improvement) rather than the native structure, which leads to underestimation of *in vivo* PD membrane distances [1].
On the other hand, NPCs are ER-located structures, which were robustly reconstituted via a combination of state-of-the-art cryo-electron tomography, cryo-electron microscopy, X-ray crystallography, nuclear magnetic resonance (NMR) spectroscopy, and interactomics studies. As NPCs are radially symmetric protein complexes, they show substantially less variability in their structure than PD, which simplifies structural analysis. Cryo-ET enabled to visualize *in situ* human NPCs, which harbor a 65 nm wide central channel and a 125 nm wide and 80 nm long core scaffold [124]. While there is variation in NPC sizes and composition between organisms, the *in situ* diameter of the central channel remains in a range of ~60 nm in yeast, algae, and humans. Until now, only a few different morphotypes of NPCs were described in between tissues. Evidently, NPCs are more than double as wide as PD, while PD are 5-10 times as long as NPCs. This raises the question how a nNUP-based PDPC could integrate at PD?

10.5. Potential localization of a NUP-based PDPC

Our SIM microscopy results indicated that CPR5 localizes adjacent to the aniline blue stained callose, presumably at the cortical ER-desmotubule interface in front of PD. NUP43 and HOS1 showed similar localizations (unpublished data, Moritz Schladt). The cortical-ER desmotubule

interface has a saddle-like membrane curvature as the nuclear pore [265] (Figure 11A&B). Membrane curvature is an important feature of the NPC, as it is required for the association of membrane-sensing NUPs like NUP35 and NUP155 [265]. Notably, the intermembrane space between the cortical ER and cell wall (8-100 nm in *P. patens*, personal communication Marcel Dickmanns) would not fit an entire inner ring complex (~25 nm wide) in all cases. Due to the discrepancy in dimensions and the fact that not all NUPs localized to PD, PDPC architecture and composition likely differs from the NPC, similar to the CPC. The plant-specific transmembrane NUP CPR5, other plant-specific NUPs, or unidentified PD-specific interactors might lead to differential structural features at the PDPC.
Even the best-localized NUPs did not localize as PD-specific as PDLP6 and showed puncta that did not overlay with callose marker aniline blue in transient overexpression (PDI_{CPR5}=1.5, $PDI_{HOS1/ELYS}$=1.5, PDI_{NUP98b} =1.6, PDI_{NUP43}=1.7, PDI_{GP210}=1.8 vs. PDI_{PDLP6}≈2.2). NUP PDIs might in increase in at native expression levels, as it was reported that in stable transgenic lines, MCTPs can have PDIs 10-fold higher than in transient overexpression [26]. Alternatively, it is possible that plant NUPs not only localize to cortical ER directly adjacent to PD but also to other cortical ER tubules with saddle-like curvature. Even if not entirely PD-specific, a concentration of FG-NUPs at the cortical ER might still enact an NPC-like permeability barrier that repels cell-autonomous proteins and simultaneously allows the facilitation of cargo transport towards PD (Figure 11C). To address this question native NUP localization will be tested in the CRISPR-generated *FP* knock-in lines (Chapter V, Gene editing in *P. patens*) or with NUP-specific anti- or nanobodies (as described above).

10.6. Indications for a NUP-based PDPC

Despite their distinct structures and dimensions, PD and NPC are involved in transporting similar cargos, including ions, metabolites, proteins, and RNAs. Some proteins that are mainly involved in nucleocytoplasmic transport in animals were shown to have additional intercellular transport roles *in planta*. Like the EXPORTIN5 homologue HST that facilitates intercellular miRNA transport or [102] the nuclear export factors ALY2/4, which are involved in long distance mRNA transport [105]. SIEL facilitates intracellular endosomal trafficking of SHR, which in turn affects PD-passage of SHR. As SIEL interacts with several other non-cell autonomous TFs it was hypothesized to function as a diverse intercellular transport receptor (for a detailed description see Chapter I, Intercellular transport of macromolecular cargo). Intriguingly, SIEL contains ARM- as well as HEAT-repeats [88,89], which are the requisite protein domains for nucleocytoplasmic shuttling in IMPα and all KAPs (including IMPβ), respectively [146]. While it was shown that the nuclear localization of SHR is essential for its intercellular transport, in the *siel* mutant background SHR has reduced intercellular mobility, but retains its nuclear localization [88,89]. Hence, SIELs ARM- and HEAT-repeats seem to be uninvolved in the nucleocytoplasmic transport of SHR. The SIEL-dependent transport pathway also highlights the importance of intracellular recruitment towards PD, which via SIEL is dependent on perinuclear microtubule-aided loading on endosomes and endosomal trafficking towards PD [89,90]. Current studies on SIEL do not indicate that it is shuttled throughout PD with SHR [266]. SIEL's ARM- and HEAT-repeats might enable the passage of an FG-based PDPC that would potentially form a barrier on the trafficking pathway towards PD.
Nucleocytoplasmic, intra- and intercellular transport pathways can be hijacked to facilitate the spread of viral particles. Interestingly, proximity-labelling of the ER integral membrane MP of *Bamboo mosaic virus* (*BaMV*) TRIPLE-GENE-BLOCK-PROTEIN (TGBP)3, identified *N. benthamiana* GP210a and GP210b as two of the most enriched candidates. Moreover, *Nb*GP210a/b, were only proximal to mobile TGBP3, while a cell-cell movement-defective TGBP3-mutant (TGBP3M) was proximal to *Nb*NUP35a, *Nb*NUp98a, and *Nb*NUP136b [267]. Movement-defective TGBP3M lacks a sorting signal that is essential for oligomerization,

targeting to cortical ER tubules and *BaMV* pathogenesis [268]. This indicates that mobile TGBP3 encounters *Nb*GP210a/b at the cortical ER proximal to PD (at the PDPC), in line with PD localization of *At*GP210. GP210 comprises the luminal ring, which likely contributes to maintaining saddle-like membrane curvature and membrane distance at the NPC [138]. TGBP2, which forms a complex with TGBP1 & 3, constricts ER-tubules by generating curvature via reticulon-like TM domains, which was implicated in increasing PD SEL. Possibly by constricting the PD proximal cortical ER and desmotubules [269]. As the butterfly-like GP210 octamer domains in the NE lumen are 20 nm high and span a length of 70 nm (in *Xenopus laevis*) [138], they would not fit inside such constricted ER tubules. TGBP3 might attenuate GP210, which would pose a steric hindrance to ER-tubule constriction and thereby contribute to facilitating *BaMV* spread. Notably, we also observed significant changes in intercellular mEGFP movement in *gp210* T-DNA insertion lines. Conversely, *gp210-1* showed reduced movement, and *gp210-2* increased movement to WT (Figure 14A, appendix). While *GP210* knock-out does not affect NPC assembly in mammalian cells [136], a *GP210* T-DNA insertion in Arabidopsis ecotype Wassilewskija was described as embryo lethal [*EMBRYO DEFECTIVE* (*EMB)3012*] [270]. *GP210* is a large gene (>11 kb) that contains 41 in-frame start codons (ATG) on its coding sequence. Hence, it is possible that the viable T-DNA insertion lines still express distinct partially functional GP210 truncations. This might be an explanation for the discrepancies in intercellular connectivity and growth ranging from embryo-lethality to WT-like phenotypes between the different mutants (Figure 14, appendix). Surprisingly, the embryo lethal *gp210* T-DNA insertion is an intron, while the viable mutants harbor insertions in exons (T-DNA insertions: *emb3012* in intron 17, *gp210-1* in exon 6 and *gp210-2* in exon 13), which complicates interpretation. Accordingly, CRISPR-mediated knock-out of *NUP* genes will allow the generation of reliable mutants.

Proxiomes of PDLP5/6 and MCTP3 all included significant enrichment of transmembrane NUP NDC1, basket NUP50a, as well as the RAN-GDP shuttle NTF2a and RAN3, a RAN-GTPase likely involved in nuclear transport [271].

The identification of NUP50a in Arabidopsis PD proxiomes is in line with our Arabidopsis PD fractions in which NUP50a was one of the highest-ranking high-confidence NUPs. Further transient overexpression of NDC1-mCitrine in *N. benthamiana* indicated overlay with PD marker aniline blue, also in line with NDC1 identification in PD proxiomes (Figure 16)

Presence of NTF2a and RAN3 highlights that also non-structural nuclear transport proteins are found in PD fractions. Our PD shoot contained 13 NTRs (XPO1B/7, IMPA6/9, IMB2-5, IPO8,TNPO3, SAD2, MOS14, and NTF2a) and 7 RAN-related proteins [RAN1, RANGAP1/2 ,PARLL1 (also a RANGAP), NIG (RAN-GTPase), RANBP1 and SIRANBP] with high confidence. These results indicate that NTRs might be transported through PD along a RAN-GTP gradient similar to NPC and CPC. Optionally, NTRs and RAN-GTP might locally accumulate at the cellular periphery/ PD, generating gradients analogous to nucleocytoplasmic RAN-GTP gradients (Chapter IV, The role of phase separation for transport through the nuclear pore complex, Figure 6). Overall, the observation of FG-dependent intercellular TetraGFP^{NTR} transport provides the first evidences that NTR-like properties and FG-repeats facilitate intercellular passage, indicating that endogenous NTRs might also be capable of PD passage.

In summary, several lines of evidence support NUP PD localization and the involvement of nuclear transport components in intercellular transport. While this thesis provides evidence for NUP localization at PD and their involvement in the PD transport mechanism, it did not investigate NUP interactions at PD. Hence, as of now, I can only state that scaffold NUPs (like CPR5 and GP210) and FG-NUPs (like NUP98a and NUP98b) seem to be involved in intercellular transport. Possibly by enacting a FG-based phase-separating permeability barrier at the cortical ER adjacent to PD. How exactly NUPs integrate at PD (or the cortical ER) and if they form a structured complex (PDPC) remains speculative.

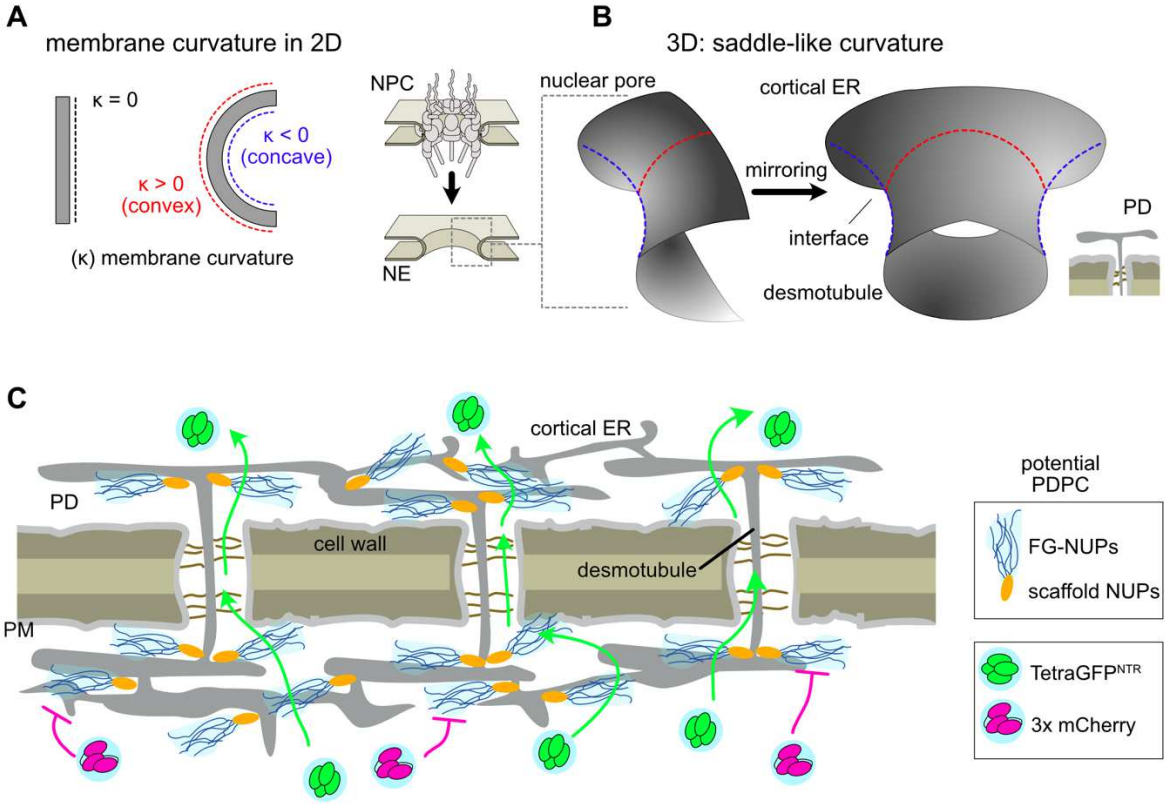

Figure 11: ER membrane curvature at NPC and PD
A Membrane curvature can be separated into convex (κ>0, positive) curvature and concave (κ <0, negative) curvature. Positive curvature at one side of a lipid-bilayer necessitates negative curvature on the other side of the lipid-bilayer (vice versa). **B** In three dimensions membranes contain two curvatures. The membrane curvature in the nuclear pore is negative in the axis of the NE (blue) but positive in the nucleocytoplasmic axis (red). Such a curvature is described as saddle-like curvature. The illustration shows that a similar saddle-like curvature is observed at the interface of desmotubule and cortical ER. **C** Potential PDPC, that localizes to saddle-like curved tubules of the cortical ER. The PDPC is indicated by a scaffold NUP portion that anchors FG-NUPs. The FG-NUPs enact a permeability barrier, which facilitates the transport of NTR-like cargo (TetraGFP^{NTR}), while it excludes non-specific molecules (3xmCherry tandem).

11. Conclusion

Despite extensive studies since the 19th century, PD remain enigmatic structures. In this thesis, I summarized current progress and models of PD function and aimed to identify new components that control plasmodesmal transport.

By extensive *in planta* localization of PD candidates, I contributed to identifying novel PD proteins of *P. patens*. With the goal of understanding the regulation of transport in analogous pores, I outline current models and research on the much better described NPC. Due to their similar cargos, we hypothesized that PD and NPCs might share similarities in their transport mechanism. Accordingly, I substantially contributed to the identification of NUPs and their functional role at PD and generated extensive genome-edited moss material to further test NUP function at PD. Lastly, I provide first evidences that NTR-FG interactions might be involved in facilitating PD passage, indicating that FG-NUPs indeed play a functional role at PD.

This thesis presents the first indications for a novel model in which NUPs were recruited to form a PD pore gating complex (PDPC), which enacts an FG-based phase separation that controls intercellular permeability and facilitates the transport of proteins with NTR-like properties.

Recruitment of a PDPC could explain how PD simultaneously enable selective transport and exclusion of non-cargos. And why many non-cell-autonomous proteins require their NLSs for their PD-mediated translocation. A PDPC-mediated transport mechanism would be highly relevant in plant physiology, signaling, development, and immunity. Further, the recruitment of a PDPC suggests intriguing perspectives for the evolution of multicellularity in the green lineage. However, the exact structure and composition of a potential PDPC will need to be studied in a more native context and at higher resolution, similar as seen for NPCs.

Lastly, this thesis provides a basis for many new research questions and hypotheses concerning the PD targeting mechanism of NUPs, the role of endogenous plant NTRs in intercellular protein and RNA transport, the role of RAN-GTPases at PD, and the interplay of plant pathogens and plasmodesmal NUPs.

12. References

1. Peters, W. S., Jensen, K. H., Stone, H. A. & Knoblauch, M. Plasmodesmata and the problems with size: interpreting the confusion. *J Plant Physiol* **257**, 153341 (2021).
2. Hillhouse, W. Einige Beobachtungen über den interzellularen Zusammenhang von Protoplasten. *Bot. Centralbl.* **14**, 121–125 (1883).
3. Strasburger, E. Über Plasmaverbindungen Pflanzlicher Zellen. (G. Borntraeger, 1901).
4. Nicolas, W. J. *et al.* Architecture and permeability of post-cytokinesis plasmodesmata lacking cytoplasmic sleeves. *Nat Plants* **3**, (2017).
5. Ding, B., Turgeon, R. & Parthasarathy, M. V. Substructure of Freeze-Substituted Plasmodesmata. Protoplasma (1992).
6. Terry, B. R., Matthews, E. K. & Haseloff, J. Molecular Characterization of Recombinant Green Fluorescent Protein by Fluorescence Correlation Microscopy. *Biochem Biophys Res Commun* **217**, 21–27 (1995).
7. Oparka, K. J. *et al.* Simple, but not branched, plasmodesmata allow the nonspecific trafficking of proteins in developing tobacco leaves. *Cell* **97**, 743–754 (1999).
8. Sager, R. E. & Lee, J.-Y. Plasmodesmata at a glance. *J Cell Sci* **131**, jcs209346 (2018).
9. Petit, J. D., Li, Z. P., Nicolas, W. J., Grison, M. S. & Bayer, E. M. Dare to change, the dynamics behind plasmodesmata-mediated cell-to-cell communication. *Curr Opin Plant Biol* **53**, 80–89 (2020).
10. Bayer, E. M. & Benitez-Alfonso, Y. Plasmodesmata: Channels Under Pressure. *Annu Rev Plant Biol* **75**, 291317 (2024).
11. Miras, M. *et al.* Plasmodesmata and their role in assimilate translocation. *Journal of Plant Physiology* vol. 270 (2022).
12. Liu, J., Zhang, L. & Yan, D. Plasmodesmata-Involved Battle Against Pathogens and Potential Strategies for Strengthening Hosts. *Front Plant Sci* **12**, (2021).
13. Aung, K. *et al.* Pathogenic bacteria target plant plasmodesmata to colonize and invade surrounding tissues[CC-by]. *Plant Cell* **32**, 595–611 (2020).
14. Brunkard, J. O. & Zambryski, P. Plant cell-cell transport via plasmodesmata is regulated by light and the circadian CLOCK. *Plant Physiol* **181**, 1459–1467 (2019).
15. Zhu, T., Lucas, W. J. & Rost, T. L. Directional Cell-to-Cell Communication in the Arabidopsis Root Apical Meristem I. An Ultrastructural and Functional Analysis. *Protoplasma* vol. 203 (1998).
16. Zhu, T., O'quinn, R. L., Lucas, W. J. & Rost, T. L. Directional Cell-to-Cell Communication in the Arabidopsis Root Apical Meristem II. Dynamics of Plasmodesmatal Formation. *Protoplasma* vol. 204 (1998).
17. Duckett, C. M., Oparka, K. J., Prior, D. A. M., Dolan, L. & Roberts, K. Dye-coupling in the root epidermis of Arabidopsis is progressively reduced during development. *Development* **120**, 3247–3255 (1994).
18. Sonnewald, U. Comparative proteomic profiling of the *choline transporter-like1* (*CHER1*) mutant provides insights into plasmodesmata composition of fully developed *Arabidopsis thaliana* leaves. **1**, 696–709 (2017).
19. Grison, M. S. *et al.* Plasma membrane-associated receptor-like kinases relocalize to plasmodesmata in response to osmotic stress. *Plant Physiol* **181**, 142–160 (2019).
20. Platre, M. P. *et al.* The receptor kinase SRF3 coordinates iron-level and flagellin dependent defense and growth responses in plants. *Nat Commun* **13**, (2022).

21. Rinne, P. L. H. *et al.* Chilling of dormant buds hyperinduces FLOWERING LOCUS T and recruits GA-inducible 1,3-β-glucanases to reopen signal conduits and release dormancy in Populus. *Plant Cell* **23**, 130–146 (2011).
22. Rinne, P. L. H., Kaikuranta, P. M. & Van Schoot, C. Der. The shoot apical meristem restores its symplasmic organization during chilling-induced release from dormancy. *Plant Journal* **26**, 249–264 (2001).
23. Wu, S. W., Kumar, R., Iswanto, A. B. B. & Kim, J. Y. Callose balancing at plasmodesmata. *J Exp Bot* **69**, 5325–5339 (2018).
24. Zavaliev, R., Ueki, S., Epel, B. L. & Citovsky, V. Biology of callose (β-1,3-glucan) turnover at plasmodesmata. *Protoplasma* **248**, 117–130 (2011).
25. Abou-Saleh, R. H. *et al.* Interactions between callose and cellulose revealed through the analysis of biopolymer mixtures. *Nat Commun* **9**, 4538 (2018).
26. Brault, M. L. *et al.* Multiple C2 domains and transmembrane region proteins (MCTP s) tether membranes at plasmodesmata. *EMBO Rep* **20**, 1–26 (2019).
27. Li, Z. P. *et al.* Plant plasmodesmata bridges form through ER-dependent incomplete cytokinesis. *Science (1979)* **386**, 538–545 (2024).
28. Pérez-Sancho, J. *et al.* Plasmodesmata act as unconventional membrane contact sites regulating inter-cellular molecular exchange in plants. *bioRxiv* 2023.12.18.572149 (2023) doi:10.1101/2023.12.18.572149.
29. Tee, E. E., Johnston, M. G., Papp, D. & Faulkner, C. A PDLP-NHL3 complex integrates plasmodesmal immune signaling cascades. *Proc Natl Acad Sci U S A* **120**, (2023).
30. Xu, B. *et al.* A calmodulin-like protein regulates plasmodesmal closure during bacterial immune responses. *New Phytologist* **215**, 77–84 (2017).
31. Oparka, K. J. & Prior, D. A. M. Direct evidence for pressure-generated closure of plasmodesmata. *The Plant Journal* **2**, 741–750 (1992).
32. Park, K., Knoblauch, J., Oparka, K. & Jensen, K. H. Controlling intercellular flow through mechanosensitive plasmodesmata nanopores. *Nat Commun* **10**, (2019).
33. Holdaway-Clarke, T. L., Walker, N. A., Hepler, P. K. & Overall, R. L. Physiological elevations in cytoplasmic free calcium by cold or ion injection result in transient closure of higher plant plasmodesmata. *Planta* **210**, 329–335 (2000).
34. Tucker, E. B. & Boss, W. F. Mastoparan-induced intracellular Ca^{2+} fluxes may regulate cell-to-cell communication in plants. *Plant Physiol* **111**, 459–467 (1996).
35. Barton, D. A. *et al.* Cell-to-cell transport via the lumen of the endoplasmic reticulum. *Plant Journal* **66**, 806–817 (2011).
36. Grabski, S., De Feijter, A. W. & Schindler Ai', M. Endoplasmic Reticulum Forms a Dynamic Continuum for Lipid Diffusion between Contiguous Soybean Root Cells. *The Plant Cell* vol. 5 (1993).
37. Hepler, P. K. Endoplasmic reticulum in the formation of the cell plate and plasmodesmata. *Protoplasma* **111**, 121–133 (1982).
38. Knox, K. *et al.* Putting the squeeze on plasmodesmata: A role for reticulons in primary plasmodesmata formation. *Plant Physiol* **168**, 1563–1572 (2015).
39. Faulkner, C., Akman, O. E., Bell, K., Jeffree, C. & Oparka, K. Peeking into Pit Fields: A Multiple Twinning Model of Secondary Plasmodesmata Formation in Tobacco. *Plant Cell* **20**, 1504–1518 (2008).
40. Ross-Elliott, T. J. *et al.* Phloem unloading in Arabidopsis roots is convective and regulated by the phloempole pericycle. *Elife* **6**, (2017).
41. Christensen, N. M., Faulkner, C. & Oparka, K. Evidence for unidirectional flow through plasmodesmata. *Plant Physiol* **150**, 96–104 (2009).

42. Ehlers, K. & Kollmann, R. Primary and Secondary Plasmodesmata: Structure, Origin, and Functioning. *Protoplasma* vol. 216 (2001).
43. Kobayashi, K., Otegui, M. S., Krishnakumar, S., Mindrinos, M. & Zambryski, P. *INCREASED SIZE EXCLUSION LIMIT2* Encodes a Putative DEVH Box RNA Helicase Involved in Plasmodesmata Function during Arabidopsis Embryogenesis. *Plant Cell* **19**, 1885–1897 (2007).
44. Stonebloom, S. *et al.* Loss of the plant DEAD-box protein ISE1 leads to defective mitochondria and increased cell-to-cell transport via plasmodesmata. *Proceedings of the National Academy of Sciences* **106**, 17229–17234 (2009).
45. Burch-Smith, T. M. & Zambryski, P. C. Loss of INCREASED SIZE EXCLUSION LIMIT (ISE)1 or ISE2 Increases the Formation of Secondary Plasmodesmata. *Current Biology* **20**, 989–993 (2010).
46. Carlotto, N. *et al.* Evidence for reduced plasmodesmata callose accumulation in *Nicotiana benthamiana* leaves with increased symplastic cell-to-cell communication caused by RNA processing defects of chloroplasts. *Plant Physiology and Biochemistry* **179**, 58–64 (2022).
47. Chambaud, C., Cookson, S. J., Ollat, N., Bayer, E. & Brocard, L. A correlative light electron microscopy approach reveals plasmodesmata ultrastructure at the graft interface. *Plant Physiol* **188**, 44–55 (2022).
48. Hertle, A. P., Haberl, B. & Bock, R. Horizontal Genome Transfer by Cell-to-Cell Travel of Whole Organelles. *Sci. Adv* vol. 7 (2021).
49. Fischer, K., Lachner, L. A. M., Olsen, S., Mulisch, M. & Krause, K. The Enigma of Interspecific Plasmodesmata: Insight From Parasitic Plants. *Front Plant Sci* **12**, (2021).
50. Weiss, G. L., Kieninger, A. K., Maldener, I., Forchhammer, K. & Pilhofer, M. Structure and Function of a Bacterial Gap Junction Analog. *Cell* **178**, 374-384.e15 (2019).
51. Maeda, S. & Tsukihara, T. Structure of the gap junction channel and its implications for its biological functions. *Cellular and Molecular Life Sciences* vol. 68 1115–1129 (2011).
52. Lai, J. *et al.* Intrinsically disordered proteins aggregate at fungal cell-to-cell channels and regulate intercellular connectivity. *Proc Natl Acad Sci U S A* **109**, 15781–15786 (2012).
53. Terauchi, M., Nagasato, C. & Motomura, T. Plasmodesmata of brown algae. *J Plant Res* **128**, 7–15 (2015).
54. Raven, J. A. Evolution of Plasmodesmata. in *Plasmodesmata* 33–52 (Wiley-Blackwell Publishing Ltd, 2007).
55. Kim, G. H. *et al.* Intercellular transport across pit-connections in the filamentous red alga *Griffithsia monilis. Algae* **37**, 75–84 (2022).
56. Brunkard, J. O. & Zambryski, P. C. Plasmodesmata enable multicellularity: new insights into their evolution, biogenesis, and functions in development and immunity. *Curr Opin Plant Biol* **35**, 76–83 (2017).
57. Wickett, N. J. *et al.* Phylotranscriptomic analysis of the origin and early diversification of land plants. *Proc Natl Acad Sci U S A* **111**, E4859–E4868 (2014).
58. Ušák, D., Haluška, S. & Pleskot, R. Callose synthesis at the center point of plant development—An evolutionary insight. *Plant Physiol* **193**, 54–69 (2023).
59. Gaudioso-Pedraza, R. & Benitez-Alfonso, Y. A phylogenetic approach to study the origin and evolution of plasmodesmata-localized glycosyl hydrolases family 17. *Front Plant Sci* **5**, (2014).

60. Lee, J. Y. *et al.* A plasmodesmata-localized protein mediates crosstalk between cell-to-cell communication and innate immunity in Arabidopsis. *Plant Cell* **23**, 3353–3373 (2011).
61. Vaattovaara, A. *et al.* Mechanistic insights into the evolution of DUF26-containing proteins in land plants. *Commun Biol* **2**, 56 (2019).
62. Zhao, Y. *et al.* Characterization and phylogenetic analysis of multiple C2 domain and transmembrane region proteins in maize. *BMC Plant Biol* **22**, 388 (2022).
63. Liu, L., Li, C., Liang, Z. & Yu, H. Characterization of Multiple C2 Domain and Transmembrane Region Proteins in Arabidopsis. *Plant Physiol* **176**, 2119–2132 (2018).
64. Tee, E. E. & Faulkner, C. Plasmodesmata and intercellular molecular traffic control. *New Phytologist* vol. 243 32–47 (2024).
65. Christensen, A. H., Stone, H. A. & Jensen, K. H. Diffusion and flow across shape-perturbed plasmodesmata nanopores in plants. *Eur Phys J Plus* **136**, (2021).
66. Schulz, A. Diffusion or bulk flow: how plasmodesmata facilitate pre-phloem transport of assimilates. *J Plant Res* **128**, 49–61 (2015).
67. Liesche, J. & Schulz, A. Modeling the parameters for plasmodesmal sugar filtering in active symplasmic phloem loaders. *Front Plant Sci* **4**, (2013).
68. Ruiz-Medrano, R., Xoconostle-Cázares, B. & Lucas, W. J. Phloem long-distance transport of *CmNACP* mRNA: implications for supracellular regulation in plants. *Development* **126**, 4405–4419 (1999).
69. Weinstein, J. N., Blumenthal, R. & Klausner, R. D. [38] Carboxyfluorescein leakage assay for lipoprotein-liposome interaction. in *Methods in Enzymology* vol. 128 657–668 (Academic Press, 1986).
70. Tucker, E. B. & Tucker, J. E. Cell-to-cell diffusion selectivity in staminal hairs of *Setcreasea purpurea*. *Protoplasma* **174**, 36–44 (1993).
71. Howell, A. H. *et al.* Electric charge controls plasmodesma conductivity. *bioRxiv* 2024.04.02.587779 (2024) doi:10.1101/2024.04.02.587779.
72. Wang, X. *et al.* Salicylic acid regulates plasmodesmata closure during innate immune responses in Arabidopsis. *Plant Cell* **25**, 2315–2329 (2013).
73. Kitagawa, M. *et al.* Abscisic Acid Acts as a Regulator of Molecular Trafficking through Plasmodesmata in the Moss *Physcomitrella patens*. *Plant Cell Physiol* **60**, 738–751 (2019).
74. Wang, Y. *et al.* Plasmodesmata mediate cell-to-cell transport of brassinosteroid hormones. *Nat Chem Biol* **19**, 1331–1341 (2023).
75. Mellor, N. L. *et al.* Auxin fluxes through plasmodesmata modify root-tip auxin distribution. *Development* **147**, dev181669 (2020).
76. Benitez-Alfonso, Y. *et al.* Symplastic Intercellular Connectivity Regulates Lateral Root Patterning. *Dev Cell* **26**, 136–147 (2013).
77. Sessions, A., Yanofsky, M. F. & Weigel, D. Cell-Cell Signaling and Movement by the Floral Transcription Factors LEAFY and APETALA1. *Science (1979)* **289**, 779–781 (2000).
78. Wu, X. *et al.* Modes of intercellular transcription factor movement in the Arabidopsis apex. *Development* **130**, 3735–3745 (2003).
79. Rim, Y. *et al.* Analysis of Arabidopsis Transcription Factor Families Revealed Extensive Capacity for Cell-to-Cell Movement as Well as Discrete Trafficking Patterns. *Mol Cells* **32**, 519–526 (2011).
80. Lucas, W. J. *et al.* Selective trafficking of KNOTTED1 homeodomain protein and its mRNA through plasmodesmata. *Science* vol. 270 1980–1983 (1995).

81. Kragler, F., Monzer, J., Shash, K., Xoconostle-Cázares, B. & Lucas, W. J. Cell-to-cell transport of proteins: Requirement for unfolding and characterization of binding to a putative plasmodesmal receptor. *Plant Journal* **15**, 367–381 (1998).
82. Xu, X. M. *et al.* Chaperonins Facilitate KNOTTED1 Cell-to-Cell Trafficking and Stem Cell Function. *Science (1979)* **333**, 1141–1143 (2011).
83. Kitagawa, M., Wu, P., Balkunde, R., Cunniff, P. & Jackson, D. An RNA Exosome Subunit Mediates Cell-to-Cell Trafficking of a Homeobox MRNA via Plasmodesmata. *Science* **375**,177-182 (2022).
84. Winter, C. M. *et al.* SHR and SCR coordinate root patterning and growth early in the cell cycle. *Nature* **626**, 611–616 (2024).
85. Gallagher, K. L., Paquette, A. J., Nakajima, K. & Benfey, P. N. Mechanisms Regulating SHORT-ROOT Intercellular Movement nontargeted movement involves a protein moving with-out interacting with the plasmodesmal apparatus. In this case, the process resembles passive diffusion, as for. *Current Biology* **14**, 1847–1851 (2004).
86. Gallagher, K. L. & Benfey, P. N. Both the conserved GRAS domain and nuclear localization are required for SHORT-ROOT movement. *The Plant Journal* **57**, 785–797 (2009).
87. Tassetto, M., Maizel, A., Osorio, J. & Joliot, A. Plant and animal homeodomains use convergent mechanisms for intercellular transfer. *EMBO Rep* **6**, 885-890–890 (2005).
88. Koizumi, K., Wu, S., MacRae-Crerar, A. & Gallagher, K. L. An essential protein that interacts with endosomes and promotes movement of the SHORT-ROOT transcription factor. *Current Biology* **21**, 1559–1564 (2011).
89. Wu, S. & Gallagher, K. L. The movement of the non-cell-autonomous transcription factor, SHORT-ROOT relies on the endomembrane system. *Plant Journal* **80**, 396–409 (2014).
90. Wu, S. & Gallagher, K. L. Intact microtubules are required for the intercellular movement of the SHORT-ROOT transcription factor. *The Plant Journal* **74**, 148–159 (2013).
91. Lee, J. Y. *et al.* Selective trafficking of non-cell-autonomous proteins mediated by NtNCAPP1. *Science (1979)* **299**, 392–396 (2003).
92. Taoka, K., Ham, B.-K., Xoconostle-Cázares, B., Rojas, M. R. & Lucas, W. J. Reciprocal Phosphorylation and Glycosylation Recognition Motifs Control NCAPP1 Interaction with Pumpkin Phloem Proteins and Their Cell-to-Cell Movement. *Plant Cell* **19**, 1866–1884 (2007).
93. Wolf, S., Deom, C. M., Beachy, R. N. & Lucas, W. J. Movement protein of tobacco mosaic virus modifies plasmodesmatal size exclusion limit. *Science (1979)* **246**, 377–379 (1989).
94. Lee, J. Y. & Lu, H. Plasmodesmata: The battleground against intruders. *Trends Plant Sci* **16**, 201–210 (2011).
95. Tilsner, J., Taliansky, M. E. & Torrance, L. Plant Virus Movement. In *eLS* (2014).
96. Yuan, C. & Lazarowitz, S. G. Identification of a Functional Plasmodesmal Localization Signal in a. *mBio* **7**, 1–10 (2016).
97. Navarro, J. A., Serra-Soriano, M., Corachán-Valencia, L. & Pallás, V. A conserved motif in three viral movement proteins from different genera is required for host factor recruitment and cell-to-cell movement. *Sci Rep* **10**, 4758 (2020).
98. Lucas, W. J., Ham, B. K. & Kim, J. Y. Plasmodesmata - bridging the gap between neighboring plant cells. *Trends in Cell Biology* vol. 19 495–503 (2009).

99. Chen, H., Ahmad, M., Rim, Y., Lucas, W. J. & Kim, J. Y. Evolutionary and molecular analysis of Dof transcription factors identified a conserved motif for intercellular protein trafficking. *New Phytologist* **198**, 1250–1260 (2013).
100. Kim, J. Y., Rim, Y., Wang, J. & Jackson, D. A novel cell-to-cell trafficking assay indicates that the KNOX homeodomain is necessary and sufficient for intercellular protein and mRNA trafficking. *Genes Dev* **19**, 788–793 (2005).
101. Yan, Y. & Ham, B.-K. The Mobile Small RNAs: Important Messengers for Long-Distance Communication in Plants. *Front Plant Sci* **13**, (2022).
102. Brioudes, F. *et al.* HASTY , the Arabidopsis EXPORTIN5 ortholog, regulates cell-to-cell and vascular microRNA movement . *EMBO J* **40**, (2021).
103. Zhang, W. *et al.* tRNA-Related Sequences Trigger Systemic mRNA Transport in Plants. *Plant Cell* **28**, 1237–1249 (2016).
104. Yang, L. *et al.* m5C Methylation Guides Systemic Transport of Messenger RNA over Graft Junctions in Plants. *Current Biology* **29**, 2465-2476.e5 (2019).
105. Xu, Y. *et al.* Systemic mRNA transport depends on m5C methylation, nuclear mRNA export factors and developmental phase changes. *bioRxiv* 2024.05.30.596576 (2024).
106. Paul, S., Jackson, D. & Kitagawa, M. Tracking the messengers: Emerging advances in mRNA-based plant communication. *Current Opinion in Plant Biology* vol. 79 (2024).
107. Luo, K. R., Huang, N. C., Chang, Y. H., Jan, Y. W. & Yu, T. S. Arabidopsis cyclophilins direct intracellular transport of mobile mRNA via organelle hitchhiking. *Nature Plants* **10**, 161–171 (2024).
108. Dross, N. *et al.* Mapping eGFP Oligomer Mobility in Living Cell Nuclei. *PLoS One* **4**, e5041- (2009).
109. Lucas, W. J. & Lee, J. Y. Plasmodesmata as a supracellular control network in plants. *Nat Rev Mol Cell Biol* **5**, 712–726 (2004).
110. Ling, Q. & Jarvis, P. Functions of plastid protein import and the ubiquitin–proteasome system in plastid development. *Biochimica et Biophysica Acta (BBA) - Bioenergetics* **1847**, 939–948 (2015).
111. Haastrup, M. O., Vikramdeo, K. S., Singh, S., Singh, A. P. & Dasgupta, S. The Journey of Mitochondrial Protein Import and the Roadmap to Follow. *International Journal of Molecular Sciences* vol. 24 (2023).
112. Wang, G., Shimada, E., Nili, M., Koehler, C. M. & Teitell, M. A. Mitochondria-Targeted RNA Import. in *Mitochondrial Medicine: Volume I, Probing Mitochondrial Function* (eds. Weissig, V. & Edeas, M.) 107–116 (Springer New York, New York, NY, 2015).
113. Berrissou, C. *et al.* Extensive import of nucleus-encoded tRNAs into chloroplasts of the photosynthetic lycophyte, *Selaginella kraussiana*. *Proceedings of the National Academy of Sciences* **121**, e2412221121 (2024).
114. Zoratti, M., Biasutto, L., Parrasia, S. & Szabo, I. Mitochondrial permeability transition pore: a snapshot of a therapeutic target. *Expert Opin Ther Targets* **28**, 1–3 (2024).
115. Christian, R., Labbancz, J., Usadel, B. & Dhingra, A. Understanding protein import in diverse non-green plastids. *Front Genet* **14**, (2023).
116. Lee, A. J. *et al.* Parallels between nuclear-pore and plasmodesmal trafficking. *Planta* **210**, 177–187 (2000).
117. Schmidt, H. B. & Görlich, D. Transport Selectivity of Nuclear Pores, Phase Separation, and Membraneless Organelles. *Trends in Biochemical Sciences* vol. 41 46–61 (2016).

118. Johnson, C. A. & Malicki, J. J. The Nuclear Arsenal of Cilia. *Developmental Cell* vol. 49 161–170 (2019).
119. Ravindran, R. *et al.* Peroxisome biogenesis initiated by protein phase separation. *Nature* **617**, 608–615 (2023).
120. Gao, Y., Skowyra, M. L., Feng, P. & Rapoport, T. A. Protein import into peroxisomes occurs through a nuclear pore–like phase. *Science (1979)* **378**, eadf3971 (2022).
121. Devos, D. P., Gräf, R. & Field, M. C. Evolution of the nucleus. *Curr Opin Cell Biol* **28**, 8–15 (2014).
122. Strambio-De-Castillia, C., Niepel, M. & Rout, M. P. The nuclear pore complex: Bridging nuclear transport and gene regulation. *Nature Reviews Molecular Cell Biology* vol. 11 490–501 (2010).
123. Beck, M. & Hurt, E. The nuclear pore complex: Understanding its function through structural insight. *Nature Reviews Molecular Cell Biology* vol. 18 73–89 (2017).
124. Petrovic, S. *et al.* Structure and Function of the Nuclear Pore Complex. *Cold Spring Harb Perspect Biol* **14**, (2022).
125. Huang, G., Zeng, C. & Shi, Y. Structure of the nuclear pore complex goes atomic. *Curr Opin Struct Biol* **78**, 102523 (2023).
126. Lin, D. H. & Hoelz, A. The Structure of the Nuclear Pore Complex (An Update). *Annu Rev Biochem* **88**, 725–783 (2019).
127. Kim, S. J. *et al.* Integrative structure and functional anatomy of a nuclear pore complex. *Nature* **555**, 475–482 (2018).
128. Bley, C. J. *et al.* Architecture of the cytoplasmic face of the nuclear pore. *Science (1979)* **376**, eabm9129 (2022).
129. Tang, Y. Plant nuclear envelope as a hub connecting genome organization with regulation of gene expression. *Nucleus* **14**, 2178201 (2023).
130. Blobel, G. Gene gating: a hypothesis. *Proceedings of the National Academy of Sciences* **82**, 8527–8529 (1985).
131. Pascual-Garcia, P. & Capelson, M. The nuclear pore complex and the genome: organizing and regulatory principles. *Curr Opin Genet Dev* **67**, 142–150 (2021).
132. Akey, C. W. *et al.* Comprehensive structure and functional adaptations of the yeast nuclear pore complex. *Cell* **185**, 361-378.e25 (2022).
133. Schuller, A. P. *et al.* The cellular environment shapes the nuclear pore complex architecture. *Nature* **598**, 667–671 (2021).
134. Zimmerli, C. E. *et al.* Nuclear pores dilate and constrict in cellulo. *Science (1979)* **374**, eabd9776 (2021).
135. Petrovic, S. *et al.* Architecture of the linker-scaffold in the nuclear pore. *Science (1979)* **376**, eabm9798 (2022).
136. Mosalaganti, S. *et al.* AI-based structure prediction empowers integrative structural analysis of human nuclear pores. *Science (1979)* **376**, eabm9506 (2022).
137. Lin, D. H. *et al.* Architecture of the symmetric core of the nuclear pore. *Science (1979)* **352**, aaf1015 (2016).
138. Zhang, Y. *et al.* Molecular architecture of the luminal ring of the *Xenopus laevis* nuclear pore complex. *Cell Res* **30**, 532–540 (2020).
139. Singh, D. *et al.* The molecular architecture of the nuclear basket. *Cell* **187**, 5267-5281.e13 (2024).
140. Sachweh, J. *et al.* The small GTPase Ran defines Nuclear Pore Complex Asymmetry. *bioRxiv* 2024.10.10.617378 (2024) doi:10.1101/2024.10.10.617378.
141. Ng, S. C. & Görlich, D. A simple thermodynamic description of phase separation of Nup98 FG domains. *Nat Commun* **13**, (2022).

142. Aramburu, I. V. & Lemke, E. A. Floppy but not sloppy: Interaction mechanism of FG-nucleoporins and nuclear transport receptors. *Semin Cell Dev Biol* **68**, 34–41 (2017).
143. Dekker, M., Van der Giessen, E. & Onck, P. R. Phase separation of intrinsically disordered FG-Nups is driven by highly dynamic FG motifs. *Proceedings of the National Academy of Sciences* **120**, e2221804120 (2023).
144. Frey, S., Richter, R. P. & Görlich, D. FG-Rich Repeats of Nuclear Pore Proteins Form a Three-Dimensional Meshwork with Hydrogel-Like Properties. *Science (1979)* **314**, 815–817 (2006).
145. Frey, S. *et al.* Surface Properties Determining Passage Rates of Proteins through Nuclear Pores. *Cell* **174**, 202-217.e9 (2018).
146. Wing, C. E., Fung, H. Y. J. & Chook, Y. M. Karyopherin-mediated nucleocytoplasmic transport. *Nat Rev Mol Cell Biol* **23**, 307–328 (2022).
147. Hoogenboom, B. W. *et al.* Physics of the nuclear pore complex: Theory, modeling and experiment. *Phys Rep* **921**, 1–53 (2021).
148. Ng, S. C. *et al.* Barrier properties of Nup98 FG phases ruled by FG motif identity and inter-FG spacer length. *Nat Commun* **14**, 747 (2023).
149. Frey, S. & Görlich, D. A Saturated FG-Repeat Hydrogel Can Reproduce the Permeability Properties of Nuclear Pore Complexes. *Cell* **130**, 512–523 (2007).
150. Celetti, G. *et al.* The liquid state of FG-nucleoporins mimics permeability barrier properties of nuclear pore complexes. *Journal of Cell Biology* **219**, (2020).
151. Cowburn, D. & Rout, M. Improving the hole picture: towards a consensus on the mechanism of nuclear transport. *Biochem Soc Trans* **51**, 871–886 (2023).
152. Yu, M. *et al.* Visualizing the disordered nuclear transport machinery *in situ*. *Nature* **617**, 162–169 (2023).
153. Lim, R. Y. H., Huang, B. & Kapinos, L. E. How to operate a nuclear pore complex by Kap-centric control. *Nucleus* **6**, 366–372 (2015).
154. Pumroy, R. A. & Cingolani, G. Diversification of importin-α isoforms in cellular trafficking and disease states. *Biochemical Journal* **466**, 13–28 (2015).
155. Yang, Y. *et al.* Nuclear transport proteins: structure, function and disease relevance. *Signal Transduct Target Ther* **8**, 425 (2023).
156. Ribbeck, K., Lipowsky, G., Kent, H. M., Stewart, M. & Görlich, D. NTF2 mediates nuclear import of Ran. *EMBO J* **17**, 6587-6598–6598 (1998).
157. Beck, M., Lučić, V., Förster, F., Baumeister, W. & Medalia, O. Snapshots of nuclear pore complexes in action captured by cryo-electron tomography. *Nature* **449**, 611–615 (2007).
158. Fiserova, J., Richards, S. A., Wente, S. R. & Goldberg, M. W. Facilitated transport and diffusion take distinct spatial routes through the nuclear pore complex. *J Cell Sci* **123**, 2773–2780 (2010).
159. Ma, J. & Yang, W. Three-dimensional distribution of transient interactions in the nuclear pore complex obtained from single-molecule snapshots. *Proceedings of the National Academy of Sciences* **107**, 7305–7310 (2010).
160. Ma, J., Goryaynov, A., Sarma, A. & Yang, W. Self-regulated viscous channel in the nuclear pore complex. *Proceedings of the National Academy of Sciences* **109**, 7326–7331 (2012).
161. Ma, J., Goryaynov, A. & Yang, W. Super-resolution 3D tomography of interactions and competition in the nuclear pore complex. *Nat Struct Mol Biol* **23**, 239–247 (2016).
162. Chowdhury, R., Sau, A. & Musser, S. M. Super-resolved 3D tracking of cargo transport through nuclear pore complexes. *Nat Cell Biol* **24**, 112–122 (2022).

163. Li, Z. *et al.* Nuclear export of pre-60S particles through the nuclear pore complex. *Nature* **618**, 411–418 (2023).
164. Mudumbi, K. C. *et al.* Nucleoplasmic signals promote directed transmembrane protein import simultaneously via multiple channels of nuclear pores. *Nat Commun* **11**, 2184 (2020).
165. Dekker, M. *et al.* Nuclear transport at full amino-acid resolution. *bioRxiv* 2024.06.23.600256 (2024) doi:10.1101/2024.06.23.600256.
166. Schleicher, K. D. *et al.* Selective transport control on molecular velcro made from intrinsically disordered proteins. *Nat Nanotechnol* **9**, 525–530 (2014).
167. Yang, W. & Musser, S. M. Nuclear import time and transport efficiency depend on importin β concentration. *Journal of Cell Biology* **174**, 951–961 (2006).
168. Kalita, J. *et al.* Karyopherin enrichment and compensation fortifies the nuclear pore complex against nucleocytoplasmic leakage. *Journal of Cell Biology* **221**, e202108107 (2022).
169. Yu, W. *et al.* Exploring Cellular Gateways: Unraveling the Secrets of Disordered Proteins within Live Nuclear Pores. *Res Sq* (2024) doi:10.21203/rs.3.rs-3504130/v1.
170. Boettcher, B. & Barral, Y. The cell biology of open and closed mitosis. *Nucleus* **4**, 160–165 (2013).
171. Otsuka, S. *et al.* A quantitative map of nuclear pore assembly reveals two distinct mechanisms. *Nature* **613**, 575–581 (2023).
172. Otsuka, S. *et al.* Postmitotic nuclear pore assembly proceeds by radial dilation of small membrane openings. *Nat Struct Mol Biol* **25**, 21–28 (2018).
173. Otsuka, S. & Ellenberg, J. Mechanisms of nuclear pore complex assembly – two different ways of building one molecular machine. *FEBS Lett* **592**, 475–488 (2018).
174. Otsuka, S. *et al.* Nuclear pore assembly proceeds by an inside-out extrusion of the nuclear envelope. *Elife* **5**, e19071 (2016).
175. Buzz, B. & Anja, S. On the origin of the nucleus: a hypothesis. *Microbiology and Molecular Biology Reviews* **87**, e00186-21 (2023).
176. Baum, D. A. & Baum, B. An inside-out origin for the eukaryotic cell. *BMC Biol* **12**, 76 (2014).
177. Donoghue, P. C. J. *et al.* Defining eukaryotes to dissect eukaryogenesis. *Current Biology* vol. 33 R919–R929 (2023).
178. Avcı, B. *et al.* Spatial separation of ribosomes and DNA in Asgard archaeal cells. *ISME J* **16**, 606–610 (2022).
179. Melnikov, S. *et al.* Archaeal Ribosomal Proteins Possess Nuclear Localization Signal-Type Motifs: Implications for the Origin of the Cell Nucleus. *Mol Biol Evol* **37**, 124–133 (2020).
180. Rodrigues-Oliveira, T. *et al.* Actin cytoskeleton and complex cell architecture in an Asgard archaeon. *Nature* **613**, 332–339 (2023).
181. Rout, M. P. & Field, M. C. The Evolution of Organellar Coat Complexes and Organization of the Eukaryotic Cell. *Annu. Rev. Biochem.* 637–657 (2017)
182. Field, M. C. & Rout, M. P. Pore timing: The evolutionary origins of the nucleus and nuclear pore complex. *F1000Research* vol. 8 (2019).
183. Makarov, A. A., Padilla-Mejia, N. E. & Field, M. C. Evolution and diversification of the nuclear pore complex. *Biochemical Society Transactions* vol. 49 1601–1619 (2021).
184. Jovanovic-Talisman, T. *et al.* Artificial nanopores that mimic the transport selectivity of the nuclear pore complex. *Nature* **457**, 1023–1027 (2009).

185. Fragasso, A. *et al.* A designer FG-Nup that reconstitutes the selective transport barrier of the nuclear pore complex. *Nat Commun* **12**, (2021).
186. Panatala, R. *et al.* Nuclear Pore Membrane Proteins Self-Assemble into Nanopores. *Biochemistry* **58**, 484–488 (2019).
187. Sanchez Carrillo, I. B., Hoffmann, P. C., Barff, T., Beck, M. & Germain, H. Preparing *Arabidopsis thaliana* root protoplasts for cryo electron tomography. *Front Plant Sci* **14**, (2023).
188. Fiserova, J., Kiseleva, E. & Goldberg, M. W. Nuclear envelope and nuclear pore complex structure and organization in tobacco BY-2 cells. *The Plant Journal* **59**, 243–255 (2009).
189. Mosalaganti, S. *et al.* In situ architecture of the algal nuclear pore complex. *Nat Commun* **9**, 2361 (2018).
190. Tamura, K., Fukao, Y., Iwamoto, M., Haraguchi, T. & Hara-Nishimura, I. Identification and characterization of nuclear pore complex components in *Arabidopsis thaliana*. *Plant Cell* **22**, 4084–4097 (2010).
191. Tamura, K., Fukao, Y., Hatsugai, N., Katagiri, F. & Hara-Nishimura, I. Nup82 functions redundantly with Nup136 in a salicylic acid-dependent defense response of *Arabidopsis thaliana. Nucleus* **8**, 301–311 (2017).
192. Gu, Y. *et al.* Nuclear Pore Permeabilization Is a Convergent Signaling Event in Effector-Triggered Immunity. *Cell* **166**, 1526-1538.e11 (2016).
193. O'Reilly, A. J., Dacks, J. B. & Field, M. C. Evolution of the Karyopherin-β Family of Nucleocytoplasmic Transport Factors; Ancient Origins and Continued Specialization. *PLoS One* **6**, e19308- (2011).
194. Zhang, B. *et al.* Linking key steps of microRNA biogenesis by TREX-2 and the nuclear pore complex in Arabidopsis. *Nat Plants* **6**, 957–969 (2020).
195. Rödel, A. *et al.* Arabidopsis mRNA export factor MOS11: molecular interactions and role in abiotic stress responses. *New Phytologist* **243**, 180–194 (2024).
196. Mermet, S. *et al.* Evolutionarily conserved protein motifs drive interactions between the plant nucleoskeleton and nuclear pores. *Plant Cell* **35**, 4284–4303 (2023).
197. Tang, Y., Ho, M. I., Kang, B.-H. & Gu, Y. GBPL3 localizes to the nuclear pore complex and functionally connects the nuclear basket with the nucleoskeleton in plants. *PLoS Biol* **20**, e3001831- (2022).
198. Huang, S., Zhu, S., Kumar, P. & MacMicking, J. D. A phase-separated nuclear GBPL circuit controls immunity in plants. *Nature* **594**, 424–429 (2021).
199. MacGregor, D. R. & Penfield, S. Exploring the pleiotropy of *hos1*. *J Exp Bot* **66**, 1661–1671 (2015).
200. Li, C., Liu, L., Teo, Z. W. N., Shen, L. & Yu, H. Nucleoporin 160 Regulates Flowering through Anchoring HOS1 for Destabilizing CO in Arabidopsis. *Plant Commun* **1**, 100033 (2020).
201. Wang, J. *et al.* Phase separation of the nuclear pore complex facilitates selective nuclear transport to regulate plant defense against pathogen and pest invasion. *Mol Plant* **16**, 1016–1030 (2023).
202. Tang, Y., Huang, A. & Gu, Y. Global profiling of plant nuclear membrane proteome in Arabidopsis. *Nat Plants* **6**, 838–847 (2020).
203. Tang, Y., Huang, A. & Gu, Y. Global profiling of plant nuclear membrane proteome in Arabidopsis. *Nat Plants* **6**, 838–847 (2020).
204. Tang, Y. *et al.* Proxiome assembly of the plant nuclear pore reveals an essential hub for gene expression regulation. *Nature Plants* (2024) doi:10.1038/s41477-024-01698-9.

205. Wang, S. *et al.* A noncanonical role for the CKI-RB-E2F cell-cycle signaling pathway in plant effector-triggered immunity. *Cell Host Microbe* **16**, 787–794 (2014).
206. Ma, M. *et al.* CPR5 positively regulates pattern-triggered immunity via a mediator protein. *J Integr Plant Biol* **65**, 1613–1619 (2023).
207. Bowling, S. A., Clarke, J. D., Liu, Y., Klessig, D. F. & Dong, X. The cpr5 mutant of Arabidopsis expresses both NPR1-dependent and NPR1-independent resistance. *Plant Cell* **9**, 1573–1584 (1997).
208. Boch, J., Verbsky, M. L., Robertson, T. L., Larkin, J. C. & Kunkel, B. N. Analysis of Resistance Gene-Mediated Defense Responses in *Arabidopsis thaliana* Plants Carrying a Mutation in CPR5. *Molecular Plant-Microbe Interactions®* **11**, 1196–1206 (1998).
209. Brininstool, G. *et al.* Constitutive Expressor of Pathogenesis-Related Genes5affects cell wall biogenesis and trichome development. *BMC Plant Biol* **8**, 58 (2008).
210. Nam, H. *et al.* CPR5-mediated nucleo-cytoplasmic localization of IAA12 and IAA19 controls lateral root development during abiotic stress. *Proceedings of the National Academy of Sciences* **120**, e2209781120 (2023).
211. Jing, H.-C., Sturre, M. J. G., Hille, J. & Dijkwel, P. P. Arabidopsis onset of leaf death mutants identify a regulatory pathway controlling leaf senescence. *The Plant Journal* **32**, 51–63 (2002).
212. Aki, T. *et al.* Distinct modulations of the hexokinase1-mediated glucose response and hexokinase1-independent processes by HYS1/CPR5 in Arabidopsis. *J Exp Bot* **58**, 3239–3248 (2007).
213. Meng, Z., Ruberti, C., Gong, Z. & Brandizzi, F. CPR5 modulates salicylic acid and the unfolded protein response to manage tradeoffs between plant growth and stress responses. *Plant Journal* **89**, 486–501 (2017).
214. Kirik, V. *et al.* CPR5 is involved in cell proliferation and cell death control and encodes a novel transmembrane protein. *Current Biology* **11**, 1891–1895 (2001).
215. Yoshida, S., Ito, M., Nishida, I. & Watanabe, A. Identification of a novel gene HYS1/CPR5 that has a repressive role in the induction of leaf senescence and pathogen-defence responses in *Arabidopsis thaliana. The Plant Journal* **29**, 427–437 (2002).
216. Xu, F. *et al.* Exportin-4 coordinates nuclear shuttling of TOPLESS family transcription corepressors to regulate plant immunity. *Plant Cell* **33**, 697–713 (2021).
217. Peng, S. *et al.* CONSTITUTIVE EXPRESSER of PATHOGENESIS-RELATED GENES 5 is an RNA-binding protein controlling plant immunity via an RNA processing complex. *Plant Cell* **34**, 1724–1744 (2022).
218. Arra, Y. *et al. Rice Yellow Mottle Virus* resistance by genome editing of the *Oryza sativa* L. ssp. japonica nucleoporin gene OsCPR5.1 but not OsCPR5.2. *Plant Biotechnol J* (2023) doi:10.1111/pbi.14266.
219. Heinß, N., Sushkin, M., Yu, M. & Lemke, E. A. Multifunctionality of F-rich nucleoporins. *Biochemical Society Transactions* vol. 48 2603–2614 (2020).
220. Ouyang, M. *et al.* Liquid-Liquid Phase Transition Drives Intra-chloroplast Cargo Sorting. *Cell* **180**, 1144-1159.e20 (2020).
221. Ho, B., Baryshnikova, A. & Brown, G. W. Unification of Protein Abundance Datasets Yields a Quantitative Saccharomyces cerevisiae Proteome. *Cell Syst* **6**, 192-205.e3 (2018).
222. Collonnier, C. *et al.* Towards mastering CRISPR-induced gene knock-in in plants: Survey of key features and focus on the model *Physcomitrella patens*. *Methods* **121–122**, 103–117 (2017).

223. Anzalone, A. V *et al.* Search-and-replace genome editing without double-strand breaks or donor DNA. *Nature* **576**, 149–157 (2019).
224. Perroud, P. F. *et al.* Prime Editing in the model plant *Physcomitrium patens* and its potential in the tetraploid potato. *Plant Science* **316**, (2022).
225. Perroud, P. F. *et al.* Improved prime editing allows for routine predictable gene editing in *Physcomitrium patens*. *J Exp Bot* **74**, 6176–6187 (2023).
226. Nelson, J. W. *et al.* Engineered pegRNAs improve prime editing efficiency. *Nat Biotechnol* **40**, 432 (2022).
227. Schladt, T. M. *et al.* Identification of nuclear pore proteins at plasmodesmata. *bioRxiv* 2024.09.02.610746 (2024) doi:10.1101/2024.09.02.610746.
228. Lampropoulos, A. *et al.* GreenGate - A novel, versatile, and efficient cloning system for plant transgenesis. *PLoS One* **8**, (2013).
229. Concordet, J.-P. & Haeussler, M. CRISPOR: intuitive guide selection for CRISPR/Cas9 genome editing experiments and screens. *Nucleic Acids Res* **46**, W242–W245 (2018).
230. Szövényi, P. *et al.* Selfing in Haploid Plants and Efficacy of Selection: Codon Usage Bias in the Model Moss *Physcomitrella patens*. *Genome Biol Evol* **9**, 1528–1546 (2017).
231. Lin, Q. *et al.* High-efficiency prime editing with optimized, paired pegRNAs in plants. *Nat Biotechnol* **39**, 923–927 (2021).
232. Charlot, F., Goudounet, G., Nogué, F. & Perroud, P.-F. *Physcomitrium patens* Protoplasting and Protoplast Transfection. in *Protoplast Technology: Methods and Protocols* (eds. Wang, K. & Zhang, F.) 3–19 (Springer US, New York, NY, 2022). doi:10.1007/978-1-0716-2164-6_1.
233. Edwards, K., Johnstone, C. & Thompson, C. A simple and rapid method for the preparation of plant genomic DNA for PCR analysis. *Nucleic Acids Res* **19**, 1349 (1991).
234. Buels, R. *et al.* JBrowse: A dynamic web platform for genome visualization and analysis. *Genome Biol* **17**, (2016).
235. Gao, G. *et al.* Arabidopsis CPR5 Independently Regulates Seed Germination and Postgermination Arrest of Development through LOX Pathway and ABA Signaling. *PLoS One* **6**, e19406- (2011).
236. Xiao, L. *et al.* Two Nucleoporin98 homologous genes jointly participate in the regulation of starch degradation to repress senescence in Arabidopsis. *BMC Plant Biol* **20**, 292 (2020).
237. Abramson, J. *et al.* Accurate structure prediction of biomolecular interactions with AlphaFold 3. *Nature* **630**, 493–500 (2024).
238. Schrödinger LLC. The PyMOL Molecular Graphics System, Version~1.8. (2015).
239. Fleming, P. J. & Fleming, K. G. HullRad: Fast Calculations of Folded and Disordered Protein and Nucleic Acid Hydrodynamic Properties. *Biophys J* **114**, 856–869 (2018).
240. Powers, M. A., Forbes, D. J., Dahlberg, J. E. & Lund, E. The Vertebrate GLFG Nucleoporin, Nup98, Is an Essential Component of Multiple RNA Export Pathways. *Journal of Cell Biology* **136**, 241–250 (1997).
241. Consortium, T. U. UniProt: the Universal Protein Knowledgebase in 2025. *Nucleic Acids Res* gkae1010 (2024).
242. Reddy Chichili, V. P., Kumar, V. & Sivaraman, J. Linkers in the structural biology of protein–protein interactions. *Protein Science* **22**, 153–167 (2013).

243. Schmidt, H. B. & Görlich, D. Nup98 FG domains from diverse species spontaneously phase-separate into particles with nuclear pore-like permselectivity. *Elife* **4**, e04251 (2015).
244. Gombos, S. *et al.* A high-confidence *Physcomitrium patens* plasmodesmata proteome by iterative scoring and validation reveals diversification of cell wall proteins during evolution. *New Phytologist* **238**, 637–653 (2023).
245. Epel, B. L. *et al.* A 41 kDa protein isolated from maize mesocotyl cell walls immunolocalizes to plasmodesmata. *Protoplasma* **191**, 70–78 (1996).
246. Sagi, G., Katz, A., Guenoune-Gelbart, D. & Epel, B. L. Class 1 reversibly glycosylated polypeptides are plasmodesmal-associated proteins delivered to plasmodesmata via the Golgi apparatus. *Plant Cell* **17**, 1788–1800 (2005).
247. Zavaliev, R., Sagi, G., Gera, A. & Epel, B. L. The constitutive expression of Arabidopsis plasmodesmal-associated class 1 reversibly glycosylated polypeptide impairs plant development and virus spread. *J Exp Bot* **61**, 131–142 (2010).
248. Burch-Smith, T. M., Cui, Y. & Zambryski, P. C. Reduced levels of class 1 reversibly glycosylated polypeptide increase intercellular transport via plasmodesmata. *Plant Signal Behav* **7**, 62–67 (2012).
249. Drakakaki, G. *et al.* Arabidopsis Reversibly Glycosylated Polypeptides 1 and 2 Are Essential for Pollen Development. *Plant Physiol* **142**, 1480–1492 (2006).
250. Lak, B. *et al.* Specific subdomain localization of ER resident proteins and membrane contact sites resolved by electron microscopy. *Eur J Cell Biol* **100**, 151180 (2021).
251. Lisenbee, C. S., Karnik, S. K. & Trelease, R. N. Overexpression and Mislocalization of a Tail-Anchored GFP Redefines the Identity of Peroxisomal ER. *Traffic* **4**, 491–501 (2003).
252. Hamed, M. & Antonin, W. Dunking into the lipid bilayer: How direct membrane binding of nucleoporins can contribute to nuclear pore complex structure and assembly. *Cells* vol. 10 (2021).
253. Berkovits, B. D. & Mayr, C. Alternative 3′ UTRs act as scaffolds to regulate membrane protein localization. *Nature* **522**, 363–367 (2015).
254. Kitagawa, M. & Fujita, T. Quantitative imaging of directional transport through plasmodesmata in moss protonemata via single-cell photoconversion of Dendra2. *J Plant Res* **126**, 577–585 (2013).
255. Kitagawa, M. & Fujita, T. A model system for analyzing intercellular communication through plasmodesmata using moss protonemata and leaves. *J Plant Res* **128**, 63–72 (2014).
256. Lin, J. *et al.* Annulate Lamellae biogenesis is essential for nuclear pore function. *bioRxiv* 2024.10.08.617205 (2024) doi:10.1101/2024.10.08.617205.
257. Scheer, U. & Franke, W. W. Annulate lamellae in plant cells: Formation during microsporogenesis and pollen development in *Canna generalis Bailey*. *Planta* **107**, 145–159 (1972).
258. Kee, H. L. *et al.* A size-exclusion permeability barrier and nucleoporins characterize a ciliary pore complex that regulates transport into cilia. *Nat Cell Biol* **14**, 431–437 (2012).
259. del Viso, F. *et al.* Congenital Heart Disease Genetics Uncovers Context-Dependent Organization and Function of Nucleoporins at Cilia. *Dev Cell* **38**, 478–492 (2016).
260. Takao, D. *et al.* An assay for clogging the ciliary pore complex distinguishes mechanisms of cytosolic and membrane protein entry. *Current Biology* **24**, 2288–2294 (2014).

261. Endicott, S. J. & Brueckner, M. NUP98 Sets the Size-Exclusion Diffusion Limit through the Ciliary Base. *Current Biology* **28**, 1643-1650.e3 (2018).
262. Dishinger, J. F. *et al.* Ciliary entry of the kinesin-2 motor KIF17 is regulated by importin-B2 and RanGTP. *Nat Cell Biol* **12**, 703–710 (2010).
263. Madugula, V. & Lu, L. A ternary complex comprising transportin1, Rab8 and the ciliary targeting signal directs proteins to ciliary membranes. *J Cell Sci* **129**, 3922–3934 (2016).
264. Han, Y. *et al.* Regulation of Gli ciliary localization and Hedgehog signaling by the PY-NLS/karyopherin-β2 nuclear import system. *PLoS Biol* **15**, e2002063- (2017).
265. Peeters, B. W. A., Piët, A. C. A. & Fornerod, M. Generating Membrane Curvature at the Nuclear Pore: A Lipid Point of View. *Cells* **11**, (2022).
266. Spiegelman, Z., Lee, C.-M. & Gallagher, K. L. KinG Is a Plant-Specific Kinesin That Regulates Both Intra- and Intercellular Movement of SHORT-ROOT . *Plant Physiol* **176**, 392–405 (2018).
267. Huang, Y.-W. *et al.* A viral movement protein co-opts endoplasmic reticulum luminal-binding protein and calreticulin to promote intracellular movement. *Plant Physiol* **191**, 904–924 (2023).
268. Wu, C.-H., Lee, S.-C. & Wang, C.-W. Viral protein targeting to the cortical endoplasmic reticulum is required for cell–cell spreading in plants. *Journal of Cell Biology* **193**, 521–535 (2011).
269. Lazareva, E. A. *et al.* Reticulon-like properties of a plant virus-encoded movement protein. *New Phytologist* **229**, 1052–1066 (2021).
270. Meinke, D. W. Genome-wide identification of - () genes required for growth and development in Arabidopsis. *New Phytologist* **226**, 306–325 (2020).
271. Li, Z., Liu, S.-L., Montes-Serey, C., Walley, J. W. & Aung, K. PLASMODESMATA-LOCATED PROTEIN 6 regulates plasmodesmal function in Arabidopsis vasculature. *Plant Cell* **36**, 3543–3561 (2024).

13. Appendix

13.1. Contributions

This thesis is a contains published manuscripts and as manuscripts in preparation.

Chapter I was entirely written by me. Figure 2 was modified from modified from Tee and Faulkner, 2024 [64]. All other Figures were prepared by me.

Chapter II is a published manuscript.

Estimated contribution 15%

Manuel Miras, Mathieu Pottier, T. Moritz Schladt, J. Obinna Ejike, Laura Redzich, Wolf B. Frommer, Ji-Yun Kim, Plasmodesmata and their role in assimilate translocation, Journal of Plant Physiology, Volume 270, 2022, 153633, ISSN 0176-1617, **https://doi.org/10.1016/j.jplph.2022.153633**.
(https://www.sciencedirect.com/science/article/pii/S0176161722000190)

I wrote the section: 7. Symplasmic domains may enable exchange of communication and sugars in zones and 3. PD protein composition. Further I contributed to proof reading and editing the manuscript.

Chapter III is a published manuscript.

Estimated contribution 15%

Gombos, S., Miras, M., Howe, V., Xi, L., Pottier, M., Kazemein Jasemi, N.S., Schladt, M., Ejike, J.O., Neumann, U., Hänsch, S., Kuttig, F., Zhang, Z., Dickmanns, M., Xu, P., Stefan, T., Baumeister, W., Frommer, W.B., Simon, R. and Schulze, W.X. (2023), A high-confidence Physcomitrium patens plasmodesmata proteome by iterative scoring and validation reveals diversification of cell wall proteins during evolution. New Phytol, 238: 637-653. https://doi.org/10.1111/nph.18730

Here I contributed by cloning and localizing 59 *P. patens* PD candidates. Also, I, established *P. patens* protoplast transfection in our lab and generated the GHL17-1-mVenus line that was used in Figure 5 of the manuscript. The localization data was a crucial requirement for the refinement of the proteome. and is depicted in Figure3, 5 &6, as well as Figure S4 & 6 of the manuscript. All figures were generated by other authors.

Chapter IV is a manuscript in preparation. It is intended to be submitted as invited review, as part of an editorial on Plasmodesmata in the Journal of Experimental Botany.

Estimated contribution 95%

The abstract was initially written by Wolf B. Frommer and rewritten by me. All other sections are written and edited by me. All figures were illustrated by me. Moritz Schladt and Wolf B. Frommer, supervised me in the writing process.

Chapter V contains two parts, the first is a finished manuscript and the second unpublished work by me.

First part manuscript (Identification of nuclear pore proteins at plasmodesmata)
An earlier version of the manuscript is available as preprint. I will cite the preprint here, as it contains links to all supplemental figures.

Estimated contribution 25%

Identification of nuclear pore proteins at plasmodesmata
T. Moritz Schladt*, Manuel Miras*, Jona Obinna Ejike*, Mathieu Pottier*, Lin Xi, Andrea Restrepo-Escobar, Masayoshi Nakamura, Niklas Pütz, Sebastian Hänsch, Chen Gao, Julia Engelhorn, Marcel Dickmanns, Gwendolyn V. Davis, Ahan Dalal, Sven Gombos, Ronja Lange, Rüdiger Simon, Waltraud X. Schulze, Wolf B. Frommer *bioRxiv* 2024.09.02.610746; doi: https://doi.org/10.1101/2024.09.02.610746
*indicates equal contribution/ shared first authorship

This is the main work I focused on in the last 3-4 years, as all shared first authors worked closely together and shared most tasks it is difficult to estimate precise contributions in some experiments. Here I contributed to the cloning and localization of Arabidopsis NUPs in Figure 2 and Figure 3 and Figure S4 (35% of the estimated workload). The bombardment assay in Figure 5 (~50 %), as well as the dye diffusion assay (~50 %). Callose quantification in Figure 5 was performed entirely by me.
Me, Moritz Schladt and Wolf B. Frommer mostly wrote the manuscript. Moritz Schladt illustrated the figures.

The second part of **Chapter V** (Gene editing in *P. patens*) is entirely done by me.

Chapter VI is unpublished work, the figures and text are entirely by me.

The 2xEGFP tandem bombardment data on 2% sucrose supplementation was bombarded and counted by Master student Oliver Kraft in my supervision.

All other experiments, analyzes and statistic test were performed by me.

Chapter VII is the discussion, here the figures and text are entirely by me.

Appendix
Figure 14A is from bombardments that were performed in the frame of the work for Schladt et al., 2024 (Chapter V), estimated contribution to experimental work and analysis 50%. The figure and statistics were done by me.
Figure 14B was done by Ronja Lange serves merely for illustration of the growth of the gp210 mutants.
Figure 15A is reused from Schladt et al., 2024 (Chapter V) for illustration.

All other Figures in the appendix are entirely by me.

13.2. Additional figures and tables

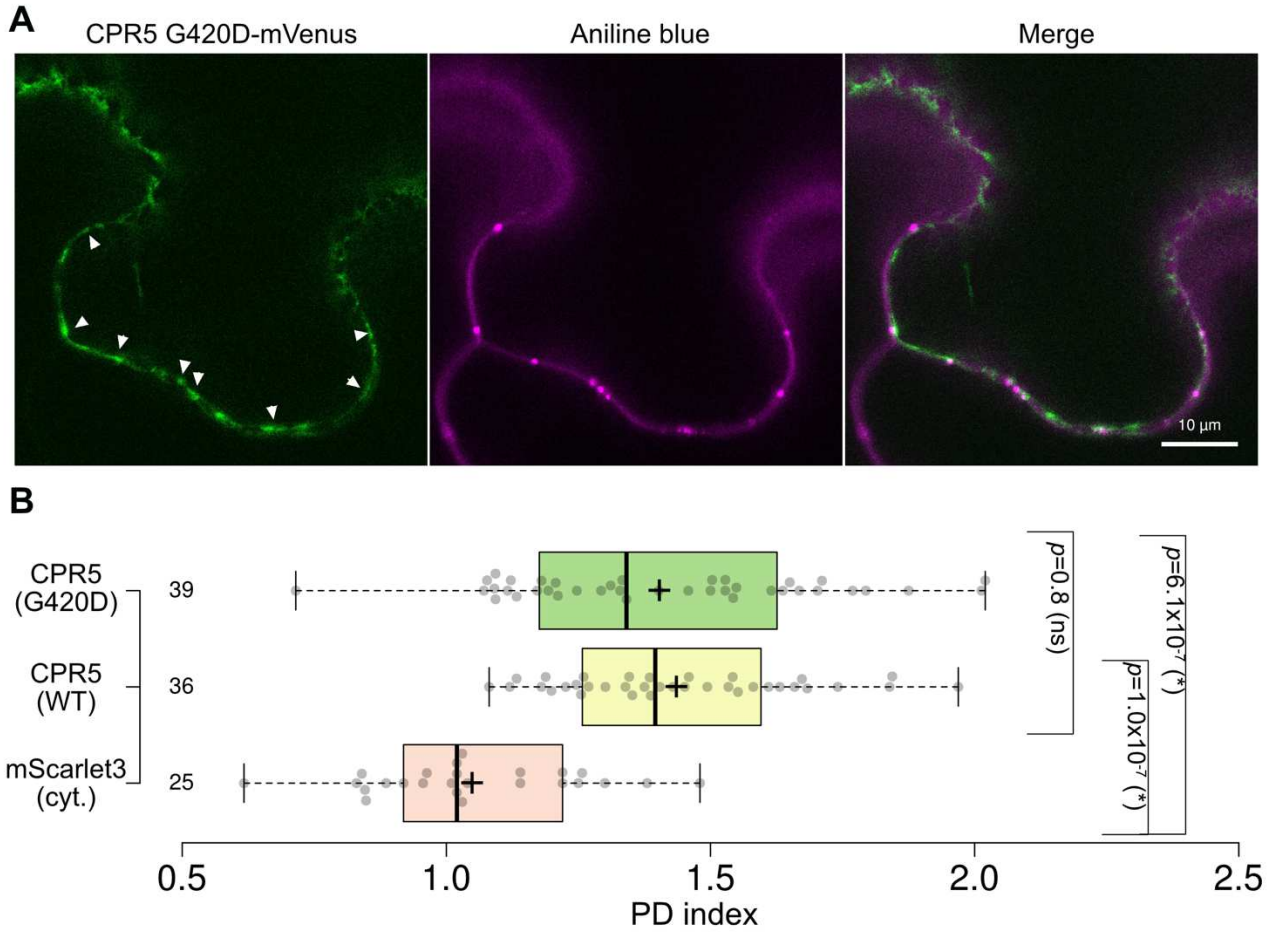

Figure 12: CPR5 G420D still localizes to PD in transient overexpression
A Localization of Arabidopsis CPR5 G420D-mVenus (green) transiently expressed under the control of the inducible XVE promoter in *N. benthamiana* epidermal cells using confocal microscopy. FP was fused to the C-terminus of CPR5 G420D. Aniline blue (magenta) was infiltrated to detect callose in pit fields as an indicator of plasmodesmata. Arrows indicate puncta with overlaying aniline blue and FP fluorescence. Localization was repeated in three independent experiments with similar results. Scale bars: 10 µm. **B** Quantification of PD indices of CPR5-mVenus (WT), CPR5 G420D-mVenus and free mScarlet3 as cytoplasmic control (cyt.). Images from three independent experiments were analyzed $n_{CPR5\ G420D}$= 39, n_{CPR5}= 36, $n_{mScarlet3}$ = 25. No significant changes (ns) were observed between WT and G420D mutant, while both had significantly increased (*) PD indices over the cytoplasmic control. The *p*-values indicated in the graph were calculated by One-way ANOVA and post-hoc Tukey HSD. Median is represented by vertical line inside the box, mean is represented by the bold +. Values between quartiles 1 and 3 are represented by box ranges, and 5th and 95th percentile are represented by error bars.

Figure 13: Examples of genotyping for edited *P. patens* lines
A Alignment of Sanger-sequenced amplicons from *Ppcpr5.1* knock-out lines with *PpCPR5.1*. The amplicons start at the *PpCPR5.1* promoter and finish in the 3'-UTR, despite their short length of ~640 bp. These results verify the full coding sequence (CDS) knock-out in the line. **B** Alignment of amplicons from *PpCPR5.1 At*G420D prime edit line, with *PpCPR5.1*. The annotations on the *PpCPR5.1* sequence indicate were the prime editor (PE) target and the reverse transcriptase (RT) template, which corresponds to the edited sequence. *P. patens* AA residue homolog to Arabidopsis CPR5 G420 is indicated. The aligned amplicons from *PpCPR5.1 At*G420D prime edit line show a precise edit from *At*G420 to D. Additionally, a second G found only in P. patens CPR5s was edited into V to ensure it does not substitute for the prime edited *At*G420 homolog. The alignments were visualized with Benchling.

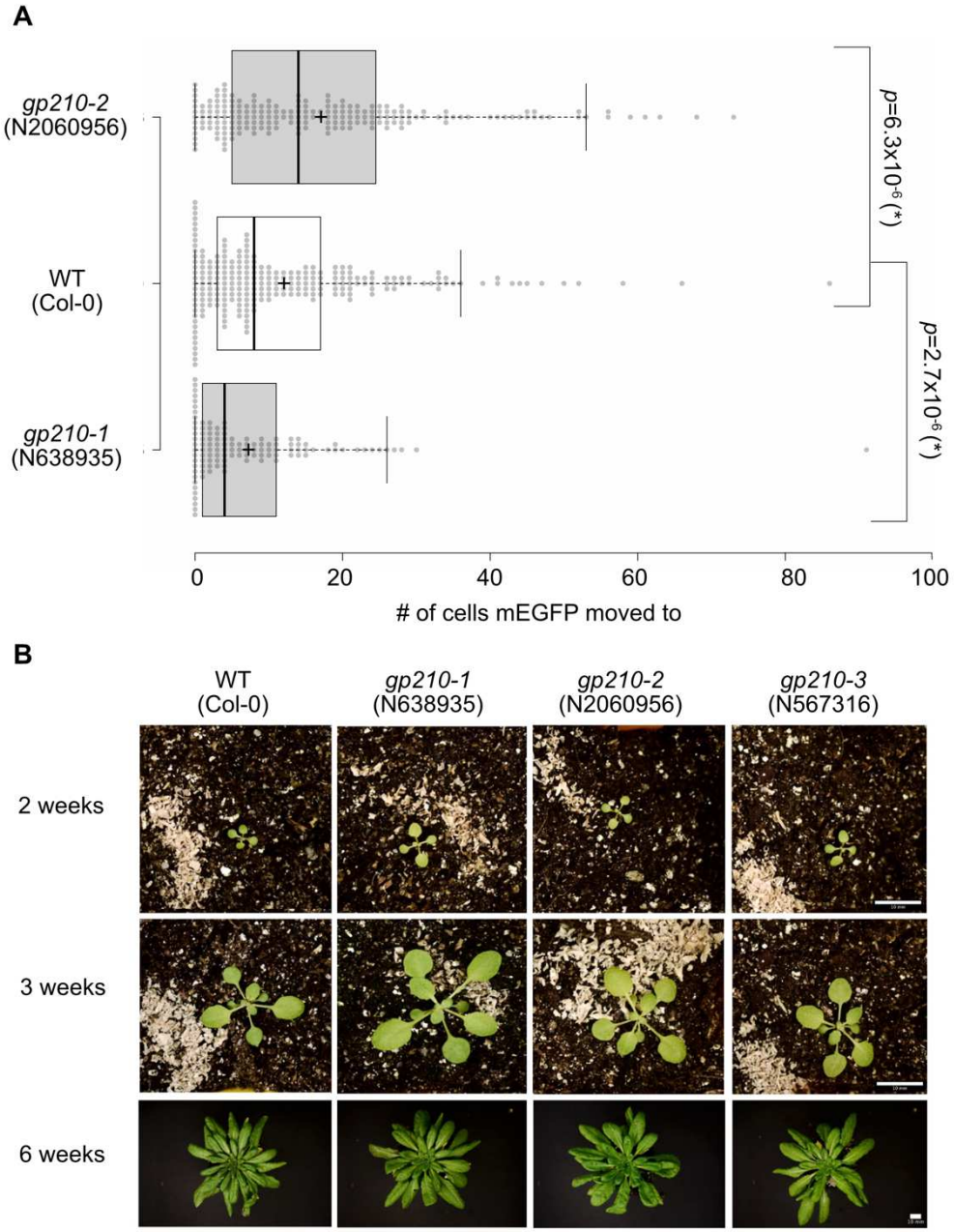

Figure 14: *gp210* mutants have altered PD transport
A Intercellular movement of mEGFP in *gp210* mutants, assayed via particle bombardment. Arabidopsis leaves were bombarded with gold particles coated with *CaMV* p35S*:mEGFP* DNA plasmids 24 h prior to the experiment. Quantification of the intercellular spread of mEGFP by counting fluorescent cells in the GFP channel. $n_{(WT)} = 244$ bombarded cells, 8 independent biological replicates. $n_{(gp210\text{-}1)} = 278$ bombarded cells, 7 independent biological replicates. $n_{(gp210\text{-}2)} = 225$ bombarded cells, three independent biological replicates. (*) indicates significant difference to WT with $p_{(gp210\text{-}1)} = 2.7 \times 10^{-6}$ and with $p_{(gp210\text{-}2)} = 6.3 \times 10^{-6}$; (Kruskal-Wallis ANOVA with post-hoc Dunn test $p = < 0.001$). Median is represented by vertical line inside the box, mean is represented by the bold +. Values between quartiles 1 and 3 are represented by box ranges, and 5th and 95th percentile are represented by error bars. **B** Growth of assayed *gp210* mutants is WT-like, *gp210-3* was not included in (A) boxplot due to insufficient n . Scale bar: 10 mm.

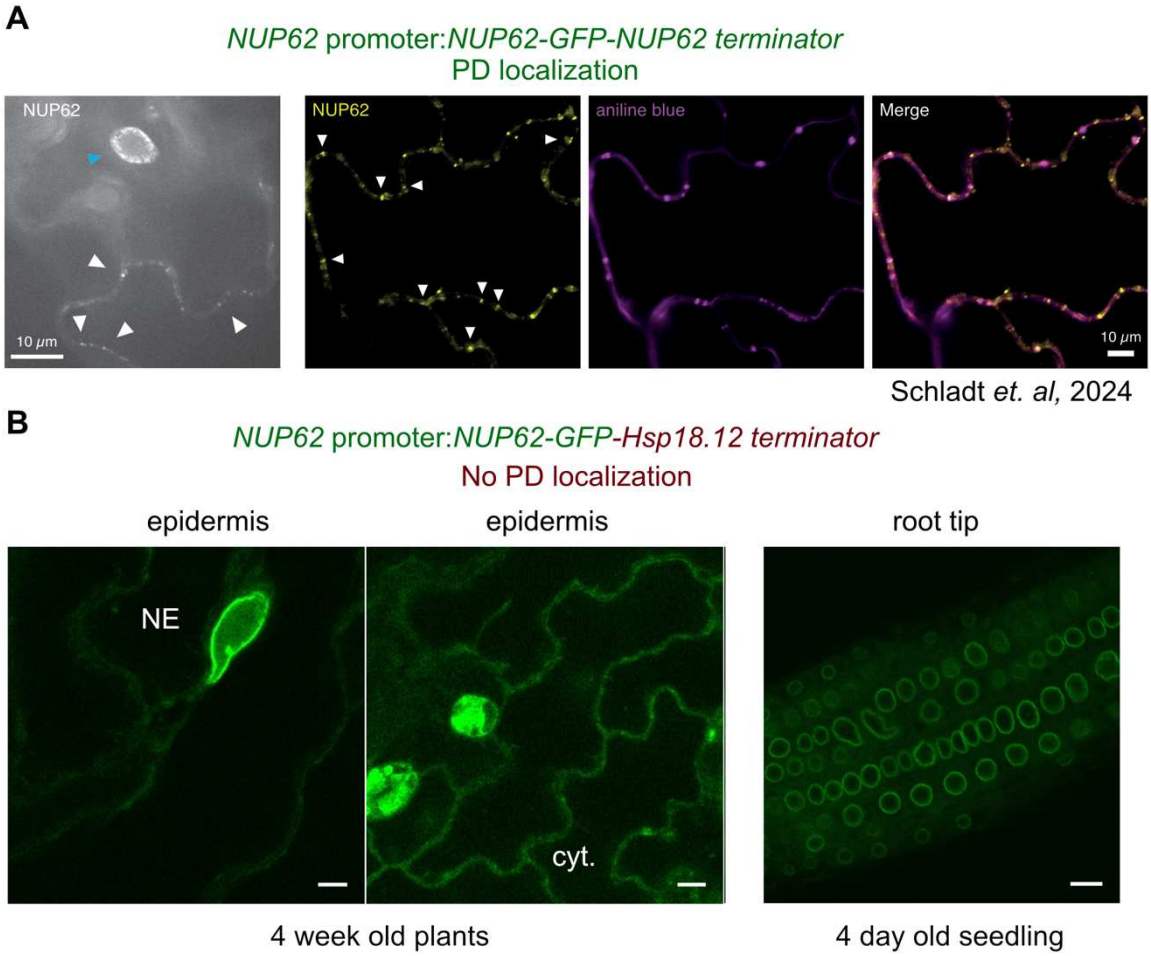

Figure 15: NUP62 PD localization might require native terminator
A *NUP62* pro:*NUP62-GFP-NUP62* ter localization to PD in *nup62* mutant background, (Figure 3, Schladt *et al*., 2024, Chapter V). **B** *NUP62* pro:*NUP62-mCitrine-Hsp18.2* ter contains non-native terminator (red) and does not localize to PD, but nuclear envelope (NE) and cytoplasm (cyt.) when expressed in *nup62* mutant background. Scale bars. 10 µm.

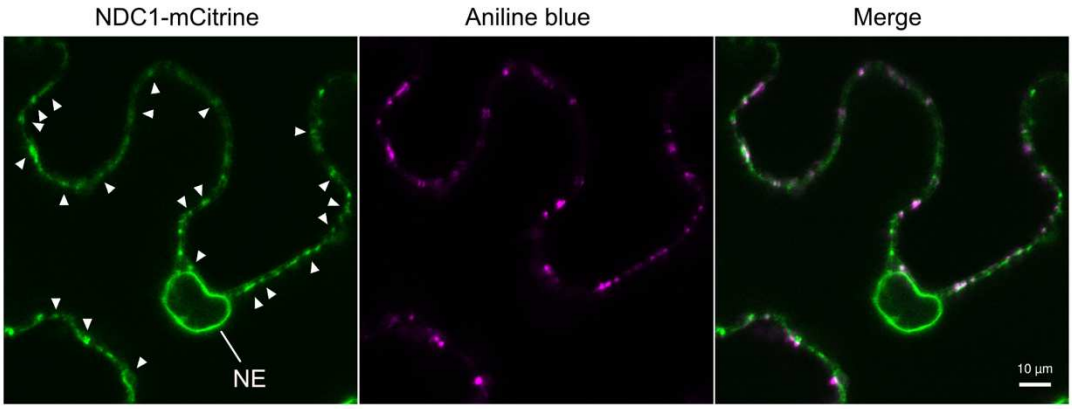

Figure 16: Transient overexpression of NDC1-mCitrine
Localization of Arabidopsis NDC1-mCitrine (green) transiently expressed under the control of the Ubi10 promoter in *N. benthamiana* epidermal cells using confocal microscopy. FP was fused to the C-terminus of NDC1. Aniline blue (magenta) was infiltrated to detect callose in pit fields as an indicator of plasmodesmata. Arrows indicate puncta with overlaying aniline

blue and FP fluorescence. NE indicates nuclear envelope localization. Localization was repeated in three independent experiments with similar results. Scale bars: 10 µm.

Table 4: Non-mobile TFs in Arabidopsis root smaller than 60 kDa SEL
Table is modified from Rim *et al*., 2011 [79], protein names and masses were annotated via Uniprot.

n	Gene ID	Entry Name	Protein names	Mass (kDa)	Mass + mcherry
1	AT5G43650	C0Z2Y1_ARATH	AT5G43650 protein	8.534	35.534
2	AT1G35515	Q0WSD8_ARATH	Putative transcription factor	11.725	38.725
3	AT2G24430	Q0WS02_ARATH	No apical meristem (NAM)-like protein	11.781	38.781
4	AT1G66380	A0A1P8AQN3_ARATH	Myb domain protein 114	12.299	39.299
5	AT1G77080	A0A1P8ARB5_ARATH	K-box region and MADS-box transcription factor family protein	14.052	41.052
6	AT5G43410	ERF96_ARATH	Ethylene-responsive transcription factor ERF096	14.343	41.343
7	AT1G80390	A0A2H1ZEF6_ARATH	Auxin-responsive protein	14.346	41.346
8	AT1G24260	Q56X18_ARATH	Floral homeotic protein, AGL9	15.922	42.922
9	AT1G20700	A0A1P8AUU8_ARATH	WUSCHEL related homeobox 14	16.815	43.815
10	AT1G01720	Q0WWG7_ARATH	Uncharacterized protein At1g01720	17.401	44.401
11	AT5G27090	B3H507_ARATH	AGAMOUS-like 54	17.951	44.951
12	AT5G09330	Q0WMC4_ARATH	Uncharacterized protein At5g09330	18.086	45.086
13	AT3G11090	LBD21_ARATH	LOB domain-containing protein 21 (ASYMMETRIC LEAVES 2-like protein 12) (AS2-like protein 12)	18.16	45.16
14	AT2G06200	A0A1P8B269_ARATH	Growth-regulating factor	20.012	47.012
15	AT5G60910	A8MRX9_ARATH	AGAMOUS-like 8	20.511	47.511
16	AT1G12630	ERF27_ARATH	Ethylene-responsive transcription factor ERF027	20.77	47.77
17	AT4G32060	C0Z2M4_ARATH	AT4G32060 protein	20.891	47.891
18	AT1G16060	A0A178W455_ARATH	ARIA-interacting double AP2 domain protein	21.346	48.346
19	AT5G11190	SHN2_ARATH	Ethylene-responsive transcription factor SHINE 2	21.409	48.409
20	AT4G32280	A0A1P8B7S3_ARATH	Auxin-responsive protein	22.384	49.384
21	AT5G35900	LBD35_ARATH	LOB domain-containing protein 35 (ASYMMETRIC LEAVES 2-like protein 27) (AS2-like protein 27)	22.816	49.816
22	AT3G06120	MUTE_ARATH	Transcription factor MUTE (Basic helix-loop-helix protein 45)	22.843	49.843
23	AT1G69120	A0A1P8AML8_ARATH	K-box region and MADS-box transcription factor family protein	23.137	50.137
24	AT4G36620	GAT19_ARATH	GATA transcription factor 19 (Protein HAN-LIKE 2)	23.319	50.319
25	AT1G12610	DRE1F_ARATH	Dehydration-responsive element-binding protein 1F (Protein DREB1F)	23.616	50.616
26	AT3G50330	HEC2_ARATH	Transcription factor HEC2 (Basic helix-loop-helix protein 37)	25.684	52.684
27	AT4G29930	A0A654FU25_ARATH	BHLH domain-containing protein	25.769	52.769
28	AT4G09960	AGL11_ARATH	Agamous-like MADS-box protein AGL11 (Protein SEEDSTICK)	26.184	53.184
29	AT1G03800	ERF77_ARATH	Ethylene-responsive transcription factor 10 (AtERF10)	26.393	53.393
30	AT3G52440	DOF35_ARATH	Dof zinc finger protein DOF3.5 (AtDOF3.5)	26.936	53.936
31	AT3G47640	BH047_ARATH	Transcription factor bHLH47 (Basic helix-loop-helix protein 47)	26.944	53.944
32	AT1G02065	Q3EDL2_ARATH	Squamosa promoter binding protein-like 8	27.504	54.504
33	AT2G41130	BH106_ARATH	Transcription factor bHLH106 (Basic helix-loop-helix protein 106)	27.978	54.978
34	AT5G19790	RA211_ARATH	Ethylene-responsive transcription factor RAP2-11 (Protein RELATED TO APETALA2 11)	28.375	55.375
35	AT4G35550	WOX13_ARATH	WUSCHEL-related homeobox 13	29.673	56.673
36	AT4G37790	HAT22_ARATH	Homeobox-leucine zipper protein HAT22	30.73	57.73
37	AT5G65670	E1A7B0_ARATH	Auxin-responsive protein	30.804	57.804
38	AT1G69490	NAC29_ARATH	NAC transcription factor 29 (AtNAC029)	31.426	58.426
39	AT5G58010	LRL3_ARATH	Transcription factor LRL3 (Basic helix-loop-helix protein 82) (AtbHLH82)	31.47	58.47
40	AT4G11140	CRF1_ARATH	Ethylene-responsive transcription factor CRF1 (Protein CYTOKININ RESPONSE FACTOR 1)	31.545	58.545
41	AT5G65320	A0A1P8BDH6_ARATH	Basic helix-loop-helix (BHLH) DNA-binding superfamily protein	31.552	58.552
42	AT1G62990	KNAT7_ARATH	Homeobox protein knotted-1-like 7 (Protein IRREGULAR XYLEM 11) (Protein KNAT7)	32.908	59.908

Table 5: Primers for *PpCPR5* amplification

Primer	Sequence
JE 344 ppCPR5.1 FW	AAAAAAGCAGGCTTAATGAGGGAAGACTATTTCGCTTGG
JE 345 ppCPR5.1 RV	CAAGAAAGCTGGGTAAATTTCCTTAACGGAAGTCAATTGG
JE 346 ppCPR5.2a FW	AAAAAAGCAGGCTTAATGCAGCATCACCTTGTCATAC
JE 347 ppCPR5.2a RV	CAAGAAAGCTGGGTACAAGAAAAGAAAGTGACAACATTTC
JE 356 c term del FW	TCTACAGGTCAGGAGCAGGGGCGG
JE 357 c term del RV	CTCCTGACCTGTAGAAATCTGAGCATGGATG

Table 6: Primers for CRISPR-Cas9 sgRNAs

Primer	Sequence
JE 359 sgRNAFwd1-Pp3c21_530	CCATGCTATGTCTCTCATGAGATGA
JE 360 sgRNAFwd2-Pp3c21_530	CCATGTTCGCTTGGCTCTTTCCGGG
JE 361 sgRNAFwd3-Pp3c21_530	CCATGAGCCACTCAACACCTGAGA
JE 362 sgRNARev1-Pp3c21_530	AAACTCATCTCATGAGAGACATAGC
JE 363 sgRNARev2-Pp3c21_530	AAACCCCGGAAAGAGCCAAGCGAAC
JE 364 sgRNARev3-Pp3c21_530	AAACTCTCAGGTGTTGAGTGGCTC
JE 365 sgRNAFwd1-Pp3c22_5670	CCATGACATTTCGCTATGAGATGG
JE 366 sgRNAFwd2-Pp3c22_5670	CCATGTTATGGTGTGAAGACTGATG
JE 367 sgRNAFwd3-Pp3c22_5670	CCATGAACCTTGTGTATTCGCCTG
JE 368 sgRNARev1-Pp3c22_5670	AAACCCATCTCATAGCGAAATGTC
JE 369 sgRNARev2-Pp3c22_5670	AAACCATCAGTCTTCACACCATAAC
JE 370 sgRNARev3-Pp3c22_5670	AAACCAGGCGAATACACAAGGTTC
JE 430 PpCPR5.1 (249/fw) FW	ccatgCTTTCCGGGTGGCAGATGTA
JE 431 PpCPR5.1 (249/fw) RV	aaacTACATCTGCCACCCGGAAAGc
JE 432 PpCPR5.2 (182/r) FW	ccatgAACCTGAAGCAGATGGACAC
JE 433 PpCPR5.2 (182/r) RV	aaacGTGTCCATCTGCTTCAGGTTc
JE 434 PpGp210 (86/r) FW	ccatgCCTATCAGTATGTGAACGAG
JE 435 PpGp210 (86/r) RV	aaacCTCGTTCACATACTGATAGGc
JE 436 PpHOS1.1 (249/r) FW	ccatgATAGTGCTGAAACACTACAG
JE 437 PpHOS1.1 (249/r) RV	aaacCTGTAGTGTTTCAGCACTATc
JE 438 PpIMB3 (222/f) FW	ccatgCACGATGGCGATGGATACGG
JE 439 PpIMB3 (222/f) RV	aaacCCGTATCCATCGCCATCGTGc
JE 440 PpNDC1 (245/r) FW	ccatgTATGCTCGGCTTAACTGACG
JE 441 PpNDC1 (245/r) RV	aaacCGTCAGTTAAGCCGAGCATAc
JE 442 PpNUP54.1 (38/r) FW	ccatgCATGTCTCGTTTCAAAACAG
JE 443 PpNUP54.1 (38/r) RV	aaacCTGTTTTGAAACGAGACATGc
JE 444 PpNUP58 (5/r) FW	ccatgAAACTTACTGTTCCTGCCGA
JE 445 PpNUP58 (5/r) RV	aaacTCGGCAGGAACAGTAAGTTTc
JE 446 PpNUP62_(95/fw) FW	ccatGCCAGCATTTGGTTCTACCG
JE 447 PpNUP62_(95/fw) RV	aaacCGGTAGAACCAAATGCTGGC
JE 448 PpNUP98 (79/f) FW	ccatgCAATGTTAGGAATTGCGTTG
JE 449 PpNUP98 (79/f) RV	aaacCAACGCAATTCCTAACATTGc
JE 450 PpSec13.1 (130/r) FW	ccatgTCAAAGTCAGAGGCTGCCAT
JE 451 PpSec13.1 (130/r) RV	aaacATGGCAGCCTCTGACTTTGAc
JE 452 PpTrp/NUA (142/f) FW	ccatGTGGCGAGTGGACTATTAGC
JE 453 PpTrp/NUA (142/f) RV	aaacGCTAATAGTCCACTCGCCAC

Table 7: Primers for *P. patens* genotyping

Primer	Sequence
JE 387 EGFP gt RV	TTGCCGTCCTCCTTGAAGTC
JE 388 mCherry gt RV	CAAGTAGTCGGGGATGTCGG
JE 389 CPR5.1 Nt gt RV	TTCCCAGGAGCGCATCAATT
JE 390 CPR5.1 3' (2) ot RV	TGCACCTCTTACTTGCACCT
JE 391 CPR5.1 3'-UTR gt RV	TCGAAGCTTTGCATAGGCCA
JE 392 CPR5.1 pro gt FW	AGTTTGCGGCACCTACGTTA
JE 393 CPR5.1 Ct gt FW	CGCTGATGAAATGGTGGCAG
JE 394 CPR5.2 3' (2) ot RV	ATTTGGCCCTCAGTGAGAGC
JE 395 CPR5.2 3' gt RV	GCTCGTCAAAAGGCTCAGGA
JE 396 CPR5.2 Ct gt FW	TCAACTGCTTACGCGGACTT
JE 397 CPR5.2 pro gt FW	GCGGGGAGCTTTGAGAAGAA

Table 8: Nuclear transport candidates in *P. patens* cell wall fractions

Leading protein ID	CW_LFQav	NUPs	2nd PDscore rank
Pp3c11_22120V3.5.p	18.3272555	IMB3	161
Pp3c20_18280V3.3.p	18.0410697	RAN GTPase 3	555
Pp3c8_8020V3.2.p	16.1934806	Tpr/NUA	778
Pp3c3_6080V3.3.p	17.8470274	Nup50a	898
Pp3c19_9370V3.2.p	17.0952315	Sec13	1320
Pp3c22_17920V3.2.p	16.5704408	Sec13	1341
Pp3c1_14980V3.1.p	18.7329501	IMPA1	1552
Pp3c1_19400V3.2.p	18.0065795	IMPA1	1572
Pp3c10_5440V3.7.p	17.4814436	XPO1	1821
Pp3c11_26710V3.2.p	18.4910508	IMB1	1924
Pp3c15_14630V3.3.p	17.6832459	Nup62	2335
Pp3c18_21020V3.3.p	17.2303324	Rae1	2712
Pp3c27_5090V3.5.p	17.9340418	IMB2	3592
Pp3c3_17910V3.6.p	16.9553538	Nup98a	3649
Pp3c7_5160V3.5.p	18.4809114	IMB1	4222
Pp3c8_3950V3.2.p	16.2527393	Nup98a	4323
Pp3c9_22260V3.2.p	18.3032236	IPO8	4393
Pp3c23_8300V3.3.p	20.3323453	RAN GTPase 3	4666
Pp3c1_15750V3.2.p	19.1950883	IMPA1	4737

Table 9: Nuclear transport related proteins in Arabidopsis shoots PD proteome

AGIcode	PD Enrichment score (transformed)	PD Feature score (transformed)	PD score (V1.5)	PD confidence cluster	NUP	NUP part	Go term
AT5G06120	0.85686247	0.53846154	1.395324	HC	XPO7	importin-beta	Nuclear transport
AT5G19320	0.82373033	0.53846154	1.36219187	HC	RANGAP2	RANGAP	Nuclear transport
AT1G33410	1	0.30769231	1.30769231	HC	NUP160	outer ring	Nuclear transport
AT1G55540	1	0.30769231	1.30769231	HC	NUP214	cytoplasmic NUP	Nuclear transport
AT1G63810	1	0.30769231	1.30769231	HC	NUCLEOLAR	n.a	Nuclear transport
AT3G03110	1	0.30769231	1.30769231	HC	XPO1B	importin-beta	Nuclear transport
AT3G18610	1	0.30769231	1.30769231	HC	RANGAP1	RANGAP1	
AT1G52380	0.76264643	0.53846154	1.30110797	HC	NUP50a	basket	
AT5G58590	0.75101301	0.53846154	1.28947455	HC	RANBP1	RANBP	Nuclear transport
AT4G13350	0.73860678	0.53846154	1.27706832	HC	NIG	RAN-GTPase	Nuclear transport
AT2G30060	0.73060539	0.53846154	1.26906693	HC	RanBP1b	n.a	Nuclear transport
AT1G07140	0.68832764	0.53846154	1.22678917	HC	SIRRANBP	RAN binding protein	Nuclear transport
AT2G39810	0.81553746	0.30769231	1.12322977	HC	ELYS/HOS1	outer ring	
AT2G41620	0.80840544	0.30769231	1.11609775	HC	NUP93a	inner ring	Nuclear transport
AT1G80680	0.80790772	0.30769231	1.11560003	HC	NUP96	outer ring	Nuclear transport
AT5G62600	0.80431643	0.30769231	1.11200874	HC	MOS14	importin-beta	Nuclear transport
AT3G63130	0.56601563	0.53846154	1.10447717	HC	RANGAP1	RANGAP1	Nuclear transport
AT1G02690	0.79207798	0.30769231	1.09977029	HC	IMPA6	importin alpha	Nuclear transport
AT5G46070	0.55988	0.53846154	1.09834154	HC	GBPL3	basket-nucleoskelteon	
AT2G40730	0.78542359	0.30769231	1.0931159	HC	CTEXP	n.a	Nuclear transport
AT5G51200	0.77911612	0.30769231	1.08680843	HC	NUP205	inner ring	
AT5G02770	0.7765703	0.30769231	1.08426261	HC	XPO1B	exportin	Nuclear transport
AT3G55620	0.76769337	0.30769231	1.07538568	HC	RPL5A	n.a	Nuclear transport
AT1G64350	0.74954011	0.30769231	1.05723242	HC	SEH1	outer ring	
AT2G05120	0.74155318	0.30769231	1.04924549	HC	NUP133	outer ring	Nuclear transport
AT5G03070	0.74105814	0.30769231	1.04875044	HC	IMPA9	importin alpha	Nuclear transport
AT4G32910	0.72911871	0.30769231	1.03681102	HC	NUP85	outer ring	Nuclear transport
AT2G16950	0.70684154	0.30769231	1.01453384	HC	IMB2	importin-beta	Nuclear transport
AT1G67120	0.70248428	0.30769231	1.01017658	HC	MOS14	n.a	Nuclear transport
AT1G12930	0.67073791	0.30769231	0.97843022	HC	TNPO3	importin-beta	Nuclear transport
AT1G27310	0.66632568	0.30769231	0.97401798	HC	NTF2a	NTR	Nuclear transport
AT5G20010	0.42886018	0.53846154	0.96732172	HC	RAN1	RAN-GTPase	Nuclear transport
AT3G53110	0.64848435	0.30769231	0.95617666	HC	LOS4	n.a	Nuclear transport
AT3G59020	0.60951494	0.30769231	0.91720725	HC	IPO8	importin-beta	Nuclear transport
AT2G31660	0.6069493	0.30769231	0.91464161	HC	SAD2	importin-beta	Nuclear transport
AT1G79280	0.59706265	0.30769231	0.90475496	HC	TPR/NUA	basket	Nuclear transport
AT1G26170	0.58348183	0.30769231	0.89117413	HC	IMB5	importin-beta	Nuclear transport
AT4G27640	0.55169723	0.30769231	0.85938954	HC	IMB4	importin-beta	Nuclear transport
AT5G19820	0.54871093	0.30769231	0.85640324	HC	IMB3	importin-beta	Nuclear transport